Universidade do Minho
Escola de Engenharia

Ihsan Çaha

Bio-functionalization of tribocorrosion resistant β type Ti-based hybrid surfaces

FCT
Fundação para a Ciência e a Tecnologia
MINISTÉRIO DA EDUCAÇÃO E CIÊNCIA

POPH
QUALIFICAR É CRESCER.

QREN
QUADRO DE REFERÊNCIA ESTRATÉGICO NACIONAL
PORTUGAL 2007.2013

Governo da República Portuguesa

UNIÃO EUROPEIA
Fundo Social Europeu

Ihsan Çaha **Bio-functionalization of tribocorrosion resistant β type Ti-based hybrid surfaces**
Uminho | 2021

february 2021

Universidade do Minho
Escola de Engenharia

Ihsan Çaha

Bio-functionalization of tribocorrosion resistant β type Ti-based hybrid surfaces

PhD thesis
in Biomedical Engineering

Work developed under the supervision of:
Ana Maria Pires Pinto
Fatih Toptan

february 2021

DIREITOS DE AUTORIA E CONDIÇÕES DE UTILIZAÇÃO DO TRABALHO POR TERCEIROS

Acknowledgements

The PhD journey has been an unimaginable experience, the most intense, and enriching period of my life. I would like to thank all who have greatly contributed to the success of this thesis.

Firstly, to my supervisor, Prof. Ana Maria Pinto for all the support, friendship, and sharing her immense knowledge. There is no word to express my sincere gratitude to my co-supervisor Dr. Fatih Toptan, for his motivation, guidance, friendship, encouragement, and support throughout the all journey.

To Prof. Elena Gordo, Dr. Sophia Alexandra Tsipas, and PhD student Caterina Chirico Rodríguez, the project partner from UC3M - Universidad Carlos III Madrid, for their kindness, comments, suggestions, and all the support along the four years.

To Prof. Carlos Roberto Grandini and his team, another project partner from UNESP - Universidade Estadual Paulista, for their kindness, comments, suggestions, and all the support.

To Prof. Luis Rocha, for his availability for scientific discussions, sharing his experience and broad knowledge in the area, providing key ideas for the successful development of the work.

To Prof. Paulo Noronha Lisboa-Filho and his team, project partner from UNESP - Universidade Estadual Paulista, for all their help, support, and scientific discussion.

To Prof. José Humberto Dias da Silva and his PhD student Lucas Jorge Affonço, project partner from UNESP - Universidade Estadual Paulista, for their always being available for help, support, and comments.

To Prof. Rodrigo Cardoso de Oliveira from USP - Universidade de São Paulo, for contribution and comments for improve this work.

To Prof. Paulo Ferreira, Dr. Enrique Carbó-Argibay and Dr. Alex Bondarchuk from INL - International Iberian Nanotechnology Laboratory, for the remarkable kindness and sympathy in welcoming me and precious mentoring during my stay at the INL.

To several colleagues and friends from our lab that I have been privileged to work. To Prof. Aníbal Guedes, Ana Costa, Luís Sousa, Caio Xavier, Bruno Costa, Natália Costa, Vinicius Manso and so many other researchers and students that had passed there.

To Dr. Alexandra Alves for the support, motivation, guidance, discussions and help during all this period.

To Dr. Edith Ariza, for always encouraging, motivation, and helping me.

Most importantly, I would especially like to thank my family. My wife, Semra, for her love and constant support, for all the late nights and early mornings, and for keeping me sane over the past years. Thank you for being my muse, editor, and proof-reader. But above of all, thank you for being my best friend, I owe you everything. Also, my beautiful daughters, Zehra Sureyya and Azra Ema who are the ones to whom I dedicate this thesis.

My acknowledgement to all my family, all of their members whose names are uncountable. Without them, nothing would be possible.

Finally, I would like to acknowledge the Portuguese Foundation for Science and Technology (FCT) Portugal, for the financial support provided through the grant NORTE-08-5369-FSE-000012.

STATEMENT OF INTEGRITY

I hereby declare having conducted this academic work with integrity. I confirm that I have not used plagiarism or any form of undue use of information or falsification of results along the process leading to its elaboration.

I further declare that I have fully acknowledged the Code of Ethical Conduct of the University of Minho.

Bio-functionalization of tribocorrosion resistant β type Ti-based hybrid surfaces

Abstract

β-Ti alloys are known for their very low Young's modulus and biocompatibility, hence they are considered as attractive metallic materials for long-term bone implant applications. However, β-Ti alloys are poor wear resistant and typically bioinert materials, thus their surfaces need to be modified to have wear resistant and bioactive properties.

The present PhD work aimed at developing TiN rich and bio-functionalized surfaces on low Young's modulus β-type Ti alloys to improve mechanical, triboelectrochemical, and biological properties. The β-type Ti-Nb alloys and TiN reinforced Ti-Nb composites were processed by both casting and powder metallurgy routes. The bio-functionalization was performed by using different surface modification approaches as anodic treatments and PVD coatings. The corrosion and tribocorrosion behavior of base material as well as the biofunctionalized surfaces were evaluated by using the electrochemical and triboelectrochemical methods in physiological solutions at body temperature.

The results showed that the cast and P/M β-type Ti-Nb alloys present a poor degradation behavior as compared to both the α+β-type Ti-Nb and commercial Ti-6Al-4V alloys. The adhesion, corrosion, and tribocorrosion behavior of the nanotubular layer formed on β-type Ti-40Nb alloy were drastically improved after a second-step anodic treatment in fluoride-free electrolyte due to the formation of an additional oxide layer in the interface, followed by heat treatment that yielded the transformation from amorphous to mixed anatase and rutile. On the other hand, the Ti-40Nb reinforced with TiN particle and further functionalization by two-step anodic treatment followed by heat treatment significantly improved the degradation behavior of the composites when compared with unreinforced alloy due to the load-carrying role of the hard reinforcement phases that gave support to the functionalized surface layer. In the case of ZnO/TiN coated Ti-12Nb alloy, results indicated that double-layer coated samples showed better degradation resistance compared to uncoated and single TiN coating samples. Particularly, a novel multi-functional material has been developed by hard TiN particle reinforcement following by bio-functionalization of its surface suggested as solution to overcome the pointed clinical limitations of load-bearing implants.

Keywords: β-type Ti alloys; Metal matrix composites; Corrosion; Tribocorrosion; Bio-functionalization

Biofuncionalização de superfícies hibridas de ligas de β-Ti resistentes à tribocorrosão

Resumo

As ligas β-Ti são consideradas um material promissor para aplicações ortopédicas devido ao seu baixo módulo de Young e biocompatibilidade. No entanto, estas ligas apresentam uma baixa resistência ao desgaste e são, normalmente, bioinertes, sendo por isso necessário proceder à modificação das suas superfícies de forma a torná-las bioativas e resistentes ao desgaste.

Este trabalho teve como objetivo a bio-funcionalização de superfícies ricas em TiN em de ligas β-Ti de baixo módulo de Young, de forma a melhorar as propriedades mecânicas, triboelectroquímicas e biológicas. As ligas β Ti-Nb bem como os compósitos Ti-Nb reforçados com TiN foram produzidas por metalurgia dos pós e por fundição. A bio-funcionalização foi efetuada recorrendo a diferentes técnicas, tais como tratamentos de anodização e deposição por PVD. O comportamento à corrosão e tribocorrosão dos dos materiais base e após a sua bio-funcionalização foi avaliado recorrendo a técnicas eletroquímicas e triboelectroquímicas em soluções fisiológicas à temperatura corporal.

Os resultados mostram que as ligas β Ti-Nb e Ti-6Al-4V (comercial) apresentam melhor resistência à degradação que as liga β-Ti. A adesão, o comportamento à corrosão e tribocorrosão da camada de nanotubos de TiO_2 formados na liga β Ti-40Nb foram significativamente melhoradas após um segundo tratamento de anodização seguido de tratamento térmico, devido à formação, entre o material de base e a camada nanotubular, de uma camada adicional de óxido e à transformação da fase amorfa numa mistura de anátase e rútilo. O comportamento à corrosão e tribocorrosão dos compósitos Ti-40Nb/TiN bio-functionalizados por anodização em dois passos seguido de tratamento térmico é francamente superior ao da liga Ti-40Nb devido ao efeito de transferência de carga das partículas de reforço que dão suporte à camada funcionalizada. Por outro lado, a dupla camada ZnO/TiN depositada na liga Ti-12Nb resulta numa melhor resistência à degradação em comparação com a liga base ou com o revestimento de TiN.

O novo material multifuncional, desenvolvido através de reforços de partículas duras de TiN seguido de bio-funcionalização de sua superfície, surge como uma solução que pode ultrapassar limitações clínicas apontadas aos materiais tradicionalmente usados em implantes.

Keywords: Ligas β-Ti; Compósitos de matriz metálica; Corrosão; Tribocorrosão; Bio-funcionalização

Table of Content

List of Abbreviations

Al_2O_3	Alumina
B-GP	β-glycerophosphate disodium salt pentahydrate
β-Ti	Beta type titanium
CA	Calcium acetate monohydrate
C	Carbon
Ca	Calcium
CaP	Calcium phosphate
$Ca_2(PO_4)_2$	Calcium Phosphate
CO_2	Carbon Dioxide
COF	Coefficient of Friction
CPE	Constant phase element
cp-Ti	Commercially pure Titanium
EDS	Energy Dispersive X-Ray Spectroscopy
EEC	Equivalent electrical circuit
$E_{(i=0)}$	Corrosion potential
EIS	Electrochemical impedance spectroscopy
E_{OCP}	Open circuit potential
F^-	Fluoride
Fe	Iron
FEG-SEM	Field emission gun scanning electron microscope
FIB	Focused ion beam
HA	Hydroxyapatite
HF	Hydrofluoric Acid
HNO_3	Nitric Acid
i_{corr}	Corrosion current density
i_{pass}	Passivation current density
K	Potassium
MAO	Micro-arc oxidation
MMC	Metal matrix composite

NTs	Nanotubes
Na	Sodium
NaF	Sodium Fluoride
O	Oxygen
OCP	Open Circuit Potential
OH^-	Hydroxide
P	Phosphorous
PBS	Phosphate Buffered Saline
P/M	Powder metallurgy
Pt	Platinum
Ra	Average Roughness
SCE	Saturated Calomel Electrode
SD	Standard Deviation
SEM	Scanning Electron Microscopy
TEM	Transmission Electron Microscopy
Ti	Titanium
TiO_2	Titanium Dioxide
TNT	TiO_2-based nanotubes
XRD	X-ray diffraction

List of Figures

Chapter 1:

Chapter 2:

Chapter 3:

Chapter 4:

Chapter 5:

Chapter 8:

Chapter 9:

Chapter 10:

List of Tables

Chapter 10:

Chapter 1: General introduction

1.1. Motivation

The global hip replacement implants market size was estimated at USD 5.56 billion in 2018 and is predicted to grow with the rate of 4.7% over the forecast period. Some major growth propelling factors for the market is an increase in demand for hip replacement surgical procedures, a rise in the geriatric population, and a high prevalence of lower extremity conditions resulted from osteoarthritis, osteoporosis and hip ailments [1,2]. For instance, according to a report by Osteoarthritis Research Society International, around 130 million people globally will suffer from Osteoarthritis by 2050 [2]. In an immortal case, all hip replacements will eventually fail because of processes such as infection, fracture, or a combination of normal tribological and biological processes, such as loosening and wear [3]. Also, the long-term survivorship of the total hip replacement is increasingly relevant due to rising the life expectancy. The main ultimate aim has not been achieved that is all hip replacements provide normal pain-free function for the rest of the recipients' lives [4].

Ti and its alloys are the most attractive metallic biomaterials used in biomedical applications due to their high strength, excellent corrosion resistance and good biocompatibility. However, there are still some major clinical issues, namely, (i) the mismatch between Young's modulus of bone and implant material, (ii) low tribocorrosion resistance, and (iii) lack of bioactivity. The mostly used α-type and α + β-type Ti based implant materials have Young's modulus around 100–120 GPa, whereas Young's modulus of bone varies in a range of 4–30 GPa [5,6]. The difference between Young's modulus of the implant and bone lead to bone resorption and eventually implant loosening, so-called stress shielding [7]. Poor tribocorrosion properties raising a particular concern for biomedical load bearing implants since they are in contact with corrosive body fluids and being subjected to relative movements resulting in the subsequent release of metallic ions and wear debris to the body, which can cause osteolysis and eventually implant failure [8]. Ti-based alloys are bioinert materials, however, their bioactivity can be improved through suitable surface modifications. In order to overcome these issues, β-Ti alloys are being developed, which are known for their low Young's modulus, non-toxicity and favorable biocompatibility [9]. Moreover, studies are being performed on those alloys in order to improve their mechanical, tribological and biological properties by applying various surface modification techniques. Regarding the stress shielding effect, the porous surfaces have been produced to decrease the Young's modulus mismatch. In case of low tribocorrosion behavior, the hard material coatings and Ti-based metal matrix composites (MMCs) have been studied. In order to improve biological properties of Ti and its alloys, bio-functionalization techniques have been carried out such as hydroxyapatite (HA) coatings and electrochemical treatments intending for creating nanotubular or porous oxide surfaces having bioactive

and/or antimicrobial agents. However, those individual approaches are lacking to provide a complete solution by failing on some points, such as the poor adhesion to substrate and the brittleness of the hard coatings, weak mechanical properties of porous metallic structures, low bioactivity on the hard ceramic phase reinforced MMC structures.

β-type Ti alloys are considered as a promising biomaterial for various orthopedic applications, however, lack of bioactivity and low tribocorrosion resistance are still major concerns. The present PhD work hypothesize that bio-functionalized TiN rich surfaces developed on low Young's modulus β-type Ti alloys can provide improved mechanical, triboelectrochemical and biological properties as compared to Ti and its alloys (Fig. 1). To validate this hypothesis, the main aim of this project was to build a bio-multifunctional material, based on low Young's modulus β-Ti alloys with hybrid bioactivated TiN rich hard surfaces.

The main innovative objectives intended to point the validation process of the main hypothesis are listed below:

- Bio-functionalization of MMCs and TiN thin film surfaces by using electrochemical treatment and PVD treatment, respectively, through incorporation of bioactive agents such as calcium, phosphorus and ZnO.
- Investigation of degradation mechanisms of bio-functionalized hybrid surfaces and TiN\ZnO coated surfaces.

Thus, this PhD work expects at finding solutions to the major clinical concerns related to the Ti-based implant materials (Fig. 1), namely;

- The stress shielding effect is aimed to be reduced by using low Young's modulus Ti-Nb alloys.
- Low tribocorrosion resistance is aimed to be increased by tribocorrosion-resistant hybrid surfaces.
- Lack of bioactivity is aimed to be improved by surface bio-functionalization, as well as by the incorporation bioactive agents.

1.2. Structure of thesis

This thesis is composed of 11 chapters. A schematic diagram of the summarized objectives together with research lines and chapters are presented in Fig. 1. Two research lines were carried out as "Bio-functionalized MMC" and "Bio-functionalized hybrid coating" in order to overcome the pointed limitations for load-bearing implants.

In order to better understand the structure of thesis, a brief overview of each section and their connections explaining as below.

The main goal of **Chapter 1** is to introduce the motivating factors that inspired the development of this project. Also, the innovative objectives pointed out together with the main hypothesis of this thesis.

Chapter 2 presents the current state of scientific knowledge on the relevant topics related with this thesis. In this chapter, an overview was presented to the available surface functionalization techniques to improve the biological properties of β-Ti alloys. Mechanical, physical, chemical, and electrochemical treatments, as well the immobilization of bio-functional molecules were discussed. The proper surface modification techniques were addressed in order to improve the bioactivity, biocompatibility, haemocompatibility, wear and/or corrosion, behavior of the β-Ti. This paper is published in Journal of Bio- and Tribo-Corrosion (2020).

Chapter 3 investigates the corrosion and tribocorrosion behavior of Ti-Nb alloys processed by powder metallurgy. The sintering time and the addition of Fe, being one of the most efficient β stabilizer alloying element, in Ti-Nb alloy was studied under different tribocorrosion environments. This paper is published in Metallurgical and Materials Transactions A (2020).

Similarly, the corrosion and tribocorrosion behavior of the cast alloys was reported in **Chapter 4.** The investigation of corrosion behavior of cast Ti-Nb alloys compared with the commercial Ti-6Al-4V alloy through an immersion period of 21 days. Also, the tribocorrosion behavior was investigated under open-circuit potential by using a ball-on-plate tribometer. Subsurface of wear track was studied and possible wear mechanisms for each alloy was illustrated. This paper is published in Corrosion Science (2020).

As a comparison of the processing method, **Chapter 5** investigates the corrosion and tribocorrosion behavior of Ti-12Nb alloy processed by casting and sintering, and compares the results with the commercial Ti-6Al-4V alloy. Different electrochemical techniques were used to access the corrosion behavior. Tribocorrosion behavior was studied at open circuit potential under continuous and intermittent sliding, and at anodic potentiostatic condition under continuous sliding. This paper is published in Corrosion Science (2020).

Based on the scientific knowledge acquired from Chapters 3, 4 and 5, **Chapter 6** aimed to form TiO_2-based nanotubular surfaces on Ti-40Nb alloy to improve its tribocorrosion behavior. The corrosion and tribocorrosion behavior of TiO_2-based surfaces was investigated. Also, a promising method to develop

TiO_2-based nanotubular surfaces on Ti-40Nb alloy with enhanced adhesion and improved tribocorrosion was proposed. This paper is published in Applied Surface Science (2020).

Chapter 7 is related to another common surface modification method, TiN coating, to improve wear resistance of β-Ti alloys. Before performing directly on novel alloys, initially the corrosion and tribocorrosion behavior of TiN thin films produced by RF sputtering on commercial Ti, and the influence of the deposition time on the tribocorrosion mechanisms was studied by characterizing worn surfaces and sub-surfaces. This paper is published in Surface Coatings and Technology (2019).

In **Chapter 8**, a novel multi-functional material has been aimed to be developed by incorporation of hard TiN particle reinforcement following by bio-functionalization through Ca and P rich oxide layer in order to overcome not only on the poor tribocorrosion behavior but also lack of bioactivity of β-Ti alloys. Also, corrosion and tribocorrosion behavior of this multi-functional material was investigated in phosphate buffer solution (PBS) at body temperature. This paper is published in Surface Coatings and Technology (2021).

In **Chapter 9,** another a novel multi-functional material has been intended to be developed through TiO_2-based nanotubular surface formation on TiN reinforced β-type Ti40Nb alloy. The corrosion and tribocorrosion behavior were investigated in PBS at body temperature. While corrosion behavior was studied by using open circuit potential, potentiodynamic polarization, and electrochemical impedance spectroscopy, tribocorrosion behavior was evaluated by reciprocating against an alumina ball during 2 h under normal load of a 0.5 N at open circuit potential. This paper is submitted to Corrosion Science.

As a following study of Chapter 7, the ZnO and TiN coatings performed on Ti-12Nb alloy is presented in **Chapter 10**. The adhesion and degradation behavior of duplex layer coating on Ti-12Nb alloy was investigated. This paper is published in Surface and Coatings Technology (2021).

The main outcomes and relations between the eight previous chapters described as a general discussion in **Chapter 11**. Also, the main conclusions are given together with proposed future works for further improvement of this project.

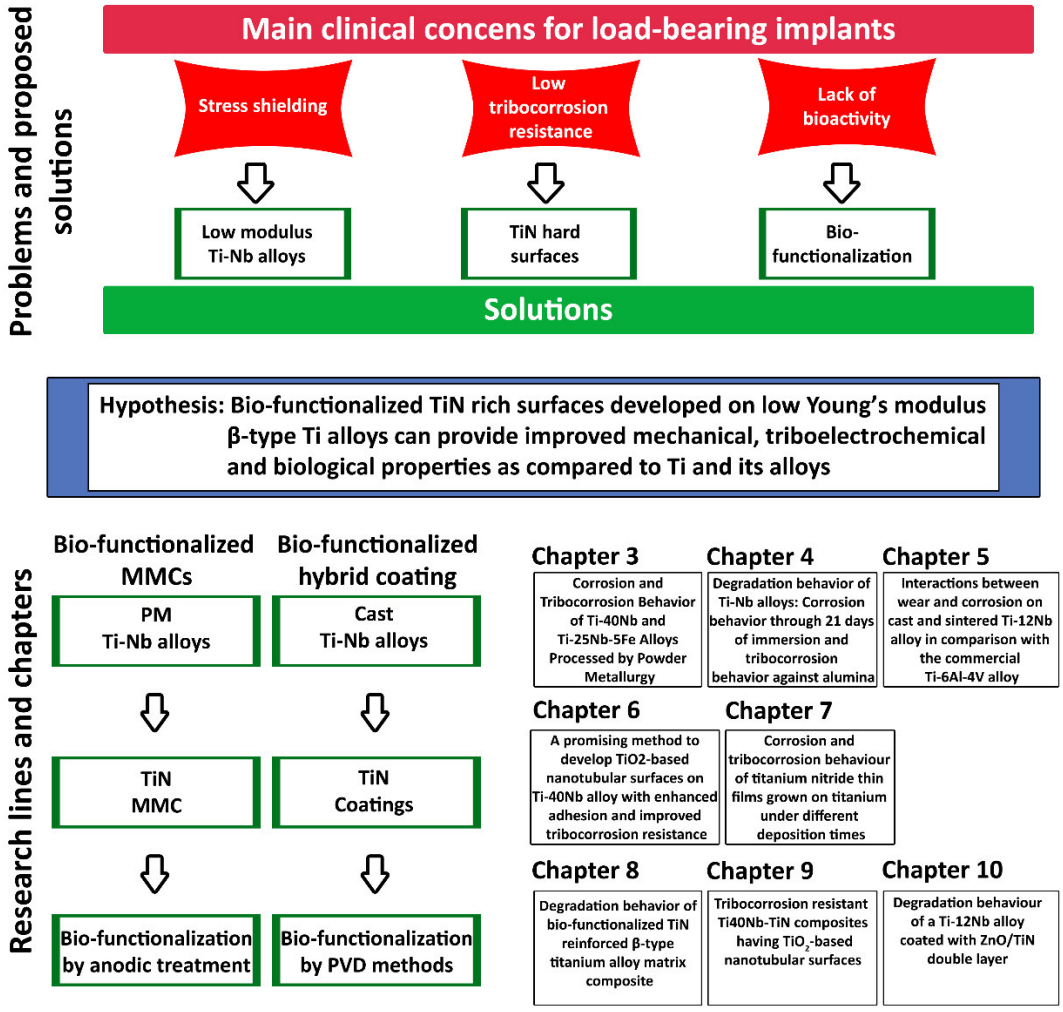

Fig. 1.1. Schematic diagram of the summarized objectives together with research lines and chapters.

References

[1] OECD, Hip and Knee Replacement Hip and Knee Replacement, Heal. a Glance 2017 OECD Indic. (2017) 178–179.

[2] H. Replacement, I. Market, B. Application, B. Region, S. Forecasts, End-use Insights, 2019 (2019).

[3] J.T. Evans, J.P. Evans, R.W. Walker, A.W. Blom, M.R. Whitehouse, A. Sayers, How long does a hip replacement last? A systematic review and meta-analysis of case series and national registry reports with more than 15 years of follow-up, Lancet (London, England). 393 (2019) 647–654. doi:10.1016/S0140-6736(18)31665-9.

[4] T. Karachalios, G. Komnos, A. Koutalos, Total hip arthroplasty: Survival and modes of failure, EFORT Open Rev. 3 (2018) 232–239. doi:10.1302/2058-5241.3.170068.

[5] M. Geetha, A.K. Singh, R. Asokamani, A.K. Gogia, Ti based biomaterials, the ultimate choice for orthopaedic implants - A review, Prog. Mater. Sci. 54 (2009) 397–425. doi:10.1016/j.pmatsci.2008.06.004.

[6] K. Miura, N. Yamada, S. Hanada, T.-K. Jung, E. Itoi, The bone tissue compatibility of a new Ti–Nb–Sn alloy with a low Young's modulus, Acta Biomater. 7 (2011) 2320–2326. doi:10.1016/j.actbio.2011.02.008.

[7] A. Panigrahi, B. Sulkowski, T. Waitz, K. Ozaltin, W. Chrominski, A. Pukenas, J. Horky, M. Lewandowska, W. Skrotzki, M. Zehetbauer, Mechanical properties, structural and texture evolution of biocompatible Ti–45Nb alloy processed by severe plastic deformation, J. Mech. Behav. Biomed. Mater. 62 (2016) 93–105. doi:10.1016/j.jmbbm.2016.04.042.

[8] P.A. Revell, The combined role of wear particles, macrophages and lymphocytes in the loosening of total joint prostheses, J. R. Soc. Interface. 5 (2008) 1263–1278. doi:10.1098/rsif.2008.0142.

[9] I. Çaha, A.C. Alves, L.A. Rocha, F. Toptan, A Review on Bio-functionalization of β-Ti Alloys, J. Bio-Tribo-Corrosion. 6 (2020) 1–31. doi:10.1007/s40735-020-00432-0.

Chapter 2: State of the art

Published in J. Bio- Tribo-Corrosion 6 (2020) 1–31.

A review on bio-functionalization of β-Ti alloys

I. Çaha[a*], A.C. Alves[a], L.A. Rocha[b,c], F. Toptan[a,d]

[a] CMEMS-UMinho - Center for MicroElectroMechanical Systems, Universidade do Minho, Azurém, 4800-058 Guimarães, Portugal

[b] IBTN/Br – Brazilian Branch of the Institute of Biomaterials, Tribocorrosion and Nanomedicine, Bauru, SP, Brazil

[c] UNESP—Univ. Estadual Paulista, Faculdade de Ciências de Bauru, Dep. Física, 17033-360 Bauru, SP, Brazil

[d] IBTN/Euro – European Branch of the Institute of Biomaterials, Tribocorrosion and Nanomedicine, Dept. Eng. Mecânica, Universidade do Minho, Azurém, 4800-058 Guimarães, Portugal

[*] Corresponding author at: CMEMS-Uminho – Center for MicroElectroMechanical Systems, Universidade do Minho, Azurém, 4800-058 Guimarães, Portugal. Tel.: +351 253 510 220; fax: +351 253 516 007. E-mail: ihsancaha@gmail.com (Ihsan Çaha).

Abstract

β-Ti alloys are known for their very low Young's modulus, excellent physical properties, and biocompatibility, hence they are considered as attractive metallic materials for long-term bone implant applications. However, β-Ti alloys are poor wear resistant and typically bioinert materials, thus their surfaces need to be modified to have wear resistant and bioactive properties. In this paper, an overview is given to the available surface functionalization techniques to improve the biological properties of β-Ti alloys. Mechanical, physical, chemical, and electrochemical treatments, as well the immobilization of bio-functional molecules are discussed. Bioactivity, biocompatibility, hemocompatibility, wear and/or corrosion, behaviour of the β-Ti alloys can be improved by using a proper surface modification technique, by altering the surface composition and topography or removing the undesired material from the alloy surface.

Keywords: β type Titanium alloys, Surface modifications, Bio-functionalization, Biomedical implants

2.1. Introduction

Several biomaterials are available for being used as implant materials, such as metals (stainless steel, Co-based alloys, Ti and its alloys), ceramics (alumina, zirconia, calcium phosphates), and synthetic or natural polymers [1]. In the last few decades, metallic biomaterials have been extensively used in biomedical applications mainly due to their excellent mechanical properties [2]. Among those, Ti and its alloys are considered as the most suitable biomaterials owing to their high strength, excellent corrosion resistance, and biocompatibility [3–5].

Ti alloys are classified as α, β, near-α, α+β, and metastable β phases [6]. In this context, the alloying elements are grouped into three categories: α-stabilizers such as Al, O, N, C, β-stabilizers such as Mo, V, Fe, Cr, Ni, Co, Nb, Ta, Mn, and neutrals such as Sn and Zr [5]. The α and near-α Ti alloys have good fracture toughness and corrosion resistance but have limited mechanical strength. On the other hand, the α+β Ti alloys exhibit higher strength, higher ductility, and higher low-cycles fatigue strength [5]. α+β type Ti-6Al-4V alloy (ASTM F1108) is the most popular Ti alloy and has been used for producing orthopaedic prostheses and dental implants due to its excellent specific strength, corrosion resistance, and biocompatibility [7]. However, ions of the alloying elements have been linked with various health problems such as neurological diseases and cytotoxic effects of Al and V, respectively [8–13].

Widely used α-type and α+β-type Ti-based implant materials have Young's modulus values around 100-120 GPa, whereas Young's modulus of bone is 5-6 times lower than those materials [14–16]. The Young's modulus of human cortical bone is about 15-20 GPa, more specifically, the Young's modulus of the fibula is about 15-20 GPa, the humerus is about 15-16 GPa, the tibia is about 16-19 GPa and the femur is about 13-15 GPa [17]. The difference in Young's modulus between implant and bone causes the unbalanced distribution of stress on bone leading to bone resorption. Therefore, it causes poor osteointegration which may subsequently lead to loosening or failure of the implant [18–20]. This mechanism, that is known as stress-shielding and it can be minimized by using an implant material having Young's modulus closer to the bone.

Ti alloys with low Young's modulus have been developed by using biocompatible, non-toxic β-stabilizers elements such as Nb, Zr, Ta, Mo [4,14,21–29]. Niinomi *et al.* [3] and Abdel-Hady *et al.* [30] reported that Young's modulus can be significantly reduced by adjusting the concentration of β-stabilizing elements. As reported by previous studies [31,32], the β-type Ti alloys especially with Nb contents have been received attention and investigated extensively because of non-toxicity, good biocompatibility, also, better cell adhesion, proliferation, and differentiation *in vitro*. During the last two decades, many novel

non-toxic and allergy-free β-Ti alloys have been produced with displaying superior corrosion resistance and good biocompatibility along with their low Young's modulus [33–35]. Some of β-Ti alloys, such as Ti-29Nb-13Ta-4.6Zr, include high cost, non-toxic and allergy-free elements such as Nb, Ta, Zr and Mo [36]. Thus, instead of these rare and expensive elements, low-cost elements such as Fe, Cr, Mn, and Sn are also used to produce low Young's modulus β-Ti alloys, like Ti-Mn-Fe [37] or Ti-Sn-Cr [38]. The load-bearing implant materials are expected to exhibit a combination of high strength and low Young's modulus [39], however, the lowest Young's modulus β-Ti alloys also have poor yield and tensile strength because, in general, these alloys are produced under solutionized conditions [40]. Therefore, the strength of β-Ti alloys needs to be increased while keeping their Young's modulus, in order to improve the performance of the implants. Some available techniques to increase the strength are cold working [41], accumulative roll bonding [42], aging treatment, spark plasma sintering (SPS), and plastic deformation (especially high-pressure torsion) [43–47]. Datta *et al.* [48] used a predictive model and showed that increased content of β-stabilizers could reduce the strength of the β-Ti alloys. The incorporation of some β-stabilizers may also increase the strength of the alloys, as in the case of Ti6Al4V that presents higher strength as compared to cp-Ti. Also, the incorporation of Ta to Ti-Nb-Zr increase tensile strength and decrease Young's modulus [28]. Nevertheless, the incorporation of elements does not always improve the mechanical properties of β-Ti alloys like in the case of incorporation of Sn to Ti-Nb which drastically decreases the tensile strength [39]. On the other hand, solid solution strengthening by oxygen is also effective in improving the strength of β-Ti alloys as maintaining their low Young's modulus [49]. Niinomi and Nakai [50] reported that a small content of oxygen resulted in an increase in the strength, however, it also led to an increase in Young's modulus for Ti-29Nb-13Ta-4.6Zr alloy.

Surface degradation of implants is one of the most important drawbacks for long-term implantation in the human body. When a metallic implant inserted into the human body, it can release metallic ions due to corrosive conditions [51]. Ti presents superior corrosion behaviour due to the spontaneously formation of a very stable oxide layer (passive film) on its surface. This passive film protects the implant materials against corrosion, reduces the release of metallic ions, and it is responsible for good biocompatibility. However, the corrosion behaviour of β-Ti alloys is determined by the role of β-stabilizing elements on the passive film.

Ti-Nb alloys have a great interest because of good biocompatibility and corrosion behaviour. Ti-Nb has better corrosion behaviour than cp-Ti [52,53] and Ti-Mo [54]. Moreover, minor incorporation of Ru [55], In [56], and Sn [57] is reported to improve the corrosion behaviour. However, the commercial

Ti-6Al-4V alloy presented better corrosion resistance than Ti-40Nb alloy through an immersion period of 21 days in NaCl solution that attributed to the formation of a more stable and thicker passive film [58]. The contribution of Zr, Ta, Mo, etc. β stabilizers in Ti-Nb alloys improved their corrosion behaviour in different physiological solution through the formation of a mixed passive oxide layer that had been reported to be more stable [59–67]. Ti-Mo, Ti-Zr, and Ti-Ta based β-Ti alloys are also popular alloys thanks to their unique properties such as non-toxicity, good mechanical properties, and relatively better corrosion resistance [68,69]. Binary Ti-Mo [70–72], Ti-Zr [73–75], and Ti-Ta [76–78] alloys presented better corrosion resistance than cp-Ti in different solutions, while the ternary and multi-nary of these alloys exhibited further improvement in their corrosion behaviour [79–82].

Tribocorrosion is defined as an irreversible degradation process on the material surfaces subjected to the combined action of wear and corrosion [83]. Ti alloys are shown to possess poor wear resistance being a limiting factor in many applications [84,85]. Although it is known that the total degradation rate after tribocorrosion can be different than the sum of the individual corrosion and wear rates, the literature reporting the synergistic interactions between corrosion and wear on β-Ti alloys is still scarce. Cvijović-Alagić *et al.* [86] investigated the tribocorrosion behaviour of Ti-13Nb-13Zr alloy in comparison with Ti-6Al-4V in Ringer's solution and found that Ti-13Nb-13Zr alloy had a substantially lower wear resistance than Ti-6Al-4V alloy. Similar behaviour was reported for Ti-40Nb alloy tested in 9 g/L NaCl solution [58]. On the other hand, Correa *et al.* [87] compared the tribocorrosion behaviour of Ti-15Zr-7.5Mo and Ti-15Zr-15Mo β-Ti alloys and reported a better behaviour for the Ti-15Zr-7.5Mo alloy. More *et al.* [88] studied the tribocorrosion behaviour of Ti–12.5Mo, Ti–13Nb–13Zr and Ti–29Nb–13Ta–4.6Zr β-Ti alloys and Ti–6Al–4Fe α+β-Ti alloy against polyethylene in Hank's balanced salt solution. The authors reported that the β-Ti alloys induced lower wear damage on the counter material. Besides, the addition of synovial fluid constituents (bovine serum albumin, hyaluronic acid, and dipalmitoylphosphatidylcholine) increased the wear volume loss on the Ti–29Nb–13Ta–4.6Zr alloy. Pina *et al.* [89] studied the influence of Sn addition on the tribocorrosion behaviour of Ti-Nb based β alloy and reported that Sn addition resulted with an increased wear volume loss in phosphate buffered solution (PBS).

In order to improve the integration of bone and tissue, several surface modification techniques have been used to tailor the topography [21,90–95]. When the properties of the implant surface can mimic the physical and chemical properties of the biological structure, tissue and implant surface integration is accomplished by adhesion, spreading and proliferation of cells on the implant surface [96].

On the other hand, coatings improve the surface properties including the hardness, wettability, elastic strain, coefficient of friction, and wear resistance. Coating materials used in joints replacement are fabricated by physical and chemical vapor deposition (PVD and CVD, respectively), electrodeposition, and ion implantation [97–101]. On the other hand, owing to their unique wear and tribocorrosion properties, metal matrix composites (MMCs) can be considered for orthopaedic and dental implants as a coating material or as a functionally graded material (FGM) [102–109]. Besides, nanostructured surfaces have also been studied to achieve better adhesion between the biomedical application and tissue [110–115].

β-Ti alloys considered as promising metallic materials for long-term bone implant applications. However, these alloys have some limitations such as poor wear resistance, still higher Young's modulus compared to that of the bone, and lack of bioactivity. Therefore, a focus is given on both producing new β-Ti alloys, and improving their mechanical, tribological, electrochemical, triboelectrochemical, and biological properties. So, the studies on β-Ti alloys, particularly bio-functionalization studies are very important for the future improvements. Hence, this review aimed at gathering and summarizing the available state-of-art techniques to bio-functionalize the β-Ti alloys in order to obtain multifunctional implants.

2.2. Bio-functionalization of β-Ti alloys

Metallic biomaterials have an attractive combination of high durability, high toughness, non-toxicity, and high strength. However, metallic biomaterials are typically artificial materials, therefore, their surfaces need modification to gain bioactive properties. The biomaterial surface plays an extremely significant role when interfacing with the biological environment (neutral tissue). Ti-based implants usually manufactured by melting, casting, forging, heat treatment, and oxidation which usually lead to a contaminated surface layer that is often stressed and plastically deformed, and non-uniform. Such native surfaces are not suitable for biomedical applications and some surface treatments should be performed. At the same time, different bio-functions are required depending on the intended implant location to achieve biological integration. For example, blood compatibility (hemocompatibility) is very important for blood-contacting biomedical devices such as stent and catheter, whereas osteointegration is a crucial parameter for bone applications. When a metallic biomaterial is implanted into a blood-contacting location, the first rapid event takes place is the blood protein adsorption leading to structural alterations that allow biological interactions. Thus, over time, a built-in protein layer is formed that affects the interaction of platelets, the adhesion, and aggregation of platelets. Concerning bone applications (orthopaedics and dentistry), once the implantation procedure occurs, the implant surface is wetted and

the biologically active molecules (such as proteins) are adsorbed quickly followed by the osteoprogenitor cells that would regenerate the tissue [116]. The two main factors affecting osteointegration are the mechanical properties of the implant and the biological interactions with the metal surface, being the second the most relevant. Another important reason for the surface modification is to increase the corrosion and wear resistance of the metallic biomaterial. As a result, bioactivity, biocompatibility, haemocompatibility, wear, and corrosion resistance of the metallic biomaterials can be improved by surface modification, altering the surface chemical composition, topography, and crystal structure or removing the undesired material from the metallic biomaterial surface. For this purpose, many techniques have been applied for the surface modification of metals, some of which have also been commercialized.

It is clear that a biomaterial response is dependent on its biocompatibility and surface properties. In the literature, the bio-functionalization of metallic biomaterials, especially Ti and Ti-6Al-4V has been extensively studied and it is still being researched as recently reviewed by Su *et al.* [117]. Despite the combination of their unique features, β-Ti alloys need to be bio-functionalized in order to increase tissue adhesion and implant integration, to decrease bacterial adhesion, and inflammatory response or to avoid the foreign body response. In the following sections, the surface modifications that are investigated for β-Ti alloys are discussed. These treatments are being applied individually or as a combination.

2.2.1. Mechanical treatments

The biomechanical properties and bioactivity of the implant surface can be improved by mechanical treatments, overviewed in Table 2.1, yielding with the nanostructured and ultrafine-grained surface with enhanced strength. Electric discharge machining (EDM) has been widely studied on cp-Ti and Ti-6Al-4V alloy to improve their hardness, corrosion and wear properties [118]. In the case of β-Ti alloys, the Ti-35Nb-7Ta-5Zr alloy has been studied by powder mixed electrical discharge machining (PMEDM). A schematic diagram of the PMEDM process and examples for the resulting microstructures on Ti-35Nb-7Ta-5Zr alloy is given in Fig. 2.1. PMEDM treated alloy presented better hardness, corrosion resistance, cell adhesion, cell spreading, and cell differentiation compared to the unmachined one, attributed to the formation of a nanoporous recast layer [119–123].

Table 2.1. Overview of mechanical treatments applied for β-Ti alloys.

Methods	Objectives	Alloys applied
Powder mixed electric discharge machining (PMEDM)	Fabricating a 3-18 μm nanoporous recast layer	Ti-35Nb-7Ta-5Zr [122–126]
Surface mechanical attrition treatment (SMAT)	Producing rough and hard a gradient nanostructured material	Ti-30Nb-8Zr-0.8Fe [127] Ti-34Nb-2Ta-0.5O [128] Ti-25Nb-3Mo-3Zr-2Sn [129] Ti-5Al-2Sn-2Zr-4Mo-4Cr [130] Ti-25Nb-3Mo-2Sn-3Zr [131] Ti-32Nb-2Sn [132]
Ultrasonic nanocrystal surface modification (UNSM)	Inducing severe plastic deformation at the surface to generate a gradient nanostructured surface	Ti-29Nb-13Ta-4.6Zr [133–135]
High pressure torsion (HPT)	Obtaining ultrafine-grained metallic materials to increase the mechanical strength and decrease or retain Young's modulus	Ti-29Nb-13Ta-4.6Zr [43,136–138] Ti-13Nb-13Zr [139,140] Ti-24Nb-4Zr-8Sn [141,142] Ti-45Nb [143] Ti-15Mo [144,145] Ti-20Mo [146] Ti-24.6Nb-5Zr-3Sn [147] Ti-19.6Nb-4.5Ta-2.4Cr [147] Ti-19Nb-7Mo-14Zr [148] Ti-28Nb-8Mo-12Zr [148] Ti-35Nb-7Zr-5Ta [149]
Accumulative roll bonding (ARB)	Production of metallic materials with ultrafine grained microstructure to improve mechanical properties	Ti-10Zr-5Nb-5Ta [150,151] Ti-25Nb-25Ta [152,153] Ti-25Nb-3Zr-3Mo-2Sn [154,155]

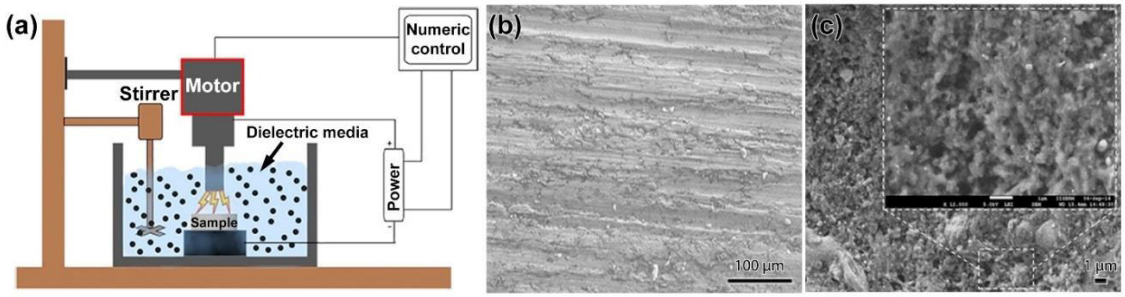

Fig. 2.1. Figure a) Schematic diagram of PMEDM process and examples for the resulting microstructures on Ti-35Nb-7Ta-5Zr alloy b) before and c) after treatment (adapted from [122] with permission from Springer).

The surface mechanical attrition treatment (SMAT) is a method that can be used to tailor the mechanical and tribological properties of a surface [124,125]. The SMAT device mainly consists of a vibration generator and a treatment chamber having balls as shown in Fig. 2.2a. The SMAT treatment was reported to improve the corrosion resistance, fatigue resistance, osteointegration, and hemocompatibility due to nanocrystallization of the cp-Ti surface [126]. Regarding β-Ti alloys, SMAT treated Ti-30Nb-8Zr-0.8Fe alloy having β grains around 150 μm (Fig. 2.2b) modified to a nanocrystalline structure having grains of several tens of nanometres (Fig. 2.2c) that led to an increase on the surface hardness [127]. The increased hardness of the surface decreased the wear rate of materials, such as the reduction of the fretting wear rate of Ti-34Nb-2Ta-0.5O alloy immersed in a 20% fetal bovine serum solution (pH = 7.4) [128]. The corrosion behaviour of Ti-25Nb-3Mo-3Zr-2Sn and Ti-34Nb-2Ta-0.5O alloys in SBF solution was improved after SMAT treatment associated with the formation of a denser passive oxide layer resulted from the grain refinement [128,129]. However, corrosion resistance of Ti-5Al-2Sn-2Zr-4Mo-4Cr alloy in 3.5% NaCl solution was decreased after SMAT treatment due to residual internal stress created from the treatment process [130]. The authors reported that stress relief heat treatment of 250 – 350 °C can significantly improve the corrosion resistance of SMAT treated alloy. In vitro cell culture studies indicated a significant improvement in cell adhesion, proliferation, differentiation, extracellular matrix mineralization, and protein absorption of SMAT treated Ti-25Nb-3Mo-2Sn-3Zr alloy as compared to the non-treated alloy due to its superior hydrophilicity, nanostructured surface, and increased surface roughness [131].

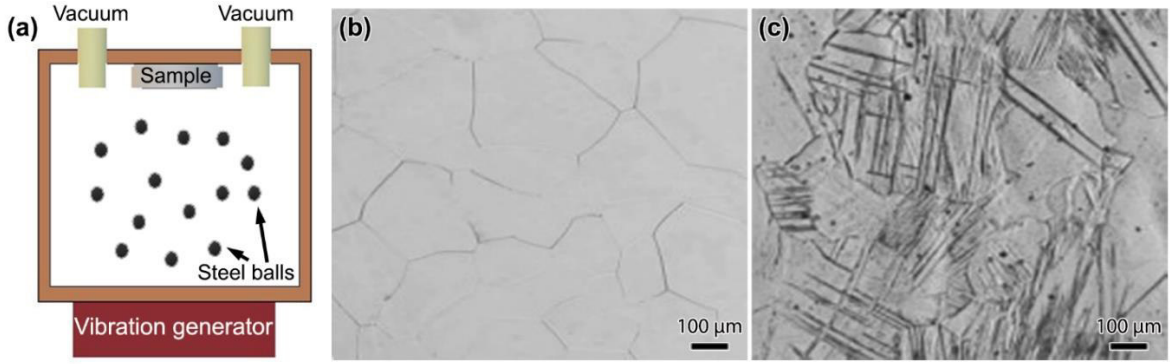

Fig. 2.2. a) Schematic diagram of SMAT process and representative microstructures on Ti-30Nb-8Zr-0.8Fe alloy b) before and c) after treatment (microstructure of alloy was taken from [127] with permission from Elsevier).

Ultrasonic nanocrystal surface modification (UNSM) is a novel method to induce severe plastic deformation at the surface in order to generate a gradient nanostructured surface layer on metallic materials. The process uses super-encapsulated ultrasonic vibration on the combination of static and

dynamic loads to create high-strain-rate plastic deformation on a material surface (Fig. 2.3a) [132]. Kheradmandfard *et al.* [133] applied the UNSM process to a Ti-29Nb-13Ta-4.6Zr alloy and obtained a significant increase on the surface hardness (≈ 385 HV) as compared to the untreated alloy (190 HV) owing to the surface structure having nanoscale lamellae and nanostructured subgrains (Fig. 2.3b), along with high dislocation density and α precipitates. The authors also reported that UNSM treated Ti-29Nb-13Ta-4.6Zr alloy presented significantly better wear resistance, cell adhesion, spreading, and proliferation attributed to both nanoscale grain refinement and micro-patterned surface effects (Fig. 2.3c) [134].

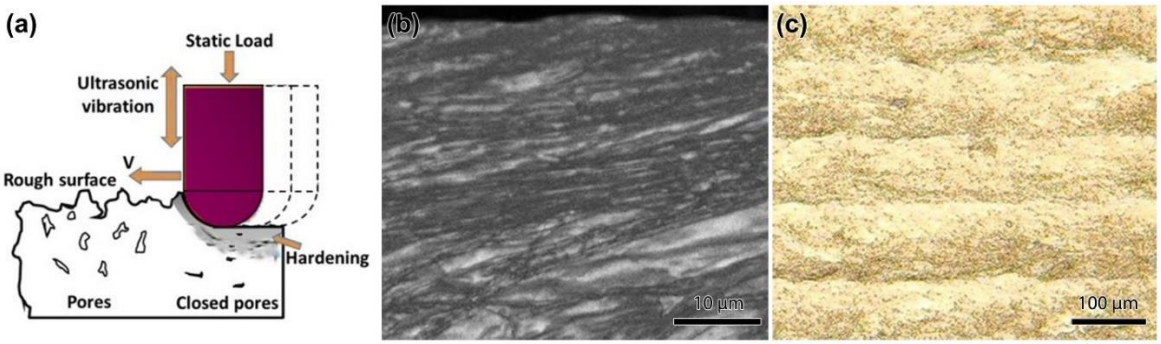

Fig. 2.3. a) Schematic diagram of the UNSM process (adapted from [132]) and representative resultant surfaces on a Ti–29Nb–13Ta–4.6Zr alloy: b) SEM image, c) laser scanning microscope image (adapted from [133] with permission from Elsevier).

High-pressure torsion (HPT) is another commonly used severe plastic deformation technique to obtain ultrafine-grained structure for improving mechanical properties, particularly hardness and ductility as well as its bio-functionality [135–139]. A schematic diagram of HPT process is given in Fig. 2.4a together with the representative microstructures on Ti-45Nb alloy before (Fig 2.4b) and after (Figs. 2.4c and 2.4d) HPT deformation with 5 GPa pressure and n=5 rotation number, where the grain size was reported to be decreased from around 20 µm to less than 100 nm [140]. As expected, HPT treatment improved the mechanical and microstructural properties of different β-Ti alloys [140–145]. Regarding corrosion, HPT treated Ti-13Nb-13Zr alloy showed significantly higher corrosion resistance in artificial saliva solution as compared to the untreated alloy associated with the grain size reduction to ultrafine range [141]. However, the quantities of released ions from HPT treated Ti-13Nb-13Zr alloy were higher than the quantities from untreated alloy, explained by its smaller grains, which was more prone to the release metallic ions [146]. *In vitro* cell culture tests revealed that the HPT treatment significantly increased the cell attachment, spreading, and proliferation on the treated samples influenced by their increased wettability due to their high internal energy given by the nano-sized grains having increased

numbers of boundaries, interfaces, and dislocation density [141,142]. Furthermore, alkaline treatment and the nanotubular layer formed on HPT treated β-Ti alloys presented better bioactivity as compared to the non-HPT treated one, explained by changing surface chemistry after chemical and anodic treatments [145].

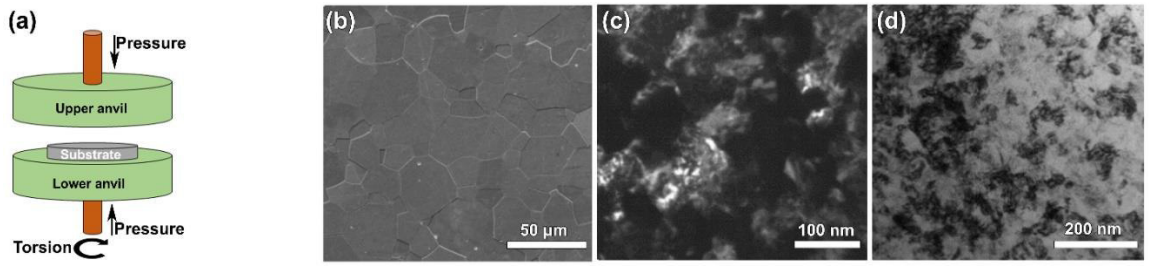

Fig. 2.4. a) Schematic diagram of HPT process and representative microstructures: b) optical microscope image of the initial Ti-45Nb alloy, c) dark and d) bright-field TEM images of the alloy after HPT treatment under 5 GPa pressure and 5 rotation number (adapted from [140] with permission from Elsevier).

Accumulative roll bonding (ARB) is another severe plastic deformation technique that has been applied to different β-Ti alloys to improve their functionality through grain refinement [147–152]. The studied β-Ti alloys presented better mechanical and corrosion behaviour as compared to the as-cast alloys due to the formation of nano-sized refined grains. However, biological studies are needed to understand the effect of ARB treatment on the bioactivity of β-Ti alloys.

2.2.2. Physical surface treatments

Physical surface treatments of β-Ti alloys including PVD, plasma spraying, plasma nitriding, gas nitriding, and ion implantation treatments are overviewed in Table 2.2 and demonstrated in Fig. 2.5 with the examples of surface and subsurface microstructural images. PVD processes are carried out in vacuum and the material are coated with positively charged ions during the process, resulting with a very strong bonding between the coating film and the substrate (Fig. 2.5c). The plasma spray process is the spraying of molten or thermally softened material to the surface to provide a coating [153]. On the other hand, ion implementation technique provides an easy control on the energy of ions, giving a good adhesion between the coating layer and the substrate resulted from gradient film coatings as shown in Figs. 2.5d and e. This technique allows to control the thickness of the coating, and eliminates the contamination since the process is carried out in vacuum [153].

Hydroxyapatite (HA, $Ca_{10}(PO_4)_6(OH)_2$) is a bio-ceramic material having a very similar chemical and crystallographic structure to human bone. HA has remarkably high biocompatibility thus it is used to

improve the osteointegration process. However, its mechanical properties such as tensile strength and fracture toughness are quite poor, making it unsuitable for load-bearing implant applications. Various types of surface modification techniques have been used to deposit HA layers on Ti and its alloys, such as plasma spraying, sol-gel method, electrochemical deposition, and radio frequency (RF) sputtering. Zhao *et al.* [154] studied the microstructures, mechanical properties, and apatite-induction abilities of HA/Ti composite coating Ti-24Nb-4Zr-7.9Sn β-type alloy by plasma spraying. The authors reported that the microstructure, mechanical properties, and apatite-induction ability were influenced by the HA/Ti powders ratio used on processing. Also, the increase on Ti content led to an increase on the mechanical properties, however, decreased the apatite-induction ability. Zhao *et al.* [155] also studied the influence of the processing temperatures on Ti-24Nb-4Zr-7.9Sn alloy surface after plasma sprayed HA coating and reported that martensitic transformation and recrystallization influenced the mechanical properties resulting with a slight increase in the tensile and yield strengths but also led to a significant increase in Young's modulus (from 56.9 to 73.2 GPa). The main disadvantage of the plasma spraying technique is the poor adhesion between HA and the substrate materials. In order to improve the adhesion between HA and β-Ti alloys, some other techniques were also studied. He *et al.* [156] produced Ti-13Nb-13Zr-10HA composites by spark plasma sintering process at sintering temperatures varying between 950 and 1150 °C. The authors reported that mechanical properties of the composite, namely compressive strength, yield strength, and hardness were increased with the increased processing temperature. However, the processing temperatures above 1050 °C led to an intense reaction between Ti and HA increased in the metal-ceramic reaction phases. Depending on the processing technique and processing temperature, the thermal decomposition of HA during the processing of Ti-HA composites may lead to a decrease in the corrosion resistance due to the formation of locally active sites on the HA-depleted zones [157]. However, if the decomposition of HA is not observed, Ti-HA composite surfaces may increase the corrosion resistance. For instance, Kim *et al.* [158] studied the surface characteristics of Ti-HA composite coatings developed on Ti-35Ta-xZr alloy surfaces having 3, 7, and 15 wt.% of Zr through RF and direct current (DC) sputtering and reported that the composite layer improved the corrosion resistance of the bare alloy by forming a stable barrier against corrosion.

The Al_2O_3–$13TiO_2$, ZrO_2 and the bilayered (ZrO_2/Al_2O_3–$13TiO_2$) nanoceramics coated by plasma spray technique on Ti–13Nb–13Zr alloy in order to improve its corrosion and wear resistance [159,160]. The bilayered nanoceramic coating presented significantly higher corrosion resistance in Hank's solution and wear resistance in SBF solution attributed to the presence of a large number of melted particles

compared to other ceramics where they presented unmelted and melted particles, lower porosity and higher hardness for bilayered nanoceramic coating compared to other samples.

Titanium nitride (TiN) coatings by plasma nitriding, sputtering, gas nitriding, plasma immersion ion implantation, and ion implantation treatments have been widely used to improve the corrosion and wear behaviour along with the bioactivity of metallic materials. TiN has attracted attention due to its excellent properties such as high hardness, chemical stability, biocompatibility, hemocompatibility, high wear, and abrasion resistance. Because of these unique properties, TiN has been used on various applications such as dental prostheses, orthopaedic implants (hip, knee, ankle joint), heart valve prostheses, and dental surgery tools. The structure and biological properties of nitrogen treatment on different β-Ti alloys have been investigated [161–175]. Mohan *et al.* [175] performed a plasma nitriding treatment on Ti-15Mo-3Nb-3Al-0.2Si alloy using inductively coupled RF plasma and studied the corrosion behaviour by electrochemical impedance spectroscopy (EIS), potentiodynamic polarization, and immersion studies in Hank's solution. It was found that the surface hardness of the nitrided samples increased with increasing annealing temperature and hydrogen dilution. Although nitrided surfaces presented lower corrosion resistance, nitrided samples with hydrogen dilution displayed higher potential for apatite growth compared to that of the sample nitrided with 100% nitrogen and the uncoated one. Gordin *et al.* [174] implanted nitrogen into Ti-25Ta-25Nb β-type alloy using an original ion implantation technique based on the use of an electron cyclotron resonance ion source to produce a multi-energetic ion beam from multi-charged ions. The corrosion resistance of the nitrogen implanted Ti alloy was evaluated in SBF complemented by *in vitro* cytocompatibility tests on human fetal osteoblasts. It was found lower corrosion and ion release rate for the nitrogen implanted surface than for the non-implanted one whereas *in vitro* tests revealed a good level of cytocompatibility for both non-treated and nitrogen implanted Ti-25Ta-25Nb alloy. A high temperature gas nitrided Ti-27Nb alloy also presented significantly better corrosion resistance than the cp-Ti and untreated Ti-27Nb alloy in artificial saliva for different pH values, together with a good level of bioactivity [161,168]. In wear point of view, the ion implantations, plasma nitrided and gas nitrided methods are more beneficial than the PVD techniques mainly due to the formation of a gradient hardened layer and the good bonding strength of the nitrided layer resulted from the diffusion of nitrogen ions. For instance, the dense TiN coating deposited by sputtering presented lower wear resistance as compared to a compact plasma nitrided layer associated with the hard compound layer maintaining its integrity with the hardened nitrogen diffusion zone during the wear test [165]. While nitriding improves the corrosion and wear resistance, gas nitriding in high temperature is reported to cause low fatigue strength due to severe grain coarsening [162]. A possible approach to

improve the tribological behaviour of the protective coatings can be achieved by increasing fracture toughness and hardness with the replacement of monolayered coatings by multilayers. The multilayered TiAlN/CrN coatings on Ti-45Nb alloy presented better wear resistance than the monolayered CrN and TiAlN coatings in dry sliding condition attributed to their small grain size, high surface hardness and adhesion resistance [166].

Another approach studied in the literature to improve the corrosion and wear behaviour of β-Ti surface is oxygen treatment by using plasma immersion ion implantation. Mohan and Anandan [176] implanted oxygen ions into Ti-13Nb-13Zr β-type alloy by plasma immersion ion implantation and investigated the influence of oxygen ion implantation on the apatite growth and corrosion behaviour in Hanks' solution. Results showed that the implanted samples had a higher potential for inducing apatite growth as compared to the untreated samples. Furthermore, the authors stated based on potentiodynamic polarization and EIS studies that the implanted layer behaved like a near-ideal capacitor with better passivation behaviour which can help in preventing the release of metallic ions from the implant material. Furthermore, the implanted surfaces displayed a lower coefficient of friction during dry sliding wear tests, as compared to the untreated samples.

Table 2.2. Overview of physical surface modification methods applied for biomedical β-Ti alloys.

Methods	Objectives	Alloys
Plasma spray	Improving wear resistance, corrosion resistance and biological properties	Ti-24Nb-4Zr-7.9Sn [154,155] Ti-13Nb-13Zr [159,160]
Gas nitriding		Ti-27Nb [161,168] Ti-16Mo [171] Ti-15Mo-5Zr-3Al [162] Ti-15Mo-3Nb-3Al-0.2Si [170]
Plasma nitriding		Ti-15Mo [164] Ti-13Nb-13Zr [165] Ti-15Mo-3Nb-3Al-0.2Si [163,175]
PVD		Ti-12Mo-6Zr-5Sn-0.4Fe [167] Ti-13Nb-13Zr [298,309,310] Ti-45Nb [166] Ti-15Mo [164]
		Ti-35Ta-xZr (x=3,7, and 15) [158] Ti-13Nb-13Zr [165]
Ion implantation	Modifying surface composition; improving wear, corrosion resistance, and biocompatibility	Ti–25Ta–25Nb [174] Ti-35Nb-7Zr-5Ta [172] Ti-10Zr-10Nb-5Ta [173]
Plasma immersion ion implantation (PIII)		Ti-13Nb-13Zr [176] Ti-15Mo-3Nb-3Al-0.2Si [311]
Glow discharge plasma	Obtaining a clean, sterilize, oxide, nitride surface; removing the native oxide layer	Ti-5Zr-3Sn-5Mo-15Nb [312]

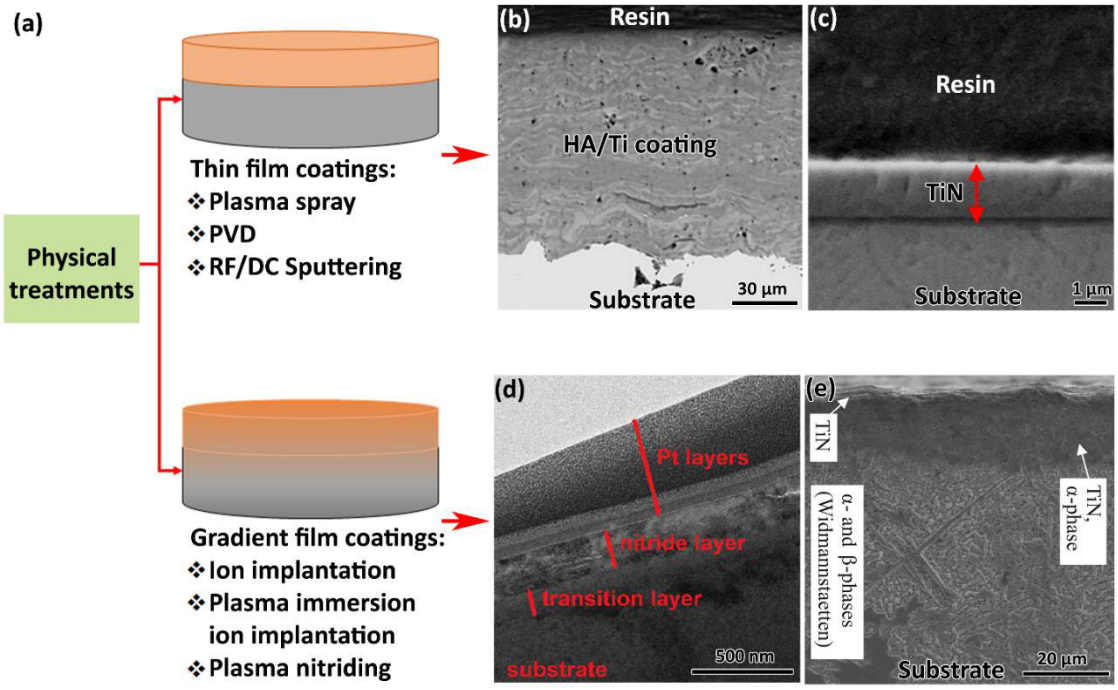

Fig. 2.5. a) Schematic illustration of physical surface functionalization with resultant images: b) cross-sectional SEM image of plasma sprayed HA/Ti coating on Ti-24Nb-4Zr-7.9Sn (adapted from [154] with permission from Elsevier), c) cross-sectional SEM image of TiN coated on Ti-13Zr-13Nb alloy using cathodic arc physical vapor deposition (CAPVD) method (adapted from [298] with permission from MDPI, d) TEM cross-section image of the nitrogen implanted Ti-35Nb-7Zr-5Ta alloy (adapted from [172] with permission from Elsevier), e) cross-section SEM image of gas nitrided of Ti-15Mo-5Zr-3Al (adapted from [162] with permission from Elsevier).

2.2.3. Chemical surface treatments

Chemical methods are attracting more attention owing to their lower cost, easier control and stronger adhesion between bones and implant surfaces compared to the samples treated by mechanical and physical methods. Through chemical surface modification, it is possible to provide direct bonding between bone and the implant. Chemical surface treatments can be used to generate a nanopatterned surface topography which is expected to be promising for the stimulation of bone tissue growth (osteointegration of bone tissue) [177]. Acid treatment (HCl, H_2SO_4, HNO_3, and HF, or a combination of them) is often used to remove the undesired material, to create a rough surface, and to obtain clean and uniform surface finishes. The schematic representation of chemical treatments and representative treated surfaces is given in Fig. 2.6, and the overview of chemical methods of β-Ti alloys are given in Table 2.3.

Acid treatments commonly performed to clean metallic surfaces or surface roughening to improve bonding quality of next coating layer or improve bioactivity of surfaces. The Ti-45Nb alloy surface modified by sandblasting, followed by acid etching in different solutions, chemical treated in H_2SO_4:H_2O_2 (volume ratio of 1:1; piranha solution) with ice cooling resulted with a nanopatterned surface that stated by the authors to be expected to stimulate bone cell interactions [178]. It has been reported significantly prolonged etching duration for Ti-Nb alloy compared to cp-Ti and Ti-6Al-4V attributed to the excellent chemical stability of Nb. Chemically treated Ti-40Nb alloy by piranha solution enhanced the adhesion and spreading of human mesenchymal stromal cells, together with better metabolic and enzyme activity [179]. However, chemically treated Ti-45Nb alloy presented lower corrosion resistance than untreated alloy due to the alterations on the surface chemistry and increase on the exposure area resulted from nanopatterning. Müller *et al.* [180] investigated the influence of different acid-alkali treatments on Ti-13Nb-13Zr alloy produced by powder metallurgy (P/M). The authors evaluated the rate of hydroxy carbonated apatite (HCA) formation during *in vitro* bioactivity tests in SBF. After etching the samples by HCl, $HF/HNO_3/H_2O$ (1:6:18), H_3PO_4, and then soaked in 10 M NaOH aqueous solution, the authors reported that the rate of HCA formation was the highest for the samples etched in HCl.

Table 2.3. Overview of chemical surface modification methods applied for β-Ti alloys.

Methods	Objectives	Alloys
Acid treatment	Removing oxide scales and contamination	Ti-40Nb [179,187,313] Ti-45Nb [178,314] Ti-13Nb-13Zr [180,190] Ti-15Mo-5Zr-3Al [181] Ti-15Zr-4Nb-4Ta [181] Ti-35Nb-10Ta-1.5Fe [315] Ti–27Nb–13Zr [316] Ti-29Nb-13Ta-4.6Zr [186,193,194,317,318] Ti-24Nb-4Zr-8Sn [192,255] Ti-5Mo-3Fe [189] Ti-20Nb-13Zr [319] Ti-15Mo [320] Ti-16In-3Nb-4Ta [183]
Alkaline treatment	Improving biocompatibility, bioactivity or bone conductivity	
Hydrogen peroxide treatment		
Sol-gel treatment		Ti-29Nb-13Ta-4.6Zr [321–324] Ti-15Mo [325]
CVD	Improving wear resistance, corrosion resistance and blood compatibility	Ti-29Nb-13Ta-4.6Zr [195] Ti-13Nb-13Zr [326,327] Ti-12Mo-6Zr-2Fe [328]
Hydrothermal treatment	Improving hard tissue compatibility	Ti-30Nb-1Fe-1Hf [213,218] Ti-29Nb-13Ta-4.6Zr [196] Ti-13Cr-1Fe-3Al [196] Ti24Nb-4Zr-7.9Sn [197,198] Ti-25Nb-3Mo-3Zr-2Sn [199,329]

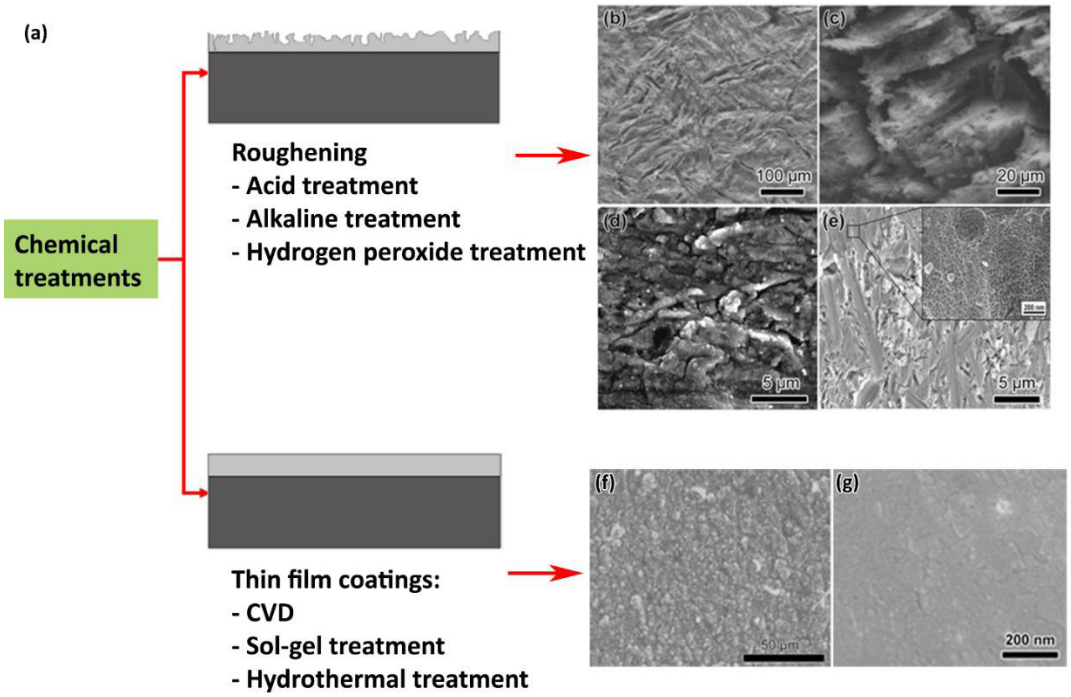

Fig. 2.6. a) Schematic representation of chemical treatment process and representative treated surface SEM images of b) HCl etched and c) subsequently immersed in NaOH surfaces of Ti-13Nb-13Zr alloy (adapted from [180] with permission from Elsevier); SEM images of d) NaOH treated and e) piranha etched surfaces of Ti-40Nb alloy (adapted from [187] with permission from Elsevier); f) representative SEM image of HA-coated surface on Ti-29Nb-13Ta-4.6Zr by MOCVD (adapted from [195] with permission from Elsevier); SEM image of a treated Ti-24Nb-4Zr-8Sn alloy surface in saturated $Ca(OH)_2$ solution boiled for 30 min (adapted from [198] with permission from Elsevier).

As abovementioned, HA has excellent bioactivity, but its application has been limited in clinics due to its poor mechanical properties. Hence, the formation of a dense and uniform bone-like apatite layer grown on Ti alloys through alkaline treatment and soaking in SBF has been attractively studied as an alternative to HA coating techniques. A schematic illustration of apatite formation mechanisms in SBF is given in Fig. 2.7. It may be expected that the precipitated apatite coatings from soaking in SBF will be close to that of the biological apatite presents in human bone, where the SBF solution reproduces the human blood plasma. After alkaline treatment, a ~1 µm thick unstable sodium titanate layer is formed, and by using heat treatment it is converted to a denser and mechanically stable layer. Acid and heat treatment was not effective for inducing apatite formation on Ti-based alloy attributed to enriched/remained alloying elements on their surfaces [181]. Also, while the chemical pre-treatments of alloy surfaces have a slight impact on apatite morphology, they do not affect the deposition process and its phase composition [182]. As can be seen from Fig. 2.7, during SBF soaking, the Ti-OH groups are

formed resulted from the exchanged Na^+ and H_3O^+ ions. The negatively charged Ti-OH groups are combined with positively charged Ca^{2+} ions through electrical force and form calcium titanate. Similarly, the positively charged surface combines with negatively charged phosphate ions to form amorphous calcium phosphate, and apatite grows on the surface spontaneously by consuming the calcium and phosphate ions. It is reported that apatite was grown more quickly on the β-Ti alloy than Ti-6Al-4V alloy [183].

The structure and bioactivity of alkali and heat treatment of β-Ti alloys have been investigated [184–192]. Takematsu *et al.* [186,193,194] performed three different alkali solution treatments (electrochemical, hydrothermal, and hydrothermal-electrochemical) on Ti-29Nb-13Ta-4.6Zr alloy and compared the bioactivities and other characteristics of the modified surfaces. The authors showed the influence of the process to the surface morphology where electrochemical treatment resulted in a flat surface, hydrothermal treatment resulted in a smooth and fine mesh-like structure, and hydrothermal-electrochemical treatment led to a rough mesh-like structure. Moreover, apatite inductivity in SBF was reported to be influenced by surface roughness and chemical composition where increased roughness and decreased Nb content on the surface led to a higher apatite induction ability. Also, the authors reported that a thicker oxide layer or presence of surface cracks decreased the adhesion strength, where cracks usually initiated as a result of thermal stress.

It has been reported that alkali [184] and alkali-hydrogen peroxide [188] treated Ti-15Mo alloy can induce bone-like apatite formation *in vitro*. The effect of alkali and hydrogen peroxide treatment on the electrochemical and biological performance of the Ti-5Mo-3Fe alloy surface was evaluated by Kumar *et al.* [189] and it was found that the alkali-treated alloy immersed in SBF solution exhibited notably higher corrosion resistance when compared with untreated and hydrogen peroxide treated samples. Furthermore, it was stated based on MG-63 *in vitro* cell culture studies that the alkali-treated samples showed better cell adhesion and spreading compared to the untreated and hydrogen peroxide treated samples. Zheng *et al.* [192] performed alkali treatment for calcium phosphate coatings on Ti-24Nb-4Zr-7.6Sn alloy and determined the adhesion and proliferation of rat osteoblast. The authors found that both the adhesion and proliferation of osteoblast cells on apatite formed Ti-24Nb-4Zr-7.6Sn were much better than on uncoated Ti-24Nb-4Zr-7.6Sn and cp-Ti.

Surface treatments with acid, alkali, hydrogen peroxide, and mechanical polishing, or a combination of these treatments are being applied in order to improve the adhesive strength of HA films [187]. Studies showed that the adhesive strength of such films can be improved by increasing the roughness of the underlying substrate. Hieda *et al.* [195] investigated the effect of acid treatment and

mechanical polishing treatments on the adhesive strength of HA films deposited on Ti-29Nb-13Ta-4.6Zr alloy through metal-organic chemical vapor deposition (MOCVD) to increase the hard tissue compatibility. The authors reported that the adhesive strength of the HA layers formed on Ti-29Nb-13Ta-4.6Zr substrates treated with an HF solution significantly increased as compared to that of the HA film deposited on a polished Ti-29Nb-13Ta-4.6Zr surface. Also, the HA films on Ti-29Nb-13Ta-4.6Zr substrates treated with an H_2SO_4 solution exhibited lower adhesive strength than HA films on Ti-29Nb-13Ta-4.6Zr substrates treated with HF solution, regardless of the surface roughness of the substrates. Additionally, it was reported that the nanoscale surface asperities contributed to the adhesive strength, which was not observed for macroscale asperities.

The hydrothermal method is found to be very useful due to the formation of uniform coatings on complicated shapes, low processing temperature, low cost, and particularly because of strengthening the adhesion between the resultant coating and substrate. The surface wettability of implants is a crucial factor in their osteoconductivity because it influences the adsorption of cell-attached proteins onto the surface. In this respect, Zuldesmi *et al.* [196] compared the polished, hydrothermal treated, and anodic treated surfaces of Ti and four different Ti alloys (Ti-6Al-4V, Ti-6Al-7Nb, Ti-29Nb-13Ta-4.6Zr, and Ti-13Cr-1Fe-3Al). Hydrothermal treatment was performed in distilled water at 180 °C for 3 h whereas anodic treatment was performed in 0.1 M H_3PO_4 solution by applying potentials from 0 V to 150 V with 0.1 V s^{-1} scanning rate. It was found that hydrothermal treatment increased the surface hydrophilicity of all types of Ti alloys and the osteoconductivity of Ti alloys after hydrothermal treatment and immersion in phosphate-buffered saline solution increased five times compared with that of the untreated samples.

Nanostructured TiO_2 coatings are found to be favourable for the early osteointegration and biocompatibility due to their bioactivity. Liu *et al.* [197] studied the biocompatibility and early osteointegration of nano-TiO_2 hydrothermally coated Ti-24Nb-4Zr-7.9Sn alloy compared with those of uncoated Ti-2448. The biocompatibility was evaluated using MTT assays, the histocompatibility was determined by observing the histological sections stained with HE (subcutaneous implantation, endosseous implantation), and the early osteointegration was tested using the alkaline phosphatase (ALP) activity and TGF-β1 expression. The authors reported an enhanced proliferation and cytocompatibility on the functionalized surfaces based on the MTT results, and better histocompatibility of the subcutaneous and endosseous implantation based on the *in vivo* studies. Zheng *et al.* [198] studied the functionalization of Ti-24Nb-4Zr-7.9Sn alloy by thermal treatment followed by hydrothermal treatments in supersaturated $Ca(OH)_2$ solution. The treatment resulted in a layer containing $CaTiO_3$, $CaCO_3$, $Ca(OH)_2$, and TiO_2, and the authors reported a formation of Ca–P layer after soaking in SBF for

3 days. Tao *et al.* [199] investigated the surface properties of the Ti-25Nb-3Zr-2Sn-3Mo alloy after functionalization by a hydrothermal treatment in urea solution at temperatures varying between 105 and 170 °C, followed by a heat treatment at 400 °C. The authors showed that changes in temperature on hydrothermal treatment affected the surface structure where nanosheet films of ammonium titanate were observed after the treatment at 105 and 120 °C, whereas nanoparticle film of anatase TiO_2 containing Nb_2O_5 was formed at 150 °C. Moreover, the authors reported enhanced hydrophilicity on the functionalized surfaces after water contact angle measurements around 68° and 10° for untreated and treated alloys, respectively.

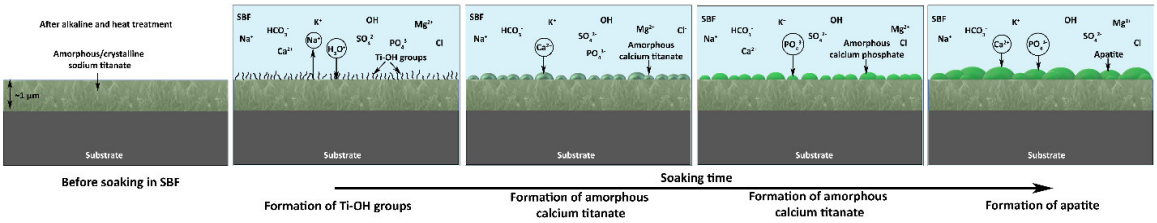

Fig. 2.7. Schematic illustration of the apatite formation mechanism on the surface of alkali and heat-treated Ti-based alloy soaked in SBF.

2.2.4. Electrochemical surface treatments

Electrochemical processes are performed by chemical action on the metal surface under an electric current passing through an electrolyte. The electrochemical setup and the examples of resultant porous with volcano-like structure, nanotubular, and HA-containing layers are presented in Fig. 2.8. These methods are simple and cost-effective, allowing the incorporation of bioactive elements, and can increase the corrosion resistance of the modified materials owing to a more stable and thicker oxide layer formed on the surface [200]. Oxide layers with different morphologies, thickness, roughness, wettability, chemical compositions, and crystalline structures are formed on the substrates depending on the applied voltage and electrolyte composition [201].

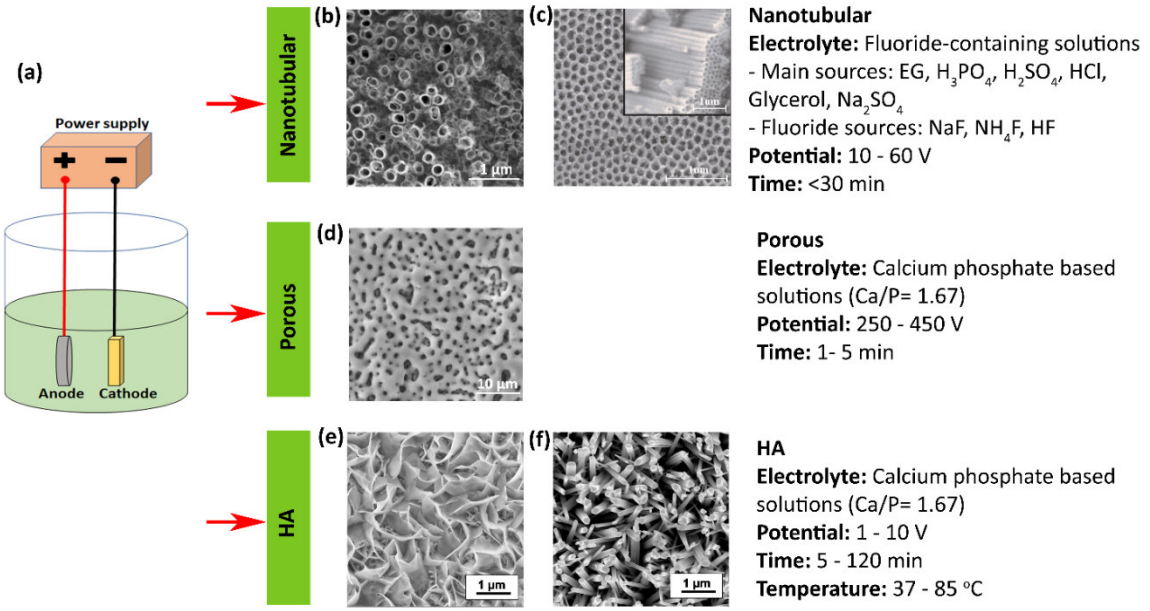

Fig. 2.8. a) Schematic representation of the electrochemical surface modification set up, and the representative resultant surfaces with process parameters: b) nanopores (adapted from [228] with permission from Elsevier, c) nanotubes (adapted from [299] with permission from Elsevier), d) porous oxide layer formed by MAO (adapted from [300] with permission from Elsevier), e) plate-like HA, and f) needle-like HA (adapted from [187] with permission from Elsevier).

2.2.4.1.MAO

MAO treatment has been used by several authors to modify the surfaces of Ti and its alloys for several biomedical applications. Rafieerad *et al.* [202] reviewed the surface characteristics and corrosion behaviour of calcium phosphate-based composite layers on Ti and its alloys via MAO treatment. The authors concluded that the fabrication of bioactive surfaces to improve the osteointegration of Ti-based implants is strongly recommended via MAO treatment. It is possible to obtain different morphologies, microstructures, thickness, and crystalline structures of the anodic layers by using different electrolytes, voltages, currents or treatment time. Furthermore, this type of treatment allows the incorporation of bioactive elements such as Ca and/or P by using electrolytes such as $Ca(H_2PO_2)_2$ [200,203–209], H_3PO_4 [203,207,209,210] or a mixture of both [203,211], calcium acetate (CA) [212–218], a mixture of CA and β-glycerophosphate (β-GP) [214,215,217–219], and NaH_2PO_4 [220]. Apart from bioactive elements, MAO also allows the incorporation of antimicrobial elements, such as Ag, Cu or Zn [221]. Some authors had reported the possibility of incorporation of bioactive additives into Ti-based alloys MAO layers such as tricalcium phosphate (TCP, $Ca_3(PO_4)_2$), wollastonite ($CaSiO_3$) or SiO_2 particles which are known to enhance osteointegration [200,204–208].

Simka *et al.* [203] and Kasek-Kesik *et al.* [204,205] treated β-Ti alloy (Ti-15Mo) via MAO. The authors used H_3PO_4, $Ca(H_2PO_2)_2$ or $(HCOO)_2Ca$ as an electrolyte and observed that the morphology and chemical composition of the anodic layers were strongly dependent on the applied voltage and chemical composition of the electrolyte used during the treatment. Independently of the electrolyte, when the voltage increased, the pore size of the anodic layers increased, however, more cracks were observed. The incorporation of Ca and/or P was, as well, dependent on the applied voltage. Moreover, the thickness of the anodic layers was dependent on both applied voltage and electrolyte concentration. For example, thicker anodic layers were observed for the highest concentration of $(HCOO)_2Ca$. MAO parameters or electrolyte concentrations also influence the crystalline structure of the anodic layers. Simka *et al.* [203] found only a single crystalline phase TiO_2 after treatment in a mixture of $Ca(H_2PO_2)_2$ and H_3PO_4 electrolytes, indicating that TiO_2 layers were amorphous. However, after decreasing the concentration of $Ca(H_2PO_2)_2$, the authors reported the existence of the anatase phase.

Kazek-Kesik *et al.* [204,208] used $Ca(H_2PO_2)_2$ as electrolyte together with TCP, wollastonite or silica particles. The authors stated that the particles from the electrolyte suspension were successfully incorporated into the porous anodic layers for voltages higher than 150 V. However, while increased concentrations of TCP and wollastonite led to an increase in Ca and P incorporation the opposite was observed on the increased silica particle addition. Regarding the surface roughness, no significant influence was found when wollastonite or silica particles were used. However, the highest roughness value was found for the highest concentration of TCP particles. Kazek-Kesik *et al.* [205] also compared the influence of the substrate (Ti-6Al-7Nb, Ti-13Nb-13Zr and Ti-15Mo) on their anodic layer characteristics after MAO treatment. The authors added TCP particles into $Ca(H_2PO_2)_2$ electrolyte for MAO treatment and observed that TCP particles were mainly deposited on the top of the anodic layers and filled the pores of the outer porous layer. Moreover, the formed oxide layers were different in terms of thickness, roughness, chemical composition, and crystalline structures, depending on the substrate. As well, their total thickness increased significantly with the incorporation of TCP particles. Oppositely, the roughness of the anodic layer with TCP particles decreased when compared with only anodized titanium alloys leading to an influence on the wettability. Bio-functionalization of Ti-13Nb-13Zr surface via MAO was studied by Kazek-Kesik *et al.* [200,222] by using a $Ca(H_2PO_2)_2$ electrolyte with the addition of TCP, wollastonite or silica particles where the microstructures and chemical composition of the anodic layers were strongly dependent on the applied voltage. Moreover, the final surface roughness reported to be increased after the treatment.

Another β-Ti alloy that had been treated by the MAO process is Ti-30Nb-1Fe-1Hf [213,217,218]. Ou *et al.* [213,218] used a calcium acetate (CA) and β-GP mixture as an MAO electrolyte and reported a three-layer structure, namely, an amorphous and crystalline outmost porous layer followed by an inner layer with several pores, and finally a thin and compact layer. Moreover, the presence of Nb promoted the formation of the amorphous phase of the anodic layer. Oppositely to cp-Ti, when the voltages on MAO treatment increased, the crystallinity of the anodic layers decreased on Ti-Nb alloys. The incorporation of Ca and P was also succeeded with a Ca/P ratio maximum of 1.91 depending on MAO parameters. On the other hand, Pan *et al.* [217] used similar electrolyte to modify the surface of the same alloy and reported that the presence of Nb in Ti alloy can promote both layer rupture voltage and dielectric breakdown voltage due to the mixture of oxides (Ti and Nb oxides) that are known to stabilize the amorphous structure and delay oxygen generation.

Gebert *et al.* [223] used a NaOH alkaline solution as electrolyte during the MAO process and reported surfaces having a compact and thin inner layer followed by a much thicker outer layer with micro-pores and micro-channels. Moreover, the presence of Nb enhanced the thickness growth of the outer layer. On the other hand, Sharkeev *et al.* [210] performed MAO treatment on Ti-40Nb by using a mixture of H_3PO_4, biological HA, and calcium carbonate. The authors pointed the need for performing crystallization annealing treatment after the MAO process in order to obtain a crystalline structure on the anodic layer. The anodic layer was formed by a thin compact oxide layer, intermediate sublayer, and the typical porous CaP layer. As the voltage of MAO treatment increased, the thickness of the anodic layer also increased linearly from 35 to 90 μm. Moreover, when the voltage ranged between 200-300 V, the CaP layer presented spheres and pores. However, when the voltage increased up to 400 V, the transformation of micro-arc discharges into arcs caused the destruction and fragmentation of the spheres leading to a decrease of the anodic layer porosity. By using voltages under 200 V, XRD analysis just showed intense peaks of Ti and Nb and poor reflexes of NbO_2 phases, mainly due to the small thickness of the anodic layer. The absence of TiO_2 phases into the anodic layers was explained by higher thermal conductivity and lower electrical resistivity as compared to Ti. When the process voltage increased up to 300 V, the anodic layer was formed by an amorphous phase and crystalline phases such as $CaHPO_4$ and β-$Ca_2P_2O_7$. Further increase on the process voltage up to 400 V led to a decrease on the peak intensity of the characteristically crystalline phases of the anodic layers.

Tao *et al.* [212] studied the effect of Nb, Zr, and Sn on the characteristics of the anodic layers formed by MAO. The authors used a CA electrolyte with an applied voltage of 250 V and after the samples

were heat-treated at 600 °C for 1h in air. The anodic layer porosity increased with increasing voltage, and at 250 V, the porous structure covered uniformly all the surfaces. Although the surface roughness increased with the working voltage, it was not affected by the heat treatment. After heat treatment, the anodic layers were mainly composed of TiO_2 (anatase and rutile), Nb_2O_5, CaO, and SnO_2. However, the diffraction intensity of Nb_2O_5, CaO, and rutile increased after heat treatment. A study using the same alloy was reported by Gao *et al.* [216] where the authors also used the similar MAO treatment parameters. However, XRD analysis only detected Ti, anatase and rutile peaks while elements such as Ca, Nb, Zr, and Sn were only detected by EDS analysis. These results showed the importance of the post-heat treatment on the crystallinity of the anodic layers as reported by Tao *et al.* [212].

Other alloys as TiZrSnMoNb [214,215], TiAlNb [205], TiCrAlFe [220] have also been modified by MAO. However, the effect of the alloying elements on the MAO treatment of the new alloys is yet to be fully understood. Besides, although the MAO process has been successfully used to modify β-Ti alloy surfaces mainly to increase the bioactivity, very little is known on the growth mechanisms of MAO layers including the incorporation process of the bioactive elements.

Apatite forming ability has been used to access the bioactivity, however, apatite forming ability depends not only on the chemical composition of the anodic layers but also on the volume of SBF solution used during the soaking process. Thus, due to these factors, different results are reported in the literature. Kasek-Kesik *et al.* [207] reported that according to the mechanism of apatite crystallization, the presence of anatase and rutile may be negatively charged in SBF and adsorbs Ca^{2+} ions. Ca^{2+} ions also attract OH^- and HPO_4^{2-} groups. If an anodic layer does not have phosphorous compounds, the formation of apatite may be delayed or not exist, however, it is still possible by the formation of calcium titanate ($CaTiO_3$) on the anodic layer since the presence of $CaTiO_3$ facilitates the adsorption of hydroxyl radicals and phosphate leading to the formation of apatite.

Several authors reported that apatite forming ability is induced on MAO treated surfaces of β-Ti alloys, independently of the chemical composition of the substrate [207,209,212,215]. Tao *et al.* [212] concluded that a heat treatment after MAO on Ti-24Nb-7Zr-7.9Sn alloy improved the apatite forming ability. The same behaviour was described by Kazek-Kesik *et al.* [207] for Ti-15Mo alloy treated by MAO and post-treated by heat treatment. On the other hand, Yu *et al.* [215] reported that in-situ formation of apatite on the MAO treated surfaces of Ti-3Zr-2Sn-3Mo-25Nb in SBF was related to Ca- and P- containing compounds. Moreover, apatite nuclei were formed after approximately 14 days of immersion and it continued to grow, firstly filling the pores and after spreading over the entire surface. Sowa *et al.* [209]

modified surfaces of Ti-13Nb-13Zr alloy by MAO and the authors were able to detect small amounts of apatite precipitates formed on the modified Ti alloy surface after immersion in SBF, although the treated surfaces presented Ca/P ratios bellow 1.67 (Ca/P atomic ratio of stoichiometric HA).

Immersion of MAO treated surfaces in SBF to promote apatite forming ability and thus bioactivity has been widely studied. However, the reliability of evaluation of bioactivity of those surfaces by simply immersing in SBF has been criticized due to the lack of proteins presence or bacterial activity. Thus, in vitro and/or in vivo studies have been reported to access the biological response of the modified surfaces. Kazek-Kesik *et al.* [205] developed multi-layered surfaces by electrophoretic deposition of TCP particles on MAO treated surfaces of V-free alloy (Ti-6Al-7Nb, Ti-13Nb-13Zr, and Ti-15Mo). The number of incorporated TCP particles was higher for Ti-13Nb-13Zr and Ti-15Mo alloys than for Ti-6Al-7Nb. The adhesion and number of MG-63 osteoblast-like cells were investigated by Kazek-Kesik *et al.* [205] and it was observed that independently of the base alloy, none of the modified surfaces were cytotoxic. The highest biological activity was found for MAO+TCP treated Ti-15Mo alloy, while the surface modification did not significantly influence the cell proliferation on Ti-6Al-7Nb and Ti-13Nb-13Zr alloys. On the other hand, another study from the Kazek-Kesik *et al.* [207] modified Ti-15Mo alloy by MAO and showed that after 5 days of culture, hBMSC cells have well adhered to all modified surfaces. However, the anodic layers with the highest atomic ratio of Ti/Ca presented higher ALP activity, collagen production, and mineralization when compared with the untreated alloy. Moreover, these surfaces showed only a single strain of attached D. desulfuricans bacteria and it was not observed the formation of bacteria biofilm. Furthermore, the Zn, Cu, and Ag-doped CaP MAO composite was formed on Ti-40Nb alloy, presented an improvement on the antibacterial activity [224].

The biological performance of low Young's modulus Ti-24Nb-4Zr-7.9Sn alloy bio-functionalized by MAO has been reported [212,216]. After heat treatment, the anodic layers consisted of TiO_2, CaO, Nb_2O_5, and SnO_2. In vitro studies on rabbit's osteoblast showed a considerable improvement in cell proliferation due to the increased roughness of the surfaces but as well due to the incorporation of Ca into the anodic layers [212]. Although no heat treatment was performed after MAO, Gao *et al.* [216] showed that MAO treated surfaces presented significantly higher absorbance of cells when compared to the untreated alloy. Moreover, the porous structure and chemistry of the anodic layers led to a stronger and faster bone response of the modified surfaces.

Ou *et al.* [218] functionalized Ti-30Nb-1Fe-1Hf alloy by MAO using a Ca- and P-rich electrolyte followed by a post hydrothermal treatment. In vitro studies with MG-63 cells indicated no significant

differences between the untreated and treated alloy on optical cell density and ALP activity. However, cell adhesion and cell spreading were reported to be improved by hydrothermal treatment. Sowa *et al.* [209,225] modified Ti-13Nb-13Zr alloy by MAO in an electrolyte containing Ca and P elements. The authors observed that the incorporation of Ca and P into the anodic layer enhanced the differentiation of hBMCs into osteoblasts. Moreover, the increased roughness after MAO promoted cell spreading. A similar improvement was achieved for Ti-45Nb alloy through 26 days of cell culture [226].

Bioactive surfaces were produced by Zhao *et al.* [214] on Ti-5Zr-3Sn-5Mo-15Nb alloy using MAO where better osteoblasts adhesion, spread, viability, and differentiation were observed. However, by increasing the applied voltage of MAO treatment, better cell spread and viability was observed. The authors stated that this behaviour might be explained by the increased roughness together with an increased Ca/P ratio obtained at the highest voltage. On the other hand, Yu *et al.* [215] used similar alloy and MAO treatment conditions but performed further activation in an aminated solution. Results showed that MC3T3-E1 cell proliferation was favoured and hard tissue implantation indicated that the activated surfaces exhibited good biocompatibility and better osteointegration than the untreated alloy. Chen *et al.* [220] bio-functionalized Ti-13Cr-3Al-1Fe alloy using MAO in NaH_2PO_4 electrolyte. In vitro tests using MC3T3-E1 cell line and in vivo tests in distal femora of Japanese white rabbits showed that the rutile-rich TiO_2 layer gave better biocompatibility and osteointegration performance than anatase rich phase, suggesting that MAO treated implant may achieve better bone formation and ongrowth.

In addition to their increased bioactivity, anodic layers on Ti-based alloy created by MAO can also increase the corrosion resistance of the base alloys. Kazek-Kesik *et al.* [200,204,205,222] reported the corrosion behaviour of different low Young's modulus alloys modified by MAO. The corrosion behaviour of Ti-6Al-7Nb, Ti-13Nb-13Zr, and Ti15Mo MAO treated alloys was studied in Ringer's solution [205]. Surface modification caused an increase in the corrosion resistance for all substrates. However, the highest differences in the electrochemical parameters were found between treated and untreated Ti-15Mo alloy.

It has been reported [204] that MAO treatment in TCP, wollastonite or silica particle-containing electrolytes improved the corrosion resistance of Ti-15Mo alloy due to the barrier-type oxide layer formed on the alloy surface. The highest corrosion resistance was recorded for the electrolyte containing TCP particles owing to the thicker and more compact oxide layer. Similar MAO treatment was performed on Ti-13Nb-13Zr by Kazek-Kesik *et al.* [200,222]. Results showed that the OCP values in Ringer's solution were much nobler on the treated samples, showing a lower tendency to corrosion when compared with

the untreated alloy. Furthermore, the polarization resistance increased and current density decreased, independently of the incorporated particles, as compared to the untreated alloy [200]. By immersing the treated alloy in Ringer's solution for 5 months, the authors could observe the degradation of the anodic layers due to the dissolution of Ti, Nb, and Zr phases [222]. The concentration of dissolved Ti ions in electrolyte was found to be influenced by the applied voltage during MAO treatment as a consequence of increased surface roughness with increasing applied potential. Apart from Ti ions, Nb and Zr ions were also detected but their amounts were very small.

2.2.4.2. Nanotubular structures

TiO_2 nanotubular surface structures have been widely reported for biomedical applications since protective stable oxides on Ti-base surfaces lead to a favourable osteointegration [204,227]. TiO_2 nanotube growth is obtained by anodic treatment using F^- containing electrolytes. The nanotube growth has been reported on binary, ternary and quaternary β-Ti alloys such as Ti-Nb [223,227], Ti-13Zr-13Nb [228,229], Ti-25Ta-xZr [230], Ti-35Nb-xZr [231,232], Ti-29Nb-13Ta-4.6Zr [233], and Ti-24Nb-4Zr-7.9Sn [234,235].

Gebert *et al.* [223] compared the growth of the nanotubes on Ti-40Nb and cp-Ti (grade 2) in fluoride-containing solutions and observed a similar growth. Moreover, the oxide nanotubes presented amorphous structures and mixed compositions as $(Ti_xNb_{1-x})O_2$. On the other hand, Jang *et al.* [227] produced nanotubular surfaces on Ti-xNb (x = 10, 20, 30 and 40 wt.%) alloys using 1.0 M H_3PO_4 electrolyte containing 0.8 wt.% NaF. The nanotubes formed on the Ti-xNb alloy surface presented a wide range of diameters (55-220 nm). More specifically, as Nb content increased, the length of the nanotubes increased from 730 nm to 2 μm. The authors also reported that the initial structure of the nanotubes was an amorphous TiO_2–Nb_2O_5 layer. After annealing at 300 and 450 °C, the formation of crystalline anatase, and after annealing at 600 °C, in addition to anatase, the formation of rutile was detected.

Ossowska *et al.* [228] and Hernández-López *et al.* [229] performed anodic treatment to obtain nanotubes on Ti-13Zr-13Nb alloy using a mixture of 1 M H_2SO_4 and 0.035 M HF. Hernández-López *et al.* [229] stated that shorter anodizing times resulted in nanostructured layers with a porous morphology, whereas after longer anodizing times, the anodic film showed a nanotubular structure. Moreover, the average molecular composition given by Rutherford backscattering spectroscopy (RBS) analysis was $(TiNbZrO)_{0.45}0.081TiF_4 0.102NbF_5 0.081ZrF_4$ for the nanoporous layers while the nanotubular layers presented a molecular composition as $(TiNbZrO)_{0.61}0.078TiF_4 0.098NbF_5 0.078ZrF_4$. On the other hand, Ossowska *et al.* [228] compared the nanotube growth on dense and porous Ti-13Zr-13Nb alloy. Results

showed a fine nanotubular structure with long nanotubes, moreover, the nanotubular structure is formed also inside the pores in the case of the porous alloy. However, the nanotube dimension was smaller on the porous alloy when compared to the dense alloy.

Li *et al.* [234] and Hao *et al.* [235] modified the surface of Ti-24Nb-4Zr-8Sn by anodic treatment. Both authors performed the anodic treatment in a neutral electrolyte with 1M $(NH_4)_2SO_4$ and 0.15M NH_4F. Hao *et al.* [235] stated that the outer diameter of the nanotubes increased from 30 to 90 nm as the treatment voltage increased from 10 to 25 V. Results showed that the contact angle decreased sharply with increased nanotube diameters from 30 to 70 nm and then was constant with the further increase of diameter to 90 nm. The authors suggested that the surface energy increases with an increase of nanotube diameter up to 70 nm, which was explained by the formation of surface oxides and their contribution to surface roughness. XPS analysis showed that the outmost nanotubular layer consisted of amorphous mixed oxides of TiO_2, Nb_2O_5, SnO_2, and ZrO_2. Similar results regarding the chemical composition of the oxides were also reported by Li *et al.* [234].

Similar to MAO-treated β-Ti alloys, studies investigating the corrosion behaviour of nanostructured surfaces on β-Ti alloys are scarce. Jang *et al.* [227] performed potentiodynamic polarization tests in 9 g/L NaCl at 36.5 ± 1 °C for nanotubes formed on Ti-xNb alloys and found that the corrosion resistance of nanotubular structured alloys was lower as compared to the untreated alloys. The authors explained this behaviour by the defected structure of the nanotubular surfaces that may promote the current transport. However, the anodic treated samples presented a wider range of a passive region when compared with the untreated alloys, suggesting that the mixture of TiO_2 and Nb_2O_5 film was more stable. On the other hand, Ossowska *et al.* [228] and Hernández-López *et al.* [229] reported that the proper formation of nanotubular structures by anodic treatment resulted with a better corrosion behaviour as compared to the bare alloy.

Nanotubular structures on ternary and quaternary β-Ti alloys have been reported to stimulate rapid cell proliferation and osteoblast differentiation as well as to accelerate osteointegration and facilitate the transport of nutrients and bone ingrowth [234,235]. It has been shown that the formation of ordered nanotubes on Ti-24Nb-4Zr-7.9Sn alloy via anodic treatment improved cytocompatibility, as well, enhanced bone-implant integration *in vitro* and *in vivo* [234]. Hao *et al.* [235] obtained nanotubular surfaces with mixed oxides (TiO_2, Nb_2O_5, SnO_2, and ZrO_2) and reported after biological studies with osteoblast-like MG-63 cells that smaller nanotube diameter was beneficial for the cell adhesion,

proliferation, and differentiation. Also, the anti-bacterial behaviour of Ti-35Nb alloy was improved with the corporation of Sn as an alloying element [236].

2.2.4.3. HA electrochemical deposition

HA and calcium phosphate ceramic coatings are widely used in the biomedical field due to their excellent response to cell adhesion and proliferation, as well as their ability to enhance bone ingrowth and osteointegration processes. The deposition conditions have a great effect on the structure and biofunctionality of HA coatings. The electrochemical deposition of HA coatings on metallic biomaterials has unique advantages and it is an attractive technique because highly complex structures can be coated quickly at low temperatures. Moreover, the coating morphology and chemical composition of HA can be well controlled by varying the electrochemical potential, current, electrolyte concentration, and temperature.

Several studies reported the electrochemical deposition of HA [187,213,237–240]. Schmidt et al. [187] studied the influence of electrolyte temperature and different chemical pre-treatments on Ti-40Nb alloy for the deposition of the HA layer. The authors performed potentiostatic deposition of HA using a mixture of $Ca(NO_3)_2$ and $NH_4H_2PO_4$ on grounded surfaces, etched surfaces with piranha solution, and alkali-treated surfaces. The morphology of the HA deposit was dependent on the electrolyte temperature. When the electrolyte temperature increased from 60 to 80°C, the morphology of HA passed from plate-like to needle-like shape. However, the use of different pre-treatments did not have a significant effect on HA layer morphology. On the other hand, Byeon *et al.* [240] performed HA deposition on Ti-xNb alloy by cyclic voltammetry in two different electrolytes (CaP - a mixture of $Ca(NO_3)_2 4H_2O$ and NH_4PO_4; and Zn-CaP - a mixture of $Ca(NO_3)_2 4H_2O$, NH_4PO_4 and $Zn(NO_3)_2 4H_2O$). Although different Ca- and P- rich electrolytes were used, the Ca/P ratio kept constant, and the HA layer presented a nano-scale rod-like HA for CaP electrolyte, while the Zn-CaP electrolyte led to a nano-scale network-like Zn-HA layer. Although the authors reported successful Zn-HA layer deposition, further studies are needed in order to get a better understanding of the formation and properties of these layers on Ti-Nb alloys.

Kim *et al.* [237] used a mixture of $Ca(NO_3)_2$ and NH_4PO_4 as an electrolyte to deposit HA by cyclic voltammetry over nanotubular structured anodic layer on Ti-25Ta-xZr alloy. Although all the deposited surfaces showed a Ca/P ratio lower than 1.68, a successful HA layer was deposited on its surfaces. The HA precipitate morphology was influenced by the Zr content of the alloy; as the Zr content increased, HA precipitates morphology changed from plate-like or leaf-like shape to needle-like or flower-like shape. A similar electrolyte was used by Kim *et al.* [238] to deposit HA layers on highly ordered nanotubular

surfaces of Ti-25Nb-xHf alloys. The authors observed that the needle-like nucleation and growth of the HA particles were promoted on the increased number of cyclic voltammetry cycles. However, the morphology of HA precipitates was influenced by Nb and Hf contents.

A study on the electrochemical deposition of HA on nanotube-formed Ti-Nb-Zr alloys was reported by Jeong *et al.* [239]. The authors studied deposition protocols using 5, 10, and 30 cycles of the pulsed current method and two electrolytes based on a mixture of $Ca(NO_3)4H_2O$ and NH_4PO_4. The HA layer morphologies changed from a mixture of rough particles and plate-like shape particles to entirely plate-like shapes depending on the number of deposition cycles and the Ca and P concentrations in the electrolyte.

2.2.5. Laser surface treatments

Most of the laser surface treatments for β-Ti alloys were performed in a nitrogen-rich environment resulted in the nitrided surface. Laser nitrided Ti-20Nb-13Zr alloy presented significantly higher hardness, hydrophilicity, coefficient of friction, and corrosion resistance in artificial saliva and SBF compared to the untreated alloy, cp-Ti, and Ti-6Al-4V alloy due to formation of a uniform 9 μm thick nitrided layer [241,242]. Similar behaviour was reported for different β-Ti alloys namely Ti-35Nb-7Zr-5Ta [243], Ti-45Nb [244], Ti-13Nb-13Zr [245], Ti-35Nb-2Ta-3Zr [246], Ti-35Nb-7Zr-5Ta [247], and Ti-35.3Nb-7.3Zr-5.7Ta [248]. Femtosecond lasers are being used to increase the surface roughness and reported to provide significant advantages for hole formation compared to nanosecond lasers. Its advantages are negligible heat transfer and the absence of a liquid phase since the vapor and plasma phase are formed very quickly. In addition to these advantages, the periodic nanostructures are self-organized in the laser-irradiated field. Jeong *et al.* [232] evaluated the nanotubular surfaces formed on the femtosecond laser-treated Ti-35Nb-xZr (x = 3 and 15 wt.%) and reported an extensive proliferation and spreading of the MG 63 cells. Similarly, laser treatment was reported as a sufficient pre-treatment for HA and β-TCP bio-ceramic coatings associated with the formation of oxides diversity and irregular morphology on Ti-15Nb alloy.

Saud *et al.* [249] investigated the microstructure, corrosion behaviour, bioactivity, and antibacterial activity of graphene oxide (GO) coated by dip coating on femtosecond laser surface modified Ti-30Nb alloy. The authors reported that laser-treated and GO-coated samples displayed higher corrosion resistance than the GO-coated and uncoated samples in SBF at 37 °C. Moreover, the GO coating on Ti-30Nb alloy led to a superior antibacterial activity against gram-negative bacteria as compared with the uncoated samples. Similarly, fibre laser nitrided Ti-35Nb-7Zr-6Ta alloy drastically improved the

mesenchymal stem cell attachment, proliferation and differentiation, and also led to a reduction on staphylococcus aureus bacterial attachment due to formation of a hard rough surface with low hydrophobicity [250,251].

2.2.6. Immobilization of biomolecules

Bioactive molecules are also used to enhance the soft tissue compatibility on metallic biomaterials. Many studies investigated the biopolymer coated cp-Ti and Ti-6Al-4V alloy, however, a very limited number of studies are available on biopolymer coated β-Ti alloys [191,252–256]. The schematic diagram for the immobilization process is presented in Fig. 2.9. Biochemical modification of the Ti-25Nb-16Hf alloy with elastin-like polymers (ELPs) was performed, and their influence on the cell response was analyzed by González *et al.* [252]. ELPs presented remarkable biocompatibility and one of these polymers contains the well-known cell adhesion amino acid sequence, arginine-glycine-aspartic (RGD). It was found that the RGD interface presented enhanced results in terms of cell adhesion and spreading but no improvement was observed on the numbers and differentiation of the cultured cells. Hsu *et al.* [253] investigated the biocompatibility of NaOH treated Ti-25Nb-8Sn alloy surface and found that the RGD peptide grafted Ti-25Nb-8Sn alloy significantly enhanced the cell adhesion, proliferation, and differentiation.

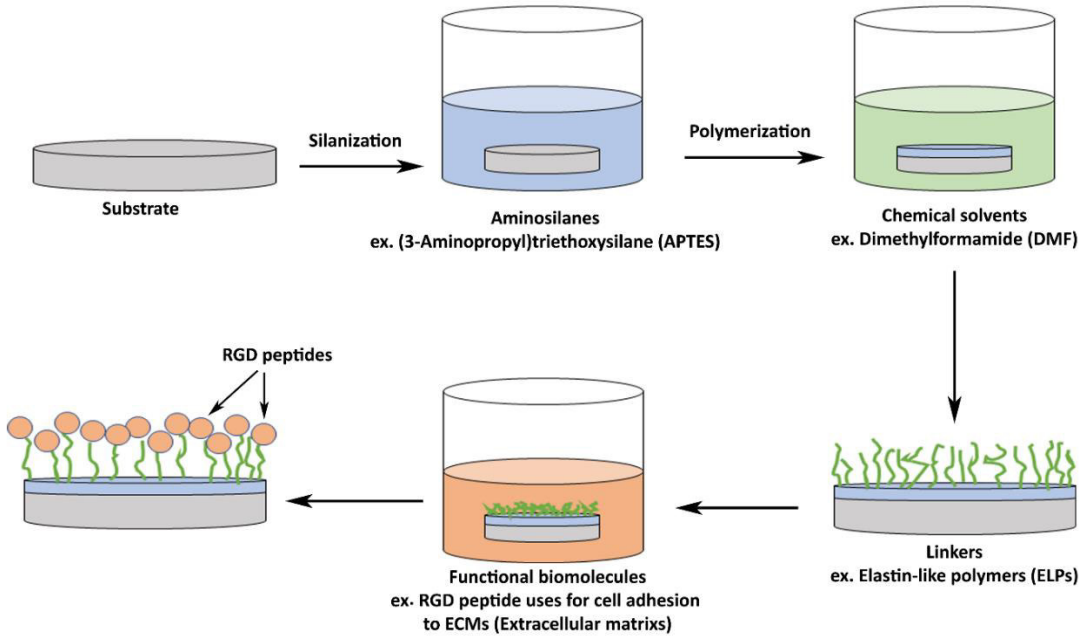

Fig. 2.9. Demonstration of the immobilization process of biomolecules on a bare surface.

Adhesiveness to metallic materials is an important issue for biomedical polymer coatings from the viewpoint of long-term durability. Silane-coupling treatment is a traditionally popular route for increasing the adhesive strength between metallic materials and polymers. Hieda *et al.* [254] investigated

the effect of terminal functional groups and silane layer thickness on the adhesive strength of Ti-29Nb-13Ta-4.6Zr alloy to segment polyurethane (SPU) and reported that silane-coupling treatment led to a significant increase on the shear bond strength for all tested types of terminal functional groups and the silane layers thickness. Moreover, an immobilized 3-aminopropyltriethoxysilane- reduced graphene oxide (APTES-RGO) nano-layer coated on Ti-29Nb-13Ta-4.6Zr alloy presented better tribological behaviour as compared to the uncoated alloy [191].

2.2.7. Hybrid/multi-layered treatments

The hybrid treatments have been aimed to effectively enhance the mechanical and biological properties, and also reduce the interfacial failure. Bio-functionalization of β-Ti alloys by combining different techniques are studied in the literature. Choe [257] developed a double-layered surface on Ti-30Nb-xZr (x = 3 and 15 wt.%) having a nanotubular inner layer formed by anodic treatment and a HA outer layer formed by electron beam-physical vapor deposition (EB-PVD). The author investigated the corrosion behaviour of the functionalized surfaces in 9 g/L NaCl solution at body temperature and reported the spalling of the HA layer on the samples only coated with a single HA layer, and cracking of the HA layer on the double-layered surfaces due to the differences on the size of the nanotubes affected the corrosion behaviour mainly leading to the appearance of a breakdown potential on the passive region, which was not observed on the bare alloy. A similar double-layered structure was also developed by Jeong *et al.* [231] on Ti-35Nb-10Zr alloy having a femtosecond laser-treated surface to increase the roughness. The authors stated that the application of femtosecond laser-treated created microscale features can be beneficial for mechanical interlocking with bone. Moreover, based on the SEM observations, the authors reported a higher trend on the attachment and spreading of MG-63 cells on the double-layered surfaces developed on the femtosecond laser-treated alloy. Similar hybrid structure (NT + HA) was developed on Ti-25Nb-xHf (x=0 and 7) [258], Ti-29Nb-xZr (x=3 and 15) [239], Ti-25Ta-xZr (x=0, 3, 7 and 15) [237], Ti-13Ta-2Mo-6Zr [259], and Ti-20Ta-1Mo-8Zr [259]. The authors reported that the HA structure was significantly influenced by morphology, diameter of tubes, and distribution of nanotubular layer, which were changing by microstructure and composition of the alloy. Apatite precipitation was also affected by nanotubes diameter, where the largest diameter presented better apatite formation for Ti-35Nb-2Zr-0.2O alloy [260]. In addition to biological improvement observed by *in vitro* studies, membranes treated by this hybrid structure on Ti-20Ta-1Mo-8Zr alloy were covered on rat calvarial defects, and tomography, histologic and fluorescent analysis indicated higher bone mineral density and a contact osseointegration, suggesting durable osteogenesis at the early stage of bone defect repair [259].

RF sputtered TiN coatings on nanotubular Ti-25Ta-xZr alloys (x = 0, 3, 7, and 15 wt.%) were studied by Kim *et al.* [230]. The authors reported that as the Zr content in the alloys increased, the average thickness of the nanotubular layer increased. For the alloy with the highest Zr content, the nanotubular surfaces were covered entirely with the RF-sputtered TiN film. The authors concluded that the Zr content affected roughness and wettability, leading to highly hydrophilic properties on the nanotubular surfaces. As discussed in section 2.6, the immobilization of biofunctional polymers is important for improving the tissue compatibility. A poly(sodium styrene sulfonate) (PNaSS) biopolymer grafted with nanotubular layer grown on Ti-15Mo and a significant improvement of bioactivity and decrease of bacterial adhesion was reported [261]. However, these polymers may not sufficiently adhere to metallic materials. Nanostructures (nanopores and nanotubes) were formed on Ti-29Nb-13Ta-4.6Zr surfaces through anodic treatment in order to improve the adhesive strength of SPU [233]. It was found that the anchor effect given by the nanostructures increased the adhesive strength of SPU.

The MAO/HA structure is another commonly studied hybrid treatments for β-Ti alloys [213,262–265]. Park *et al*[262] electrochemically deposited HA on MAO layer grown on Ti-3Ta-xNb (x=0 and 10), and it was found that the particle size and morphology of HA was affected by the composition of the alloy and alkaline treatment. Also, a biodegradable poly(lactide-co-glycolide) (PLGA) polymer was deposited on the MAO layer formed on the Ti-15Mo alloy [206]. Additionally, the PLGA loaded with the drug of amoxicillin layer was coated on MAO layer of Ti-15Mo using a dip coating technique, and it was reported an improvement on corrosion and bacterial resistance of substrate [265]. The main goal of the polymer-oxide layer was to explore the active substance to be released after implantation.

2.2.8. Other methods

In the literature, other methods such as producing composite layers (metal matrix composite and HA biocomposite) or bioactive element addition were also studied. Xiaopeng *et* al. [266] produced Ti-35Nb-2.5Sn – 15 wt% HA bio-composite with mechanical alloying followed by sintering under high vacuum at 1100°C. The authors reported that the samples ball-milled during 4 h presented a relative density of 95.55% and Young's modulus of 20 GPa (defined by compressions tests). On the other hand, biological studies performed with MC-3T3 osteoblast-like cells revealed higher cell viability and proliferation. Majumdar *et al.* produced TiB in-situ reinforced Ti-35Nb-5.7Ta-7.2Zr [267] and Ti-13Zr-13Nb [268] matrix composites with addition of 0.5 wt% B particle to improve the wear resistance, however, the biological studies performed with MG63 cells revealed a decreased cell proliferation on the in-situ composites, which may be explained by cytotoxicity of B. For instance, Málek *et al.* [269] produced

in-situ TiB reinforced Ti-35Nb-6Ta matrix composites with 0.05, 0.1, 0.3 and 0.5 wt.% B particle and claimed that 0.1% and higher B addition had a slightly adverse effect on cytotoxicity.

Ou *et* al produced Ti-27.5Nb alloy with the addition of 0.2, 0.7 and 1.2 wt% Ag by arc melting to obtain antibacterial properties [270]. The authors did not observe any influence of Ag on the adhesion and proliferation of MG-63 and NIH-3T3 cells, however, reported excellent antibacterial properties against *Staphylococcus aureus* and *Escherichia coli* with antibacterial rates approaching 100%.

Another important approach is producing highly porous alloy to facilitate the ingrowth of bone tissue through the pores, leading firm fixation, allowing the transportation of body fluid into implant acting a living prosthesis, and to reduce the Young's modulus [271,272]. Several processing methods have been used such as powder metallurgy with space-holder technique, microwave sintering, polymeric sponge process, gel-casting, and selective laser melting (SLM) to produce porous β-Ti Ti-Nb and Ti-Mo based alloys [273–277]. Furthermore, several morphologies of HA was electrochemically deposited on porous low Young's modulus Ti-40Nb alloy by various electrolytes and treatment times [274].

2.3. Discussion

Particularly during the last decade, β-Ti alloys have been extensively developed to reduce the high Young's modulus of cp-Ti and Ti-6Al-4V alloy. Although the developed β-Ti alloys still have higher Young's modulus compared to bone, the values close to 45 GPa reported for several alloys by adjusting the amount and type of β stabilizer alloying elements [278–281]. Similar to cp-Ti and Ti-6Al-4V, β-Ti alloys are bioinert materials, thus require surface modifications in order to obtain bioactivity. Furthermore, lower corrosion, wear, and tribocorrosion behaviour of β-Ti alloys have been recently reported compared to Ti-6Al-4V alloy, which are other crucial factors for long-term implants [58,86,282–284].

Mechanical treatments are being performed to form a nanocrystalline surface layer and grain refinement in order to improve the surface roughness and hardness or to alter the surface topography to gain bio-functions [285]. The mechanical, corrosion, wear, and biological behaviour of β-Ti alloys have been improved by HPT, SMAT, UNSM, and ARB severe plastic deformation techniques mainly due to the grain refinement from coarse grains to ultrafine grains. The ultrafine-grained Ti alloys prepared by severe plastic deformation are reported to have higher strength and cell bioactivity than the untreated ones [68]. However, tribocorrosion behaviour of severe plastic deformed β-Ti alloys are, to the best of our knowledge, yet to be studied.

Physical surface treatments of β-Ti alloys including PVD, plasma spraying, plasma nitriding, gas nitriding, and ion implantation treatments have been widely used to improve the corrosion and wear behaviour along with the bioactivity of metallic materials. Although physical surface treatments can improve the wear resistance of β-Ti alloys to some extent, physical deposition methods mostly require complex equipment and the resulting surfaces prone to delaminate under sliding conditions [95].

Chemical and electrochemical methods, allowing the incorporation of bioactive elements and providing stronger adhesion between bones and implant surfaces compared to the materials treated by mechanical and physical methods, are attracting more attention owing to their lower cost and easier process control. These surface treatments can be used to generate a nanopatterned surface topography which is expected to be promising for the stimulation of bone tissue growth (osteointegration of bone tissue) [177]. One of the most used methods for bio-functionalization of β-Ti alloys is MAO treatment. As described previously, the MAO-layers on β-Ti alloys are characterized in terms of biological response by *in vitro* and *in vivo* studies. However, studies on the corrosion behaviour of these layers is still scarce and there is still lack of information regarding their corrosion mechanisms mainly, particularly the role of oxides of β stabilizer alloying elements, which may change the chemistry, structure and mechanical properties of MAO layer. Moreover, the corrosion behaviour should also be studied under conditions closer to *in vivo*, for instance, in a dynamic electrolyte and/or under the presence of proteins, enzymes, microorganisms, and biofilms. After implantation, micro-movements occur between the implant and the hosting bone, or between the parts of the prosthesis, thus, understanding the effect of the combined action of corrosion and wear (tribocorrosion) is extremely important. Furthermore, the combined actions of corrosion and mechanical solicitations (fatigue-corrosion) also needs to be studied.

The nanotubular layer formation on β-Ti alloys is another common surface functionalization method. The nanotubular layer formation on the new alloys and its corrosion behaviour has been studied in the literature, however, the wear and tribocorrosion behaviour of these nanotubular layers are scarcely researched. The nanotubular layer grown on Ti has significantly poor adhesion to the substrate. Although some efforts are given in the literature [286–293], adhesion is still a major limitation for different applications [287,294,295]. To our best knowledge, there is no published study yet that investigates the tribocorrosion behaviour of nanotubular layer formed on β-Ti alloys, but the dry sliding behaviour of nanotubular layer formed on Ti-35Nb are reported, where the nanotubular layer improved the tribological behaviour of Ti-35Nb alloy even though this improvement was due to the tribolayer formed after smashing of the nanotubular layer during sliding [296].

Laser surface treatment is becoming one of the most efficient and versatile surface modification techniques, allowing to control changes in the mechanical, chemical, and physical properties of the surface through direct interaction of beam and substrate [297]. Laser treatment is being used to modify the substrate surfaces like texturing, hardening, remelting, and cladding, which can also be used to add calcium phosphate or HA. Based on the published studies, it can be stated that laser surface treatments are beneficial pre-treatments for the adhesion of nanotubes and bio-ceramic coatings, also they make a positive influence on corrosion, wear, and bioactivity of β-Ti alloys. However, laser texture and remelting may cause cracks on the surface, and the heat affected zone under the melting layer may lead to poor mechanical integrity. Also, *in vitro* and *in vivo* biological behaviour of laser-treated substrates are yet to be completely understood.

Recently, hybrid/multi-layered treatments have been attracted attention as a route to multifunctional materials. Depending on the target implant application, the surface of β-Ti alloys can be tailored by hybrid treatments. So far, HA/Nanotubes and HA/MAO has been the most studied hybrid treatments mainly in order to improve the adhesion of the HA layer through mechanical interlocking. Also, TiN coating on nanotubes has been studied to improve the wear resistance [230]. However, as discussed above, the main concern with nanotubular layers is the poor adhesion strength of nanotubes to the substrate. Thus, if a sufficient adhesion is not obtained between the substrate and the nanotubular layer, detached hard TiN particles may lead to catastrophic wear by acting as extra abrasives during relative movements. Therefore, even though each treatment has promising behaviour, individually, overall mechanical and tribo-electrochemical responses of the hybrid/multi-layered surfaces need to be explored.

2.4. Concluding remarks

β-Ti alloys show high durability, high toughness, non-toxicity, and high strength, which are specific advantages against other biomaterials. However, β-Ti alloys are typical artificial materials having bioinert behaviour. Therefore, the surface of a β-Ti alloy needs modification to improve the wear resistance and bioactive properties. In this review, an overview was given on the surface bio-functionalization methods applied to β-Ti alloys. Mechanical, physical, chemical, electrochemical methods, and immobilization of bio-functional molecules were discussed. The bioactivity, biocompatibility, hemocompatibility, wear and corrosion (tribocorrosion) resistance of β-Ti alloys can be improved by surface modification with desired properties, altering the surface composition or removing the undesired material from the alloy surface. Mainly, the bio-functionalization of β-Ti alloys include

increasing the surface roughness and incorporating bioactive agents (Ca, P, Sr, Ag, Zn) or coating with HA and biomolecules. Undoubtedly, the ongoing work in this area will bring new materials and new techniques to enhance the quality of implant materials, which eventually can improve the quality of patient lifestyle.

Acknowledgments

This work was supported by FCT national funds, under the national support to R&D units grant, through the reference project UIDB/04436/2020 and UIDP/04436/2020, together with M-ERA-NET/0001/2015 project. I. Çaha is grateful for financial support through PhD grant under the NORTE-08-5369-FSE-000012 project.

References

[1] D. Mihov, B. Katerska, Some Biocompatible Materials Used in Medical Practice., Trakia J. Sci. 8 (2010) 119–125. doi:10.2320/matertrans.L-MRA2008828.

[2] E. Pandey, K. Srivastava, S. Gupta, S. Srivastava, N. Mishra, Some biocompatible materials used in medical practices- a review, Int. J. Pharm. Sci. Res. 7 (2016) 2748–2755. http://www.embase.com/search/results?subaction=viewrecord&from=export&id=L611363723%5Cnhttp://dx.doi.org/10.13040/IJPSR.0975-8232.7(7).2748-55.

[3] M. Niinomi, Recent metallic materials for biomedical applications, Metall. Mater. Trans. A. 33 (2002) 477–486. doi:10.1007/s11661-002-0109-2.

[4] M. Niinomi, Mechanical biocompatibilities of titanium alloys for biomedical applications, J. Mech. Behav. Biomed. Mater. 1 (2008) 30–42. doi:10.1016/j.jmbbm.2007.07.001.

[5] M. Geetha, A.K. Singh, R. Asokamani, A.K. Gogia, Ti based biomaterials, the ultimate choice for orthopaedic implants - A review, Prog. Mater. Sci. 54 (2009) 397–425. doi:10.1016/j.pmatsci.2008.06.004.

[6] D.R.N. Correa, F.B. Vicente, T.A.G. Donato, V.E. Arana-Chavez, M.A.R. Buzalaf, C.R. Grandini, The effect of the solute on the structure, selected mechanical properties, and biocompatibility of Ti-Zr system alloys for dental applications, Mater. Sci. Eng. C. 34 (2014) 354–359. doi:10.1016/j.msec.2013.09.032.

[7] Y. Kirmanidou, M. Sidira, M.-E. Drosou, V. Bennani, A. Bakopoulou, A. Tsouknidas, N. Michailidis, K. Michalakis, New Ti-Alloys and Surface Modifications to Improve the Mechanical Properties and the Biological Response to Orthopedic and Dental Implants: A Review, Biomed Res. Int. 2016

(2016) 1–21. doi:10.1155/2016/2908570.

[8] Y. Okazaki, A new Ti-15Zr-4Nb-4Ta alloy for medical applications, Curr. Opin. Solid State Mater. Sci. 5 (2001) 45–53. doi:10.1016/S1359-0286(00)00025-5.

[9] R. Godley, D. Starosvetsky, I. Gotman, Corrosion behavior of a low modulus β-Ti-45 % Nb alloy for use in medical implants, J. Mater. Scince Med. 17 (2006) 63–67. doi:https://doi.org/10.1007/s10856-006-6330-6.

[10] D.P. Perl, Relationship of aluminum to Alzheimer's disease, Environ. Health Perspect. VOL. 63 (1985) 149–153. doi:10.1289/ehp.8563149.

[11] R. Boyer, G. Welsch, Materials Properties Handbook: Titanium Alloys, 1994.

[12] M. Niinomi, Mechanical properties of biomedical titanium alloys, Mater. Sci. Eng. A. 243 (1998) 231–236. doi:10.1016/S0921-5093(97)00806-X.

[13] Department of Health and Human Services, Public Health Statement for Aluminum, Agency Toxic Subst. Dis. Regist. (2008) 9. http://www.atsdr.cdc.gov/phs/phs.asp?id=1076&tid=34.

[14] D. Kuroda, M. Niinomi, M. Morinaga, Y. Kato, T. Yashiro, Design and mechanical properties of new i type titanium alloys for implant materials, Mater. Sci. Eng. A243. 243 (1998) 244–249. doi:10.1016/S0921-5093(97)00808-3.

[15] M. Long, H.J. Rack, Titanium alloys in total joint replacement—a materials science perspective, Biomaterials. 19 (1998) 1621–1639. doi:10.1016/S0142-9612(97)00146-4.

[16] M. Niinomi, Fatigue performance and cyto-toxicity of low rigidity titanium alloy, Ti-29Nb-13Ta-4.6Zr, Biomaterials. 24 (2003) 2673–2683. doi:10.1016/S0142-9612(03)00069-3.

[17] F.G. Evans, Mechanical properties and histology of cortical bone from younger and older men., Anat. Rec. 185 (1976) 1–11. doi:10.1002/ar.1091850102.

[18] M. Science, S. Science, B. Responses, M. Applications, Titanium in Medicine, 49 (2001) 69126. doi:10.1007/978-3-642-56486-4.

[19] W.F. Ho, C.P. Ju, J.H. Chern Lin, Structure and properties of cast binary Ti-Mo alloys, Biomaterials. 20 (1999) 2115–2122. doi:10.1016/S0142-9612(99)00114-3.

[20] D. Raabe, B. Sander, M. Friák, D. Ma, J. Neugebauer, Theory-guided bottom-up design of β-

titanium alloys as biomaterials based on first principles calculations: Theory and experiments, Acta Mater. 55 (2007) 4475–4487. doi:10.1016/j.actamat.2007.04.024.

[21] A. Cimpean, V. Mitran, C.M. Ciofrangeanu, B. Galateanu, E. Bertrand, D.M. Gordin, D. Iordachescu, T. Gloriant, Osteoblast cell behavior on the new beta-type Ti-25Ta-25Nb alloy, Mater. Sci. Eng. C. 32 (2012) 1554–1563. doi:10.1016/j.msec.2012.04.042.

[22] M. Ikeda, S.-Y. Komatsu, I. Sowa, M. Niinomi, Aging behavior of the Ti-29Nb-13Ta-4.6Zr new beta alloy for medical implants, Metall. Mater. Trans. A. 33 (2002) 487–493. doi:10.1007/s11661-002-0110-9.

[23] M. Niinomi, T. Hattori, K. Morikawa, T. Kasuga, A. Suzuki, H. Fukui, S. Niwa, Development of Low Rigidity .BETA.-type Titanium Alloy for Biomedical Applications., Mater. Trans. 43 (2002) 2970–2977. doi:10.2320/matertrans.43.2970.

[24] D.M. Gordin, T. Gloriant, G. Nemtoi, R. Chelariu, N. Aelenei, A. Guillou, D. Ansel, Synthesis, structure and electrochemical behavior of a beta Ti-12Mo-5Ta alloy as new biomaterial, Mater. Lett. 59 (2005) 2959–2964. doi:10.1016/j.matlet.2004.09.064.

[25] J.I. Qazi, H.J. Rack, Metastable beta titanium alloys for orthopedic applications, Adv. Eng. Mater. 7 (2005) 993–998. doi:10.1002/adem.200500060.

[26] R. Banerjee, S. Nag, H.. Fraser, A novel combinatorial approach to the development of beta titanium alloys for orthopaedic implants., Mater. Sci. Eng. C. 25 (2005) p282-289. doi:https://doi.org/10.1016/j.msec.2004.12.010.

[27] S. Nag, R. Banerjee, H.L. Fraser, Microstructural evolution and strengthening mechanisms in Ti-Nb-Zr-Ta, Ti-Mo-Zr-Fe and Ti-15Mo biocompatible alloys, in: Mater. Sci. Eng. C, 2005: pp. 357–362. doi:10.1016/j.msec.2004.12.013.

[28] L.M. Elias, S.G. Schneider, S. Schneider, H.M. Silva, F. Malvisi, Microstructural and mechanical characterization of biomedical Ti-Nb-Zr(-Ta) alloys, Mater. Sci. Eng. A. 432 (2006) 108–112. doi:10.1016/j.msea.2006.06.013.

[29] T. Gloriant, G. Texier, F. Prima, D. Laillé, D.M. Gordin, I. Thibon, D. Ansel, Synthesis and phase transformations of beta metastable Ti-based alloys containing biocompatible Ta, Mo and Fe beta-stabilizer elements, Adv. Eng. Mater. 8 (2006) 961–965. doi:10.1002/adem.200600106.

[30] M. Abdel-Hady, K. Hinoshita, M. Morinaga, General approach to phase stability and elastic properties of β-type Ti-alloys using electronic parameters, Scr. Mater. 55 (2006) 477–480. doi:10.1016/j.scriptamat.2006.04.022.

[31] H. Matsuno, A. Yokoyama, F. Watari, M. Uo, T. Kawasaki, Biocompatibility and osteogenesis of refractory metal implants, titanium, hafnium, niobium, tantalum and rhenium, Biomaterials. 22 (2001) 1253–1262. doi:10.1016/S0142-9612(00)00275-1.

[32] E. Eisenbarth, D. Velten, M. Müller, R. Thull, J. Breme, Biocompatibility of β-stabilizing elements of titanium alloys, Biomaterials. 25 (2004) 5705–5713. doi:10.1016/j.biomaterials.2004.01.021.

[33] M. Niinomi, Recent Research and Development in Metallic Materials for Biomedical, Dental and Healthcare Products Applications, in: THERMEC 2006, Trans Tech Publications, 2007: pp. 193–200. doi:10.4028/www.scientific.net/MSF.539-543.193.

[34] N.S. More, S.N. Paul, M. Roy, Electrochemical Corrosion Behaviour of Ti–29Nb–13Ta–4.6Zr Alloy in Physiological Solution Containing Various Synovial Joint Lubricants, J. Bio- Tribo-Corrosion. 4 (2018) 0. doi:10.1007/s40735-018-0156-x.

[35] I. Çaha, A. Alves, C. Chirico, A. Pinto, S. Tsipas, E. Gordo, F. Toptan, Corrosion and Tribocorrosion Behavior of Ti-40Nb and Ti-25Nb-5Fe Alloys Processed by Powder Metallurgy, Metall. Mater. Trans. A Phys. Metall. Mater. Sci. 51 (2020) 3256–3267. doi:10.1007/s11661-020-05757-6.

[36] M. Niinomi, Biologically and Mechanically Biocompatible Titanium Alloys, Mater. Trans. 49 (2008) 2170–2178. doi:10.2320/matertrans.L-MRA2008828.

[37] M. Niinomi, M. Ogawa, T. Kinoshita, M. Ikeda, M. Ueda, Influence of Fe Content of Ti-Mn-Fe Alloys on Phase Constitution and Heat Treatment Behavior, in: THERMEC 2011, Trans Tech Publications, 2012: pp. 1893–1898. doi:10.4028/www.scientific.net/MSF.706-709.1893.

[38] H. Hosoda, H. Kyogoku, S. Ashida, Fabrication of Ti-Sn-Cr Shape Memory Alloy by PM Process and its Properties, in: THERMEC 2011, Trans Tech Publications, 2012: pp. 1943–1947. doi:10.4028/www.scientific.net/MSF.706-709.1943.

[39] S. Griza, D.H.G. de Souza Sá, W.W. Batista, J.C.G. de Blas, L.C. Pereira, Microstructure and mechanical properties of hot rolled TiNbSn alloys, Mater. Des. 56 (2014) 200–208. doi:10.1016/j.matdes.2013.10.067.

[40] M. Niinomi, Y. Liu, M. Nakai, H. Liu, H. Li, Biomedical titanium alloys with Young's moduli close to that of cortical bone, Regen. Biomater. 3 (2016) 173–185. doi:10.1093/rb/rbw016.

[41] T. Akahori, M. Niinomi, H. Fukui, M. Ogawa, H. Toda, Improvement in fatigue characteristics of newly developed beta type titanium alloy for biomedical applications by thermo-mechanical treatments, in: Mater. Sci. Eng. C, 2005: pp. 248–254. doi:10.1016/j.msec.2004.12.007.

[42] G. Wang, S. Hui, W. Ye, X. Mi, Y. Wang, W. Zhang, Microstructure and tensile properties of low cost titanium alloys at different cooling rate, Rare Met. 31 (2012) 531–536. doi:10.1007/s12598-012-0552-1.

[43] H. Yilmazer, M. Niinomi, M. Nakai, J. Hieda, Y. Todaka, T. Akahori, T. Miyazaki, Heterogeneous structure and mechanical hardness of biomedical β-type Ti-29Nb-13Ta-4.6Zr subjected to high-pressure torsion, J. Mech. Behav. Biomed. Mater. 10 (2012) 235–245. doi:10.1016/j.jmbbm.2012.02.022.

[44] H. Yilmazer, M. Niinomi, M. Nakai, K. Cho, J. Hieda, Y. Todaka, T. Miyazaki, Mechanical properties of a medical ??-type titanium alloy with specific microstructural evolution through high-pressure torsion, Mater. Sci. Eng. C. 33 (2013) 2499–2507. doi:10.1016/j.msec.2013.01.056.

[45] Y. Tian, Z. Yu, C.Y.A. Ong, D. Kent, G. Wang, Microstructure, elastic deformation behavior and mechanical properties of biomedical ??-type titanium alloy thin-tube used for stents, J. Mech. Behav. Biomed. Mater. 45 (2015) 132–141. doi:10.1016/j.jmbbm.2015.02.001.

[46] M.T. Mohammed, Z.A. Khan, M. Geetha, A.N. Siddiquee, Microstructure, mechanical properties and electrochemical behavior of a novel biomedical titanium alloy subjected to thermo-mechanical processing including aging, J. Alloys Compd. 634 (2015) 272–280. doi:10.1016/j.jallcom.2015.02.095.

[47] Y.Y. Li, L.M. Zou, C. Yang, Y.H. Li, L.J. Li, Ultrafine-grained Ti-based composites with high strength and low modulus fabricated by spark plasma sintering, Mater. Sci. Eng. A. 560 (2013) 857–861. doi:10.1016/j.msea.2012.09.047.

[48] S. Datta, M. Mahfouf, Q. Zhang, P.P. Chattopadhyay, N. Sultana, Imprecise knowledge based design and development of titanium alloys for prosthetic applications, J. Mech. Behav. Biomed. Mater. 53 (2016) 350–365. doi:10.1016/j.jmbbm.2015.08.039.

[49] F. Geng, M. Niinomi, M. Nakai, Observation of yielding and strain hardening in a titanium alloy

having high oxygen content, Mater. Sci. Eng. A. 528 (2011) 5435–5445. doi:10.1016/j.msea.2011.03.064.

[50] M. Niinomi, M. Nakai, Unusual Effect of Oxygen on the Mechanical Behavior of a β-Type Titanium Alloy Developed for Biomedical Applications, Mater. Sci. Forum. 706–709 (2012) 135–142. doi:10.4028/www.scientific.net/MSF.706-709.135.

[51] G. Manivasagam, D. Dhinasekaran, A. Rajamanickam, Biomedical Implants: Corrosion and its Prevention - A Review, Recent Patents Corros. Sci. 2 (2010) 40–54. doi:10.2174/1877610801002010040.

[52] M.K. Han, J.Y. Kim, M.J. Hwang, H.J. Song, Y.J. Park, Effect of Nb on the microstructure, mechanical properties, corrosion behavior, and cytotoxicity of Ti-Nb alloys, Materials (Basel). 8 (2015) 5986–6003. doi:10.3390/ma8095287.

[53] Y. Bai, Y. Deng, Y. Zheng, Y. Li, R. Zhang, Y. Lv, Q. Zhao, S. Wei, Characterization, corrosion behavior, cellular response and in vivo bone tissue compatibility of titanium-niobium alloy with low Young's modulus, Mater. Sci. Eng. C. 59 (2016) 565–576. doi:10.1016/j.msec.2015.10.062.

[54] Y.J. Bai, Y.B. Wang, Y. Cheng, F. Deng, Y.F. Zheng, S.C. Wei, Comparative study on the corrosion behavior of Ti-Nb and TMA alloys for dental application in various artificial solutions, Mater. Sci. Eng. C. 31 (2011) 702–711. doi:10.1016/j.msec.2010.12.010.

[55] A. Biesiekierski, D.H. Ping, Y. Yamabe-Mitarai, C. Wen, Impact of ruthenium on microstructure and corrosion behavior of ??-type Ti-Nb-Ru alloys for biomedical applications, Mater. Des. 59 (2014) 303–309. doi:10.1016/j.matdes.2014.02.058.

[56] A. Gebert, S. Oswald, A. Helth, A. Voss, P.F. Gostin, M. Rohnke, J. Janek, M. Calin, J. Eckert, Effect of indium (In) on corrosion and passivity of a beta-type Ti-Nb alloy in Ringer's solution, Appl. Surf. Sci. 335 (2015) 213–222. doi:10.1016/j.apsusc.2015.02.058.

[57] A. Dalmau, V. Guiñón Pina, F. Devesa, V. Amigó, A. Igual Muñoz, Electrochemical behavior of near-beta titanium biomedical alloys in phosphate buffer saline solution, Mater. Sci. Eng. C. 48 (2015) 56–62. doi:10.1016/j.msec.2014.11.036.

[58] I. Çaha, A.C. Alves, P.A.B. Kuroda, C.R. Grandini, A.M.P. Pinto, L.A. Rocha, F. Toptan, Degradation behavior of Ti-Nb alloys: Corrosion behavior through 21 days of immersion and

tribocorrosion behavior against alumina, Corros. Sci. 167 (2020) 108488. doi:10.1016/j.corsci.2020.108488.

[59] P.E.L. Moraes, R.J. Contieri, E.S.N. Lopes, A. Robin, R. Caram, Effects of Sn addition on the microstructure, mechanical properties and corrosion behavior of Ti-Nb-Sn alloys, Mater. Charact. 96 (2014) 273–281. doi:10.1016/j.matchar.2014.08.014.

[60] M. Atapour, A.L. Pilchak, G.S. Frankel, J.C. Williams, Corrosion behavior of β titanium alloys for biomedical applications, Mater. Sci. Eng. C. 31 (2011) 885–891. doi:10.1016/j.msec.2011.02.005.

[61] W.Y. Guo, J. Sun, J.S. Wu, Electrochemical and XPS studies of corrosion behavior of Ti-23Nb-0.7Ta-2Zr-O alloy in Ringer's solution, Mater. Chem. Phys. 113 (2009) 816–820. doi:10.1016/j.matchemphys.2008.08.043.

[62] A. Robin, O.A.S. Carvalho, S.G. Schneider, S. Schneider, Corrosion behavior of Ti-xNb-13Zr alloys in Ringer's solution, Mater. Corros. 59 (2008) 929–933. doi:10.1002/maco.200805014.

[63] J. Málek, F. Hnilica, J. Veselý, B. Smola, K. Kolařík, J. Fojt, M. Vlach, V. Kodetová, The effect of Zr on the microstructure and properties of Ti-35Nb-XZr alloy, Mater. Sci. Eng. A. 675 (2016) 1–10. doi:10.1016/j.msea.2016.07.069.

[64] A.L.R. Ribeiro, P. Hammer, L.G. Vaz, L.A. Rocha, Are new TiNbZr alloys potential substitutes of the Ti6Al4V alloy for dental applications? An electrochemical corrosion study, Biomed. Mater. 8 (2013). doi:10.1088/1748-6041/8/6/065005.

[65] S.L. Assis, I. Costa, Electrochemical evaluation of Ti-13Nb-13Zr, Ti-6Al-4V and Ti-6Al-7Nb alloys for biomedical application by long-term immersion tests, Mater. Corros. 58 (2007) 329–333. doi:10.1002/maco.200604027.

[66] S. Yang, D.C. Zhang, M. Wei, H.X. Su, W. Wu, J.G. Lin, Effects of the Zr and Mo contents on the electrochemical corrosion behavior of Ti-22Nb alloy, Mater. Corros. 64 (2013) 402–407. doi:10.1002/maco.201106478.

[67] I. Çaha, A.C. Alves, C. Chirico, S.A. Tsipas, I.R. Rodrigues, A.M.P. Pinto, C.R. Grandini, L.A. Rocha, E. Gordo, F. Toptan, Interactions between wear and corrosion on cast and sintered Ti-12Nb alloy in comparison with the commercial Ti-6Al-4V alloy, Corros. Sci. 176 (2020) 108925. doi:10.1016/j.corsci.2020.108925.

[68] L.C. Zhang, L.Y. Chen, A Review on Biomedical Titanium Alloys: Recent Progress and Prospect, Adv. Eng. Mater. 21 (2019) 1–29. doi:10.1002/adem.201801215.

[69] X. Liu, S. Chen, J.K.H. Tsoi, J.P. Matinlinna, Binary titanium alloys as dental implant materials-a review, Regen. Biomater. 4 (2017) 315–323. doi:10.1093/rb/rbx027.

[70] Y.L. Zhou, D.M. Luo, Corrosion behavior of Ti-Mo alloys cold rolled and heat treated, J. Alloys Compd. 509 (2011) 6267–6272. doi:10.1016/j.jallcom.2011.03.045.

[71] N.T.C. Oliveira, A.C. Guastaldi, Electrochemical behavior of Ti-Mo alloys applied as biomaterial, Corros. Sci. 50 (2008) 938–945. doi:10.1016/j.corsci.2007.09.009.

[72] N.T.C. Oliveira, A.C. Guastaldi, Electrochemical stability and corrosion resistance of Ti-Mo alloys for biomedical applications, Acta Biomater. 5 (2009) 399–405. doi:10.1016/j.actbio.2008.07.010.

[73] J.M. Calderon Moreno, E. Vasilescu, P. Drob, P. Osiceanu, C. Vasilescu, S.I. Drob, M. Popa, Surface analysis and electrochemical behavior of Ti-20Zr alloy in simulated physiological fluids, Mater. Sci. Eng. B Solid-State Mater. Adv. Technol. 178 (2013) 1195–1204. doi:10.1016/j.mseb.2013.07.006.

[74] H. Michelle Grandin, S. Berner, M. Dard, A review of Titanium Zirconium (TiZr) alloys for use in endosseous dental implants, Materials (Basel). 5 (2012) 1348–1360. doi:10.3390/ma5081348.

[75] T. Akimoto, T. Ueno, Y. Tsutsumi, H. Doi, T. Hanawa, N. Wakabayashi, Evaluation of corrosion resistance of implant-use Ti-Zr binary alloys with a range of compositions, J. Biomed. Mater. Res. - Part B Appl. Biomater. 106 (2018) 73–79. doi:10.1002/jbm.b.33811.

[76] Y.L. Zhou, M. Niinomi, T. Akahori, H. Fukui, H. Toda, Corrosion resistance and biocompatibility of Ti-Ta alloys for biomedical applications, Mater. Sci. Eng. A. 398 (2005) 28–36. doi:10.1016/j.msea.2005.03.032.

[77] D. Mareci, R. Chelariu, D.M. Gordin, G. Ungureanu, T. Gloriant, Comparative corrosion study of Ti-Ta alloys for dental applications, Acta Biomater. 5 (2009) 3625–3639. doi:10.1016/j.actbio.2009.05.037.

[78] S.F. Ou, C.Y. Wang, Effects of bioceramic particles in dielectric of powder-mixed electrical

discharge machining on machining and surface characteristics of titanium alloys, J. Mater. Process. Technol. 245 (2017) 70–79. doi:10.1016/j.jmatprotec.2017.02.018.

[79] N.S. Manam, W.S.W. Harun, D.N.A. Shri, S.A.C. Ghani, T. Kurniawan, M.H. Ismail, M.H.I. Ibrahim, Study of corrosion in biocompatible metals for implants: A review, J. Alloys Compd. 701 (2017) 698–715. doi:10.1016/j.jallcom.2017.01.196.

[80] P. Xue, Y. Li, K. Li, D. Zhang, C. Zhou, Superelasticity, corrosion resistance and biocompatibility of the Ti-19Zr-10Nb-1Fe alloy, Mater. Sci. Eng. C. 50 (2015) 179–186. doi:10.1016/j.msec.2015.02.004.

[81] P.S. Nnamchi, C.S. Obayi, I. Todd, M.W. Rainforth, Mechanical and electrochemical characterisation of new Ti-Mo-Nb-Zr alloys for biomedical applications, J. Mech. Behav. Biomed. Mater. 60 (2016) 68–77. doi:10.1016/j.jmbbm.2015.12.023.

[82] J.M. Cordeiro, T. Beline, A.L.R. Ribeiro, E.C. Rangel, N.C. da Cruz, R. Landers, L.P. Faverani, L.G. Vaz, L.M.G. Fais, F.B. Vicente, C.R. Grandini, M.T. Mathew, C. Sukotjo, V.A.R. Barão, Development of binary and ternary titanium alloys for dental implants, Dent. Mater. 33 (2017) 1244–1257. doi:10.1016/j.dental.2017.07.013.

[83] D. Landolt, S. Mischler, M. Stemp, S. Barril, Third body effects and material fluxes in tribocorrosion systems involving a sliding contact, Wear. 256 (2004) 517–524. doi:10.1016/S0043-1648(03)00561-1.

[84] Y.S. Tian, C.Z. Chen, L.X. Chen, Q.H. Huo, Microstructures and wear properties of composite coatings produced by laser alloying of Ti-6Al-4V with graphite and silicon mixed powders, Mater. Lett. 60 (2006) 109–113. doi:10.1016/j.matlet.2005.07.082.

[85] S. Fouvry, C. Paulin, S. Deyber, Impact of contact size and complex gross-partial slip conditions on Ti-6Al-4V/Ti-6Al-4V fretting wear, Tribol. Int. 42 (2009) 461–474. doi:10.1016/j.triboint.2008.08.005.

[86] I. Cvijović-Alagić, Z. Cvijović, S. Mitrović, V. Panić, M. Rakin, Wear and corrosion behaviour of Ti-13Nb-13Zr and Ti-6Al-4V alloys in simulated physiological solution, Corros. Sci. 53 (2011) 796–808. doi:10.1016/j.corsci.2010.11.014.

[87] D.R.N. Correa, P.A.B. Kuroda, C.R. Grandini, L.A. Rocha, F.G.M. Oliveira, A.C. Alves, F. Toptan, Tribocorrosion behavior of β-type Ti-15Zr-based alloys, Mater. Lett. 179 (2016) 118–121.

doi:10.1016/j.matlet.2016.05.045.

[88] N.S. More, N. Diomidis, S.N. Paul, M. Roy, S. Mischler, Tribocorrosion behavior of β titanium alloys in physiological solutions containing synovial components, Mater. Sci. Eng. C. 31 (2011) 400–408. doi:10.1016/j.msec.2010.10.021.

[89] V.G. Pina, A. Dalmau, F. Devesa, V. Amigó, A.I. Muñoz, Tribocorrosion behavior of beta titanium biomedical alloys in phosphate buffer saline solution, J. Mech. Behav. Biomed. Mater. 46 (2015) 59–68. doi:10.1016/j.jmbbm.2015.02.016.

[90] R. Narayanan, S.K. Seshadri, Phosphoric acid anodization of Ti-6Al-4V - Structural and corrosion aspects, Corros. Sci. 49 (2007) 542–558. doi:10.1016/j.corsci.2006.06.021.

[91] D.D. Deligianni, N. Katsala, S. Ladas, D. Sotiropoulou, J. Amedee, Y.F. Missirlis, Effect of surface roughness of the titanium alloy Ti-6Al-4V on human bone marrow cell response and on protein adsorption, Biomaterials. 22 (2001) 1241–1251. doi:10.1016/S0142-9612(00)00274-X.

[92] P.F. Gostin, A. Helth, A. Voss, R. Sueptitz, M. Calin, J. Eckert, A. Gebert, Surface treatment, corrosion behavior, and apatite-forming ability of ti-45Nb implant alloy, J. Biomed. Mater. Res. - Part B Appl. Biomater. 101 B (2013) 269–278. doi:10.1002/jbm.b.32836.

[93] A. Zareidoost, M. Yousefpour, B. Ghaseme, A. Amanzadeh, The relationship of surface roughness and cell response of chemical surface modification of titanium, J. Mater. Sci. Mater. Med. 23 (2012) 1479–1488. doi:10.1007/s10856-012-4611-9.

[94] M. Lorenzetti, I. Dogša, T. Stošicki, D. Stopar, M. Kalin, S. Kobe, S. Novak, The influence of surface modification on bacterial adhesion to titanium-based substrates, ACS Appl. Mater. Interfaces. 7 (2015) 1644–1651. doi:10.1021/am507148n.

[95] Y. Sasikumar, K. Indira, N. Rajendran, Surface Modification Methods for Titanium and Its Alloys and Their Corrosion Behavior in Biological Environment: A Review, J. Bio- Tribo-Corrosion. 5 (2019) 0. doi:10.1007/s40735-019-0229-5.

[96] L. Ponsonnet, K. Reybier, N. Jaffrezic, V. Comte, C. Lagneau, M. Lissac, C. Martelet, Relationship between surface properties (roughness, wettability) of titanium and titanium alloys and cell behaviour, Mater. Sci. Eng. C. 23 (2003) 551–560. doi:10.1016/S0928-4931(03)00033-X.

[97] M. Hoseini, A. Jedenmalm, A. Boldizar, Tribological investigation of coatings for artificial joints,

Wear. 264 (2008) 958–966. doi:10.1016/j.wear.2007.07.003.

[98] S.W. Jiang, B. Jiang, Y. Li, Y.R. Li, G.F. Yin, C.Q. Zheng, Friction and wear study of diamond-like carbon gradient coatings on Ti6Al4V substrate prepared by plasma source ion implant-ion beam enhanced deposition, Appl. Surf. Sci. 236 (2004) 285–291. doi:10.1016/j.apsusc.2004.04.032.

[99] T.M. Manhabosco, I.L. Muller, Electrodeposition of diamond-like carbon (DLC) films on Ti, Appl. Surf. Sci. 255 (2009) 4082–4086. doi:10.1016/j.apsusc.2008.10.087.

[100] T. Ma, T. Chen, W.Y. Li, S. Wang, S. Yang, Formation mechanism of linear friction welded Ti-6Al-4V alloy joint based on microstructure observation, Mater. Charact. 62 (2011) 130–135. doi:10.1016/j.matchar.2010.11.009.

[101] I. Çaha, A.C. Alves, L.J. Affonço, P.N. Lisboa-Filho, J.H.D. da Silva, L.A. Rocha, A.M.P. Pinto, F. Toptan, Corrosion and tribocorrosion behaviour of titanium nitride thin films grown on titanium under different deposition times, Surf. Coatings Technol. 374 (2019) 878–888. doi:10.1016/j.surfcoat.2019.06.073.

[102] J. Xu, W. Hu, Z.H. Xie, P. Munroe, Reactive-sputter-deposited β-Ta2O5 and TaON nanoceramic coatings on Ti-6Al-4V alloy against wear and corrosion damage, Surf. Coatings Technol. 296 (2016) 171–184. doi:10.1016/j.surfcoat.2016.04.004.

[103] A.M. Ribeiro, A.C. Alves, L.A. Rocha, F.S. Silva, F. Toptan, Synergism between corrosion and wear on CoCrMo-Al2O3 biocomposites in a physiological solution, Tribol. Int. (2014) 198–205. doi:10.1016/j.triboint.2015.01.018.

[104] F. Toptan, A. Rego, A.C. Alves, A. Guedes, Corrosion and tribocorrosion behavior of Ti-B4C composite intended for orthopaedic implants, J. Mech. Behav. Biomed. Mater. 61 (2016) 152–163. doi:10.1016/j.jmbbm.2016.01.024.

[105] J.I. Silva, A.C. Alves, A.M. Pinto, F.S. Silva, F. Toptan, Dry sliding wear behaviour of Ti-TiB-TiNx in-situ composite synthesised by reactive hot pressing, Int. J. Surf. Sci. Eng. 10 (2016) 317–329. doi:10.1504/IJSURFSE.2016.077533.

[106] J.I. Silva, A.C. Alves, A.M. Pinto, F. Toptan, Corrosion and tribocorrosion behavior of Ti–TiB–TiNx in-situ hybrid composite synthesized by reactive hot pressing, J. Mech. Behav. Biomed. Mater. 74 (2017) 195–203. doi:10.1016/j.jmbbm.2017.05.041.

[107] Z. Doni, A.C. Alves, F. Toptan, A.M. Pinto, L.A. Rocha, M. Buciumeanu, L. Palaghian, F.S. Silva, Tribocorrosion behaviour of hot pressed CoCrMo–Al2O3 composites for biomedical applications, Tribol. - Mater. Surfaces Interfaces. 8 (2014) 201–208. doi:10.1179/1751584X14Y.0000000078.

[108] Z. Doni, A.C. Alves, F. Toptan, L.A. Rocha, M. Buciumeanu, L. Palaghian, F.S. Silva, Tribocorrosion behaviour of hot pressed CoCrMo-HAP biocomposites, Tribol. Int. 91 (2014) 221–227. doi:10.1016/j.triboint.2015.04.009.

[109] E. Gordo, R.G. das Neves, B. Ferrari, A. Jiménez-Morales, A. Lima, A.C. Alves, A.M. Pinto, F. Toptan, Corrosion and Tribocorrosion Behavior of Ti-Alumina Composites, Key Eng. Mater. 704 (2016) 28–37. doi:10.4028/www.scientific.net/KEM.704.28.

[110] S.A. Alves, S.B. Patel, C. Sukotjo, M.T. Mathew, P.N. Filho, J.P. Celis, L.A. Rocha, T. Shokuhfar, Synthesis of calcium-phosphorous doped TiO2nanotubes by anodization and reverse polarization: A promising strategy for an efficient biofunctional implant surface, Appl. Surf. Sci. 399 (2017) 682–701. doi:10.1016/j.apsusc.2016.12.105.

[111] N.R. Rodrigues, A.C. Alves, F. Toptan, L.A. Rocha, Preliminary investigation on the tribocorrosion behaviour of nanotubular structured Ti6Al4V surfaces, Mater. Lett. 213 (2018) 214–217. doi:10.1016/j.matlet.2017.11.067.

[112] M. Sarraf, E. Zalnezhad, A.R. Bushroa, A.M.S. Hamouda, A.R. Rafieerad, B. Nasiri-Tabrizi, Effect of microstructural evolution on wettability and tribological behavior of TiO2 nanotubular arrays coated on Ti–6Al–4V, Ceram. Int. 41 (2015) 7952–7962. doi:10.1016/j.ceramint.2015.02.136.

[113] E. Zalnezhad, S. Baradaran, A.R. Bushroa, A.A.D. Sarhan, Mechanical property enhancement of Ti-6Al-4V by Multilayer thin solid film Ti/TiO2nanotubular array coating for biomedical application, Metall. Mater. Trans. A Phys. Metall. Mater. Sci. 45 (2014) 785–797. doi:10.1007/s11661-013-2043-x.

[114] N.K. Awad, S.L. Edwards, Y.S. Morsi, A review of TiO2 NTs on Ti metal: Electrochemical synthesis, functionalization and potential use as bone implants, Mater. Sci. Eng. C. 76 (2017) 1401–1412. doi:10.1016/j.msec.2017.02.150.

[115] M. Mansoorianfar, M. Tavoosi, R. Mozafarinia, A. Ghasemi, A. Doostmohammadi, Preparation and characterization of TiO2 nanotube arrays on Ti6Al4V surface for enhancement of cell

treatment, Surf. Coatings Technol. 321 (2017) 409–415. doi:10.1016/j.surfcoat.2017.05.016.

[116] A. Taubert, J.F. Mano, J.C. Rodríguez-Cabello, Biomaterials surface science, 2013. doi:10.1002/9783527649600.

[117] Y. Su, C. Luo, Z. Zhang, H. Hermawan, D. Zhu, J. Huang, Y. Liang, G. Li, L. Ren, Bioinspired surface functionalization of metallic biomaterials, J. Mech. Behav. Biomed. Mater. 77 (2018) 90–105. doi:10.1016/j.jmbbm.2017.08.035.

[118] C. Prakash, H.K. Kansal, B.S. Pabla, S. Puri, A. Aggarwal, Electric discharge machining - A potential choice for surface modification of metallic implants for orthopedic applications: A review, Proc. Inst. Mech. Eng. Part B J. Eng. Manuf. 230 (2016) 331–353. doi:10.1177/0954405415579113.

[119] C. Prakash, H.K. Kansal, B.S. Pabla, S. Puri, Processing and Characterization of Novel Biomimetic Nanoporous Bioceramic Surface on β-Ti Implant by Powder Mixed Electric Discharge Machining, J. Mater. Eng. Perform. 24 (2015) 3622–3633. doi:10.1007/s11665-015-1619-6.

[120] C. Prakash, H.K. Kansal, B.S. Pabla, S. Puri, Multi-objective optimization of powder mixed electric discharge machining parameters for fabrication of biocompatible layer on β-Ti alloy using NSGA-II coupled with Taguchi based response surface methodology, J. Mech. Sci. Technol. 30 (2016) 4195–4204. doi:10.1007/s12206-016-0831-0.

[121] C. Prakash, H.K. Kansal, B.S. Pabla, S. Puri, Experimental investigations in powder mixed electric discharge machining of Ti–35Nb–7Ta–5Zrβ-titanium alloy, Mater. Manuf. Process. 32 (2017) 274–285. doi:10.1080/10426914.2016.1198018.

[122] C. Prakash, H.K. Kansal, B.S. Pabla, S. Puri, On the Influence of Nanoporous Layer Fabricated by PMEDM on β-Ti Implant: Biological and Computational Evaluation of Bone-Implant Interface, Mater. Today Proc. 4 (2017) 2298–2307. doi:10.1016/j.matpr.2017.02.078.

[123] C. Prakash, M.S. Uddin, Surface modification of β-phase Ti implant by hydroaxyapatite mixed electric discharge machining to enhance the corrosion resistance and in-vitro bioactivity, Surf. Coatings Technol. 326 (2017) 134–145. doi:10.1016/j.surfcoat.2017.07.040.

[124] J. Azadmanjiri, C.C. Berndt, A. Kapoor, C. Wen, Development of Surface Nano-Crystallization in Alloys by Surface Mechanical Attrition Treatment (SMAT), Crit. Rev. Solid State Mater. Sci. 40 (2015) 164–181. doi:10.1080/10408436.2014.978446.

[125] X. Yang, H. Pan, J. Zhang, H. Gao, B. Shu, Y. Gong, X. Zhu, Progress in mechanical properties of gradient structured metallic materials induced by surface mechanical attrition treatment, Mater. Trans. 60 (2019) 1543–1552. doi:10.2320/matertrans.MF201911.

[126] S. Bahl, B.T. Aleti, S. Suwas, K. Chatterjee, Surface nanostructuring of titanium imparts multifunctional properties for orthopedic and cardiovascular applications, Mater. Des. 144 (2018) 169–181. doi:10.1016/j.matdes.2018.02.022.

[127] L. Jin, W. Cui, X. Song, L. Zhou, The formation mechanisms of surface nanocrystallites in β-type biomedical TiNbZrFe alloy by surface mechanical attrition treatment, Appl. Surf. Sci. 347 (2015) 553–560. doi:10.1016/j.apsusc.2015.04.137.

[128] S. Acharya, A.G. Panicker, V. Gopal, S.S. Dabas, G. Manivasagam, S. Suwas, K. Chatterjee, Surface mechanical attrition treatment of low modulus Ti-Nb-Ta-O alloy for orthopedic applications, Mater. Sci. Eng. C. 110 (2020) 110729. doi:10.1016/j.msec.2020.110729.

[129] R. Huang, Y. Han, The effect of SMAT-induced grain refinement and dislocations on the corrosion behavior of Ti-25Nb-3Mo-3Zr-2Sn alloy, Mater. Sci. Eng. C. 33 (2013) 2353–2359. doi:10.1016/j.msec.2013.01.068.

[130] M. Wang, Y. Fan, Electrochemical corrosion property of nanostructure layer of Ti-5Al-2Sn-2Zr-4Mo-4Cr titanium alloy, Int. J. Adv. Manuf. Technol. 96 (2018) 1601–1606. doi:10.1007/s00170-017-0660-z.

[131] R. Huang, L. Zhang, L. Huang, J. Zhu, Enhanced in-vitro osteoblastic functions on β-type titanium alloy using surface mechanical attrition treatment, Mater. Sci. Eng. C. 97 (2019) 688–697. doi:10.1016/j.msec.2018.12.082.

[132] C. Ma, M.T. Andani, H. Qin, N.S. Moghaddam, H. Ibrahim, A. Jahadakbar, A. Amerinatanzi, Z. Ren, H. Zhang, G.L. Doll, Y. Dong, M. Elahinia, C. Ye, Improving surface finish and wear resistance of additive manufactured nickel-titanium by ultrasonic nano-crystal surface modification, J. Mater. Process. Technol. 249 (2017) 433–440. doi:10.1016/j.jmatprotec.2017.06.038.

[133] M. Kheradmandfard, S.F. Kashani-Bozorg, C.-L. Kim, A.Z. Hanzaki, Y.-S. Pyoun, J.-H. Kim, A. Amanov, D.-E. Kim, Nanostructured β-type titanium alloy fabricated by ultrasonic nanocrystal surface modification, Ultrason. Sonochem. (2017). doi:10.1016/j.ultsonch.2017.03.061.

[134] M. Kheradmandfard, S.F. Kashani-Bozorg, J.S. Lee, C.L. Kim, A.Z. Hanzaki, Y.S. Pyun, S.W. Cho,

A. Amanov, D.E. Kim, Significant improvement in cell adhesion and wear resistance of biomedical β-type titanium alloy through ultrasonic nanocrystal surface modification, J. Alloys Compd. 762 (2018) 941–949. doi:10.1016/j.jallcom.2018.05.088.

[135] W. Xu, X. Wu, R.B. Figueiredo, M. Stoica, M. Calin, J. Eckert, T.G. Langdon, K. Xia, Nanocrystalline body-centred cubic beta-titanium alloy processed by high-pressure torsion, in: Int. J. Mater. Res., 2009: pp. 1662–1667. doi:10.3139/146.110229.

[136] W. Xu, D.P. Edwards, X. Wu, M. Stoica, M. Calin, U. Kühn, J. Eckert, K. Xia, Promoting nano/ultrafine-duplex structure via accelerated α precipitation in a β-type titanium alloy severely deformed by high-pressure torsion, Scr. Mater. 68 (2013) 67–70. doi:10.1016/j.scriptamat.2012.09.023.

[137] H. Yilmazer, M. Niinomi, K. Cho, M. Nakai, J. Hieda, S. Sato, Y. Todaka, Microstructural evolution of precipitation-hardened β-type titanium alloy through high-pressure torsion, Acta Mater. 80 (2014) 172–182. doi:10.1016/j.actamat.2014.07.041.

[138] H. Yilmazer, M. Niinomi, M. Nakai, K. Cho, J. Hieda, Y. Todaka, T. Miyazaki, Mechanical properties of a medical β-type titanium alloy with specific microstructural evolution through high-pressure torsion, Mater. Sci. Eng. C. 33 (2013) 2499–2507. doi:10.1016/j.msec.2013.01.056.

[139] S. Gatina, I. Semenova, J. Leuthold, R. Valiev, Nanostructuring and Phase Transformations in the β-Alloy Ti-15Mo during High-Pressure Torsion, Adv. Eng. Mater. 17 (2015) 1742–1747. doi:10.1002/adem.201500104.

[140] M. Delshadmanesh, G. Khatibi, M.Z. Ghomsheh, M. Lederer, M. Zehetbauer, H. Danninger, Influence of microstructure on fatigue of biocompatible β-phase Ti-45Nb, Mater. Sci. Eng. A. 706 (2017) 83–94. doi:10.1016/j.msea.2017.08.098.

[141] H. Yilmazer, M. Şen, M. Niinomi, M. Nakai, L. Huihong, K. Cho, Y. Todaka, H. Shiku, T. Matsue, Developing biomedical nano-grained β-type titanium alloys using high pressure torsion for improved cell adherence, RSC Adv. 6 (2016) 7426–7430. doi:10.1039/C5RA23454A.

[142] I. Dimić, I. Cvijović-Alagić, A. Hohenwarter, R. Pippan, V. Kojić, J. Bajat, M. Rakin, Electrochemical and biocompatibility examinations of high-pressure torsion processed titanium and Ti–13Nb–13Zr alloy, J. Biomed. Mater. Res. - Part B Appl. Biomater. 106 (2018) 1097–1107. doi:10.1002/jbm.b.33919.

[143] K. Sharman, P. Bazarnik, T. Brynk, A. Gunay Bulutsuz, M. Lewandowska, Y. Huang, T.G. Langdon, Enhancement in mechanical properties of a β-titanium alloy by high-pressure torsion, J. Mater. Res. Technol. 4 (2015) 79–83. doi:10.1016/j.jmrt.2014.10.010.

[144] M. Janeček, J. Čížek, J. Stráský, K. Václavová, P. Hruška, V. Polyakova, S. Gatina, I. Semenova, Microstructure evolution in solution treated Ti15Mo alloy processed by high pressure torsion, Mater. Charact. 98 (2014) 233–240. doi:10.1016/j.matchar.2014.10.024.

[145] D.A.G. Pérez, A.M. Jorge Junior, V. Roche, J.C. Lepretre, C.R.M. Afonso, D.N. Travessa, G.H. Asato, C. Bolfarini, W.J. Botta, Severe plastic deformation and different surface treatments on the biocompatible Ti13Nb13Zr and Ti35Nb7Zr5Ta alloys: Microstructural and phase evolutions, mechanical properties, and bioactivity analysis, J. Alloys Compd. 812 (2020). doi:10.1016/j.jallcom.2019.152116.

[146] I. Dimić, I. Cvijović-Alagić, B. Völker, A. Hohenwarter, R. Pippan, D. Veljović, M. Rakin, B. Bugarski, Microstructure and metallic ion release of pure titanium and Ti-13Nb-13Zr alloy processed by high pressure torsion, Mater. Des. 91 (2016) 340–347. doi:10.1016/j.matdes.2015.11.088.

[147] A. Nocivin, D. Raducanu, I. Cinca, C. Trisca-Rusu, M. Butu, I. Thibon, V.D. Cojocaru, X-ray Diffraction Study and Texture Evolution for a Ti-Nb-Ta Biomedical Alloy Processed by Accumulative Roll Bonding, J. Mater. Eng. Perform. 24 (2015) 1587–1601. doi:10.1007/s11665-015-1414-4.

[148] I. Cinca, D. Raducanu, A. Nocivin, D.M. Gordin, V.D. Cojocaru, Formation of nano-sized grains in Ti-10Zr-5Nb-5Ta biomedical alloy processed by accumulative roll bonding (ARB), Kov. Mater. 51 (2013) 165–172. doi:10.4149/km.2013.3.165.

[149] D. Raducanu, E. Vasilescu, V.D. Cojocaru, I. Cinca, P. Drob, C. Vasilescu, S.I. Drob, Mechanical and corrosion resistance of a new nanostructured Ti-Zr-Ta-Nb alloy, J. Mech. Behav. Biomed. Mater. 4 (2011) 1421–1430. doi:10.1016/j.jmbbm.2011.05.012.

[150] D. Raducanu, C. Vasilescu, A. Nocivin, S.I. Drob, I. Cinca, D. Gordin, M. Marcu, V.D. Cojocaru, Promoting structural and anticorrosive performances via accumulative roll bonding to a Ti-Ta-Nb alloy, Int. J. Electrochem. Sci. 10 (2014) 4346–4358.

[151] D. Kent, G. Wang, Z. Yu, X. Ma, M. Dargusch, Strength enhancement of a biomedical titanium alloy through a modified accumulative roll bonding technique, J. Mech. Behav. Biomed. Mater. 4

(2011) 405–416. doi:10.1016/j.jmbbm.2010.11.013.

[152] D. Kent, W.L. Xiao, G. Wang, Z. Yu, M.S. Dargusch, Thermal stability of an ultrafine grain β-Ti alloy, Mater. Sci. Eng. A. 556 (2012) 582–587. doi:10.1016/j.msea.2012.07.030.

[153] B. Moore, E. Asadi, G. Lewis, Deposition methods for Microstructured and Nanostructured coatings on metallic bone implants: A review, Adv. Mater. Sci. Eng. 2017 (2017). doi:10.1155/2017/5812907.

[154] G. Zhao, L. Xia, G. Wen, L. Song, X. Wang, K. Wu, Microstructure and properties of plasma-sprayed bio-coatings on a low-modulus titanium alloy from milled HA/Ti powders, Surf. Coatings Technol. 206 (2012) 4711–4719. doi:10.1016/j.surfcoat.2011.08.033.

[155] G.L. Zhao, G. Wen, Y. Song, K. Wu, Near surface martensitic transformation and recrystallization in a Ti-24Nb-4Zr-7.9Sn alloy substrate after application of a HA coating by plasma spraying, Mater. Sci. Eng. C. 31 (2011) 106–113. doi:10.1016/j.msec.2010.08.003.

[156] Y.H. He, Y.Q. Zhang, Y.H. Jiang, R. Zhou, Microstructure evolution and enhanced bioactivity of Ti-Nb-Zr alloy by bioactive hydroxyapatite fabricated via spark plasma sintering, RSC Adv. 6 (2016) 100939–100953. doi:10.1039/C6RA22986G.

[157] F. Toptan, A.C. Alves, M.A. Ferreira, C.I. da Silva Oliveira, A.M.P. Pinto, Effect of HAP decomposition on the corrosion behavior of Ti-HAP biocomposites, Mater. Corros. (2018) 1–8. doi:10.1002/maco.201810049.

[158] W.G. Kim, H.C. Choe, Surface characteristics of hydroxyapatite/titanium composite layer on the Ti-35Ta-xZr surface by RF and DC sputtering, Thin Solid Films. 519 (2011) 7045–7049. doi:10.1016/j.tsf.2011.04.090.

[159] S. Sathish, M. Geetha, S.T. Aruna, N. Balaji, K.S. Rajam, R. Asokamani, Studies on plasma sprayed bi-layered ceramic coating on bio-medical Ti-13Nb-13Zr alloy, Ceram. Int. 37 (2011) 1333–1339. doi:10.1016/j.ceramint.2010.12.012.

[160] S. Sathish, M. Geetha, S.T. Aruna, N. Balaji, K.S. Rajam, R. Asokamani, Sliding wear behavior of plasma sprayed nanoceramic coatings for biomedical applications, Wear. 271 (2011) 934–941. doi:10.1016/j.wear.2011.03.023.

[161] Y. Bédouin, D.M. Gordin, P. Pellen-Mussi, F. Pérez, S. Tricot-Doleux, C. Vasilescu, S.I. Drob, D.

Chauvel-Lebret, T. Gloriant, Enhancement of the biocompatibility by surface nitriding of a low-modulus titanium alloy for dental implant applications, J. Biomed. Mater. Res. - Part B Appl. Biomater. 107 (2019) 1483–1490. doi:10.1002/jbm.b.34240.

[162] M. Akita, Y. Uematsu, T. Kakiuchi, M. Nakajima, Y. Bai, K. Tamada, Fatigue behavior of bulk β-type titanium alloy Ti-15Mo-5Zr-3Al annealed in high temperature nitrogen gas, Mater. Sci. Eng. A. 627 (2015) 351–359. doi:10.1016/j.msea.2015.01.022.

[163] L. Mohan, M.D. Raja, T.S. Uma, N. Rajendran, C. Anandan, In-Vitro Biocompatibility Studies of Plasma-Nitrided Titanium Alloy β-21S Using Fibroblast Cells, J. Mater. Eng. Perform. 25 (2016) 1508–1514. doi:10.1007/s11665-015-1860-z.

[164] G. Cassar, A. Matthews, A. Leyland, Triode plasma diffusion treatment of titanium alloys, Surf. Coatings Technol. 212 (2012) 20–31. doi:10.1016/j.surfcoat.2012.09.006.

[165] W. Tian, Y. Guo, X. Li, B. Tang, A. Fan, Friction and wear behavior of modified layer prepared on Ti-13Nb-13Zr alloy by magnetron sputtering and plasma nitriding, J. Wuhan Univ. Technol. Mater. Sci. Ed. 32 (2017) 951–957. doi:10.1007/s11595-017-1695-6.

[166] O. Çomakli, Influence of CrN, TiAlN monolayers and TiAlN/CrN multilayer ceramic films on structural, mechanical and tribological behavior of β-type Ti45Nb alloys, Ceram. Int. 46 (2020) 8185–8191. doi:10.1016/j.ceramint.2019.12.046.

[167] V. Krishnan, A. Krishnan, R. Remya, K.K. Ravikumar, S.A. Nair, S.M.A. Shibli, H.K. Varma, K. Sukumaran, K.J. Kumar, Development and evaluation of two PVD-coated β-titanium orthodontic archwires for fluoride-induced corrosion protection, Acta Biomater. 7 (2011) 1913–1927. doi:10.1016/j.actbio.2010.11.026.

[168] R. Ion, Y. Bédouin, T. Gloriant, G. Andruseac, D.M. Gordin, A. Cimpean, In vitro study of human endothelial progenitor cells behaviour on nitrided Ni-free Ti–27Nb alloy, Prog. Nat. Sci. Mater. Int. 29 (2019) 466–471. doi:10.1016/j.pnsc.2019.08.001.

[169] A. Zhecheva, S. Malinov, W. Sha, Titanium alloys after surface gas nitriding, Surf. Coatings Technol. 201 (2006) 2467–2474. doi:10.1016/j.surfcoat.2006.04.019.

[170] C. Yang, J. Liu, Intermittent vacuum gas nitriding of TB8 titanium alloy, Vacuum. 163 (2019) 52–58. doi:10.1016/j.vacuum.2018.11.059.

[171] D.M. Gordin, I. Thibon, A. Guillou, M. Cornen, T. Gloriant, Microstructural characterization of nitrided beta Ti-Mo alloys at 1400 °C, Mater. Charact. 61 (2010) 376–380. doi:10.1016/j.matchar.2009.12.010.

[172] P. Vlcak, J. Fojt, Z. Weiss, J. Kopeček, V. Perina, The effect of nitrogen saturation on the corrosion behaviour of Ti-35Nb-7Zr-5Ta beta titanium alloy nitrided by ion implantation, Surf. Coatings Technol. 358 (2019) 144–152. doi:10.1016/j.surfcoat.2018.11.004.

[173] S. Carquigny, J. Takadoum, S. Ivanescu, Comparative study of nitrogen implantation effect on mechanical and tribological properties of Ti-6Al-4V and Ti-10Zr-10Nb-5Ta alloys, EPJ Appl. Phys. 85 (2019) 5–10. doi:10.1051/epjap/2019180149.

[174] D.M. Gordin, D. Busardo, A. Cimpean, C. Vasilescu, D. H??che, S.I. Drob, V. Mitran, M. Cornen, T. Gloriant, Design of a nitrogen-implanted titanium-based superelastic alloy with optimized properties for biomedical applications, Mater. Sci. Eng. C. 33 (2013) 4173–4182. doi:10.1016/j.msec.2013.06.008.

[175] L. Mohan, C. Anandan, Effect of gas composition on corrosion behavior and growth of apatite on plasma nitrided titanium alloy Beta-21S, Appl. Surf. Sci. 268 (2013) 288–296. doi:10.1016/j.apsusc.2012.12.080.

[176] L. Mohan, C. Anandan, Wear and corrosion behavior of oxygen implanted biomedical titanium alloy Ti-13Nb-13Zr, Appl. Surf. Sci. 282 (2013) 281–290. doi:10.1016/j.apsusc.2013.05.120.

[177] T. Kokubo, S. Yamaguchi, Bioactive Titanate Layers Formed on Titanium and Its Alloys by Simple Chemical and Heat Treatments, Open Biomed. Eng. J. 9 (2015) 29–41. doi:10.2174/1874120701509010029.

[178] P.F. Gostin, A. Helth, A. Voss, R. Sueptitz, M. Calin, J. Eckert, A. Gebert, Surface treatment, corrosion behavior, and apatite-forming ability of Ti-45Nb implant alloy, J. Biomed. Mater. Res. - Part B Appl. Biomater. 101 B (2013) 269–278. doi:10.1002/jbm.b.32836.

[179] A. Helth, P.F. Gostin, S. Oswald, H. Wendrock, U. Wolff, U. Hempel, S. Arnhold, M. Calin, J. Eckert, A. Gebert, Chemical nanoroughening of Ti40Nb surfaces and its effect on human mesenchymal stromal cell response, J. Biomed. Mater. Res. - Part B Appl. Biomater. 102 (2014) 31–41. doi:10.1002/jbm.b.32976.

[180] F.A. Müller, M.C. Bottino, L. Müller, V.A.R. Henriques, U. Lohbauer, A.H.A. Bressiani, J.C.

Bressiani, In vitro apatite formation on chemically treated (P/M) Ti-13Nb-13Zr, Dent. Mater. 24 (2008) 50–56. doi:10.1016/j.dental.2007.02.005.

[181] S. Yamaguchi, H. Hashimoto, R. Nakai, H. Takadama, Impact of surface potential on apatite formation in Ti alloys subjected to acid and heat treatments, Materials (Basel). 10 (2017). doi:10.3390/ma10101127.

[182] R. Schmidt, V. Hoffmann, A. Helth, P.F. Gostin, M. Calin, J. Eckert, A. Gebert, Electrochemical deposition of hydroxyapatite on beta-Ti-40Nb, Surf. Coatings Technol. 294 (2016) 186–193. doi:10.1016/j.surfcoat.2016.03.063.

[183] B.H. Lee, Y. Do Kim, J.H. Shin, K.H. Lee, Surface modification by alkali and heat treatments in titanium alloys, J. Biomed. Mater. Res. 61 (2002) 466–473. doi:10.1002/jbm.10190.

[184] Y. Sasikumar, M. Karthega, N. Rajendran, In vitro bioactivity of surface-modified ??-Ti alloy for biomedical applications, J. Mater. Eng. Perform. 20 (2011) 1271–1277. doi:10.1007/s11665-010-9772-4.

[185] S. Ban, Effect of alkaline treatment of pure titanium and its alloys on the bonding strength of dental veneering resins., J. Biomed. Mater. Res. A. 66 (2003) 138–45. doi:10.1002/jbm.a.10566.

[186] E. Takematsu, K. Katsumata, K. Okada, M. Niinomi, N. Matsushita, Bioactive surface modification of Ti-29Nb-13Ta-4.6Zr alloy through alkali solution treatments, Mater. Sci. Eng. C. 62 (2016) 662–667. doi:10.1016/j.msec.2016.01.041.

[187] R. Schmidt, V. Hoffmann, A. Helth, P.F. Gostin, M. Calin, J. Eckert, A. Gebert, Electrochemical deposition of hydroxyapatite on beta-Ti-40Nb, Surf. Coatings Technol. 294 (2016) 186–193. doi:10.1016/j.surfcoat.2016.03.063.

[188] Y. Sasikumar, N. Rajendran, Influence of surface modification on the apatite formation and corrosion behavior of Ti and Ti-15Mo alloy for biomedical applications, Mater. Chem. Phys. 138 (2013) 114–123. doi:10.1016/j.matchemphys.2012.11.025.

[189] A.M. Kumar, P. Sudhagar, S. Ramakrishna, Y.S. Kang, H. Kim, Z.M. Gasem, N. Rajendran, Evaluation of chemically modified Ti-5Mo-3Fe alloy surface: Electrochemical aspects and in vitro bioactivity on MG63 cells, Appl. Surf. Sci. 307 (2014) 52–61. doi:10.1016/j.apsusc.2014.03.146.

[190] A.K. Shukla, R. Balasubramaniam, Effect of surface treatment on electrochemical behavior of CP Ti, Ti-6Al-4V and Ti-13Nb-13Zr alloys in simulated human body fluid, Corros. Sci. 48 (2006) 1696–1720. doi:10.1016/j.corsci.2005.06.003.

[191] P.F. Li, Y. Xu, X.H. Cheng, Chemisorption of thermal reduced graphene oxide nano-layer film on TNTZ surface and its tribological behavior, Surf. Coatings Technol. 232 (2013) 331–339. doi:10.1016/j.surfcoat.2013.05.030.

[192] C.Y. Zheng, S.J. Li, X.J. Tao, Y.L. Hao, R. Yang, L. Zhang, Calcium phosphate coating of Ti-Nb-Zr-Sn titanium alloy, Mater. Sci. Eng. C. 27 (2007) 824–831. doi:10.1016/j.msec.2006.09.021.

[193] E. Takematsu, K. Cho, J. Hieda, M. Nakai, K. Katsumata, K. Okada, M. Niinomi, N. Matsushita, Adhesive strength of bioactive oxide layers fabricated on TNTZ alloy by three different alkali-solution treatments, J. Mech. Behav. Biomed. Mater. 61 (2016) 174–181. doi:10.1016/j.jmbbm.2015.12.046.

[194] E. Takematsu, K. Noguchi, K. Kuroda, T. Ikoma, M. Niinomi, N. Matsushita, In vivo osteoconductivity of surface modified Ti-29Nb-13Ta-4.6Zr alloy with low dissolution of toxic trace elements, PLoS One. 13 (2018) 1–12. doi:10.1371/journal.pone.0189967.

[195] J. Hieda, M. Niinomi, M. Nakai, K. Cho, T. Gozawa, H. Katsui, R. Tu, T. Goto, Enhancement of adhesive strength of hydroxyapatite films on Ti-29Nb-13Ta-4.6Zr by surface morphology control, J. Mech. Behav. Biomed. Mater. 18 (2013) 232–239. doi:10.1016/j.jmbbm.2012.11.013.

[196] M. Zuldesmi, A. Waki, K. Kuroda, M. Okido, Hydrothermal treatment of titanium alloys for the enhancement of osteoconductivity, Mater. Sci. Eng. C. 49 (2015) 430–435. doi:10.1016/j.msec.2015.01.031.

[197] X.H. Liu, L. Wu, H.J. Ai, Y. Han, Y. Hu, Cytocompatibility and early osseointegration of nanoTiO2-modified Ti-24 Nb-4 Zr-7.9 Sn surfaces, Mater. Sci. Eng. C. 48 (2015) 256–262. doi:10.1016/j.msec.2014.12.011.

[198] C.Y. Zheng, S.J. Li, X.J. Tao, Y.L. Hao, R. Yang, Surface modification of Ti-Nb-Zr-Sn alloy by thermal and hydrothermal treatments, Mater. Sci. Eng. C. 29 (2009) 1245–1251. doi:10.1016/j.msec.2008.10.008.

[199] F. Tao, S. Wei, Hydrothermal Surface Modification of a Low Modulus Ti-Nb Based Alloy, Rare Met. Mater. Eng. 43 (2014) 291–295. doi:10.1016/S1875-5372(14)60061-8.

[200] A. Kazek-Kęsik, G. Dercz, K. Suchanek, I. Kalemba-Rec, J. Piotrowski, W. Simka, Biofunctionalization of Ti–13Nb–13Zr alloy surface by plasma electrolytic oxidation. Part I, Surf. Coatings Technol. 276 (2015) 59–69. doi:10.1016/j.surfcoat.2015.06.034.

[201] S. Minagar, C.C. Berndt, J. Wang, E. Ivanova, C. Wen, A review of the application of anodization for the fabrication of nanotubes on metal implant surfaces, Acta Biomater. 8 (2012) 2875–2888. doi:10.1016/j.actbio.2012.04.005.

[202] A.R. Rafieerad, M.R. Ashra, R. Mahmoodian, A.R. Bushroa, Surface characterization and corrosion behavior of calcium phosphate-base composite layer on titanium and its alloys via plasma electrolytic oxidation: A review paper, Mater. Sci. Eng. C. 57 (2015) 397–413. doi:10.1016/j.msec.2015.07.058.

[203] W. Simka, A. Krząkała, D.M. Korotin, I.S. Zhidkov, E.Z. Kurmaev, S.O. Cholakh, K. Kuna, G. Dercz, J. Michalska, K. Suchanek, T. Gorewoda, Modification of a Ti-Mo alloy surface via plasma electrolytic oxidation in a solution containing calcium and phosphorus, Electrochim. Acta. 96 (2013) 180–190. doi:10.1016/j.electacta.2013.02.102.

[204] A. Kazek-Kęsik, M. Krok-Borkowicz, E. Pamuła, W. Simka, Electrochemical and biological characterization of coatings formed on Ti-15Mo alloy by plasma electrolytic oxidation, Mater. Sci. Eng. C. 43 (2014) 172–181. doi:10.1016/j.msec.2014.07.021.

[205] A. Kazek-Kęsik, M. Krok-Borkowicz, G. Dercz, A. Donesz-Sikorska, E. Pamuła, W. Simka, Multilayer coatings formed on titanium alloy surfaces by plasma electrolytic oxidation-electrophoretic deposition methods, Electrochim. Acta. 204 (2016) 294–306. doi:10.1016/j.electacta.2016.02.193.

[206] A. Kazek-Kęsik, J. Jaworska, M. Krok-Borkowicz, M. Gołda-Cępa, M. Pastusiak, M. Brzychczy-Włoch, E. Pamuła, A. Kotarba, W. Simka, Hybrid oxide-polymer layer formed on Ti-15Mo alloy surface enhancing antibacterial and osseointegration functions, Surf. Coatings Technol. 302 (2016) 158–165. doi:10.1016/j.surfcoat.2016.05.073.

[207] A. Kazek-Kęsik, K. Kuna, W. Dec, M. Widziołek, G. Tylko, A.M. Osyczka, W. Simka, In vitro bioactivity investigations of Ti-15Mo alloy after electrochemical surface modification, J. Biomed. Mater. Res. - Part B Appl. Biomater. 104 (2016) 903–913. doi:10.1002/jbm.b.33442.

[208] A. Kazek-Kęsik, G. Dercz, I. Kalemba, K. Suchanek, A.I. Kukharenko, D.M. Korotin, J. Michalska,

A. Krząkała, J. Piotrowski, E.Z. Kurmaev, S.O. Cholakh, W. Simka, Surface characterisation of Ti-15Mo alloy modified by a PEO process in various suspensions, Mater. Sci. Eng. C. 39 (2014) 259–272. doi:10.1016/j.msec.2014.03.008.

[209] M. Sowa, M. Piotrowska, M. Widziołek, G. Dercz, G. Tylko, T. Gorewoda, A.M. Osyczka, W. Simka, Bioactivity of coatings formed on Ti-13Nb-13Zr alloy using plasma electrolytic oxidation, Mater. Sci. Eng. C. 49 (2015) 159–173. doi:10.1016/j.msec.2014.12.073.

[210] Y. Sharkeev, E. Komarova, M. Sedelinikova, Z. ming Sun, Q. fang Zhu, J. Zhang, T. Tolkacheva, P. Uvarkin, Structure and properties of micro-arc calcium phosphate coatings on pure titanium and Ti-40Nb alloy, Trans. Nonferrous Met. Soc. China (English Ed. 27 (2017) 125–133. doi:10.1016/S1003-6326(17)60014-1.

[211] A. Kazek-Kęsik, M. Krok-Borkowicz, A. Jakóbik-Kolon, E. Pamuła, W. Simka, Biofunctionalization of Ti–13Nb–13Zr alloy surface by plasma electrolytic oxidation. Part II, Surf. Coatings Technol. 276 (2015) 23–30. doi:10.1016/j.surfcoat.2015.06.035.

[212] X.J. Tao, S.J. Li, C.Y. Zheng, J. Fu, Z. Guo, Y.L. Hao, R. Yang, Z.X. Guo, Synthesis of a porous oxide layer on a multifunctional biomedical titanium by micro-arc oxidation, Mater. Sci. Eng. C. 29 (2009) 1923–1934. doi:10.1016/j.msec.2009.03.004.

[213] S.F. Ou, C.S. Lin, Y.N. Pan, Microstructure and surface characteristics of hydroxyapatite coating on titanium and Ti-30Nb-1Fe-1Hf alloy by anodic oxidation and hydrothermal treatment, Surf. Coatings Technol. 205 (2011) 2899–2906. doi:10.1016/j.surfcoat.2010.10.063.

[214] L. Zhao, Y. Wei, J. Li, Y. Han, R. Ye, Y. Zhang, Initial osteoblast functions on Ti-5Zr-3Sn-5Mo-15Nb titanium alloy surfaces modified by microarc oxidation, J. Biomed. Mater. Res. - Part A. 92 (2010) 432–440. doi:10.1002/jbm.a.32348.

[215] S. Yu, Z.T. Yu, G. Wang, J.Y. Han, X.Q. Ma, M.S. Dargusch, Preparation and osteoinduction of active micro-arc oxidation films on Ti-3Zr-2Sn-3Mo-25Nb alloy, Trans. Nonferrous Met. Soc. China (English Ed. 21 (2011) 573–580. doi:10.1016/S1003-6326(11)60753-X.

[216] Y. Gao, B. Gao, R. Wang, J. Wu, L.J. Zhang, Y.L. Hao, X.J. Tao, Improved biological performance of low modulus Ti-24Nb-4Zr-7.9Sn implants due to surface modification by anodic oxidation, Appl. Surf. Sci. 255 (2009) 5009–5015. doi:10.1016/j.apsusc.2008.12.054.

[217] Y.N. Pan, C.S. Lin, K.K. Wang, S.F. Ou, Effect of Nb addition on anodic behavior of Ti alloy in

electrolyte containing calcium and phosphorus, Surf. Coatings Technol. 258 (2014) 1016–1024. doi:10.1016/j.surfcoat.2014.07.037.

[218] S.F. Ou, H.H. Chou, C.S. Lin, C.J. Shih, K.K. Wang, Y.N. Pan, Effects of anodic oxidation and hydrothermal treatment on surface characteristics and biocompatibility of Ti-30Nb-1Fe-1Hf alloy, Appl. Surf. Sci. 258 (2012) 6190–6198. doi:10.1016/j.apsusc.2012.02.109.

[219] D.R.N. Correa, L.A. Rocha, A.R. Ribeiro, S. Gemini-Piperni, B.S. Archanjo, C.A. Achete, J. Werckmann, C.R.M. Afonso, M. Shimabukuro, H. Doi, Y. Tsutsumi, T. Hanawa, Growth mechanisms of Ca- and P-rich MAO films in Ti-15Zr-xMo alloys for osseointegrative implants, Surf. Coatings Technol. 344 (2018) 373–382. doi:10.1016/j.surfcoat.2018.02.099.

[220] H.-T. Chen, C.-J. Chung, T.-C. Yang, I.-P. Chiang, C.-H. Tang, K.-C. Chen, J.-L. He, Osteoblast growth behavior on micro-arc oxidized β-titanium alloy, Surf. Coatings Technol. 205 (2010) 1624–1629. doi:10.1016/j.surfcoat.2010.07.027.

[221] X. He, X. Zhang, X. Wang, L. Qin, Review of Antibacterial Activity of Titanium-Based Implants' Surfaces Fabricated by Micro-Arc Oxidation, Coatings. 7 (2017) 45. doi:10.3390/coatings7030045.

[222] A. Kazek-Kesik, M. Krok-Borkowicz, A. Jakóbik-Kolon, E. Pamuła, W. Simka, Biofunctionalization of Ti-13Nb-13Zr alloy surface by plasma electrolytic oxidation. Part II, Surf. Coatings Technol. 276 (2015) 23–30. doi:10.1016/j.surfcoat.2015.06.035.

[223] A. Gebert, D. Eigel, P.F. Gostin, V. Hoffmann, M. Uhlemann, A. Helth, S. Pilz, R. Schmidt, M. Calin, M. Göttlicher, M. Rohnke, J. Janek, Oxidation treatments of beta-type Ti-40Nb for biomedical use, Surf. Coatings Technol. 302 (2016) 88–99. doi:10.1016/j.surfcoat.2016.05.036.

[224] M.B. Sedelnikova, E.G. Komarova, Y.P. Sharkeev, A. V. Ugodchikova, L.S. Mushtovatova, M.R. Karpova, V. V. Sheikin, L.S. Litvinova, I.A. Khlusov, Zn-, Cu- or Ag-incorporated micro-arc coatings on titanium alloys: Properties and behavior in synthetic biological media, Surf. Coatings Technol. 369 (2019) 52–68. doi:10.1016/j.surfcoat.2019.04.021.

[225] J. Michalska, M. Sowa, M. Piotrowska, M. Widziołek, G. Tylko, G. Dercz, R.P. Socha, A.M. Osyczka, W. Simka, Incorporation of Ca ions into anodic oxide coatings on the Ti-13Nb-13Zr alloy by plasma electrolytic oxidation, Mater. Sci. Eng. C. 104 (2019) 109957.

doi:10.1016/j.msec.2019.109957.

[226] C.E. Tanase, M. Golozar, S.M. Best, R.A. Brooks, Cell response to plasma electrolytic oxidation surface-modified low-modulus β-type titanium alloys, Colloids Surfaces B Biointerfaces. 176 (2019) 176–184. doi:10.1016/j.colsurfb.2018.12.064.

[227] S.H. Jang, H.C. Choe, Y.M. Ko, W.A. Brantley, Electrochemical characteristics of nanotubes formed on Ti-Nb alloys, Thin Solid Films. 517 (2009) 5038–5043. doi:10.1016/j.tsf.2009.03.166.

[228] A. Ossowska, S. Sobieszczyk, M. Supernak, A. Zielinski, Morphology and properties of nanotubular oxide layer on the "Ti-13Zr-13Nb" alloy, Surf. Coatings Technol. 258 (2014) 1239–1248. doi:10.1016/j.surfcoat.2014.06.054.

[229] J.M. Hernández-López, A. Conde, J. de Damborenea, M.A. Arenas, Correlation of the nanostructure of the anodic layers fabricated on Ti13Nb13Zr with the electrochemical impedance response, Corros. Sci. 94 (2015) 61–69. doi:10.1016/j.corsci.2015.01.041.

[230] H.J. Kim, Y.H. Jeong, H.C. Choe, W.A. Brantley, Surface morphology of TiN-coated nanotubular Ti-25Ta-xZr alloys for dental implants prepared by RF sputtering, Thin Solid Films. 549 (2013) 131–134. doi:10.1016/j.tsf.2013.09.045.

[231] Y.H. Jeong, H.C. Choe, W.A. Brantley, I.B. Sohn, Hydroxyapatite thin film coatings on nanotube-formed Ti-35Nb-10Zr alloys after femtosecond laser texturing, Surf. Coatings Technol. 217 (2013) 13–22. doi:10.1016/j.surfcoat.2012.11.066.

[232] Y.H. Jeong, H.C. Choe, W.A. Brantley, Nanostructured thin film formation on femtosecond laser-textured Ti-35Nb-xZr alloy for biomedical applications, Thin Solid Films. 519 (2011) 4668–4675. doi:10.1016/j.tsf.2011.01.014.

[233] J. Hieda, M. Niinomi, M. Nakai, K. Cho, T. Mohri, T. Hanawa, Adhesive strength of medical polymer on anodic oxide nanostructures fabricated on biomedical β-type titanium alloy, Mater. Sci. Eng. C. 36 (2014) 244–251. doi:10.1016/j.msec.2013.12.012.

[234] X. Li, T. Chen, J. Hu, S. Li, Q. Zou, Y. Li, N. Jiang, H. Li, J. Li, Modified surface morphology of a novel Ti-24Nb-4Zr-7.9Sn titanium alloy via anodic oxidation for enhanced interfacial biocompatibility and osseointegration, Colloids Surfaces B Biointerfaces. 144 (2016) 265–275. doi:10.1016/j.colsurfb.2016.04.020.

[235] Y.Q. Hao, S.J. Li, Y.L. Hao, Y.K. Zhao, H.J. Ai, Effect of nanotube diameters on bioactivity of a multifunctional titanium alloy, Appl. Surf. Sci. 268 (2013) 44–51. doi:10.1016/j.apsusc.2012.11.142.

[236] N.C. Verissimo, B.M. Geilich, H.G. Oliveira, R. Caram, T.J. Webster, Reducing Staphylococcus aureus growth on Ti alloy nanostructured surfaces through the addition of Sn, J. Biomed. Mater. Res. - Part A. 103 (2015) 3757–3763. doi:10.1002/jbm.a.35517.

[237] H.J. Kim, Y.H. Jeong, H.C. Choe, W.A. Brantley, Surface characteristics of hydroxyapatite coatings on nanotubular Ti-25Ta-xZr alloys prepared by electrochemical deposition, Surf. Coatings Technol. 259 (2014) 274–280. doi:10.1016/j.surfcoat.2014.03.013.

[238] S.H. Kim, Y.H. Jeong, H.C. Choe, W.A. Brantley, Morphology change of HA films on highly ordered nanotubular Ti-Nb-Hf alloys as a function of electrochemical deposition cycle, Surf. Coatings Technol. 259 (2014) 281–289. doi:10.1016/j.surfcoat.2014.03.006.

[239] Y.H. Jeong, E.J. Kim, W.A. Brantley, H.C. Choe, Morphology of hydroxyapatite nanoparticles in coatings on nanotube-formed Ti-Nb-Zr alloys for dental implants, Vacuum. 107 (2014) 297–303. doi:10.1016/j.vacuum.2014.03.004.

[240] I.S. Byeon, K. Lee, H.C. Choe, W.A. Brantley, Surface morphology of Zn-containing hydroxyapatite (Zn-HA) deposited electrochemically on Ti-xNb alloys, Thin Solid Films. 587 (2015) 163–168. doi:10.1016/j.tsf.2015.01.028.

[241] M.A. Hussein, A.M. Kumar, B.S. Yilbas, N. Al-Aqeeli, Laser Nitriding of the Newly Developed Ti-20Nb-13Zr at.% Biomaterial Alloy to Enhance Its Mechanical and Corrosion Properties in Simulated Body Fluid, J. Mater. Eng. Perform. 26 (2017) 5553–5562. doi:10.1007/s11665-017-2955-5.

[242] M.A. Hussein, B. Yilbas, A.M. Kumar, R. Drew, N. Al-Aqeeli, Influence of Laser Nitriding on the Surface and Corrosion Properties of Ti-20Nb-13Zr Alloy in Artificial Saliva for Dental Applications, J. Mater. Eng. Perform. 27 (2018) 4655–4664. doi:10.1007/s11665-018-3569-2.

[243] X. Zhao, P. Zhang, X. Wang, Y. Chen, H. Liu, L. Chen, Y. Sheng, W. Li, In-situ formation of textured TiN coatings on biomedical titanium alloy by laser irradiation, J. Mech. Behav. Biomed. Mater. 78 (2018) 143–153. doi:10.1016/j.jmbbm.2017.11.019.

[244] C.W. Chan, X. Chang, M.A. Bozorgzadeh, G.C. Smith, S. Lee, A single parameter approach to

enhance the microstructural and mechanical properties of beta Ti-Nb alloy via open-air fiber laser nitriding, Surf. Coatings Technol. 383 (2020) 125269. doi:10.1016/j.surfcoat.2019.125269.

[245] M. Geetha, U.K. Mudali, N.D. Pandey, R. Asokamani, B. Raj, Microstructural and corrosion evaluation of laser surface nitrided Ti-13Nb-13Zr alloy, Surf. Eng. 20 (2004) 68–74. doi:10.1179/026708404225010595.

[246] T. Zhang, Q. Fan, X. Ma, W. Wang, K. Wang, P. Shen, J. Yang, Microstructure and Mechanical Properties of Ti-35Nb-2Ta-3Zr Alloy by Laser Quenching, Front. Mater. 6 (2019) 1–9. doi:10.3389/fmats.2019.00318.

[247] H. Mohseni, P. Nandwana, A. Tsoi, R. Banerjee, T.W. Scharf, In situ nitrided titanium alloys: Microstructural evolution during solidification and wear, Acta Mater. 83 (2015) 61–74. doi:10.1016/j.actamat.2014.09.026.

[248] C.W. Chan, S. Lee, G. Smith, G. Sarri, C.H. Ng, A. Sharba, H.C. Man, Enhancement of wear and corrosion resistance of beta titanium alloy by laser gas alloying with nitrogen, Appl. Surf. Sci. 367 (2016) 80–90. doi:10.1016/j.apsusc.2016.01.091.

[249] S.N. Saud, S. Raheleh Hosseinian, H.R. Bakhsheshi-Rad, F. Yaghoubidoust, N. Iqbal, E. Hamzah, C.H.R. Ooi, Corrosion and bioactivity performance of graphene oxide coating on Ti-Nb shape memory alloys in simulated body fluid, Mater. Sci. Eng. C. 68 (2016) 687–694. doi:10.1016/j.msec.2016.06.048.

[250] C. Lubov Donaghy, R. McFadden, S. Kelaini, L. Carson, A. Margariti, C.W. Chan, Creating an antibacterial surface on beta TNZT alloys for hip implant applications by laser nitriding, Opt. Laser Technol. 121 (2020) 105793. doi:10.1016/j.optlastec.2019.105793.

[251] C.L. Donaghy, R. McFadden, G.C. Smith, S. Kelaini, L. Carson, S. Malinov, A. Margariti, C.W. Chan, Fibre laser treatment of beta TNZT titanium alloys for load-bearing implant applications: Effects of surface physical and chemical features on mesenchymal stem cell response and Staphylococcus aureus bacterial attachment, Coatings. 9 (2019). doi:10.3390/COATINGS9030186.

[252] M. González, E. Salvagni, J.C. Rodríguez-Cabello, E. Rupérez, F.J. Gil, J. Peña, J.M. Manero, A low elastic modulus Ti-Nb-Hf alloy bioactivated with an elastin-like protein-based polymer enhances osteoblast cell adhesion and spreading, J. Biomed. Mater. Res. - Part A. 101 A (2013)

819–826. doi:10.1002/jbm.a.34388.

[253] S.-K. Hsu, W.-F. Ho, S.-C. Wu, Y.-S. Chen, H.-C. Hsu, In vitro study of Ti-Nb-Sn alloy surface modified with RGD peptide, Thin Solid Films. 620 (2016) 139–144. doi:10.1016/j.tsf.2016.09.063.

[254] J. Hieda, M. Niinomi, M. Nakai, H. Kamura, H. Tsutsumi, T. Hanawa, Effect of terminal functional groups of silane layers on adhesive strength between biomedical Ti-29Nb-13Ta-4.6Zr alloy and segment polyurethanes, Surf. Coatings Technol. 206 (2012) 3137–3141. doi:10.1016/j.surfcoat.2011.12.044.

[255] Y.S. Sun, C.Y. Huang, C.S. Chen, J.H. Chang, W.T. Hou, S.J. Li, Y.L. Hao, H. Pan, H.H. Huang, Bone cell responses to a low elastic modulus titanium alloy surface immobilized with the natural cross-linker genipin, Surf. Coatings Technol. 350 (2018) 918–924. doi:10.1016/j.surfcoat.2018.03.069.

[256] C.F. Liu, S.J. Li, W.T. Hou, Y.L. Hao, H.H. Huang, Enhancing corrosion resistance and biocompatibility of interconnected porous β-type Ti-24Nb-4Zr-8Sn alloy scaffold through alkaline treatment and type I collagen immobilization, Appl. Surf. Sci. 476 (2019) 325–334. doi:10.1016/j.apsusc.2019.01.084.

[257] H.C. Choe, Photofunctionalization of EB-PVD HA-coated nano-pore surface of Ti-30Nb-xZr alloy for dental implants, Surf. Coatings Technol. 228 (2013) S470–S476. doi:10.1016/j.surfcoat.2012.05.018.

[258] S.H. Kim, Y.H. Jeong, H.C. Choe, W.A. Brantley, Morphology change of HA films on highly ordered nanotubular Ti-Nb-Hf alloys as a function of electrochemical deposition cycle, Surf. Coatings Technol. 259 (2014) 281–289. doi:10.1016/j.surfcoat.2014.03.006.

[259] P.M.H. Nguyen, D.H. Won, B.S. Kim, Y.S. Jang, T.D.T. Nguyen, M.H. Lee, T.S. Bae, The effect of two-step surface modification for Ti-Ta-Mo-Zr alloys on bone regeneration: An evaluation using calvarial defect on rat model, Appl. Surf. Sci. 442 (2018) 630–639. doi:10.1016/j.apsusc.2018.02.211.

[260] J. Fojt, L. Joska, V. Hybasek, E. Pruchova, J. Malek, Impedance technique for monitoring of apatite precipitation from simulated body fluid, Electrochim. Acta. 271 (2018) 158–164. doi:10.1016/j.electacta.2018.03.120.

[261] A.L.R. Rangel, C. Falentin-Daudré, B.N.A. da Silva Pimentel, C.E. Vergani, V. Migonney, A.P.R. Alves Claro, Nanostructured titanium alloy surfaces for enhanced osteoblast response: A combination of morphology and chemistry, Surf. Coatings Technol. 383 (2020) 125226. doi:10.1016/j.surfcoat.2019.125226.

[262] S.Y. Park, C.I. Jo, H.C. Choe, W.A. Brantley, Hydroxyapatite deposition on micropore-formed Ti-Ta-Nb alloys by plasma electrolytic oxidation for dental applications, Surf. Coatings Technol. 294 (2016) 15–20. doi:10.1016/j.surfcoat.2016.03.056.

[263] A. Kazek-Kęsik, K. Leśniak, B.U. Orzechowska, M. Drab, A. Wiśniewska, W. Simka, Alkali treatment of anodized titanium alloys affects cytocompatibility, Metals (Basel). 8 (2018). doi:10.3390/met8010029.

[264] A. Kazek-Kęsik, K. Leśniak, I.S. Zhidkov, D.M. Korotin, A.I. Kukharenko, S.O. Cholakh, I. Kalemba-Rec, K. Suchanek, E.Z. Kurmaev, W. Simka, Influence of alkali treatment on anodized titanium alloys in wollastonite suspension, Metals (Basel). 7 (2017). doi:10.3390/met7090322.

[265] A. Kazek-Kęsik, A. Nosol, J. Płonka, M. Śmiga-Matuszowicz, M. Gołda-Cępa, M. Krok-Borkowicz, M. Brzychczy-Włoch, E. Pamuła, W. Simka, PLGA-amoxicillin-loaded layer formed on anodized Ti alloy as a hybrid material for dental implant applications, Mater. Sci. Eng. C. 94 (2019) 998–1008. doi:10.1016/j.msec.2018.10.049.

[266] X. Wang, Y. Chen, L.J. Xu, S. Xiao, F. Kong, K. Do Woo, Ti-Nb-Sn-hydroxyapatite composites synthesized by mechanical alloying and high frequency induction heated sintering, J. Mech. Behav. Biomed. Mater. 4 (2011) 2074–2080. doi:10.1016/j.jmbbm.2011.07.006.

[267] P. Majumdar, S.B. Singh, S. Dhara, M. Chakraborty, Influence of in situ TiB reinforcements and role of heat treatment on mechanical properties and biocompatibility of ?? Ti-alloys, J. Mech. Behav. Biomed. Mater. 10 (2012) 1–12. doi:10.1016/j.jmbbm.2012.02.014.

[268] P. Majumdar, S.B. Singh, S. Dhara, M. Chakraborty, Influence of boron addition to Ti-13Zr-13Nb alloy on MG63 osteoblast cell viability and protein adsorption, Mater. Sci. Eng. C. 46 (2015) 62–68. doi:10.1016/j.msec.2014.10.012.

[269] J. Málek, F. Hnilica, J. Veselý, B. Smola, V. Březina, K. Kolařík, The effect of boron addition on microstructure and mechanical properties of biomedical Ti35Nb6Ta alloy, Mater. Charact. 96 (2014) 166–176. doi:10.1016/j.matchar.2014.07.015.

[270] K.L. Ou, C.C. Weng, Y.H. Lin, M.S. Huang, A promising of alloying modified beta-type Titanium-Niobium implant for biomedical applications: Microstructural characteristics, in??vitro biocompatibility and antibacterial performance, J. Alloys Compd. 697 (2017) 231–238. doi:10.1016/j.jallcom.2016.12.120.

[271] Y.H. Li, X.Y. Shang, Recent progress in porous TiNb-based alloys for biomedical implant applications, Mater. Sci. Technol. (United Kingdom). 36 (2020) 385–392. doi:10.1080/02670836.2020.1724415.

[272] A. Manoj, A.K. Kasar, P.L. Menezes, Tribocorrosion of Porous Titanium Used in Biomedical Applications, J. Bio- Tribo-Corrosion. 5 (2019) 0. doi:10.1007/s40735-018-0194-4.

[273] Y. Li, Y. Ding, K. Munir, J. Lin, M. Brandt, A. Atrens, Y. Xiao, J.R. Kanwar, C. Wen, Novel β-Ti35Zr28Nb alloy scaffolds manufactured using selective laser melting for bone implant applications, Acta Biomater. 87 (2019) 273–284. doi:10.1016/j.actbio.2019.01.051.

[274] K. Zhuravleva, A. Chivu, A. Teresiak, S. Scudino, M. Calin, L. Schultz, J. Eckert, A. Gebert, Porous low modulus Ti40Nb compacts with electrodeposited hydroxyapatite coating for biomedical applications, Mater. Sci. Eng. C. 33 (2013) 2280–2287. doi:10.1016/j.msec.2013.01.049.

[275] I. Mutlu, S. Yeniyol, E. Oktay, Production and Precipitation Hardening of Beta-Type Ti-35Nb-10Cu Alloy Foam for Implant Applications, J. Mater. Eng. Perform. 25 (2016) 1586–1593. doi:10.1007/s11665-016-1982-y.

[276] M.R. Soran, I. Mutlu, Production and anodising of highly porous Ti–Ta–Zr–Co alloy for biomedical implant applications, Corros. Eng. Sci. Technol. 54 (2019) 54–61. doi:10.1080/1478422X.2018.1527820.

[277] J. Xu, J. Zhang, L. Bao, T. Lai, J. Luo, Y. Zheng, Preparation and bioactive surface modification of the microwave sintered porous ti-15mo alloys for biomedical application, Sci. China Mater. 61 (2018) 545–556. doi:10.1007/s40843-017-9098-2.

[278] S. Guo, Q. Meng, X. Zhao, Q. Wei, H. Xu, Design and fabrication of a metastable β-type titanium alloy with ultralow elastic modulus and high strength, Sci. Rep. 5 (2015) 14688. doi:10.1038/srep14688.

[279] L.C. Zhang, D. Klemm, J. Eckert, Y.L. Hao, T.B. Sercombe, Manufacture by selective laser melting and mechanical behavior of a biomedical Ti-24Nb-4Zr-8Sn alloy, Scr. Mater. 65 (2011) 21–24.

doi:10.1016/j.scriptamat.2011.03.024.

[280] Y.H. Li, C. Yang, F. Wang, H.D. Zhao, S.G. Qu, X.Q. Li, W.W. Zhang, Y.Y. Li, Biomedical TiNbZrTaSi alloys designed by d-electron alloy design theory, Mater. Des. 85 (2015) 7–13. doi:10.1016/j.matdes.2015.06.176.

[281] S.X. Liang, X.J. Feng, L.X. Yin, X.Y. Liu, M.Z. Ma, R.P. Liu, Development of a new β-Ti alloy with low modulus and favorable plasticity for implant material, Mater. Sci. Eng. C. 61 (2016) 338–343. doi:10.1016/j.msec.2015.12.076.

[282] X. Yang, C.R. Hutchinson, Corrosion-wear of β-Ti alloy alloy TMZF (Ti-12Mo-6Zr-2Fe) in simulated body fluid, Acta Biomater. 42 (2016) 429–439. doi:10.1016/j.actbio.2016.07.008.

[283] Y.S. Lee, M. Niinomi, M. Nakai, K. Narita, K. Cho, Predominant factor determining wear properties of β-type and (α+β)-type titanium alloys in metal-to-metal contact for biomedical applications, J. Mech. Behav. Biomed. Mater. 41 (2015) 208–220. doi:10.1016/j.jmbbm.2014.10.005.

[284] Y. Lee, M. Niinomi, M. Nakai, K. Narita, K. Cho, Differences in Wear Behaviors at Sliding Contacts for β-Type and (α + β)-Type Titanium Alloys in Ringer' s Solution and Air, Mater. Trans. 56 (2015) 317–326.

[285] E. Gongadze, D. Kabaso, S. Bauer, T. Slivnik, P. Schmuki, U. van Rienen, A. Iglič, Adhesion of osteoblasts to a nanorough titanium implant surface., Int. J. Nanomedicine. (2011). doi:10.2147/IJN.S21755.

[286] J. Xiong, X. Wang, Y. Li, P.D. Hodgson, Interfacial chemistry and adhesion between titanium dioxide nanotube layers and titanium substrates, J. Phys. Chem. C. 115 (2011) 4768–4772. doi:10.1021/jp111651d.

[287] D. Yu, X. Zhu, Z. Xu, X. Zhong, Q. Gui, Y. Song, S. Zhang, X. Chen, D. Li, Facile method to enhance the adhesion of TiO2 nanotube arrays to Ti substrate, ACS Appl. Mater. Interfaces. 6 (2014) 8001–8005. doi:10.1021/am5015716.

[288] S. Cao, W. Huang, L. Wu, M. Tian, Y. Song, On the Interfacial Adhesion between TiO2 Nanotube Array Layer and Ti Substrate, Langmuir. 34 (2018) 13888–13896. doi:10.1021/acs.langmuir.8b03408.

[289] T. Li, K. Gulati, N. Wang, Z. Zhang, S. Ivanovski, Understanding and augmenting the stability of

therapeutic nanotubes on anodized titanium implants, Mater. Sci. Eng. C. 88 (2018) 182–195. doi:10.1016/j.msec.2018.03.007.

[290] Y. Zhang, Y. Han, L. Zhang, Interfacial structure of the firmly adhered TiO2 nanotube films to titanium fabricated by a modified anodization, Thin Solid Films. 583 (2015) 151–157. doi:10.1016/j.tsf.2015.03.060.

[291] A.C.C.A. Fontes, L. Sopchenski, C.A.H. Laurindo, R.D. Torres, K.C. Popat, P. Soares, Annealing a Effect on Tribocorrosion and Biocompatibility Properties of TiO2 Nanotubes, J. Bio- Tribo-Corrosion. 6 (2020) 1–12. doi:10.1007/s40735-020-00363-w.

[292] S.A. Alves, A.L. Rossi, A.R. Ribeiro, F. Toptan, A.M. Pinto, J.P. Celis, T. Shokuhfar, L.A. Rocha, Tribo-electrochemical behavior of bio-functionalized TiO2 nanotubes in artificial saliva: Understanding of degradation mechanisms, Wear. 384–385 (2017) 28–42. doi:10.1016/j.wear.2017.05.005.

[293] S.A. Alves, A.L. Rossi, A.R. Ribeiro, F. Toptan, A.M. Pinto, T. Shokuhfar, J.P. Celis, L.A. Rocha, Improved tribocorrosion performance of bio-functionalized TiO2 nanotubes under two-cycle sliding actions in artificial saliva, J. Mech. Behav. Biomed. Mater. 80 (2018) 143–154. doi:10.1016/j.jmbbm.2018.01.038.

[294] M. Sun, D. Yu, L. Lu, W. Ma, Y. Song, X. Zhu, Effective approach to strengthening TiO2 nanotube arrays by using double or triple reinforcements, Appl. Surf. Sci. 346 (2015) 172–176. doi:10.1016/j.apsusc.2015.04.004.

[295] H.M. Ouyang, G.T. Fei, Y. Zhang, H. Su, Z. Jin, S.H. Xu, L. De Zhang, Large scale free-standing open-ended TiO2 nanotube arrays: Stress-induced self-detachment and in situ pore opening, J. Mater. Chem. C. 1 (2013) 7498–7506. doi:10.1039/c3tc31642d.

[296] A.R. Luz, G.B. De Souza, C.M. Lepienski, N.K. Kuromoto, C.J.M. Siqueira, Tribological properties of nanotubes grown on Ti-35Nb alloy by anodization, Thin Solid Films. 660 (2018) 529–537. doi:10.1016/j.tsf.2018.06.050.

[297] S. Mukherjee, S. Dhara, P. Saha, Laser surface remelting of Ti and its alloys for improving surface biocompatibility of orthopaedic implants, Mater. Technol. 33 (2018) 106–118. doi:10.1080/10667857.2017.1390931.

[298] A. Shah, S. Izman, S.N.F. Ismail, H. Mas Ayu, C.G. Che Kob, R. Daud, M.R. Abdul Kadir, The

influence of ultrasonic vibration frequency on the properties of TiN coated biomedical Ti-13Zr-13Nb, Metals (Basel). 8 (2018) 1–10. doi:10.3390/met8050317.

[299] P. Wang, H. Li, Y. Zhang, H. Liu, Y. Guo, Z. Liu, S. Zhao, J. Yin, Y. Guo, Morphology of nanotube arrays grown on Ti-35Nb-2Ta-3Zr alloys with different deformations, Appl. Surf. Sci. 290 (2014) 308–312. doi:10.1016/j.apsusc.2013.11.073.

[300] S.J. CLi, C.Y. Zheng, J. Fu, Z. Guo, Y.L. Hao, R. Yang, Z.X. Guo, Synthesis of a porous oxide layer on a multifunctional biomedical titanium by micro-arc oxidation, Mater. Sci. Eng. C. 29 (2009) 1923–1934. doi:10.1016/j.msec.2009.03.004.

[301] S. Bahl, S.R.K. Meka, S. Suwas, K. Chatterjee, Surface Severe Plastic Deformation of an Orthopedic Ti-Nb-Sn Alloy Induces Unusual Precipitate Remodeling and Supports Stem Cell Osteogenesis through Akt Signaling, ACS Biomater. Sci. Eng. 4 (2018) 3132–3142. doi:10.1021/acsbiomaterials.8b00406.

[302] M. Kheradmandfard, S.F. Kashani-Bozorg, C.L. Kim, A.Z. Hanzaki, Y.S. Pyoun, J.H. Kim, A. Amanov, D.E. Kim, Nanostructured β-type titanium alloy fabricated by ultrasonic nanocrystal surface modification, Ultrason. Sonochem. 39 (2017) 698–706. doi:10.1016/j.ultsonch.2017.03.061.

[303] M. Kheradmandfard, S.F. Kashani-Bozorg, K.H. Kang, O. V. Penkov, A. Zarei Hanzaki, Y.S. Pyoun, A. Amanov, D.E. Kim, Simultaneous grain refinement and nanoscale spinodal decomposition of β phase in Ti-Nb-Ta-Zr alloy induced by ultrasonic mechanical impacts, J. Alloys Compd. 738 (2018) 540–549. doi:10.1016/j.jallcom.2017.12.049.

[304] H. Yilmazer, M. Şen, M. Niinomi, M. Nakai, L. Huihong, K. Cho, Y. Todaka, H. Shiku, T. Matsue, Developing biomedical nano-grained β-type titanium alloys using high pressure torsion for improved cell adherence, RSC Adv. 6 (2016) 7426–7430. doi:10.1039/c5ra23454a.

[305] H. Yilmazer, M. Niinomi, M. Nakai, K. Cho, J. Hieda, Y. Todaka, T. Miyazaki, Mechanical properties of a medical β-type titanium alloy with specific microstructural evolution through high-pressure torsion, Mater. Sci. Eng. C. 33 (2013) 2499–2507. doi:10.1016/j.msec.2013.01.056.

[306] Z.B. Zhang, Y.L. Hao, S.J. Li, R. Yang, Fatigue behavior of ultrafine-grained Ti-24Nb-4Zr-8Sn multifunctional biomedical titanium alloy, Mater. Sci. Eng. A. 577 (2013) 225–233. doi:10.1016/j.msea.2013.04.051.

[307] S.A. Gatina, I.P. Semenova, E. V. Ubyyvovk, R.Z. Valiev, Phase Transformations, Strength, and Modulus of Elasticity of Ti–15Mo Alloy Obtained by High-Pressure Torsion, Inorg. Mater. Appl. Res. 9 (2018) 14–20. doi:10.1134/S2075113318010136.

[308] Y.R. Kolobov, O.A. Golosova, S.S. Manokhin, Regularities of Formation and Degradation of the Microstructure and Properties of New Ultrafine-Grained Low-Modulus Ti–Nb–Mo–Zr Alloys, Russ. J. Non-Ferrous Met. 59 (2018) 393–402. doi:10.3103/S1067821218040090.

[309] A.C. Hee, P.J. Martin, A. Bendavid, S.S. Jamali, Y. Zhao, Tribo-corrosion performance of filtered-arc-deposited tantalum coatings on Ti-13Nb-13Zr alloy for bio-implants applications, Wear. 400–401 (2018) 31–42. doi:10.1016/j.wear.2017.12.017.

[310] S. Gnanavel, S. Ponnusamy, L. Mohan, Biocompatible response of hydroxyapatite coated on near-β titanium alloys by E-beam evaporation method, Biocatal. Agric. Biotechnol. 15 (2018) 364–369. doi:10.1016/j.bcab.2018.07.014.

[311] C. Anandan, L. Mohan, In vitro corrosion behavior and apatite growth of oxygen plasma ion implanted titanium alloy β-21S, J. Mater. Eng. Perform. 22 (2013) 3507–3516. doi:10.1007/s11665-013-0628-6.

[312] L. Guo, L. Qin, F. Kong, H. Yi, B. Tang, Improving tribological properties of Ti-5Zr-3Sn-5Mo-15Nb alloy by double glow plasma surface alloying, Appl. Surf. Sci. 388 (2016) 203–211. doi:10.1016/j.apsusc.2016.01.201.

[313] E. Yılmaz, A. Gökçe, F. Findik, Ho.O. Gulsoy, Metallurgical properties and biomimetic HA deposition performance of Ti-Nb PIM alloys, J. Alloys Compd. 746 (2018) 301–313. doi:10.1016/j.jallcom.2018.02.274.

[314] I. Lauria, T.N. Kutz, F. Böke, S. Rütten, D. Zander, H. Fischer, Influence of nanoporous titanium niobium alloy surfaces produced via hydrogen peroxide oxidative etching on the osteogenic differentiation of human mesenchymal stromal cells, Mater. Sci. Eng. C. 98 (2019) 635–648. doi:10.1016/j.msec.2019.01.023.

[315] J. Lario, A. Amigó, F. Segovia, V. Amigó, Surface modification of Ti-35Nb-10Ta-1.5Fe by the double acid-etching process, Materials (Basel). 11 (2018) 1–11. doi:10.3390/ma11040494.

[316] M.W.D. Mendes, C.G. Ágreda, A.H.A. Bressiani, J.C. Bressiani, A new titanium based alloy Ti-27Nb-13Zr produced by powder metallurgy with biomimetic coating for use as a biomaterial,

Mater. Sci. Eng. C. 63 (2016) 671–677. doi:10.1016/j.msec.2016.03.052.

[317] S. Ban, Effect of alkaline treatment of pure titanium and its alloys on the bonding strength of dental veneering resins, J. Biomed. Mater. Res. - Part A. 66 (2003) 138–145. doi:10.1002/jbm.a.10566.

[318] H. Fajri, W. Ariani, Gunawarman, D.H. Tjong, M. Manjas, Corrosion Behaviour of Collagen Coated and Uncoated Biomedical Titanium Alloy (TNTZ) Within Human Synovial Fluid, IOP Conf. Ser. Mater. Sci. Eng. 547 (2019). doi:10.1088/1757-899X/547/1/012007.

[319] M.K. Arumugam, M.A. Hussein, A.Y. Adesina, N. Al-Aqeeli, In vitro corrosion and bioactivity performance of surface-treated Ti-20Nb-13Zr alloys for orthopedic applications, Coatings. 9 (2019) 1–13. doi:10.3390/COATINGS9050344.

[320] Y. Sasikumar, N. Rajendran, Influence of surface modification on the apatite formation and corrosion behavior of Ti and Ti-15Mo alloy for biomedical applications, Mater. Chem. Phys. 138 (2013) 114–123. doi:10.1016/j.matchemphys.2012.11.025.

[321] T. Kasuga, T. Mizuno, M. Watanabe, M. Nogami, M. Niinomi, Calcium phosphate invert glass-ceramic coatings joined by self-development of compositionally gradient layers on a titanium alloy, Biomaterials. 22 (2001) 577–582. doi:10.1016/S0142-9612(00)00216-7.

[322] B. Dikici, M. Niinomi, M. Topuz, Y. Say, B. Aksakal, H. Yilmazer, M. Nakai, Synthesis and Characterization of Hydroxyapatite/TiO2 Coatings on the β-Type Titanium Alloys with Different Sintering Parameters using Sol-Gel Method, Prot. Met. Phys. Chem. Surfaces. 54 (2018) 457–462. doi:10.1134/S2070205118030255.

[323] B. Dikici, M. Niinomi, M. Topuz, S.G. Koc, M. Nakai, Synthesis of biphasic calcium phosphate (BCP) coatings on β–type titanium alloys reinforced with rutile-TiO2 compounds: adhesion resistance and in-vitro corrosion, J. Sol-Gel Sci. Technol. 87 (2018) 713–724. doi:10.1007/s10971-018-4755-2.

[324] T. Kasuga, M. Nogami, M. Niinomi, T. Hattori, Bioactive calcium phosphate invert glass-ceramic coating on ??-type Ti-29Nb-13Ta-4.6Zr alloy, Biomaterials. 24 (2003) 283–290. doi:10.1016/S0142-9612(02)00316-2.

[325] M.L. dos Santos, C. dos Santos Riccardi, E. de Almeida Filho, A.C. Guastaldi, Sol–gel based calcium phosphates coatings deposited on binary Ti–Mo alloys modified by laser beam irradiation

for biomaterial/clinical applications, J. Mater. Sci. Mater. Med. 29 (2018). doi:10.1007/s10856-018-6091-z.

[326] S. Gnanavel, S. Ponnusamy, L. Mohan, R. Radhika, C. Muthamizhchelvan, K. Ramasubramanian, Electrochemical Behavior of Biomedical Titanium Alloys Coated with Diamond Carbon in Hanks' Solution, J. Mater. Eng. Perform. 27 (2018) 1635–1641. doi:10.1007/s11665-018-3250-9.

[327] V. Gopal, M. Chandran, M.S.R. Rao, S. Mischler, S. Cao, G. Manivasagam, Tribocorrosion and electrochemical behaviour of nanocrystalline diamond coated Ti based alloys for orthopaedic application, Tribol. Int. 106 (2017) 88–100. doi:10.1016/j.triboint.2016.10.040.

[328] D.N. Travessa, A.S. da S. Sobrinho, A.M.J. Júnior, V. Roche, Surface plasma nitriding of beta-titanium alloy bio-material, Key Eng. Mater. 813 KEM (2019) 328–333. doi:10.4028/www.scientific.net/KEM.813.328.

[329] H. Li, T. Fu, W. Li, Z. Alajmi, J. Sun, Hydrothermal growth of TiO2-CaP nano-films on a Ti–Nb-based alloy in concentrated calcium phosphate solutions, J. Nanoparticle Res. 18 (2016) 1–7. doi:10.1007/s11051-015-3315-8.

Chapter 3: Corrosion and tribocorrosion behavior of Ti-40Nb and Ti-25Nb-5Fe alloys processed by powder metallurgy

Published in Metall. Mater. Trans. A Phys. Metall. Mater. Sci., 51 (2020) 3256–3267

Corrosion and tribocorrosion behavior of Ti-40Nb and Ti-25Nb-5Fe alloys processed by powder metallurgy

Ihsan Çaha[a], Alexandra Alves[a], Caterina Chirico[b], Ana Maria Pinto[a,c], Sophia Tsipas[b,d], Elena Gordo[b,d], and Fatih Toptan[a,c,e]

[a] CMEMS-UMinho - Center for MicroElectroMechanical Systems, Universidade do Minho, Azurém, 4800-058 Guimarães, Portugal

[b] Universidad Carlos III de Madrid, Avda. Universidad, 30, 28911 Leganés, Spain

[c] Universidade do Minho, Dept. Eng. Mecânica, Azurém, 4800-058 Guimarães, Portugal

[d] Instituto "Álvaro Alonso Barba", 30, 28911 Leganés, Madrid

[e] IBTN/Br – Brazilan Branch of the Institute of Biomaterials, Tribocorrosion and Nanomedicine, 17033-360 Bauru, SP, Brazil

[*] Corresponding author at: CMEMS-Uminho – Center for MicroElectroMechanical Systems, Universidade do Minho, Azurém, 4800-058 Guimarães, Portugal. Tel.: +351 253 510 220; fax: +351 253 516 007. E-mail: ihsancaha@gmail.com (Ihsan Çaha).

Abstract

The requirement of good mechanical properties, lower Young's modulus, superior corrosion resistance, and excellent biocompatibility makes β-type titanium alloys attractive materials for orthopedic implants. In this study, Ti-25Nb-5Fe and Ti-40Nb β-type titanium alloys were designed and produced by powder metallurgy route using titanium hydride, niobium, and iron powders. The effect of sintering conditions on microstructure, corrosion, and tribocorrosion behavior was explored. Electrochemical behavior was investigated in saline solution (9 g/L NaCl) at body temperature by using potentiodynamic polarization and electrochemical impedance spectroscopy. Tribocorrosion behavior was evaluated by reciprocating against an alumina ball at open circuit potential, as well, under anodic and cathodic potentiostatic conditions in saline solution (9 g/L NaCl) at body temperature. The physical, electrochemical, and tribo-electrochemical behavior of both alloys was improved with increasing sintering time at 1250 °C from 2 h to 4 h and decreasing Fe particle size for Ti-25Nb-5Fe alloy. Degradation under tribocorrosion conditions was mainly governed by mechanical wear on Ti-25Nb-5Fe alloy; however,

Ti-40Nb alloy exhibited an antagonistic effect between corrosion and wear during testing under anodic applied potential due to the formation of a denser tribolayer.

Keywords: Beta Titanium alloys, Powder metallurgy, Corrosion, Tribocorrosion

3.1. Introduction

Ti and its alloys have attracted attention in biomedical field due to their good corrosion resistance, high biocompatibility, lower Young's modulus as compared to stainless steel and CoCrMo, and superior mechanical properties. Although α-type commercially pure Ti (cp-Ti) and α+β-type Ti-6Al-4V alloy are commonly employed for implants, they exhibit some clinical concerns. As reviewed by Niinomi and Nakai [1], the Young's modulus of cp-Ti and α+β-type Ti-6Al-4V alloy (~110 GPa) is much higher than that of bone (20 GPa for cortical bone), which leads to the stress-shielding effect caused by the mismatch in Young's modulus between the implant and surrounding bone, eventually resulting in bone resorption and aseptic implant loosening. Moreover, as the most popular Ti alloy, Ti-6Al-4V alloy has raised concerns as a result of Al and V ion release that may cause adverse effects on tissues. For instance, Hallab *et al.* [2] reported that Al and V ions reduced proliferation, viability, and affected the morphology of human peri-implant cells (osteoblast, fibroblasts, and lymphocytes). Therefore, β-type Ti alloys have gained attention due to their composition having non-toxic and allergy free β stabilizer elements including Nb, Zr, Mo, Ta as reported by Okazaki *et al.* [3], better corrosion resistance compared to cp-Ti as shown by Bai et al. for β-type Ti-45Nb alloy [4], and also lower Young's modulus as reviewed by Gepreel and Niinomi [5] for different β-type Ti alloys.

Fang *et al.*[6] has recently reviewed powder metallurgy (P/M) of Ti and pointed the limitation on implant fabrication by melt-wrought techniques due to high cost, complex fabrication, and subsequent machining processes where P/M offers an attractive alternative to enable near-net-shape processing with adjusted chemical composition, or even porosity, that is known to be favourable for biological response and for further reduction on Young's modulus.

According to a review by Niinomi *et al.*[7,8], among the β-type Ti alloys, Ti-Nb based alloys have been the most studied system not only due to their mechanical properties and biocompatibility, but also due to their good corrosion resistance. For instance, the Ti-20Nb-10Zr-5Ta alloy was presented a promising material due to combined properties of low Young's modulus, very low corrosion rate, and good biocompatibility.[9] Accordingly, Bai *et al.*[4] studied the electrochemical behavior of Ti-45Nb alloy in different electrolytes including simulated body fluid and artificial-saliva-based solutions and reported a

better response as compared to cp-Ti. However, load bearing biomedical implants not only suffer to corrosion, but also suffer to tribocorrosion since they are subjected to relative movements in corrosive environments (body fluids) of the human body. Limited studies are available in the literature on the tribocorrosion behavior of β-type Ti alloys. Correa *et al.*[10] compared the tribocorrosion behavior of Ti-15Zr-xMo (x=7.5 and 15) alloys with cp-Ti by performing tests under 1.5 N load, 2 Hz sliding frequency against 10 mm diameter alumina ball in simulated body fluid and reported lower corrosion tendency under sliding, as well as improved repassivation behavior as compared to cp-Ti. Pina *et al.*[11] studied the tribocorrosion behavior of P/M Ti-30Nb-xSn (x=0, 2, and 4) Ti alloys in phosphate buffered saline against 6 mm diameter alumina ball under 5 N and reported increased mechanically activated corrosion after Sn addition due to elevated dissolution rate. More *et al.*[12] studied tribocorrosion behavior of β-type (Ti-12.5Mo, Ti-13Nb-13Zr, and Ti-29Nb-13Ta-4.6Zr) and α+β-type (Ti-6Al-4Fe) alloys against ultra-high molecular weight polyethylene (UHMWPE) in Hank's balanced salt solution with and without incorporation of some synovial fluid constituents under relatively lower contact pressures of 34-35 MPa. The authors reported only a very weak tribo-electrochemical influence for the alloys whereas the wear of UHMWPE counter-material was governed by the adhered third bodies on the surfaces.

Regarding the literature, Ti-40Nb alloy presents an appropriate combination of promising properties in Ti-Nb binary alloys for implants. Calin *et al.*[13] reported the Young's modulus of casted and heat treated Ti-40Nb alloy as 69 GPa. Helth *et al.*[14] investigated the adhesion and spreading of human mesenchymal stromal cell on cp-Ti and Ti-40Nb alloy and reported more pronounced behavior for Ti-40Nb alloy. On the other hand, Fe has gained attention as β stabilizer in Ti due to its non-toxicity and low cost (particularly compared to Nb). Chaves *et al.*[15] explored the microstructural properties and mechanical behavior of β-type Ti-(10, 15, and 25)Nb-3Fe alloys and reported that Ti-25Nb-3Fe alloy exhibited improved phase stability and the lowest Young's modulus (65 GPa). Mohan *et al.*[16] produced Ti-12Mo-6Zr-xFe (x=1, 2, 3, and 4) alloys by P/M and reported that additions of small amounts of Fe improved the β-phase stability. Apart from structural and mechanical properties, biological response of cast Ti-5Nb-xFe (x=0, 1, 2, 3, 4, and 5) alloys was investigated by Hsu *et al.*[17] where all studied alloys were reported as biocompatible. Ehtemam-Haghighi *et al.*[18] investigated the wear behavior of Ti-xNb-7Fe (x=0, 1, 4, 6, 9, and 11) alloys sliding against a stainless steel disc in ambient atmospheric condition under 25 N normal load and indicated that the increasing amount of Nb decreased the hardness/Young's modulus ratio resulting in increased wear rate.

In the last decade, different β-type Ti alloys have been developed for biomedical applications, however, their degradation behavior is yet to be fully understood. Since degradation has been reported as one of the main reasons of early revision of hip implants resulted from breakdown and depassivation of passive film due to relative micro-motions, leading to the release of metallic ions and wear products to around tissues[19,20], this work aimed to study the degradation behavior of Ti-40Nb and Ti-25Nb-5Fe alloys produced by P/M, with diverse electrochemical and tribo-electrochemical tests. Ti-xNb-5Fe system was proposed with small addition of Fe and the value of x was theoretically simulated to obtain a similar β phase fraction to that in Ti-40Nb alloy.

3.2. Materials and methods

3.2.1. Materials and design of novel Ti alloys

Commercial TiH_2 (GfE, D_{50}: 27μm), Nb (Alfa Aesar, D_{50}: 15μm), and two kinds of Fe powders with a coarse particle size (Pomenton, D_{50}: 34 μm) and with a finer particle size (H.C. Starck, D_{50}: 4 μm) were used as raw material. Specifically, two P/M Ti alloys were designed as Ti-40Nb and Ti-25Nb-5Fe. Ti-40Nb was considered as starting composition and the Thermocalc software was used to assess the fraction of β phase by simulation of Ti-Nb phase diagram. In order to obtain the highest β phase fraction together with decreasing Nb percentage, Ti-xNb-5Fe system was also studied. The necessary amount of Nb was simulated by the same software to achieve a similar β phase fraction to that of Ti-40Nb alloy at the same temperature (400 °C) on Ti-Nb-Fe phase diagram and Ti-25Nb-5Fe composition was defined.

3.2.2. Processing

Two different mixtures containing Ti-40Nb and Ti-25Nb-5Fe (in weight percentage) were homogenized by mixing in a multi-directional mixer (Turbula®) for 1 h. The mixtures were prepared with TiH_2 as a raw material to obtain the designed final compositions after dehydrogenization. The samples (14 mm in diameter and about 4 mm in height) were obtained under 700 MPa constant pressure following the compaction procedure previously explained elsewhere.[21] The samples were sintered under high vacuum (10^{-5} mbar) in a tubular furnace by following Cycle 1 and Cycle 2 (Fig. 3.1) and the samples were labeled as c1 and c2, respectively. Preliminary studies (data not shown) showed that Ti-25Nb-5Fe alloy produced with coarser Fe particles by following the c2 sintering cycle presented fully β phase, but it did not present a reduction on porosity (6.1 ± 0.6 %). Therefore, Ti-25Nb-5Fe c2 group of samples were processed with finer Fe particles.

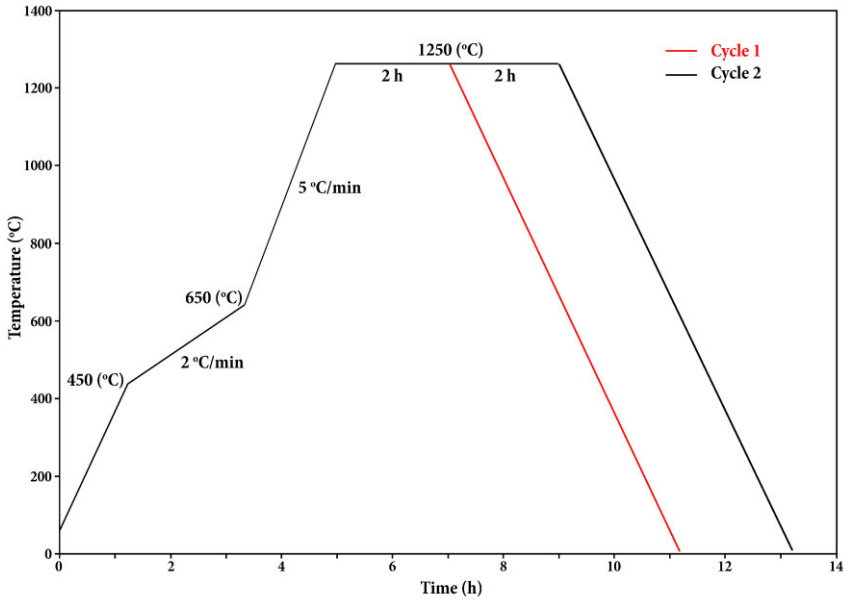

Fig. 3.1. Sintering cycles

Prior to structural characterization, samples were grounded with SiC papers down to 1000 mesh size and mirror finished by using OPS (colloidal silica with particle size of 0.06 μm). Finally, the samples were placed in an ultrasonic bath, cleaned with propanol for 10 min and rinsed with distilled water for 5 min.

For corrosion and tribocorrosion tests, the samples were ground by SiC papers down to 1200 mesh. Afterwards, the samples were cleaned by following the previously described procedure and held up in a desiccator for 1 day before starting each test. All tests were repeated at least three times in order to ensure the reproducibility and the results were given as the arithmetic mean ± standard deviation.

3.2.3. Corrosion tests

Corrosion tests were carried out in a three electrode electrochemical cell (adapted from ASTM: G3-89) having a saturated calomel electrode (SCE) as reference electrode (RE), a Pt electrode as counter electrode (CE), and the samples having 0.38 cm^2 of exposure area as working electrode (WE), connected to Gamry Potentiostat/Galvanostat/ZRA (model Reference 600+). Electrochemical impedance spectroscopy (EIS), and potentiodynamic polarization tests were performed in a saline solution (9 g/L NaCl), as a simple physiological solution, at 37 ± 2 °C temperature. The open circuit potential (OCP) was monitored for the stabilization of native oxide film on the alloy surfaces and afterwards EIS tests were performed at OCP with a frequency range between 10^{-2} to 10^{5} Hz with 7 points per frequency

decade and 10 mV amplitude of sinusoidal signal. After EIS test, potentiodynamic polarization test was employed with 0.5 mV/s scanning rate from −0.25 V_{OCP} up to 1.5 V_{SCE} in anodic direction.

3.2.4. Tribocorrosion tests

Tribocorrosion tests were performed in a tribo-electrochemical cell located in a reciprocating ball-on-plate tribometer (CETR-UMT-2) and connected to a potentiostat (Gamry, Potentiostat/Galvanostat/ZRA model Reference 600) with three electrode configurations that used in the corrosion tests. The experiments were carried out in 30 ml of saline solution (9 g/L NaCl) at 37 ± 2 °C against an alumina ball (Ceratec, 10 mm in diameter). Tribological parameters were chosen as 1 N normal load, 1 Hz frequency, 3 mm of total stroke length, and 30 min of sliding time. Tests were performed under OCP, as well, under anodic (+0.5 V_{SCE}) and cathodic (−0.3 V_{OCP}) potentiostatic conditions, to study the interplay between corrosion and wear. The anodic potential was selected as a potential corresponding to the passive region whereas the cathodic potential was selected considering the susceptibility of Ti alloys to hydrogen absorption and consequent embrittlement that observed as an in vivo mechanism by Rodrigues *et al.*[22] for retrieved Ti alloy hip implants.

3.2.5. Characterization

Porosity (P_{Total}) was estimated according to Eq. 1 where ρ_s and ρ_{th} correspond to the bulk-sintered and theoretical density, respectively. The ρ_s was obtained by the geometrical approach and the ρ_{th} was calculated through the rule of mixtures. The ρ_{th} of Ti was considered as 4.51 g/cm^3 and complete dehydrogenation of TiH_2 was assumed.

$$P_{Total} = (1 - \frac{\rho_s}{\rho_{th}}) \times 100 \qquad \text{Eq. (1)}$$

Hardness was attained by microindentation measurements under 0.5 N load and 20 s dwelling time using a microhardness tester (Zwick Roell, model ZHVμ) over three samples with at least 10 indentations for each one.

Microstructures were evaluated by scanning electron microscope (SEM, Phillips XL-30) and structural analysis was performed by X-ray diffraction (XRD, X'pert Phillips diffractometer with Cu-Kα radiation of 1.54 Å and 40 kV). The phase percentages were calculated by following Eq. (2), where I is the intensity.

$$\%\, phase_\alpha = \frac{\sum I_{\alpha\, peaks}}{\sum I_{all\, peaks}} \quad \text{Eq. (2)}$$

After tribocorrosion tests, samples were cleaned with abovementioned procedures and the worn surfaces were analyzed by using field emission gun (SEM FEI Nova 200) equipped with energy dispersive spectrometer (EDS, EDAX - Pegasus X4M). Wear volume loss were calculated over the 2D profiles obtained by a contact profilometer (Veeco, Dektak 150) using the model and the methodology previously described by Doni *et al.*.[23]

3.3. Results

3.3.1. Physical properties and microstructure

Porosity and hardness values of samples are given in Table 3.1. Both alloys presented lower average values of porosity on the c2 condition where the difference was more pronounced on Ti-25Nb-5Fe alloy.

Table 3.1. Porosity and hardness values.

Samples	Porosity (%)	Hardness ($HV_{0.05}$)
Ti-40Nb c1	5.1 ± 0.3	228 ± 19
Ti-40Nb c2	4.5 ± 1.6	243 ± 40
Ti-25Nb-5Fe c1	4.9 ± 0.3	284 ± 14
Ti-25Nb-5Fe c2	1.0 ± 0.7	310 ± 15

According to the XRD pattern (Fig. 3.2), all samples were mainly constituted of β-Ti, however, Nb peaks found on Ti-40Nb samples showing undiffused Nb on this alloy. According to Eq. (2), Ti-40Nb c1 was composed of 2.4% α-Ti, 91.1% β-Ti and 6.5% Nb, while Ti-40Nb c2 was composed of 94.5% β-Ti and 5.5% Nb. Also, it can be seen that more α-Ti phase transformed to β-Ti phase and the percentage of Nb decreased with c2 for Ti-40Nb alloy. Ti-25Nb-5Fe alloys presented entirely β-Ti phase.

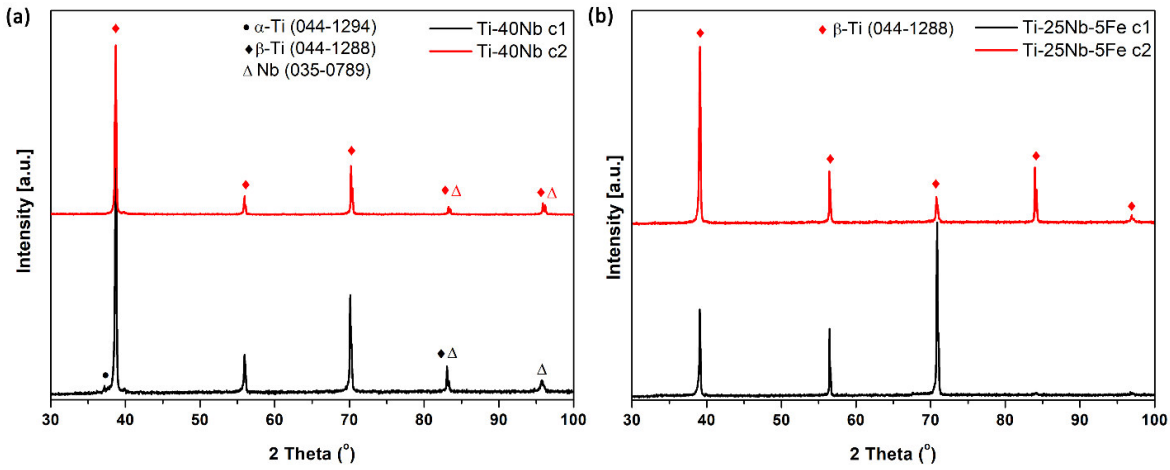

Fig. 3.2. XRD pattern of a) Ti-40Nb and b) Ti-25Nb-5Fe alloys for both processing conditions.

BSE-SEM images for both alloys and processing conditions are given in Fig. 3.3. Both alloys presented predominantly β-Ti microstructure, however, backscattering electrons revealed some areas rich in Nb (bright spots) for Ti-40Nb alloy, as in accordance with the XRD results. Since Fe addition improved the diffusion processes between Nb and Ti, Nb-rich bright spots were not observed on Ti-5Fe-25Nb alloy. On the other hand, although total porosity was similar between two alloys produced at c1, bigger pores were observed on Ti-5Fe-25Nb alloy. After processing under c2, both alloys presented lower porosity and similar pore size.

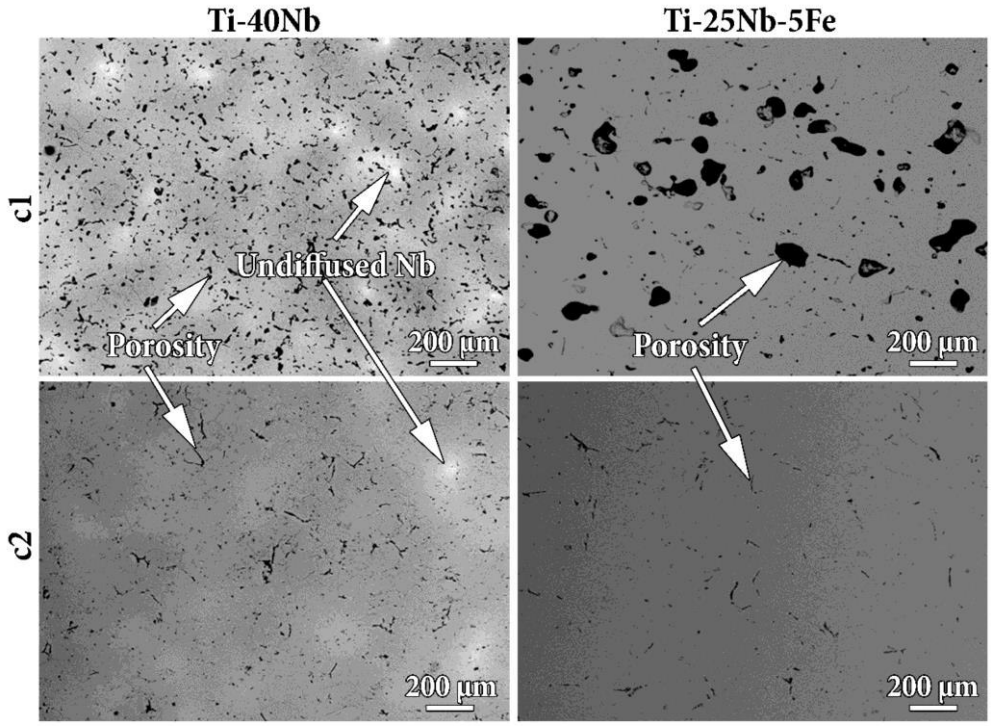

Fig. 3.3. BSE-SEM images of Ti-40Nb and Ti-25Nb-5Fe alloys for c1 and c2 conditions.

3.3.2. Corrosion behavior

Representative potentiodynamic polarization curves for all samples are given in Fig. 3.4, extracted values of passivation current density (i_{pass}) and corrosion potential ($E_{(i=0)}$) are presented in Table 3.2. All samples presented well defined passivation plateaus started at average 0 mV_{SCE}, 260 mV_{SCE}, 200 mV_{SCE}, and 380 mV_{SCE} for Ti-40Nb c1, Ti-40Nb c2, Ti-25Nb-5Fe c1, and Ti-25Nb-5Fe c2, respectively. The results indicated that Ti-25Nb-5Fe samples showed slightly higher average $E_{(i=0)}$ and lower average i_{pass} values as compared to Ti-40Nb samples. The same trend was also observed on both alloys processed under c2, in comparison to the alloys processed under c1.

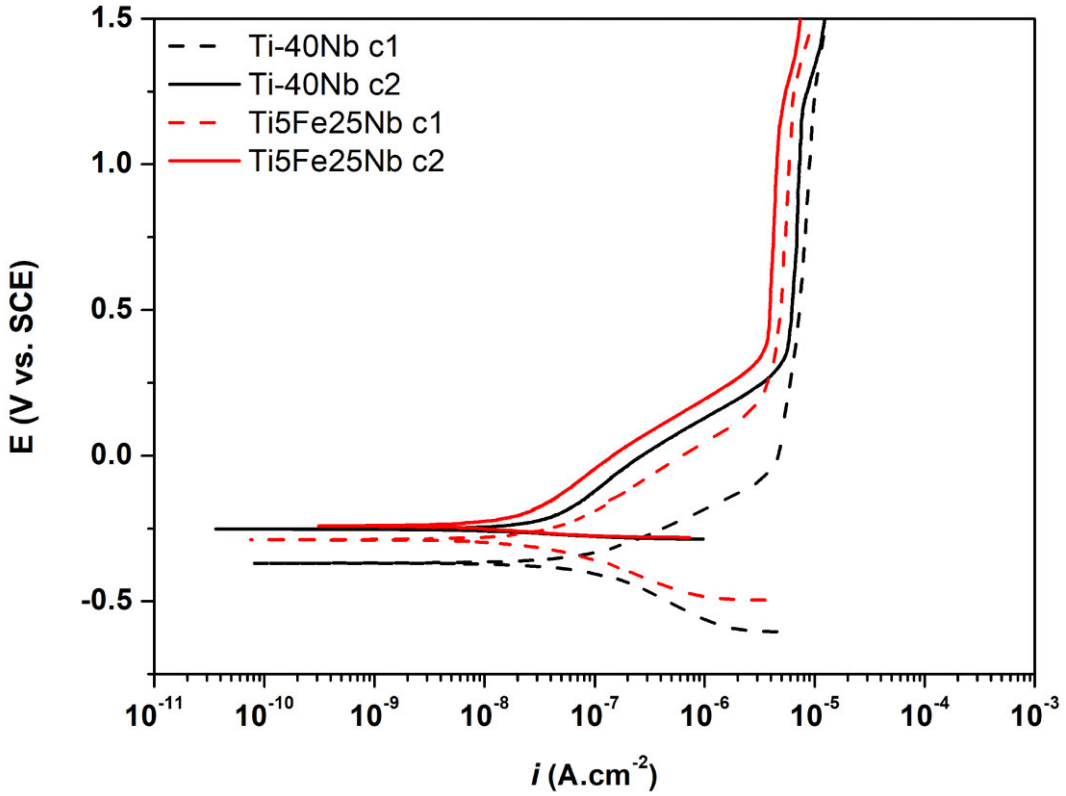

Fig. 3.4. Potentiodynamic polarization curves for Ti-40Nb and Ti-25Nb-5Fe alloys.

Table 3.2. Corrosion potential ($E_{(i=0)}$) and passivation current density (i_{pass}) values for Ti-40Nb and Ti-25Nb-5Fe alloys.

	$E_{(i=0)}$ (mV_{SCE})	i_{pass} ($\mu A.cm^{-2}$)
Ti-40Nb c1	−359 ± 9	8.28 ± 0.84
Ti-40Nb c2	−280 ± 33	6.58 ± 0.78
Ti-25Nb-5Fe c1	−289 ± 14	5.00 ± 0.55
Ti-25Nb-5Fe c2	−229 ± 22	4.03 ± 0.16

The representative Bode diagram of EIS spectra given in Fig. 3.5a. The constant values of |Z| and near 0° phase angle were observed at the high-frequency range (10^3-10^5 Hz) owing to the electrolyte resistance. Near −90° of phase angle values in the medium and low ranges of frequency indicated the typical capacitive behavior of a passive oxide film. The phase angle values in medium frequency range were decreased and the |Z| values in low frequency range were increased for both alloys processed under c2.

The electrical equivalent circuit (EEC) with one-time constant, modified Randles circuit, used to simulate the EIS experimental data by using Echem Analyst software shown in Fig. 3.5b and the EEC parameters are given in Table 3.3. The EEC includes R_e, R_{ox}, and Q_{ox} corresponding to an electrolyte resistance, the resistance of the oxide film, and a constant phase element (CPE), respectively. The CPE, demonstrating a shift from an ideal capacitor was used in the EEC. The impedance of a CPE is defined as $Z_{CPE} = [Y_0(j\omega)^n]^{-1}$, where Y_0 is the admittance of CPE, ω is the angular frequency, $j=\sqrt{-1}$ is the imaginary number, and n *is* the exponential factor, $-1 \leq n \leq 1$. When n value is 1, 0, and −1, the CPE response is an ideal capacitor, a resistor, and an inductor, respectively. The n value is associated with surface heterogeneities and roughness. The C_{ox} values converted from Q_{ox} values through Eq. (3) derived from Brug's equation;

$$C_{ox} = \left[Q_{ox} R_e^{(1-n)}\right]^{\frac{1}{n}} \quad (3)$$

The quality of fitting on the EEC was assessed by the goodness of fitting where the proposed model showed values below 10^{-3} (Table 3.3). According to these values, the C_{ox} values only slightly decreased from Ti-40Nb to Ti-25Nb-5Fe, however, Ti-25Nb-5Fe exhibited noticeably higher R_{ox} values. When two processing conditions were compared, no clear trend was observed on R_{ox}, but relatively lower C_{ox} values were observed on both alloys processed under c2. Moreover, both alloys presented very similar n values whereas the values were noticeably higher on both alloys processed under c2.

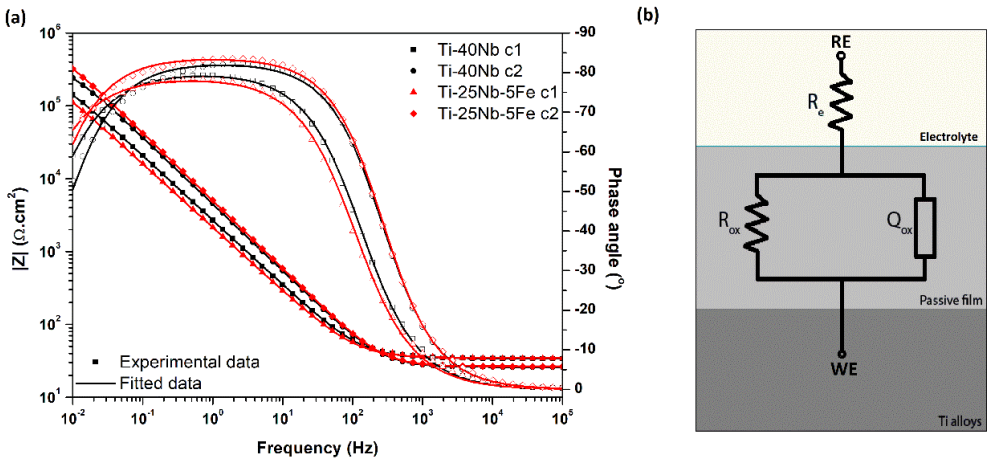

Fig. 3.5. Bode diagram (a) and EEC (b) of Ti-40Nb and Ti-25Nb-5Fe alloys.

Table 3.3. Electrochemical parameters obtained from the proposed EEC.

Sample	R_{ox} (x10^5 Ω.cm²)	C_{ox} (μF.cm^{-2})	n	χ^2 (x10^{-4})
Ti-40Nb c1	3.5 ± 0.7	39.4 ± 12.4	0.88 ± 0.03	4.4 ± 2.7
Ti-40Nb c2	3.8 ± 0.9	26.0 ± 4.8	0.92 ± 0.01	3.2 ± 0.3
Ti-25Nb-5Fe c1	9.0 ± 2.9	33.0 ± 9.4	0.88 ± 0.01	5.5 ± 4.0
Ti-25Nb-5Fe c2	8.4 ± 0.5	21.2 ± 2.4	0.93 ± 0.01	2.2 ± 0.8

3.3.3. Tribocorrosion behavior

3.3.3.1. Tribocorrosion at OCP

The OCP evolution before, during and after sliding, together with the corresponding COF values are presented in Fig. 3.6. When sliding started, values of OCP dropped abruptly for all samples indicating a damage given to the passive film by the exposure of the bare metal (worn area) to the electrolyte. After sliding, the values immediately increased approximately near to the values obtained before sliding owing to spontaneous repassivation. During sliding, the average OCP values obtained from three tests for Ti-40Nb c1, Ti-40Nb c2, Ti-25Nb-5Fe c1, and Ti-25Nb-5Fe c2 samples were −622 ± 71 mV_{SCE}, −510 ± 59 mV_{SCE}, −589 ± 39 mV_{SCE}, and −511 ± 19 mV_{SCE}, respectively, indicating relatively more positive values for c2 for both alloys. COF values presented a relatively stable evolution for all samples. The average COF values of Ti-40Nb c1, Ti-40Nb c2, Ti-25Nb-5Fe c1, and Ti-25Nb-5Fe c2 samples were 0.71 ± 0.003, 0.61 ± 0.10, 0.64 ± 0.12, and 0.54 ± 0.03, respectively, where slightly lower values

obtained on Ti-25Nb-5Fe alloy and decreased values were observed for both alloys processed under c2.

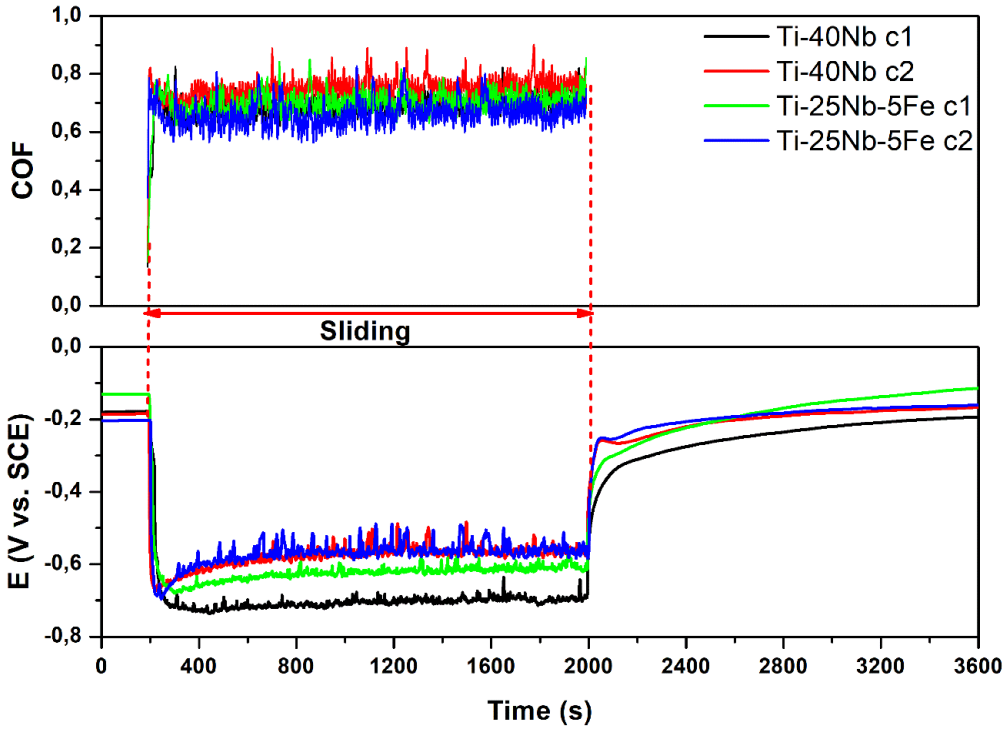

Fig. 3.6. Tribocorrosion at OCP: evolution of OCP together with corresponding COF values.

3.3.3.2. Tribocorrosion at applied potentials

In order to investigate the interactions between wear and corrosion, tribocorrosion tests were performed under anodic (AP) and cathodic (CP) applied potentials to simulate the degradation due to wear/corrosion and mechanical wear, respectively. Fig. 3.7 presents the anodic current evolution before, during, and after sliding at an applied potential of +0.5 V_{SCE}, as well, the corresponding COF values. Before sliding, the current density values were stable due to the presence of a stable oxide film formed on the surfaces. Under sliding, the current evolution of Ti-40Nb was significantly different than Ti-25Nb-5Fe for both c1 and c2 conditions. When sliding started, Ti-40Nb c1 and Ti-40Nb c2 presented only a very small increase on current density than remained relatively stable around these values for around 2 and 5 min, respectively. Afterwards, sharp increases on current density were observed for both samples then the values decreased close to the values recorded on the onset of the sliding. Regarding Ti-25Nb-5Fe samples, larger current density values were recorded during all sliding period as compared to Ti-40Nb alloy. When the counter-material unloaded, the current density fell for all samples to the values close to the ones recorded before sliding indicating the repassivation of the worn track area. Also, the anodic charge, Q, was estimated through integration of the current curves over sliding time. The Q values of

Ti-40Nb c1, Ti-40Nb c2, Ti-25Nb-5Fe c1, and Ti-25Nb-5Fe c2 samples were calculated as $2.1\times10^{-2} \pm 0.09\times10^{-2}$, $1.2\times10^{-2} \pm 0.3\times10^{-2}$, $11.8\times10^{-2} \pm 1.1\times10^{-2}$, and $10.8\times10^{-2} \pm 2.7\times10^{-2}$ coulombs, respectively. Ti-25Nb-5Fe samples presented approx. 10 times higher Q values than Ti-40Nb alloys for both c1 and c2 conditions, indicating significantly higher corrosion kinetics under sliding. When Q values obtained for both processing conditions are compared, although some small decreases were obtained for the c2 condition, considering the standard deviation values, no obvious difference can be pointed.

In case of Ti-40Nb samples, when sliding started, COF values were gradually increased till the corresponding current density values decreased close to the ones observed on the onset of sliding, afterwards, remained relatively stable during the remaining sliding period. However, when an increase occurred on the current density values, larger fluctuations were detected on the corresponding COF values. Regarding Ti-25Nb-5Fe alloys, when the sliding started, COF values were suddenly increased up to the values around 0.64 ± 0.02 and 0.62 ± 0.05 for Ti-25Nb-5Fe c1 and Ti-25Nb-5Fe c2, respectively, and then evolved around these values till the end of sliding.

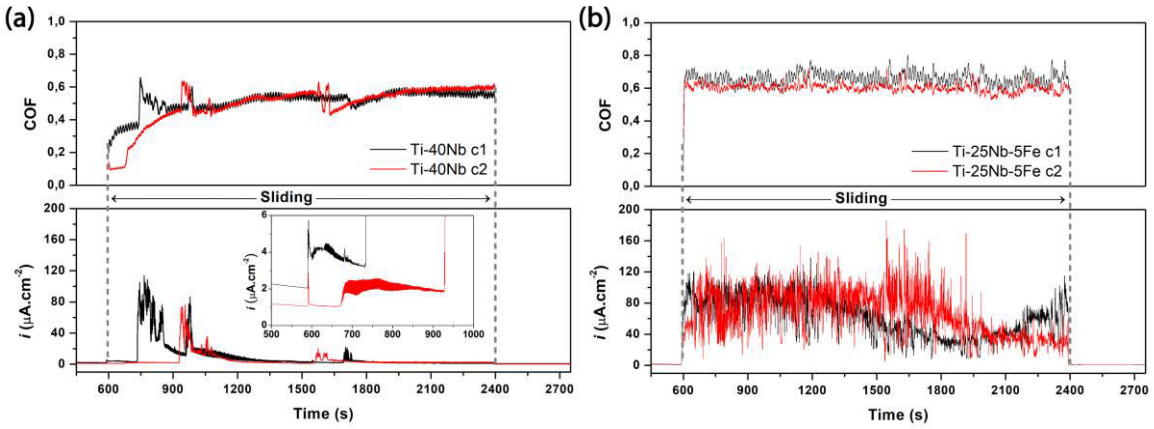

Fig. 3.7. Tribocorrosion at anodic applied potential: evolution of current density together with corresponding COF values for a) Ti-40Nb and b) Ti-25Nb-5Fe alloys.

3.3.3.3. Wear morphology

SEM images of surfaces worn under OCP, AP, and CP are given in Fig. 3.8. All worn surfaces presented typical wear surface morphologies known for Ti and Ti alloys, most predominantly, parallel ploughing grooves and abrasion scratches, together with a discontinuous tribolayer (oxidized patches) particularly for the samples tested under OCP and AP as also previously had been reported by Silva *et al.*[24] for Ti, by Runa *et al.*[25] for Ti-6Al-4V, and by Correa *et al.*[10] for Ti-15Zr-xMo (x=7.5 and 15). Discontinuous tribolayer appeared to be denser on the Ti-40Nb alloys tested under AP conditions, as evidenced on BSE images with darker regions.

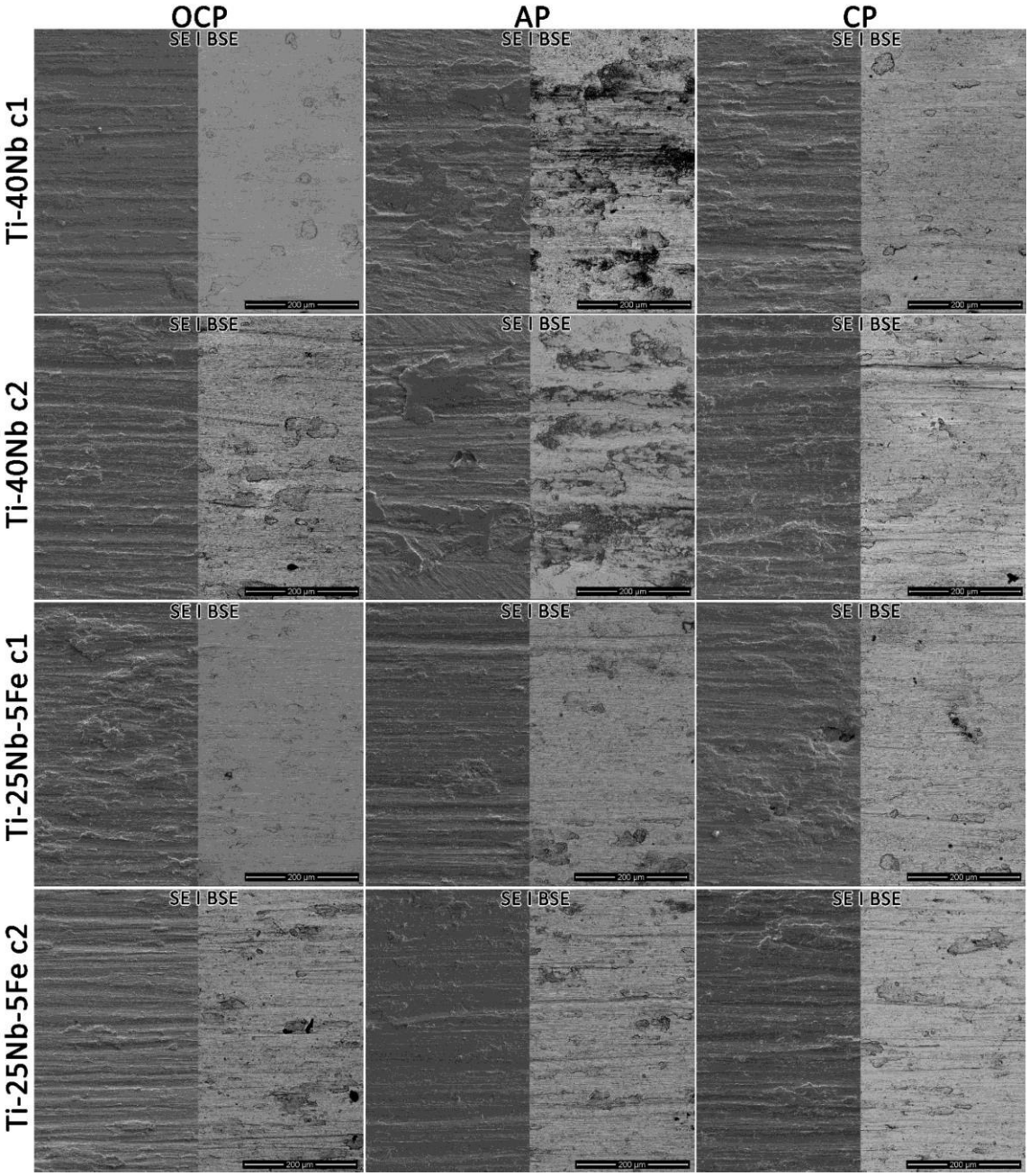

Fig. 3.8. SE- and BSE-SEM images of wear tracks for Ti-40Nb c1, Ti-40Nb c2, Ti-25Nb-5Fe c1, and Ti-25Nb-5Fe c2 of the samples tested under OCP, AP, and CP.

Fig. 3.9 shows the SEM images of the worn alumina ball surfaces (counter-material) together with the respective EDS spectra. The visible wear damage on balls worn against Ti-40Nb alloy tested at AP condition were less severe for both processing conditions. Transferred material from samples to the counter-material was confirmed by EDS analysis for all conditions where lower visible amount of transferred material was observed on the balls slid against Ti-40Nb alloy at AP condition.

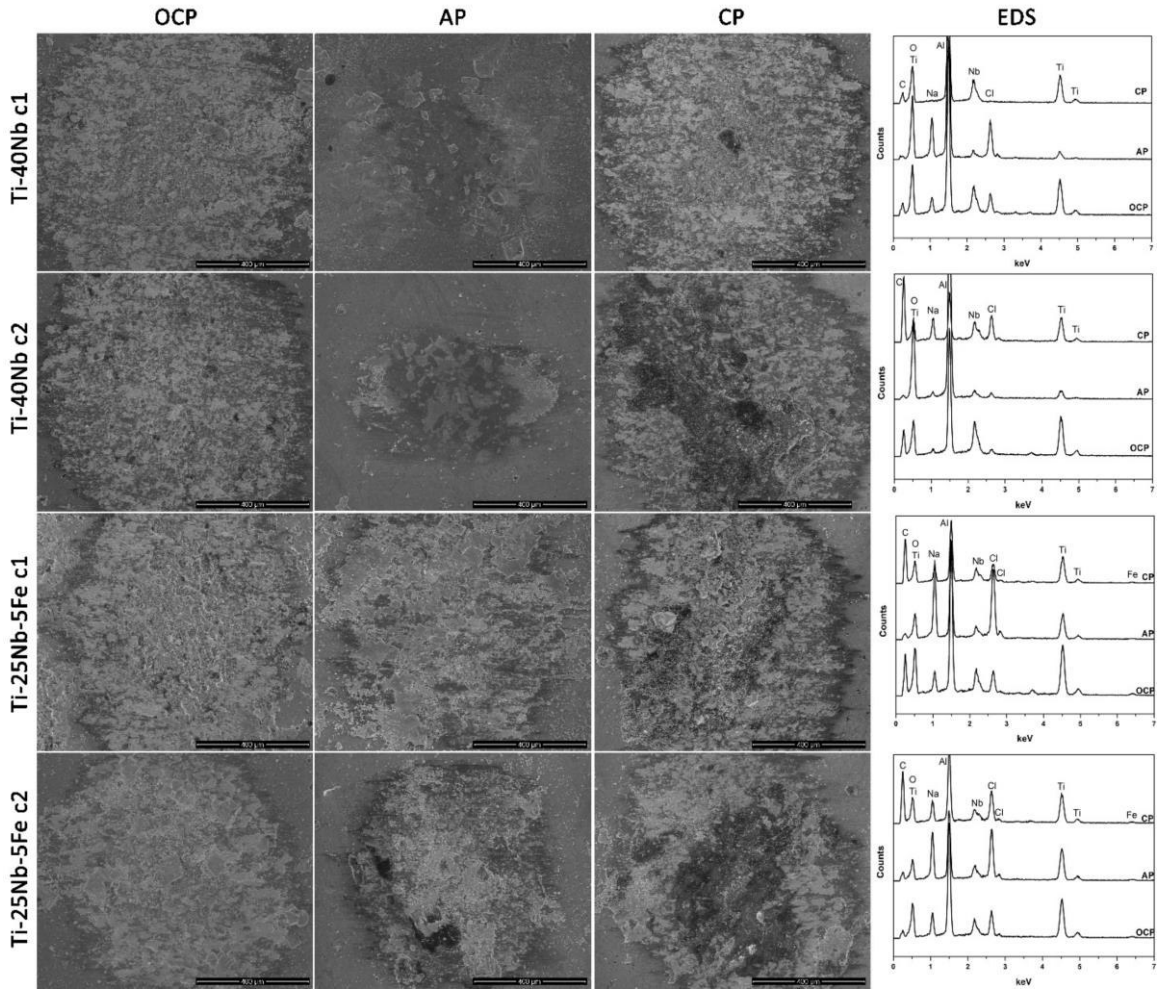

Fig. 3.9. SE-SEM images and respective EDS spectra of the alumina ball surfaces worn against Ti-40Nb c1, Ti-40Nb c2, Ti-25Nb-5Fe c1, and Ti-25Nb-5Fe c2 tested under OCP, AP, and CP.

Fig. 3.10 shows representative profiles taken from the center of the wear tracks, together with the total wear volume loss values. Ti-25Nb-5Fe exhibited relatively lower average wear volume loss under OCP and CP, however, clearly, the opposite trend was observed for AP. Regarding the tribo-electrochemical testing conditions, Ti-25Nb-5Fe alloys exhibited similar values for all conditions whereas the wear volume loss values for Ti-40Nb alloys decreased from OCP to AP where the effect of cathodic polarization was relatively small, but the effect of anodic polarization was clearly predominant. On the other hand, within the same alloys, no clear effect of processing conditions on the wear loss was observed.

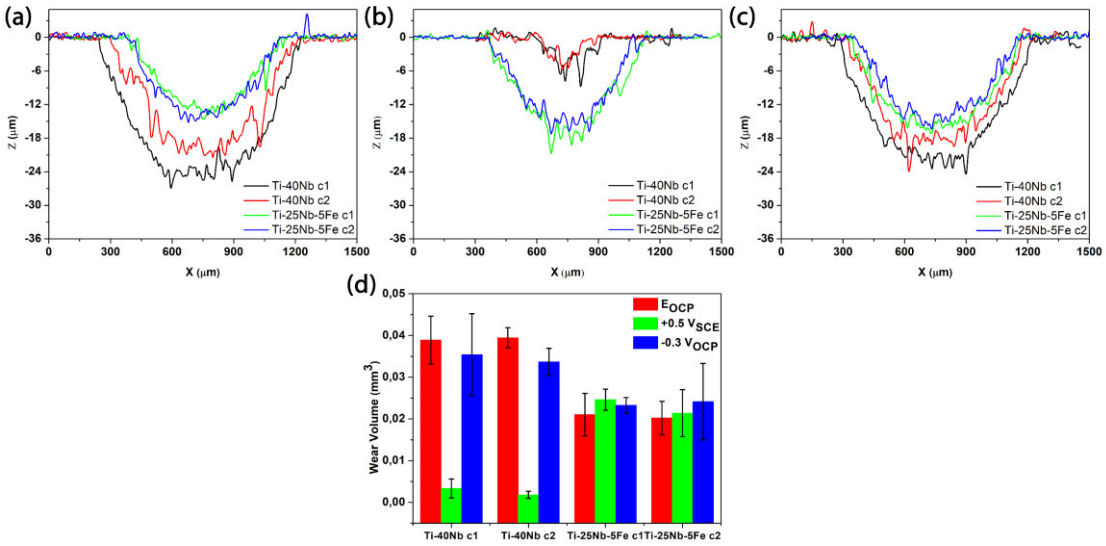

Fig. 3.10. Representative 2D wear track profiles of samples for testing at a) OCP, b) AP, c) CP conditions, and d) wear volume loss values.

3.4. Discussion

3.4.1. Physical properties

The microstructure, porosity, hardness, and phase distribution were significantly influenced by sintering conditions. Guo *et al.*[26] indicated that the decreasing porosity for Ti-24Nb-4Zr-7.9Sn alloy with increasing holding times in 1250 °C was due to the β grain coarsening and the dissolution of prior α phases in the β matrix, which might also be the reason for decreasing porosity on c2 condition. The results pointed that Fe addition increased the hardness, and also the hardness of both alloys slightly increased when processed under c2 condition. As pointed out by Sharma *et al.*[27], the hardness increased with the increasing sintering time due to more homogenous distribution of the phases in its microstructure. Ti-25Nb-5Fe alloy presented fully β phase for both conditions due to the well-known β stabilizing effect of Fe, which was reported by Niinomi *et al.*[28] as a one of the most effective β stabilizer element. According to John,[29] the atomic radius of Fe (1.24 Å) is smaller than Ti (1.45 Å) and Nb (1.43 Å). The peaks of Ti-25Nb-5Fe were shifted to right due to the decrease on the lattice parameters of the β phase. The (110) peak at 2θ=38.5°, representing body-centered cubic (bcc) structure, became most intense and two additional β peaks were observed with c2 condition as result of a longer sintering stage.

3.4.2. Corrosion behavior

The potentiodynamic polarization and EIS results indicated that increased sintering time may lead to formation of a more stable and protective oxide film in contact with NaCl solution, leading to an improved corrosion performance. Although all tested samples presented similar corrosion mechanism, as represented by the same EEC, Ti-25Nb-5Fe alloy presented better corrosion resistance and lower corrosion rate as compared to Ti-40Nb alloy, evidenced by higher R_{ox} and lower i_{pass} values. This better behavior of Ti-25Nb-5Fe alloy may be linked with the fully diffused Nb and obtaining a fully β phase structure. However, incorporation of iron oxides to the passive film of Ti-25Nb-5Fe alloy may also influence the corrosion behavior that needs further investigations by XPS analysis before and after corrosion tests.

Samples processed under c2 condition showed higher corrosion resistance than samples processed under the c1 condition for both alloys, evidenced by lower i_{pass}, lower C_{ox}, and higher phase angle values, which indicates lower corrosion rate and higher quality of passive film. Guo *et al.*[26] studied the influence of sintering temperature and sintering time on microstructure, mechanical properties, and electrochemical response of β-type Ti-24Nb-4Zr-7.9Sn alloy. The authors found that sintering at 1250 °C for 2 hours yielded with higher corrosion resistance in simulated body environments due to the transformation of the α phase to β phase and due to lower porosity. Tamilselvi and Rajendran[30] studied corrosion behavior of Ti-5Al-2Nb-1Ta alloy immersed in Hanks' solution for 0 h, 120 h, 240 h, and 360 h using EIS test. Also, Alves *et al.*[31] investigated the electrochemical behavior Ti and Ti6Al-4V alloy immersed in Hanks' solution for 5 min, 24 h and 7 days tested by the same technique. Both investigations reported that the *n* values were related to the non-uniform current distribution as a consequence of surface roughness or inhomogeneity. Therefore, the better quality of the passive film obtained for both alloys produced under c2 condition may be explained by increased *n* values indicating a better phase distribution, thus, improved homogeneity.

3.4.3. Tribocorrosion behavior

Thermodynamic tendency to corrosion under sliding can be evaluated through the evolution OCP values. Although no clear trend was observed between the testing groups when considering the results together with the standard deviation, alloys produced under c2 condition presented slightly higher average E_{OCP} values indicating lower tendency to corrosion, that may be linked with the improved surface homogeneity.

Generally, wear loss under tribocorrosion conditions occurs through several mechanisms: wear accelerated corrosion (W_{wac}), mechanical wear (W_{mec}), and corrosion (W_{cor}). As Landolt *et al.*[32] demonstrated, the W_{cor} can be neglected in case of passive materials, thus the overall wear volume loss (W_{tot}) is expressed as the sum of W_{wac} and W_{mec}.

Mischler *et al.* [33] investigated the role of passive oxide films on carbon steel sliding against alumina ball and reported that the total wear volume loss of passive alloys in tribocorrosion system at AP condition resulted in combined influences of corrosion and wear, while the total wear volume loss in CP condition is attributed to mechanical wear (without the influence of corrosion). Usually, as reviewed by Cao and Mischler [34] the wear volume loss in AP conditions is expected to be higher than those in CP and OCP conditions due to the synergistic interplay between corrosion and wear. However, the average wear volume losses on Ti-25Nb-5Fe alloy were similar after testing under OCP, AP, and CP, suggesting that the degradation process was mainly governed by mechanical wear. Regarding Ti-40Nb alloy, the average wear volume loss in AP condition was significantly lower as compared to the ones obtained on CP and OCP conditions, indicating an antagonistic effect between corrosion and wear. This was most probably due to the area covered by the discontinuous tribolayer that was substantially increased on Ti-40Nb alloys tested under AP, that played a protective role against tribocorrosion, evidenced with lower current density under sliding, lower COF, lower Q, and lower wear volume loss. Relatively lower corrosion resistance of Ti-40Nb, more specifically its lower R_{ox} and higher i_{pass} (i.e. higher corrosion kinetics) may lead to the formation of a denser tribolayer during repetitive disturbance of the passive film under AP condition. This denser tribolayer may give a protection against wear and corrosion, however, after reaching a certain thickness, may be removed by the counter-material resulting in a rapid increase on the current density values (Fig. 3.7a). Afterward, the tribolayer starts to form itself again and consequently the current density values decrease near to the values obtained on the onset of the sliding. Nevertheless, the undiffused Nb may also play a role on this behavior, that needs further understanding by performing XPS analysis before and after corrosion and tribocorrosion tests for understanding the variations on the chemical composition of the native oxide film. Besides, lower wear volume loss values obtained on Ti-25Nb-5Fe alloy tested under OCP and CP conditions, where the influence of the mechanical wear was more predominant as compared to AP condition, were most likely affected by the higher hardness of this alloy as compared to Ti-40Nb.

Microstructural and chemical analysis of the worn sample and the counter-material surfaces indicated that wear was mainly dominated by mixed abrasive/adhesive wear mechanism. However, it

was evident by the characterization of the worn counter-material surfaces that the influence of the adhesive wear was significantly reduced for Ti-40Nb alloy tested at AP condition due to the reduced direct contact area between the testing alloy and the counter-material surfaces after formation of a denser tribolayer on the worn surface (Fig. 3.9).

3.5. Conclusion

Corrosion and tribocorrosion behavior of Ti-25Nb-5Fe and Ti-40Nb alloys processed by P/M was investigated in saline solution (9 g/L NaCl). Electrochemical studies showed that Ti-25Nb-5Fe alloy presented higher corrosion resistance than Ti-40Nb alloy and the corrosion resistance of both alloys improved with the improved surface homogeneity. Ti-25Nb-5Fe alloys did not present a considerable difference on the wear volume loss after tribocorrosion tests performed under OCP or under anodic and cathodic potentiostatic conditions, indicating that the dominant degradation mechanism was mechanical wear. However, Ti-40Nb alloy exhibited significantly lower wear volume loss after tribocorrosion tests performed at anodic potentiostatic conditions, pointing an antagonistic effect between wear and corrosion due to formation of a denser tribolayer on the worn surfaces.

Acknowledgements

This work is supported by FCT with the reference project UID/EEA/04436/2019, together with M-ERA-NET/0001/2015, as well, by MINECO (Spain) through the program PCIN-2016-123 and the Ramón y Cajal project RYC-2014-15014. I. Caha is grateful for the financial support through a Ph.D. grant under the NORTE-08-5369-FSE-000012 project.

References

[1] M. Niinomi, M. Nakai, Titanium-based biomaterials for preventing stress shielding between implant devices and bone, Int. J. Biomater. (2011) 1–10. doi:10.1155/2011/836587.

[2] N.J. Hallab, S. Anderson, M. Caicedo, A. Brasher, K. Mikecz, J.J. Jacobs, Effects of soluble metals on human peri-implant cells, J. Biomed. Mater. Res. - Part A. 74 (2005) 124–140. doi:10.1002/jbm.a.30345.

[3] Y. Okazaki, Y. Ito, K. Kyo, T. Tateishi, Corrosion resistance and corrosion fatigue strength of new titanium alloys for medical implants without V and Al, Mater. Sci. Eng. A. 213 (1996) 138–147. doi:10.1016/0921-5093(96)10247-1.

[4] Y. Bai, Y. Deng, Y. Zheng, Y. Li, R. Zhang, Y. Lv, Q. Zhao, S. Wei, Characterization, corrosion behavior, cellular response and in vivo bone tissue compatibility of titanium-niobium alloy with

low Young's modulus, Mater. Sci. Eng. C. 59 (2016) 565–576. doi:10.1016/j.msec.2015.10.062.

[5] M.A. Gepreel, M. Niinomi, Biocompatibility of Ti-alloys for long-term implantation, J. Mech. Behav. Biomed. Mater. 20 (2013) 407–415. doi:10.1016/j.jmbbm.2012.11.014.

[6] Z.Z. Fang, J.D. Paramore, P. Sun, K.S.R. Chandran, Y. Zhang, Y. Xia, F. Cao, M. Koopman, M. Free, Powder metallurgy of titanium – past, present, and future, Int. Mater. Rev. 63 (2017) 1–53. doi:10.1080/09506608.2017.1366003.

[7] M. Niinomi, M. Nakai, J. Hieda, Development of new metallic alloys for biomedical applications, Acta Biomater. 8 (2012) 3888–3903. doi:10.1016/j.actbio.2012.06.037.

[8] M. Niinomi, Recent metallic materials for biomedical applications, Metall. Mater. Trans. A. 33 (2002) 477–486. doi:10.1007/s11661-002-0109-2.

[9] M. Popa, J.M. Calderon Moreno, C. Vasilescu, S.I. Drob, E.I. Neacsu, A. Coer, J. Hmeljak, G. Zerjav, I. Milošev, Structural analysis, electrochemical behavior, and biocompatibility of novel quaternary titanium alloy with near β structure, Metall. Mater. Trans. A Phys. Metall. Mater. Sci. 45 (2014) 3130–3143. doi:10.1007/s11661-014-2254-9.

[10] D.R.N. Correa, P.A.B. Kuroda, C.R. Grandini, L.A. Rocha, F.G.M. Oliveira, A.C. Alves, F. Toptan, Tribocorrosion behavior of β-type Ti-15Zr-based alloys, Mater. Lett. 179 (2016) 118–121. doi:10.1016/j.matlet.2016.05.045.

[11] V.G. Pina, A. Dalmau, F. Devesa, V. Amigó, A.I. Muñoz, Tribocorrosion behavior of beta titanium biomedical alloys in phosphate buffer saline solution, J. Mech. Behav. Biomed. Mater. 46 (2015) 59–68. doi:10.1016/j.jmbbm.2015.02.016.

[12] N.S. More, N. Diomidis, S.N. Paul, M. Roy, S. Mischler, Tribocorrosion behavior of β titanium alloys in physiological solutions containing synovial components, Mater. Sci. Eng. C. 31 (2011) 400–408. doi:10.1016/j.msec.2010.10.021.

[13] M. Calin, A. Helth, J.J. Gutierrez Moreno, M. Bönisch, V. Brackmann, L. Giebeler, T. Gemming, C.E. Lekka, A. Gebert, R. Schnettler, J. Eckert, Elastic softening of β-type Ti-Nb alloys by indium (In) additions, J. Mech. Behav. Biomed. Mater. 39 (2014) 162–174. doi:10.1016/j.jmbbm.2014.07.010.

[14] A. Helth, P.F. Gostin, S. Oswald, H. Wendrock, U. Wolff, U. Hempel, S. Arnhold, M. Calin, J. Eckert, A. Gebert, Chemical nanoroughening of Ti40Nb surfaces and its effect on human mesenchymal stromal cell response, J. Biomed. Mater. Res. - Part B Appl. Biomater. 102 (2014) 31–41. doi:10.1002/jbm.b.32976.

[15] J.M. Chaves, O. Florêncio, P.S. Silva, P.W.B. Marques, C.R.M. Afonso, Influence of phase transformations on dynamical elastic modulus and anelasticity of beta Ti-Nb-Fe alloys for biomedical applications, J. Mech. Behav. Biomed. Mater. 46 (2015) 184–196. doi:10.1016/j.jmbbm.2015.02.030.

[16] P. Mohan, A.B. Elshalakany, T.A. Osman, V. Amigo, A. Mohamed, Effect of Fe content, sintering temperature and powder processing on the microstructure, fracture and mechanical behaviours of Ti-Mo-Zr-Fe alloys, J. Alloys Compd. 729 (2017) 1215–1225. doi:10.1016/j.jallcom.2017.09.255.

[17] H.C. Hsu, S.K. Hsu, S.C. Wu, C.J. Lee, W.F. Ho, Structure and mechanical properties of as-cast Ti-5Nb-xFe alloys, Mater. Charact. 61 (2010) 851–858. doi:10.1016/j.matchar.2010.05.003.

[18] S. Ehtemam-Haghighi, K.G. Prashanth, H. Attar, A.K. Chaubey, G.H. Cao, L.C. Zhang, Evaluation of mechanical and wear properties of Ti-xNb-7Fe alloys designed for biomedical applications, Mater. Des. 111 (2016) 592–599. doi:10.1016/j.matdes.2016.09.029.

[19] S. Virtanen, I. Milošev, E. Gomez-Barrena, R. Trebše, J. Salo, Y.T. Konttinen, Special modes of corrosion under physiological and simulated physiological conditions, Acta Biomater. 4 (2008) 468–476. doi:10.1016/j.actbio.2007.12.003.

[20] E.K. Ocran, L.E. Guenther, J.M. Brandt, U. Wyss, O.A. Ojo, Corrosion and Fretting Corrosion Studies of Medical Grade CoCrMo Alloy in a Clinically Relevant Simulated Body Fluid Environment, Metall. Mater. Trans. A Phys. Metall. Mater. Sci. 46 (2015) 2696–2709. doi:10.1007/s11661-015-2834-3.

[21] C. Chirico, S. Tsipas, F. Toptan, E. Gordo, Development of Ti–Nb and Ti–Nb–Fe beta alloys from TiH2 powders, Powder Metall. 62 (2019) 44–53. doi:10.1080/00325899.2018.1563953.

[22] D.C. Rodrigues, R.M. Urban, J.J. Jacobs, J.L. Gilbert, In vivo severe corrosion and hydrogen embrittlement of retrieved modular body titanium alloy hip-implants, J. Biomed. Mater. Res. - Part B Appl. Biomater. 88B (2009) 206–219. doi:10.1002/jbm.b.31171.

[23] Z. Doni, A.C. Alves, F. Toptan, J.R. Gomes, A. Ramalho, M. Buciumeanu, L. Palaghian, F.S. Silva, Dry sliding and tribocorrosion behaviour of hot pressed CoCrMo biomedical alloy as compared with the cast CoCrMo and Ti6Al4V alloys, Mater. Des. 52 (2013) 47–57. doi:10.1016/j.matdes.2013.05.032.

[24] J.I. Silva, A.C. Alves, A.M. Pinto, F. Toptan, Corrosion and tribocorrosion behavior of Ti–TiB–TiNx in-situ hybrid composite synthesized by reactive hot pressing, J. Mech. Behav. Biomed. Mater. 74 (2017) 195–203. doi:10.1016/j.jmbbm.2017.05.041.

[25] M.J. Runa, M.T. Mathew, L.A. Rocha, Tribocorrosion response of the Ti6Al4V alloys commonly used in femoral stems, Tribiology Int. 68 (2013) 85–93. doi:10.1016/j.triboint.2013.09.022.

[26] S. Guo, A. Chu, H. Wu, C. Cai, X. Qu, Effect of sintering processing on microstructure, mechanical properties and corrosion resistance of Ti-24Nb-4Zr-7.9Sn alloy for biomedical applications, J. Alloys Compd. 597 (2014) 211–216. doi:10.1016/j.jallcom.2014.01.087.

[27] B. Sharma, S.K. Vajpai, K. Ameyama, Microstructure and properties of beta Ti-Nb alloy prepared by powder metallurgy route using titanium hydride powder, J. Alloys Compd. 656 (2015) 978–986. doi:10.1016/j.jallcom.2015.10.053.

[28] M. Niinomi, T. Akahori, S. Katsura, K. Yamauchi, M. Ogawa, Mechanical characteristics and microstructure of drawn wire of Ti-29Nb-13Ta-4.6Zr for biomedical applications, Mater. Sci. Eng. C. 27 (2007) 154–161. doi:10.1016/j.msec.2006.04.008.

[29] E. John, An A-Z Guide to The Elements, Oxford Univ. Press. (2001). doi:978-0-19-960563-7.

[30] S. Tamilselvi, N. Rajendran, In vitro corrosion behaviour of Ti-5Al-2Nb-1Ta alloy in Hanks solution, Mater. Corros. 58 (2007) 285–289. doi:10.1002/maco.200604001.

[31] V.A. Alves, R.Q. Reis, I.C.B. Santos, D.G. Souza, T. de, M.A. Pereira-da-Silva, A. Rossi, L.A. da Silva, In situ impedance spectroscopy study of the electrochemical corrosion of Ti and Ti-6Al-4V in simulated body fluid at 25 °C and 37 °C, Corros. Sci. 51 (2009) 2473–2482. doi:10.1016/j.corsci.2009.06.035.

[32] D. Landolt, S. Mischler, M. Stemp, S. Barril, Third body effects and material fluxes in tribocorrosion systems involving a sliding contact, Wear. 256 (2004) 517–524. doi:10.1016/S0043-1648(03)00561-1.

[33] S. Mischler, A. Spiegel, D. Landolt, The role of passive oxide films on the degradation of steel in tribocorrosion systems, Wear. 225–229 (1999) 1078–1087. doi:10.1016/S0043-1648(99)00056-3.

[34] S. Cao, S. Mischler, Modeling tribocorrosion of passive metals – A review, Curr. Opin. Solid State Mater. Sci. (2018) 1–15. doi:10.1016/j.cossms.2018.06.001.

Chapter 4: Degradation behavior of Ti-Nb alloys: Corrosion behavior through 21 days of immersion and tribocorrosion behavior against alumina

Published in Corrossion Science, 167 (2020) 108488.

Degradation behavior of Ti-Nb alloys: Corrosion behavior through 21 days of immersion and tribocorrosion behavior against alumina

I. Çaha[a], A.C. Alves[a], P.A.B. Kuroda[b,c], C.R. Grandini[b,c], A.M.P. Pinto[a,d], L.A. Rocha[b,c], F. Toptan[a,b]

[a] CMEMS-UMinho - Center for MicroElectroMechanical Systems, Universidade do Minho, Azurém, 4800-058 Guimarães, Portugal

[b] IBTN/Br – Brazilan Branch of the Institute of Biomaterials, Tribocorrosion and Nanomedicine, Bauru, SP, Brazil

[c] UNESP—Univ. Estadual Paulista, Faculdade de Ciências de Bauru, Dep. Física, 17033-360 Bauru, SP, Brazil

[d] Universidade do Minho, Dept. Eng. Mecânica, Azurém, 4800-058 Guimarães, Portugal

[*] Corresponding author at: CMEMS-Uminho – Center for MicroElectroMechanical Systems, Universidade do Minho, Azurém, 4800-058 Guimarães, Portugal. Tel.: +351 253 510 220; fax: +351 253 516 007. E-mail: ihsancaha@gmail.com (I. Çaha).

Abstract

Non-toxic and allergic free β-type Ti alloys are attractive metallic implant materials due to their lower Young's modulus and good biocompatibility, but the corrosion and tribocorrosion behavior are yet to be fully understood. In this study, corrosion behavior of Ti-15Nb and Ti-40Nb alloys was investigated and compared with the commercial Ti-6Al-4V alloy through an immersion period of 21 days. The tribocorrosion behavior was investigated under open-circuit potential by using a ball-on-plate tribometer. Results suggested that the β-type Ti-40Nb alloy having 51 GPa Young's modulus had lower corrosion and wear resistance as compared to the α+β-type Ti-15Nb and Ti-6Al-4V alloys.

Keywords: Titanium alloys; Biomaterials; Corrosion; Immersion; Tribocorrosion

4.1. Introduction

Ti and its alloys are the most attractive metallic biomaterials used in biomedical applications due to their high strength, excellent corrosion resistance and favorable biocompatibility. The α+β-type Ti-6Al-4V alloy has been widely used in orthopedic implants, particularly for total hip arthroplasties [1]. However, mostly used α-type and α+β-type Ti based implant materials have Young's modulus around 100-120 GPa, whereas Young's modulus of bone varies in a range of 4-30 GPa [1,2]. The difference between Young's moduli of the implant and bone lead to bone resorption and eventually implant

loosening, so-called stress shielding [3]. The most commonly used material in bone replacement and repair is Ti-6Al-4V alloy, however, the alloying elements present in this alloy raises some clinical concerns such as neurological diseases and cytotoxic effects [4–6]. Therefore, novel Ti based alloys having low Young's modulus and having non-toxic and allergic-free elements are needed for bone and tissue applications [7].

The low Young's modulus Ti alloys have been developed with toxic-free elements, better mechanical properties, good corrosion resistance and excellent biocompatibility, by using β-stabilizing and biocompatible elements such as Nb, Mo, Ta, Zr, especially for orthopedic implant applications. Among these alloys, Ti-Nb based alloys draw a considerable attention for biomedical applications not only due to their non-toxicity, good corrosion behavior and biocompatibility, but also due to the presence of Nb that is reported as favorable for osteogenesis [8], cell adhesion, proliferation, and differentiation *in vitro* [9,10].

The spontaneously formed native passive oxide film on Ti and its alloys not only determines the corrosion resistance and release of metallic ions but also influences the biocompatibility of implants [11]. Accordingly, the corrosion behavior and biocompatibility of β-type Ti-xNb alloys are influenced by Nb stabilizing element in the passive film consisted of a mixture of protective oxides (TiO_2 and Nb_2O_5) [12]. For instance, Han *et al.* [13] reported a higher corrosion resistance for Ti-xNb (x=5, 10, 15, and 20 wt%) alloys as compared to cp-Ti in 9 g/L NaCl solution at body temperature, due to a more protective natural oxide layer. Apart from the structure of the passive film, the microstructure also has an effect on the corrosion behavior [14]. Cremasco *et al.* [15] investigated the effect of water quenching and furnace cooling on the corrosion behavior of Ti-35Nb alloy by electrochemical impedance spectroscopy and potentiodynamic polarization. It was found that water quenching decreased the corrosion performance of the alloy due to its microstructure consisting of acicular martensitic phase. Bai *et al.* [16] studied the corrosion behavior of Ti-xNb (x=45 and 55 wt.%) alloy and commercial Ti-11Mo-6Zr-4Sn alloy in artificial saliva, and with addition of lactic acid and sodium fluoride solution. It was reported that the better corrosion resistance of Ti-xNb alloy over Ti-Mo-Zr-Sn alloy in fluoridated saliva and fluoridated acidified saliva was due to the precipitation of acicular martensitic α″ phase in β phase for Ti-Mo-Zr-Sn alloy. Bai *et al.* [17] investigated the biocompatibility and corrosion behavior of Ti-45Nb alloy and cp-Ti in different solutions (simulated body fluid, modified Fusayama-Meyer artificial saliva, and fluoridated acidified artificial saliva) and found that the Ti-45Nb alloy presented better cell attachment and superior corrosion resistance than Ti due to the nobler behavior of Nb.

Most of the implants are exposed to tribocorrosion that is the degradation of material surfaces due to the simultaneous corrosion and mechanical interactions in a tribological contact [18]. For instance, tribocorrosion observed in hip joints since relative moments occur between femoral head and acetabular cup, as well, between femoral stem and cortical bone in the presence of body fluids [19]. More *et al.* [20] studied the tribocorrosion behavior of Ti-12.5Mo, Ti-13Nb-13Zr and Ti-29Nb-13Ta-4.6Zr β-type titanium alloys and Ti-6Al-4Fe α+β-type Ti alloy under open circuit potential (OCP) and passive applied potential against ultra-high molecular weight polyethylene in Hank's balanced salt solution. The authors showed that the polyethylene presented low wear against β-type alloys and β-type alloys exhibited repassivation even during sliding, at passive potential and OCP.

Surface degradation of implants is one of the most important drawbacks for long-term implantation in the human body. In the last decade, many efforts have been spent for the development β-type Ti alloys, but the degradation behavior of these alloys are yet to be fully understood. Therefore, the present work aimed at studying the degradation behavior of Ti-15Nb and Ti-40Nb alloys in a simple physiological solution at body temperature, in comparison with Ti-6Al-4V as the most popular Ti alloy, by performing corrosion tests during prolonged times of immersion (up to 21 days), as well, by performing tribocorrosion tests against a hard and inert counter material.

4.2. Experimental procedure

4.2.1. Materials and processing

The raw materials used to produce alloys were cp-Ti (99.7% purity, Sandinox Biometais, Brazil) and Nb (99.8% purity, Brazilian Metallurgy and Mining Company). In order to remove superficial impurities, Ti and Nb raw materials were chemically cleaned in an HNO_3:HF (4:1) and HNO_3:HF:H_2O (2:2:1) solutions respectively. After chemical cleaning, the materials were immersed in acetone and cleaned in an ultrasonic bath for 20 minutes. These metals were melted by using an arc-melting furnace with water cooled copper crucible, non-consumable tungsten electrode under controlled atmosphere of argon. After that, the samples were subjected to heat treatment (1000 °C/24 h) in an ultra-vacuum furnace for homogenization. Then, the ingots with 15 wt.% and 40 wt.% of Nb were obtained by a hot-rolling process at 900 °C. After the hot-rolling, the samples were submitted to a new heat treatment of 8 hours in vacuum to relieve the residual stress resulted from the machining procedure. In order to compare the results, commercial Ti-6Al-4V (VSMPO Tirus, US, ASTM B348, Grade 5) alloy was used in all tests.

Before microstructural characterization and microhardness measurements, samples were grinded down to 2400 mesh SiC paper, polished with colloidal silica suspension (Buehler, 0.02 μm) for 5 min in polishing machine (Aropol-2v, Arotec), and afterwards, etched with Kroll's reagent (%3 HF + %6 HNO_3 + %91 H_2O). For corrosion and tribocorrosion tests, samples were grinded with SiC papers down to 1200 mesh then cleaned in propanol and in distilled water for 10 min and 5 min respectively in ultrasonic bath. Before starting each test, samples were stored in a desiccator for 1 day.

4.2.2. Corrosion and tribocorrosion tests

Corrosion tests included of OCP measurements, potentiodynamic polarization and electrochemical impedance spectroscopy (EIS) were employed on 1.0 cm^2 of exposed area in 200 mL of saline solution (9 g/L NaCl) using Gamry Potentiostat/Galvanostat (model Reference-600+). A saturated calomel electrode (SCE) was used as reference electrode (RE), a Pt electrode was used as the counter electrode (CE) and the samples were used as working electrode (WE). Prior to potentiodynamic polarization, OCP employed till stabilization of native oxide film ($\Delta E < 60$ mV vs. SCE) and afterwards, the polarization scan was performed with 0.5 mV/s scan rate, starting at –0.25 V_{OCP} up to 1.5 V_{SCE}. EIS measurements were performed after 4 h, 1 day, 2 days, 4 days, 8 days, 16 days, and 21 days of immersion. Gamry Echem Analyst software was used for fitting the raw data and the quality of the proposed the electrical equivalent circuit (EEC) was evaluated by the goodness of fitting (χ^2). The potential of each sample was monitored during 30 min in test solution before each EIS measurement. The EIS measurements at OCP was carried out with a 10 mV of sinusoidal amplitude by scanning a range of frequencies from 10^5 Hz to 10^2 Hz with counting 7 points per frequency decade.

Tribocorrosion tests were performed at body temperature in saline (9 g/L NaCl) electrolyte using a tribometer (CETR-UMT-2) with pin-on-plate reciprocating sliding configuration. A two-electrode set-up was used where the samples were placed as WE against an alumina ball (10 mm in diameter, Ceratec) using a Gamry Potentiostat/Galvanostat/ZRA (model Reference-600). The tests were carried out under a reciprocating sliding frequency of 1 Hz, normal load of 1 N corresponding to maximum Hertzian contact pressures of 0.37 GPa, 0.27, and 0.42 GPa for Ti-15Nb, Ti-40Nb, and Ti-6Al-4V alloys respectively, and amplitude of 3 mm. Sliding started after stabilization of OCP ($\Delta E < 60$ mV vs. SCE) and continued during 30 min. Afterwards, the counter material was removed and OCP recorded for further 20 min in order to observe the repassivation.

All corrosion and tribocorrosion tests were triplicated on three different samples and all results were presented as the arithmetic mean ± standard deviation.

4.2.3. Characterization

Microstructures and chemical compositions were analyzed by optical microscope (Leica, DM2500), scanning electron microscope (SEM, EVO LS15 Carl Zeiss, with software SmartSEM), equipped with X-ray energy dispersive spectroscopy (EDS). Structural characterization of Ti-Nb alloys was performed by X-ray diffraction (XRD, DMAX-2100, Rigaku) and the quantification of phases estimated through the Rietveld's method by using the General Analyzer System Structure (GSAS) [22]. Vickers microhardness were determined by 5 identations performed randomly per sample using an Emcotest Durascan tester at a load of 9.8 N (1 kgf) during 15 s. The measurements of the elastic modulus were carried out in a dynamic manner using the Sonelastic® equipment (ATCP) based on ASTM-E1876 standard from 10 measurements, using the technique of excitation by impulse, with the samples placed in flexural vibration.

After each tribocorrosion test, the samples were cleaned by an ultrasonic bath in propanol and in distilled water for 10 min and 5 min respectively. The worn surfaces and collected wear debris were investigated by using FEG-SEM (FEI Nova 200) with backscattered (BSE) and secondary electron (SE) configuration, and analyzed with EDS. The total wear volume loss was determined by following the calculation procedure given elsewhere [21] through wear track profiles obtained by a surface profiler (Veeco, Dektak 150).

4.3. Results and discussion

4.3.1. Microstructural and mechanical characterization

Microstructural analysis revealed a homogenous distribution of Nb in both alloys, without any segregations (Figs. 4.1a and 4.1b). Nevertheless, the amount of Nb in Ti matrix significantly affected the microstructure. XRD pattern (Figs. 4.1c and 4.1d) revealed that while Ti-15Nb alloy is composed of hexagonal-Ti (α-Ti) and body centered cubic-Ti (β-Ti) phases, which is composed by 56% α-Ti - 44% β-Ti, while 100% β-Ti was calculated for the Ti-40Nb alloy. Microstructural analysis revealed typical Widmanstätten α+β structure for the Ti-15Nb alloy (Fig. 4.1e), whereas the Ti-40Nb alloy exhibited single-phase β microstructure (Fig. 4.1f). These microstructural differences also affected the mechanical properties, resulting with in a slight increase on hardness from the Ti-15Nb to the Ti-40Nb (249 ± 3 and 262 ± 5 $HV_{0.3}$, respectively) together with a significant decrease on the Young's modulus (88 ± 1 for the Ti15Nb and 51 ± 1 GPa for the Ti-40Nb). For comparison, it is worth to note that the hardness of the commercial Ti-6Al-4V alloy is 350 ± 5 $HV_{0.3}$, and its Young's modulus is known from the literature to be 112 GPa [1].

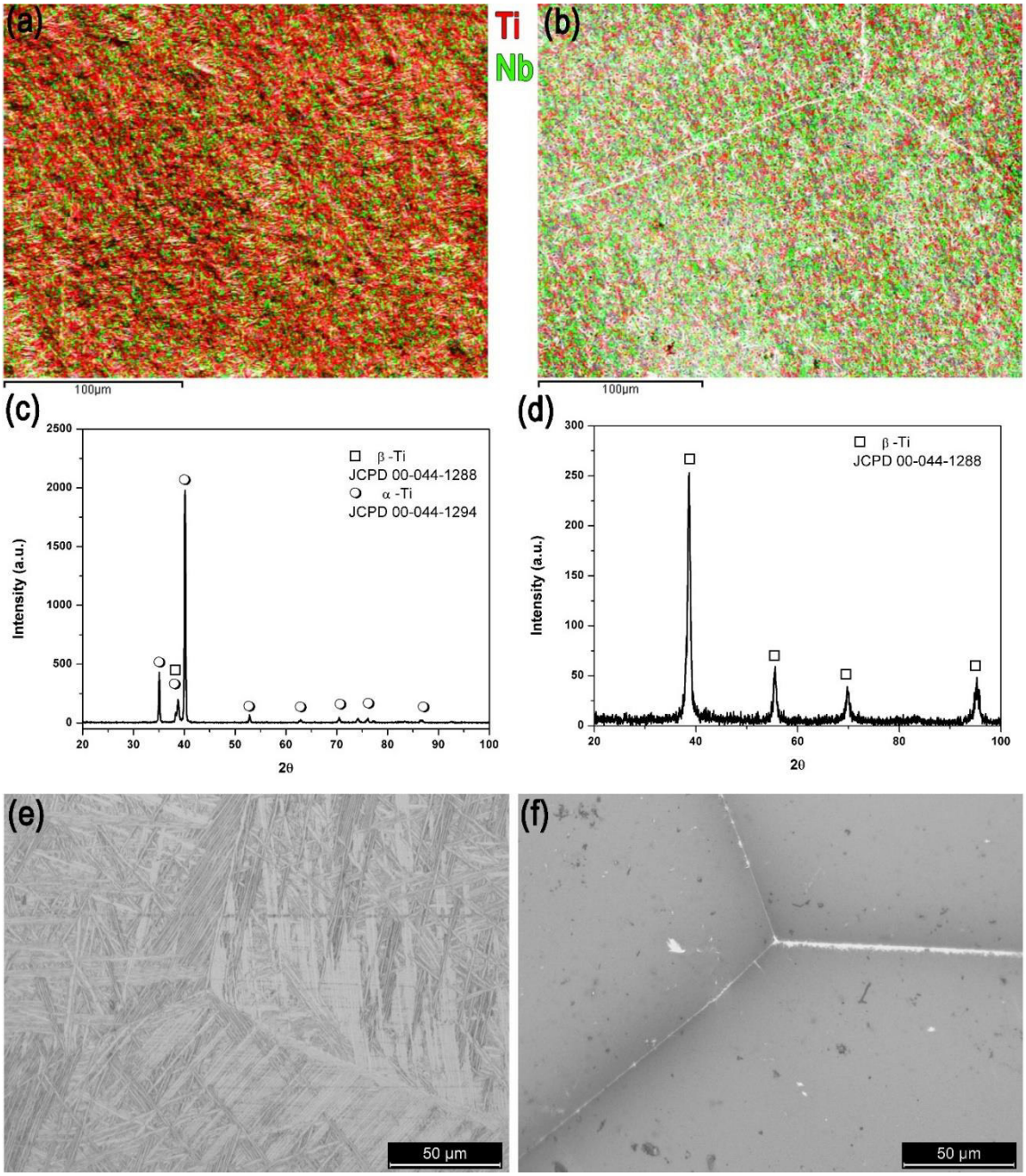

Fig. 4.1. EDS mapping (a, b), XRD pattern (c,d), and OM images (e, f) of Ti-15Nb and Ti-40Nb alloys respectively.

4.3.2. Corrosion behavior

Representative results of the potentiodynamic polarization tests are plotted in Fig. 4.2, together with a table depicting the corrosion potential ($E_{(i=0)}$) and the passivation current density (i_{pass}) at 0.5 V_{SCE}. A well-defined passivation plateau was observed for all alloys. The i_{pass} for the Ti-6Al-4V and Ti-15Nb were very similar and lower than the ones observed for the Ti-40Nb.

The corrosion behavior of passive materials is determined by the nature of the passive film spontaneously created on their surfaces. For Ti-Nb alloys it is reported that the passive film can be composed of TiO_2 and Nb_2O_5, while TiO_2, Al_2O_3, and V_2O_5 were found in the passive film of the Ti-6Al-4V alloy [23,24]. Nevertheless, the relative ratio of oxides is strongly dependent of the formation conditions and environmental history [24]. The Ti-15Nb and Ti-6Al-4V alloys presented very similar potentiodynamic polarization curves, whereas the curve of Ti-40Nb shifted slightly to the right indicating relatively accelerated kinetics. The i_{pass} values observed in this work are in accordance with those found by Gostin et al. [25] and Pilz et al. [12], who studied the potentiodynamic polarization of alloys in Ringer's solution and Tris-buffered saline (pH 7.6), respectively, where lower i_{pass} values were reported for the Ti-6Al-4V alloy than the Ti-40Nb alloy. However, an opposite trend was reported by Yilmaz *et al.* [26] after evaluating the corrosion behavior of powder injection molded α+β-type Ti-16Nb and Ti-40Nb alloys (mostly β phase but it was included a small amount of α phase) in simulated body fluid by using potentiodynamic polarization curves. The authors reported that the increased amount of Nb resulted with lower anodic current density values that was linked to the presence of Nb_2O_5 on the passive film that was indicated as more stable as compared to Al_2O_3 and V_2O_5 oxide compounds. These controversial results reported in the literature points that the effect of the nature of the passive film and the microstructure on the corrosion behavior of Ti-Nb alloys requires further electrochemical analysis.

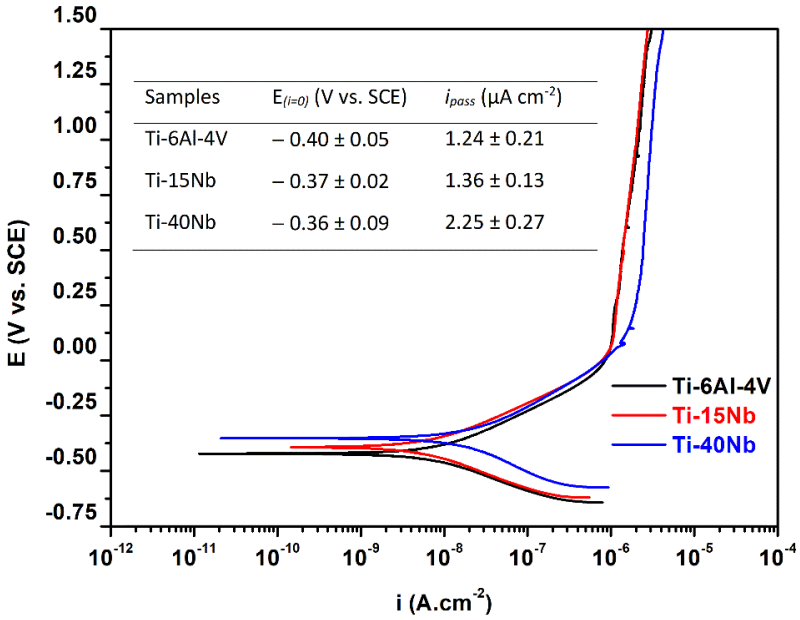

Fig. 4.2. Representative potentiodynamic polarization curves.

The evolution of OCP through immersion time for the Ti-6Al-4V, Ti-15Nb, and Ti-40Nb alloys is presented in Fig. 4.3. The OCP values increased during the first 192 h (8 days) for all alloys, reaching

similar electrochemical potentials (close to 0 V vs. SCE). Afterwards the values of Ti-15Nb and Ti-40Nb were remained relatively stable while the electrochemical potential of the Ti-6Al-4V alloy slightly increased reaching approximately 0.1 V_{SCE} at the end of the immersion period. The increase of OCP indicates a decrease in reactivity of the alloys and is usually associated with the thickening of the passive film in contact with the electrolyte, and/or to changes in the composition and structure of the passive film [23,27].

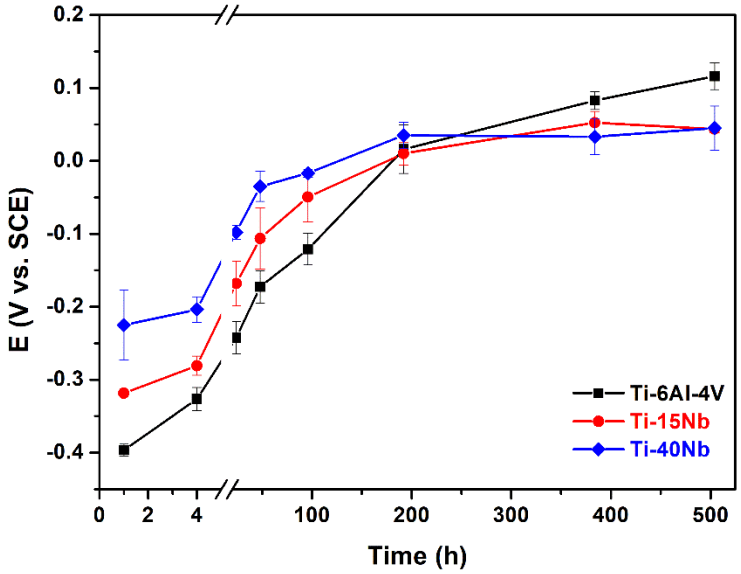

Fig. 4.3. Evolution of OCP during 21 days in 9 g/L NaCl.

The Bode diagrams of EIS spectra for 4 h, 2 days, 8 days, and 21 days of immersion are given in Fig. 4.4, together with the EEC used for simulation of the experimental data, representing a naturally formed oxide layer on the surface. All alloys presented the goodness of fitting below the 10^{-4} indicated a perfect agreement between the experimental data and the proposed EEC. At low and middle frequencies (10^{2} – 10^{2} Hz), the phase angle values of all samples were close to –90° indicating a capacitive behavior of a compact layer whereas the constant |Z| values near 0° at high frequencies (10^{2} – 10^{5} Hz) presents the response of the electrolyte resistance.

Regarding the EEC, R_e is the electrolyte resistance, R_{ox} is the resistance of the native oxide film, and Q_{ox} is the constant phase element (CPE) indicating the deviation from an ideal capacitive behavior. The impedance of a CPE is given as $Z_{CPE} = [Y_0(jw)^n]^{-1}$, where Y_0 is CPE admittance in $\Omega^{-1}s^n cm^{-2}$ units, $j = \sqrt{-1}$ is the imaginary unit, $w = 2\pi f$ is the angular frequency in rad/s, and n is dimensionless number. The n values varies in $-1 \leq n \leq 1$ range and the CPE indicates an inductor, a resistor, and a capacitor behavior when $n = -1$, $n = 0$, and $n = 1$, respectively. The n value about

1 presents a non-deal capacitor behavior by CPE where it is related to a non-uniform current distribution due to the surface roughness and inhomogeneity.

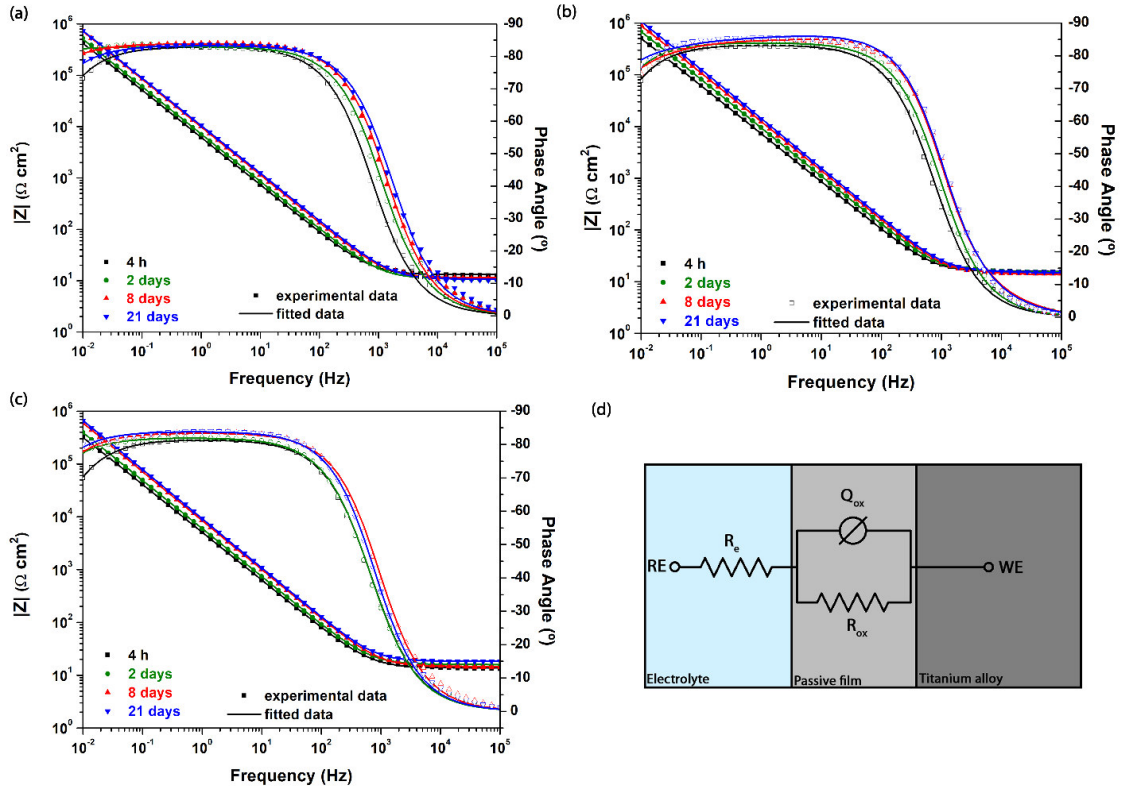

Fig. 4.4. Bode diagrams of a) Ti-6Al-4V, b) Ti-15Nb, and c) Ti-40Nb alloys in 9 g/L NaCl solution for different immersion times, together with d) the proposed EEC.

Fig. 4.5 presents the R_{ox} and Q_{ox} evolution as function of immersion time. After 4 h of immersion, the average R_{ox} values were similar for all alloys. However, R_{ox} increased after 4h, where the increase was more noticeable on Ti-6Al-4V alloy. On the other hand, Q_{ox} values decreased during the immersion time where Ti-15Nb alloy presented lower values as compared to the other alloys. As it is known, Q_{ox} is directly proportional to C_{ox} (capacitance of the natural oxide film), which is defined by $C = \frac{\varepsilon_0 \varepsilon_r A}{d}$, where ε_o is the vacuum primitivity ($\varepsilon_0 \approx 8.9\text{x}10^{-14} Fcm^{-1}$), ε_r is dielectric constant number, A is the exposure area, and d is the thickness of the oxide layer [28]. Therefore, the decrease on Q_{ox} during the immersion period may be linked with the thickening of the passive film, indicating an improvement on its quality [29].

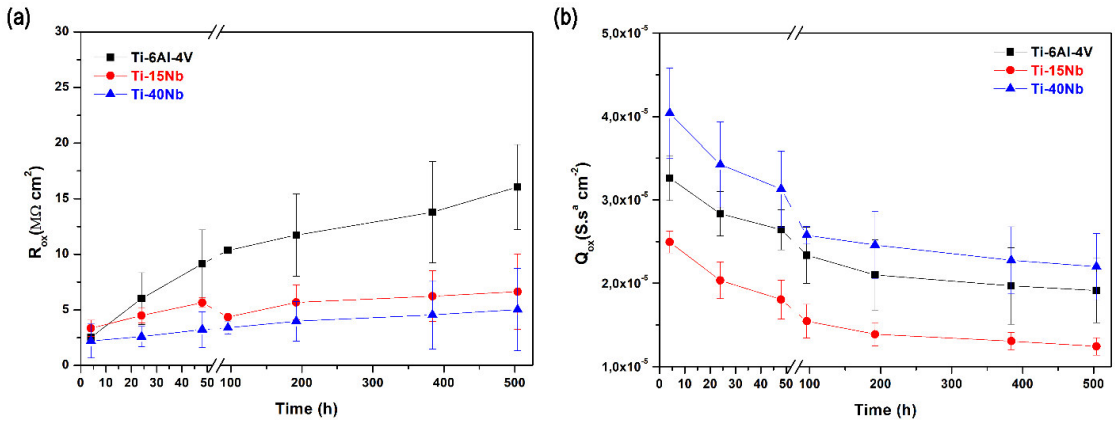

Fig. 4.5. Evolution of R_{ox} and Q_{ox} with immersion time.

The increase of R_{ox} for all alloys with the immersion period shows that the natural oxide film formed on the alloys became more resistive. The variations in the R_{ox} may be linked to the structural changes in the oxide layer and/or changes in the ionic or electrical conductivity of the oxide layer that may happen during the immersion period [30]. The average R_{ox} value of Ti-6Al-4V alloy was higher than that of the Ti-xNb alloys after 21 days of immersion, while the Q_{ox} values of the Ti-6Al-4V alloy evolved in between the values of Ti-15Nb and Ti-40Nb alloys. Normally, higher R_{ox} of Ti-6Al-4V is expected to give lower Q_{ox} value. This contradiction behavior of the Ti-6Al-4V alloy may be linked with the structure of the oxide film. It had been suggested in the literature that the oxide film naturally formed on the Ti-6Al-4V alloy surface is mainly composed by titanium oxides (mainly at the metal/oxide interface), however at the oxide/electrolyte interface this layer also contains aluminum oxides, along with vanadium oxides [31]. Metikoš-Huković *et al.* [32] stated that V is able to diffuse up to the Ti-6Al-4V alloy surface leading to the formation of V_2O_5 and other suboxides at the outermost surface. Moreover, vanadium oxide dissolution causes generation of vacancies in the oxide film [30,32]. However, these oxides are not as protective as TiO_2 films, thus the presence of these oxides leads to lower general quality of the passive film formed on Ti-6Al-4V alloy, particularly with the presence of chloride ions in the solution. This mechanism can also be understood by observing the variation of Q_{ox} values. While the all tested alloys showed similar trend with immersion time, the Ti-6Al-4V alloy presents higher values compared to Ti-15Nb that may be explained by the dissolution of vanadium and aluminum oxides. Cordeiro *et al.* [33] studied the corrosion behavior of Ti-Zr and Ti-Nb-Zr alloys in comparison with Ti and Ti-6Al-4V by using potentiodynamic polarization and EIS in SBF solution. The authors reported a higher corrosion resistance for α+β-type Ti-6Al-4V alloy than β-type Ti-35Nb-10Zr alloy and linked the difference with the less protective behavior of the passive film formed on β phase, as well as the higher hardness of Ti-6Al-4V alloy, that gave a better support to the oxide layer. This favorable effect of the hardness had also previously been reported

by Cvijović-Alagić *et al.* [31] for Ti-6Al-4V and Ti-13Nb-13Zr alloys where higher hardness of the Ti–6Al–4V alloy reported to support a thicker and more firmly adhered oxide layer as compared to a softer one. Regarding Ti-Nb alloys, lower Q_{ox} values of Ti-15Nb than Ti-40Nb alloy indicates the formation of a thicker and higher quality of oxide film, that requires further investigation particularly regarding its structure.

4.3.3. Tribocorrosion behavior

4.3.3.1. Worn surface analysis

In order to have an understanding on the tribocorrosion mechanism, worn surfaces and wear debris were characterized by SEM/EDS. Fig. 4.6 shows the wear track surfaces where parallel ploughing grooves and adhered/oxidized patches can be observed on all alloys. The fine aligned grooves indicated that abrasive wear occurred for all tested samples. Relatively denser oxidized patches were observed on Ti-6Al-4V surfaces as compared to both Ti-Nb alloys, as evidenced on the BSE images, that may be related with the higher hardness of the Ti-6Al-4V alloy that gave a better support to those patches, as previously explained by Lee *et al.* [34] on the wear behavior of β-type Ti-29Nb-13Ta-4.6Zr and α+β-type Ti-6Al-4V alloys. On the other hand, Ti-6Al-4V produced finer and more regular blocky debris, whereas flake-like wear debris were observed on the Ti-Nb alloys. Moreover, the EDS spectra taken from the debris produced on Ti-6Al-4V exhibited higher oxygen peak compared to the ones obtained on Ti-Nb alloys. SEM images of the wear scars together with detached pieces from samples (insert images) on alumina ball and the EDS taken from the worn area are given in Fig. 4.6. EDS spectra suggested that material from the samples was transferred to the ball, clearly indicating the adhesive wear, that appeared to happen more on Ti-Nb alloys than Ti-6Al-4V alloy. The wear scar on the alumina ball slid against the Ti-40Nb alloy was relatively larger than the wear scar against the Ti-15Nb alloy, while the smallest wear scar was obtained ball slid against the Ti-6Al-4V alloy.

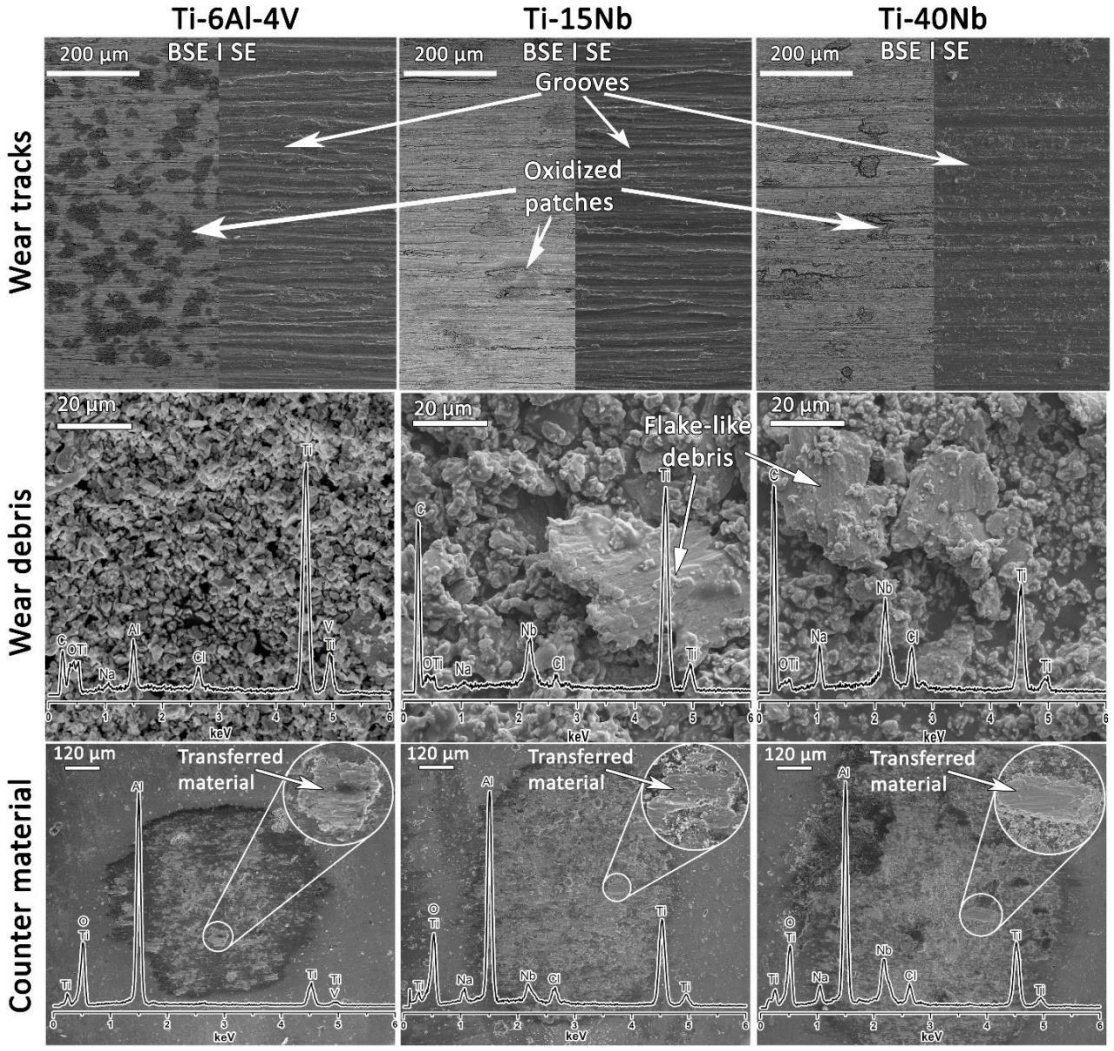

Fig. 4.6. SE and BSE-SEM wear track images, SE-SEM wear debris images together with corresponding EDS spectra, and wear scar images of counter material together with corresponding EDS spectra for Ti-6Al-4V, Ti-15Nb, and Ti-40Nb.

Total wear volume loss and hardness of Ti-6Al-4V, Ti-15Nb, and Ti-40Nb alloy measured outside and inside the wear tracks are given in Table 4.1. The Ti-6Al-4V alloy presented significantly lower wear volume loss than both Ti-Nb alloys. Hardness of both Ti-Nb alloys did not vary significantly between the measurements taken on the worn and unworn surfaces whereas the hardness of Ti-6Al-4V alloy was significantly higher on the wear tracks. In addition to work hardening and the formation of the oxide patches, the plastic deformation at the subsurface of the wear track may led to lower wear volume loss for Ti-6Al-4V alloy. Fig. 4.7 shows BSE images of the subsurface of the wear track for all samples. A clear deformation zone was observed at the subsurface of Ti-6Al-4V alloy, while it was not observed evidences of deformation for both Ti-Nb alloys. It may be assumed that the higher stress level during sliding tended to produce a greater amount of dislocations in the subsurface zone and therefore led to a higher

hardness. This subsurface deformation on Ti-6Al-4V wear track accompanied by strain hardening improved the resistance against wear. While Ti-6Al-4V and Ti-15Nb alloys were composed of α+β phase, the higher wear volume loss values of Ti-15Nb alloy can be explained by its lower hardness value and lack of strain hardening resulted from its microstructure. Significantly higher wear volume loss of Ti-40Nb alloy may be explained by the elevated contribution of delamination wear as evidenced by relatively rougher wear track surface and subsurface cracks (insert Fig. 4.7c). In delamination wear mechanism [35], it is assumed that the contact asperities have an increased plastic deformation during the relative movement, which accumulates during repetitive interactions. When the accumulated strain reaches a critical level, the subsurface cracks are nucleated below the wear track. When the crack becomes large enough, it fractures to yield flake-like debris (delamination). The similar subsurface cracks and flake-like wear debris behavior were reported by Lee *et al.* [36] for β-type Ti-29Nb-13Ta-4.6Zr alloy that tested in Ringer's solution and air explained by dominantly adhesive and delamination wear mechanisms.

Table 4.1. Wear volume loss and hardness of samples outside and inside wear tracks.

Samples	Wear volume loss	Hardness (HV_1)	
	(mm^3)	Outside wear track	Inside wear track
Ti-6Al-4V	0.006 ± 0.001	350 ± 8	423 ± 26
Ti-15Nb	0.016 ± 0.003	251 ± 7	269 ± 10
Ti-40Nb	0.041 ± 0.004	258 ± 8	265 ± 16

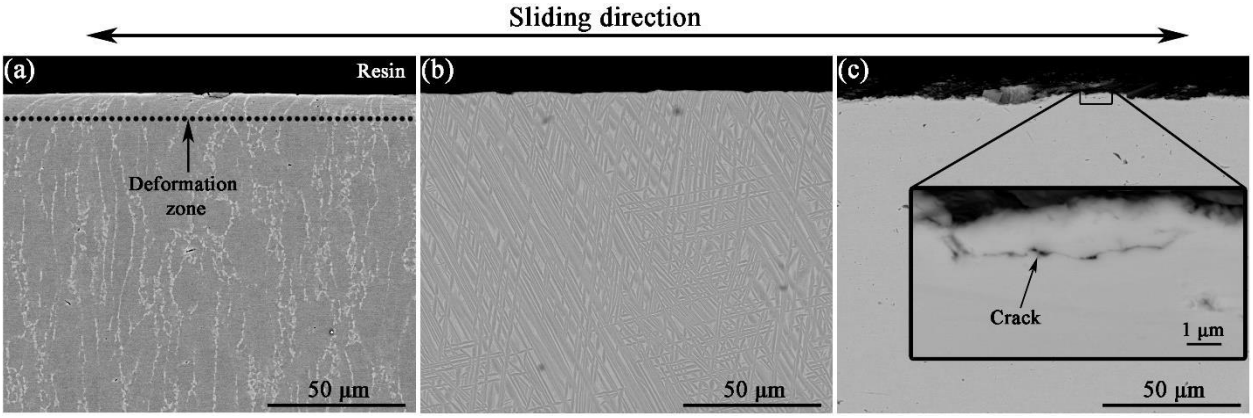

Fig. 4.7. Cross-sectional BSE SEM images of wear tracks parallel to the sliding direction for (a) Ti-6Al-4V, (b) Ti-15Nb, and (c) Ti-40Nb.

According to Archard's law, the wear volume loss of Ti-6Al-4V and Ti-Nb alloys should be correlated with their hardness [37]. However, this assumption does not take into account the role of

hardening and oxides formation during sliding [38]. For instance, Yang *et al.* [39] studied the tribocorrosion behavior β-type Ti-12Mo-6Zr-2Fe alloy and α+β-type Ti-6Al-4V alloy in SBF and reported much higher wear volume loss values for Ti-12Mo-6Zr-2Fe alloy as compared to Ti-6Al-4V alloy. The authors suggested that elevated wear volume loss was due to lack of strain hardening on β-type Ti alloys, that may also be the reason for more severe wear on fully β-type Ti-40Nb alloy observed in the present study.

4.3.3.2. Tribocorrosion analysis

The monitored OCP and coefficient of friction (COF) is given in Fig. 4.8. When sliding started, all alloys presented a sudden decrease on potentials (cathodic shift) because of the mechanical damage given to the passive oxide film, showing an increase on the tendency to corrosion [20,40–42]. Afterwards, the potential values were slightly increased and then exhibited a steady state with oscillations resulting from repetitive repassivation-depassivation actions. When the sliding stopped, the OCP values were immediately increased close to the values observed before sliding due to the repassivation of the worn areas [20,40–42]. As can be seen on Fig. 4.8, no significant difference was obtained on the evolution of OCP between the testing alloys.

Regarding the evolution of COF, relatively stable values were observed during all sliding period, having average values of 0.38 ± 0.04, 0.45 ± 0.01, and 0.69 ± 0.02 for Ti-6Al-4V, Ti-15Nb, and Ti-40Nb alloys respectively. The higher COF of the Ti-40Nb alloy than those of the α+β-type Ti-15Nb and Ti-6Al-4V alloys may be linked with the elevated influence of the delamination wear and consequently, increased formation of flake-like wear debris. On the other hand, the formation of oxidized patches can significantly affect the COF values due to reduced contact between metal and counter material [43] that can explain the relatively lower COF values for the Ti-6Al-4V alloy (Fig. 4.6). Denser oxidized patches observed on the worn Ti-6Al-4V alloy surfaces may be explained by the higher hardness value of this alloy, since, as reported by Cvijović-Alagić *et al.* [31], the harder material is able to hold a thicker oxide layer more uniformly as compared to a softer material. Therefore, while the OCP evolution of both Ti-Nb alloy were similar, COF values were significantly affected by their microstructures.

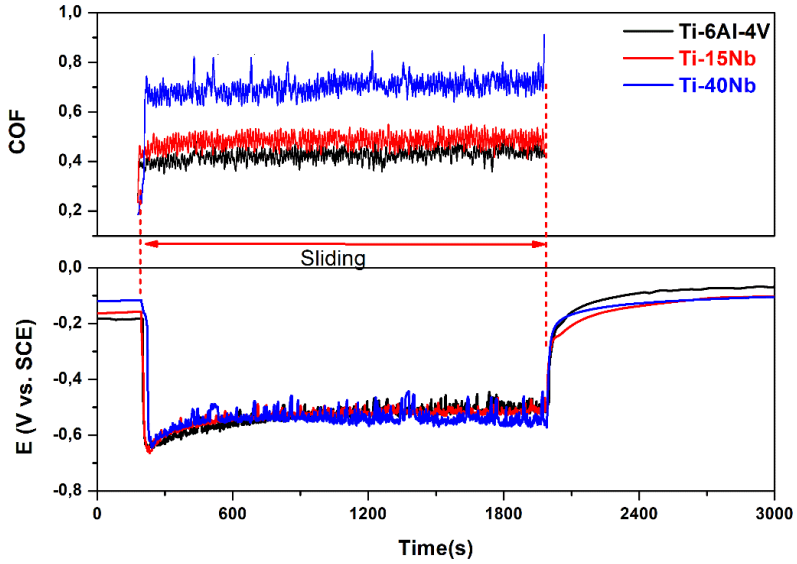

Fig. 4.8. OCP and COF evaluation of alloys in saline solution.

4.3.3.3. Tribocorrosion mechanism

The wear process usually involves more than one simultaneous wear mechanism [44]. Fig. 4.9 schematically show the wear mechanism suggested for Ti-6Al-4V, Ti-15Nb and Ti-40Nb alloys. Abrasive and adhesive wear mechanisms were observed for all alloys although adhesive wear was more evident for Ti-Nb alloys. Also, the worn region of the Ti-6Al-4V alloy was characterized by a discontinuous tribolayer and subsurface plastic deformation. Finally, although both Ti-Nb alloys exhibited similar worn surface features, the Ti-40Nb alloy presented significantly higher wear loss and higher COF values, linked with formation of a more severe delamination wear, evidenced by elevated formation of subsurface cracks and flake-like wear debris.

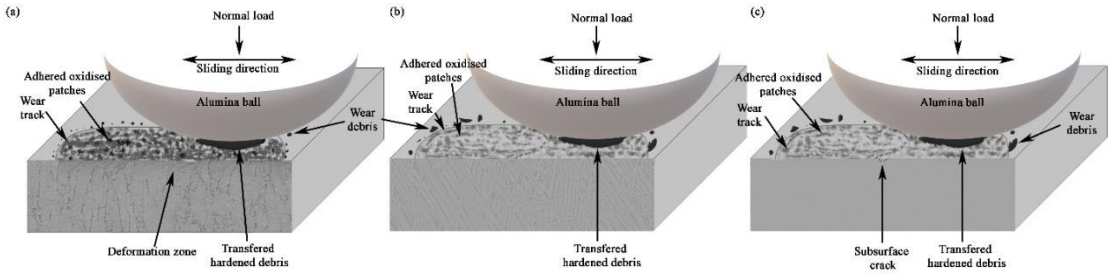

Fig. 4.9. Schematic illustration of wear mechanism of (a) Ti-6Al-4V (b) Ti-15Nb, and (c) Ti-Nb alloys.

4.4. Conclusion

Corrosion and tribocorrosion behavior of α+β-type Ti-15Nb and β-type Ti-40Nb alloys were investigated in compared with the commercial Ti-6Al-4V alloy. Although β-type Ti-40Nb alloy appears to

be promising for osseointegrated implants, due to its lower Young's modulus (51 GPa), it exhibited lower corrosion resistance evidenced by lower resistance of the native oxide film and higher values of constant phase element through all immersion period suggestion a difference on the thickness and quality of the film. Ti-40Nb alloy also exhibited lower resistance to tribocorrosion particularly due to elevated influence of delamination wear. Therefore, these results showed that corrosion and tribocorrosion behavior of β-type Ti alloys should carefully be investigated and when necessary, suitable surface modification techniques should be considered before using them in load-bearing implant applications.

Acknowledgements

This work is supported by FCT with the reference project UID/EEA/04436/2019 and M-ERA-NET/0001/2015 (FAPESP proc. #2015/50.280-5), CNPq (307.279/2013-8) and FAPESP (2015/09.480-0). The authors would also like to acknowledge Prof. Graça Minas for the provision of the profilometry. I. Çaha is grateful for financial support through PhD grant under NORTE-08-5369-FSE-000012 project.

References

[1] M. Geetha, A.K. Singh, R. Asokamani, A.K. Gogia, Ti based biomaterials, the ultimate choice for orthopaedic implants - A review, Prog. Mater. Sci. 54 (2009) 397–425. doi:10.1016/j.pmatsci.2008.06.004.

[2] K. Miura, N. Yamada, S. Hanada, T.K. Jung, E. Itoi, The bone tissue compatibility of a new Ti-Nb-Sn alloy with a low Young's modulus, Acta Biomater. 7 (2011) 2320–2326. doi:10.1016/j.actbio.2011.02.008.

[3] A. Panigrahi, B. Sulkowski, T. Waitz, K. Ozaltin, W. Chrominski, A. Pukenas, J. Horky, M. Lewandowska, W. Skrotzki, M. Zehetbauer, Mechanical properties, structural and texture evolution of biocompatible Ti–45Nb alloy processed by severe plastic deformation, J. Mech. Behav. Biomed. Mater. 62 (2016) 93–105. doi:10.1016/j.jmbbm.2016.04.042.

[4] J.A. Davidson, A.K. Mishra, P. Kovacs, R.A. Poggie, New surface-hardened, low-modulus, corrosion-resistant Ti-13Nb-13Zr alloy for total hip arthroplasty, Biomed. Mater. Eng. 4 (1994) 231–243. doi:10.3233/BME-1994-4310.

[5] Y. Okazaki, E. Gotoh, Comparison of metal release from various metallic biomaterials in vitro, Biomaterials. 26 (2005) 11–21. doi:10.1016/j.biomaterials.2004.02.005.

[6] Y. Okazaki, Cytocompatibility of Various Metals and Development of New Titanium Alloy for Medical Implant., Mater. Sci. Eng. A. 243 (1988) 250–256. doi:10.2320/materia.37.838.

[7] M. Niinomi, M. Nakai, J. Hieda, Development of new metallic alloys for biomedical applications, Acta Biomater. 8 (2012) 3888–3903. doi:10.1016/j.actbio.2012.06.037.

[8] H. Matsuno, A. Yokoyama, F. Watari, M. Uo, T. Kawasaki, Biocompatibility and osteogenesis of refractory metal implants, titanium, hafnium, niobium, tantalum and rhenium, Biomaterials. 22 (2001) 1253–1262. doi:10.1016/S0142-9612(00)00275-1.

[9] E. Eisenbarth, D. Velten, M. Müller, R. Thull, J. Breme, Nanostructured niobium oxide coatings influence osteoblast adhesion, J. Biomed. Mater. Res. - Part A. 79 (2006) 166–175. doi:10.1002/jbm.a.30823.

[10] M. Kushwaha, X. Pan, J.A. Holloway, I.L. Denry, Differentiation of human mesenchymal stem cells on niobium-doped fluorapatite glass-ceramics, Dent. Mater. 28 (2012) 252–260. doi:10.1016/j.dental.2011.10.010.

[11] A. Revathi, A. Dalmau, A. Igual, C. Richard, G. Manivasagam, Degradation mechanisms and future challenges of titanium and its alloys for dental implant applications in oral environment, Mater. Sci. Eng. C. (2017). doi:10.1016/j.msec.2017.02.159.

[12] S. Pilz, A. Gebert, A. Voss, S. Oswald, M. Göttlicher, U. Hempel, J. Eckert, M. Rohnke, J. Janek, M. Calin, Metal release and cell biological compatibility of beta-type Ti-40Nb containing indium, J. Biomed. Mater. Res. - Part B Appl. Biomater. (2017) 1686–1697. doi:10.1002/jbm.b.33976.

[13] M.K. Han, J.Y. Kim, M.J. Hwang, H.J. Song, Y.J. Park, Effect of Nb on the microstructure, mechanical properties, corrosion behavior, and cytotoxicity of Ti-Nb alloys, Materials (Basel). 8 (2015) 5986–6003. doi:10.3390/ma8095287.

[14] F. Toptan, A.C. Alves, Ó. Carvalho, F. Bartolomeu, A.M.P. Pinto, F. Silva, G. Miranda, Corrosion and tribocorrosion behaviour of Ti6Al4V produced by selective laser melting and hot pressing in comparison with the commercial alloy, J. Mater. Process. Technol. 266 (2019) 239–245. doi:10.1016/j.jmatprotec.2018.11.008.

[15] A. Cremasco, W.R. Osório, C.M.A. Freire, A. Garcia, R. Caram, Electrochemical corrosion behavior of a Ti-35Nb alloy for medical prostheses, Electrochim. Acta. 53 (2008) 4867–4874. doi:10.1016/j.electacta.2008.02.011.

[16] Y.J. Bai, Y.B. Wang, Y. Cheng, F. Deng, Y.F. Zheng, S.C. Wei, Comparative study on the corrosion behavior of Ti-Nb and TMA alloys for dental application in various artificial solutions, Mater. Sci. Eng. C. 31 (2011) 702–711. doi:10.1016/j.msec.2010.12.010.

[17] Y. Bai, Y. Deng, Y. Zheng, Y. Li, R. Zhang, Y. Lv, Q. Zhao, S. Wei, Characterization, corrosion behavior, cellular response and in vivo bone tissue compatibility of titanium-niobium alloy with low Young's modulus, Mater. Sci. Eng. C. 59 (2016) 565–576. doi:10.1016/j.msec.2015.10.062.

[18] F. Galliano, E. Galvanetto, S. Mischler, D. Landolt, Tribocorrosion behavior of plasma nitrided Ti-6Al-4V alloy in neutral NaCl solution, Surf. Coatings Technol. 145 (2001) 121–131. doi:10.1016/S0257-8972(01)01309-3.

[19] N. Diomidis, S. Mischler, N.S. More, M. Roy, Tribo-electrochemical characterization of metallic biomaterials for total joint replacement, Acta Biomater. 8 (2012) 852–859. doi:10.1016/j.actbio.2011.09.034.

[20] N.S. More, N. Diomidis, S.N. Paul, M. Roy, S. Mischler, Tribocorrosion behavior of β titanium alloys in physiological solutions containing synovial components, Mater. Sci. Eng. C. 31 (2011) 400–408. doi:10.1016/j.msec.2010.10.021.

[21] Z. Doni, A.C. Alves, F. Toptan, J.R. Gomes, A. Ramalho, M. Buciumeanu, L. Palaghian, F.S. Silva, Dry sliding and tribocorrosion behaviour of hot pressed CoCrMo biomedical alloy as compared with the cast CoCrMo and Ti6Al4V alloys, Mater. Des. 52 (2013) 47–57. doi:10.1016/j.matdes.2013.05.032.

[22] R. Von Dreele, A. Larson, General structure analysis system (GSAS), Los Alamos Natl. Lab. Rep. LAUR. (2000). doi:10.1103/PhysRevLett.101.107006.

[23] A. Gebert, S. Oswald, A. Helth, A. Voss, P.F. Gostin, M. Rohnke, J. Janek, M. Calin, J. Eckert, Effect of indium (In) on corrosion and passivity of a beta-type Ti-Nb alloy in Ringer's solution, Appl. Surf. Sci. 335 (2015) 213–222. doi:10.1016/j.apsusc.2015.02.058.

[24] A.L.R. Ribeiro, P. Hammer, L.G. Vaz, L.A. Rocha, Are new TiNbZr alloys potential substitutes of the Ti6Al4V alloy for dental applications? An electrochemical corrosion study, Biomed. Mater. 8 (2013). doi:10.1088/1748-6041/8/6/065005.

[25] P.F. Gostin, A. Helth, A. Voss, R. Sueptitz, M. Calin, J. Eckert, A. Gebert, Surface treatment,

corrosion behavior, and apatite-forming ability of ti-45Nb implant alloy, J. Biomed. Mater. Res. - Part B Appl. Biomater. 101 B (2013) 269–278. doi:10.1002/jbm.b.32836.

[26] E. Yılmaz, A. Gökçe, F. Findik, Ho.O. Gulsoy, Metallurgical properties and biomimetic HA deposition performance of Ti-Nb PIM alloys, J. Alloys Compd. 746 (2018) 301–313. doi:10.1016/j.jallcom.2018.02.274.

[27] S.L. Assis, I. Costa, Electrochemical evaluation of Ti-13Nb-13Zr, Ti-6Al-4V and Ti-6Al-7Nb alloys for biomedical application by long-term immersion tests, Mater. Corros. 58 (2007) 329–333. doi:10.1002/maco.200604027.

[28] M.E. Orazem, B. Tribollet, Electrochemical Impedance Spectroscopy, 2008. doi:10.1002/9780470381588.

[29] M. Aziz-Kerrzo, K.G. Conroy, A.M. Fenelon, S.T. Farrell, C.B. Breslin, Electrochemical studies on the stability and corrosion resistance of titanium-based implant materials, Biomaterials. 22 (2001) 1531–1539. doi:10.1016/S0142-9612(00)00309-4.

[30] A.K. Shukla, R. Balasubramaniam, S. Bhargava, Properties of passive film formed on CP titanium , Ti – 6Al – 4V and Ti – 13 . 4Al – 29Nb alloys in simulated human body conditions, Intermetallics. 13 (2005) 631–637. doi:10.1016/j.intermet.2004.10.001.

[31] I. Cvijović-Alagić, Z. Cvijović, S. Mitrović, V. Panić, M. Rakin, Wear and corrosion behaviour of Ti-13Nb-13Zr and Ti-6Al-4V alloys in simulated physiological solution, Corros. Sci. 53 (2011) 796–808. doi:10.1016/j.corsci.2010.11.014.

[32] M. Metikoš-Huković, A. Kwokal, J. Piljac, The influence of niobium and vanadium on passivity of titanium-based implants in physiological solution, Biomaterials. 24 (2003) 3765–3775. doi:10.1016/S0142-9612(03)00252-7.

[33] J.M. Cordeiro, T. Beline, A.L.R. Ribeiro, E.C. Rangel, N.C. da Cruz, R. Landers, L.P. Faverani, L.G. Vaz, L.M.G. Fais, F.B. Vicente, C.R. Grandini, M.T. Mathew, C. Sukotjo, V.A.R. Barão, Development of binary and ternary titanium alloys for dental implants, Dent. Mater. 33 (2017) 1244–1257. doi:10.1016/j.dental.2017.07.013.

[34] Y.S. Lee, M. Niinomi, M. Nakai, K. Narita, K. Cho, Predominant factor determining wear properties of β-type and (α+β)-type titanium alloys in metal-to-metal contact for biomedical applications, J. Mech. Behav. Biomed. Mater. 41 (2015) 208–220. doi:10.1016/j.jmbbm.2014.10.005.

[35] N.P. Suh, An overview of the delamination theory of wear, Wear. 44 (1977) 1–16. doi:https://doi.org/10.1016/0043-1648(77)90081-3.

[36] Y. Lee, M. Niinomi, M. Nakai, K. Narita, K. Cho, Differences in Wear Behaviors at Sliding Contacts for β-Type and (α + β)-Type Titanium Alloys in Ringer' s Solution and Air, Mater. Trans. 56 (2015) 317–326.

[37] J.F. Archard, Contact and rubbing of flat surfaces, J. Appl. Phys. 24 (1953) 981–988. doi:10.1063/1.1721448.

[38] A. Ball, On the importance of work hardening in the design of wear-resistant materials, Wear. (1983). doi:10.1016/0043-1648(83)90254-5.

[39] X. Yang, C.R. Hutchinson, Corrosion-wear of β-Ti alloy alloy TMZF (Ti-12Mo-6Zr-2Fe) in simulated body fluid, Acta Biomater. 42 (2016) 429–439. doi:10.1016/j.actbio.2016.07.008.

[40] V.G. Pina, A. Dalmau, F. Devesa, V. Amigó, A.I. Muñoz, Tribocorrosion behavior of beta titanium biomedical alloys in phosphate buffer saline solution, J. Mech. Behav. Biomed. Mater. 46 (2015) 59–68. doi:10.1016/j.jmbbm.2015.02.016.

[41] J. Ureña, S. Tsipas, A.M. Pinto, F. Toptan, E. Gordo, A. Jiménez-Morales, Corrosion and tribocorrosion behaviour of β-type Ti-Nb and Ti-Mo surfaces designed by diffusion treatments for biomedical applications, Corros. Sci. (2018) 0–1. doi:10.1016/j.corsci.2018.06.024.

[42] I. Golvano, I. Garcia, A. Conde, W. Tato, A. Aginagalde, Influence of fluoride content and pH on corrosion and tribocorrosion behaviour of Ti13Nb13Zr alloy in oral environment, J. Mech. Behav. Biomed. Mater. 49 (2015) 186–196. doi:10.1016/j.jmbbm.2015.05.008.

[43] Z. Doni, A.C. Alves, F. Toptan, A.M. Pinto, L.A. Rocha, M. Buciumeanu, L. Palaghian, F.S. Silva, Tribocorrosion behaviour of hot pressed CoCrMo–Al2O3 composites for biomedical applications, Tribol. - Mater. Surfaces Interfaces. 8 (2014) 201–208. doi:10.1179/1751584X14Y.0000000078.

[44] G.W. Stachowiak, A.W. Batchelor, Engineering Tribology: Fourth Edition, 2013. doi:10.1016/C2011-0-07515-4.

Chapter 5: Interactions between wear and corrosion on cast and sintered Ti-12Nb alloy in comparison with the commercial Ti-6Al-4V alloy

Published in Corrosion Science, 176 (2020) 108925

Interactions between wear and corrosion on cast and sintered Ti-12Nb alloy in comparison with the commercial Ti-6Al-4V alloy

I. Çaha[a], A.C. Alves[a], C. Chirico[b], S.A. Tsipas[b,f], I.R. Rodrigues[d,e] A.M.P. Pinto[a,c] , C.R. Grandini[d,e], L.A. Rocha[d,e], E. Gordo[b,f], F. Toptan[a,e]

[a] CMEMS-UMinho - Center for MicroElectroMechanical Systems, Universidade do Minho, Azurém, 4800-058 Guimarães, Portugal

[b] Universidad Carlos III de Madrid, Avda. Universidad, 30, 28911 Leganés, Spain

[c] Universidade do Minho, Dept. Eng. Mecânica, Azurém, 4800-058 Guimarães, Portugal

[d] UNESP—Univ. Estadual Paulista, Faculdade de Ciências de Bauru, Dep. Física, 17033-360 Bauru, SP, Brazil

[e] IBTN/Br – Brazilan Branch of the Institute of Biomaterials, Tribocorrosion and Nanomedicine, 17033-360 Bauru, SP, Brazil

[f] Instituto "Álvaro Alonso Barba", 30, 28911 Leganés, Madrid

[*] Corresponding author at: CMEMS-Uminho – Center for MicroElectroMechanical Systems, Universidade do Minho, Azurém, 4800-058 Guimarães, Portugal. Tel.: +351 253 510 220; fax: +351 253 516 007. E-mail: ihsancaha@gmail.com (Ihsan Çaha).

Abstract

This work investigates the corrosion and tribocorrosion behavior of α+β Ti-12Nb alloy processed by casting and sintering, in 9 g/l NaCl solution at body temperature, and compares the results with the commercial Ti-6Al-4V alloy. Different electrochemical techniques were used to access the corrosion behavior. Tribocorrosion behavior was studied at open circuit potential under continuous and intermittent sliding, and at anodic potentiostatic condition under continuous sliding. Results revealed that Ti-12Nb alloys presented similar tribocorrosion behavior although the sintered one exhibited a better corrosion behavior. Nevertheless, Ti-6Al-4V presented better overall degradation resistance than both Ti-12Nb alloys.

Keywords: Titanium alloys, Casting, Powder metallurgy, Corrosion, Tribocorrosion

5.1. Introduction

Titanium alloys are chosen for biomedical applications due to their superior corrosion resistance, excellent mechanical strength, and good biocompatibility. Among these alloys, the α+β Ti-6Al-4V alloy has been extensively used in biomedical implants owing to the combination of unique physical and mechanical properties. However, considerable controversy has been raised due to possible long term adverse effects of released Al and V ions from Ti-6Al-4V alloy [1]. Also, its Young's modulus (~110 GPa) is much higher than that of human bone (~20 GPa) [2]. The mismatch in Young's modulus may lead to inhomogeneous transfer of stress between the implant and bone resulting in resorption of bone (stress shielding phenomenon) [3].

Ti-Nb based alloys have attracted attention due to their lower Young's moduli [4], good corrosion resistance [5], and superior biocompatibility [6]. Yilmaz *et al.* [7] presented that the good corrosion resistance of Ti-Nb alloys over Ti has been governed by the stable behavior of Nb_2O_5 oxide. In addition to the effect of the alloying elements, the microstructure also has a significant effect on corrosion behavior [8]. Sintered alloys usually have higher porosity as compared to the cast alloys, that can also influence the corrosion behavior [9].

Some biomedical applications such as hip prosthesis constitute a tribocorrosion system due to the presence of relative movements between bone and implant, and between the modular parts of the prosthesis during the movement of the human body. The release of metallic ions due to corrosion and wear can cause osteolysis and eventually implant failure [10]. Corrosion and tribocorrosion behavior of Ti and Ti-6Al-4V have been well studied in different conditions. For instance, Dimah *et al.* [11] studied the corrosion and tribocorrosion behavior of cp-Ti, Ti-6Al-4V, and Ti-6Al-4V-ELI in phosphate buffered solution (PBS) with and without the addition of bovine serum albumin. It was reported that the produced wear debris was affected by the testing solution. The authors also studied the influence of repassivation rate and passive film growth on the tribocorrosion behavior of the Ti-6Al-4V-ELI alloy through intermittent sliding tests and it was found that the wear rate increased with increasing of the resting time between the sliding cycles due to the growth of the passive films during the pause periods. On the other hand, regarding the effect of the processing route, Licausi *et al.* [12] investigated the corrosion and tribocorrosion behavior of Ti-6Al-4V alloy processed by either casting or powder metallurgy (P/M), in artificial saliva (with or without the addition of fluoride) and commercial mouth wash. Although the results were influenced by the testing solutions, as general, the authors reported better tribocorrosion behavior for the sintered alloys.

While its toxicity and high Young's modulus is still a concern, the α+β type Ti-6Al-4V alloy is still the dominant Ti-based implant material. Although vanadium-free Ti-6Al-7Nb alloy was developed for biomedical applications, especially for hip prothesis [13], this alloy has still higher Young's modulus (110 GPa) [13] and still include Al, that is suspected to be associated with Alzheimer's disease [1,14]. Recently, several studies reported lower wear resistance for low Young's modulus and non-toxic β-type Ti alloys tested in 9 g/l NaCl solution [15], Ringer's solution [16], simulated body solution [17], and under dry sliding condition [18], mainly due to the low strain hardening behavior of the β phase. Further understanding is needed on the tribocorrosion behavior of non-toxic and low Young's modulus Ti alloys being developed as an alternative to Ti-6Al-4V for load-bearing implant applications. Accordingly, this study aims to process the α+β Ti-12Nb alloy either by casting and P/M and to investigate the influence of the processing method on the degradation behavior in comparison with the commercial Ti-6Al-4V alloy.

5.2. Experimental procedure

5.2.1. Materials and processing

The raw materials used to produce cast Ti-12Nb alloy were Ti (99.7% purity, Sandinox Biometais, Brazil) and Nb (99.8% purity, Brazilian Metallurgy and Mining Company), whereas TiH_2 (GfE, D_{50}: 27μm) and Nb (Alfa Aesar, D_{50}: 15μm) powders were used to produce the sintered Ti-12Nb alloy. Regarding the cast alloy, the raw metals were arc-melted on a water-cooled copper crucible under an argon inert atmosphere with a non-consumable tungsten electrode. The ingots were re-melted several times then heat treated at 1000 °C for 24 h in an ultra-vacuum furnace for homogenization. Afterwards, the ingot was submitted to a hot-rolling treatment carried out at 900 °C and, finally, another heat treatment at 1000 °C for 24 h in a vacuum to relieve the residual stress during the machining procedure (complete details of the processing are given elsewhere [15]). In the case of the alloy produced by P/M, TiH_2 and Nb powders were homogenized by mixing for 1 h in a Turbula® multidirectional mixer. Green compacts (16 mm in diameter and about 3-4 mm in thickness) were acquired under 700 MPa pressure using zinc stearate as a die wall lubricant. The samples were sintered in a tubular furnace under a high vacuum (10^{-5} mbar) by holding 4 hours at 1250 °C (complete details of the processing are given elsewhere [19]). Commercial Ti-6Al-4V alloy (VSMPO Tirus, US, ASTM B348, Grade 5) was used as a control group.

5.2.2. Characterization of alloys

The microstructure of the alloys was characterized by optical microscopy (Leica, DM2500) after preparing the samples by grinding down to 1200 grit SiC paper, then polished with colloidal silica

suspension (0.02 μm particle size), and etched by Kroll's reagent (3 ml HF, 6 ml HNO_3, and 91 ml H_2O). The structural characterization of Ti-12Nb alloys was performed by X-ray diffraction (XRD, DMAX-2100, Rigaku). The phase percentages were calculated with the Rietveld refinement method by using Topas-Academic software. Microhardness of the alloys was determined by 10 indentations with a load of 4.90 N (0.50 kgf) during 30 s. The Young's modulus of the cast and sintered Ti-12Nb alloys was obtained from 10 measurements by using a dynamic manner with the Sonelastic® equipment (ATCP) based on ASTM-E1876 standard, using the technique of excitation by impulse, with the samples placed in flexural vibration. Roughness of the alloys was taken by a non-contact profilometer (Veeco, Dektak 150).

5.2.3. Corrosion tests

The corrosion behavior was analyzed through electrochemical impedance spectroscopy (EIS), and potentiodynamic polarization measurements in saline (9 g/l NaCl) solution at body temperature (37 ± 2 °C) using Gamry Potentiostat/Galvanostat/ZRA (model Reference-600+). In order to observe the stabilization of the native oxide film formed on the sample surfaces, OCP was monitored until obtaining $\Delta E < 60\ mV/h$ [20]. Afterwards, EIS tests were carried out with scanning between 10^{-2} to 10^{5} Hz with 7 points per frequency decade with 10 mV of the amplitude of a sinusoidal signal. The potentiodynamic polarization scans were studied from −0.25 V_{OCP} to 1.5 V_{SCE} with a scan rate of 0.5 mV s^{-1}. All electrochemical tests were performed in a three-electrode cell with 180 ml of the electrolyte where samples were used as the working electrode (WE), with an exposed area of 0.38 cm^2, a Pt electrode was used as the counter electrode (CE), and a saturated calomel electrode (SCE) was used as the reference electrode (RE).

5.2.4. Tribocorrosion tests

Tribocorrosion tests were performed in an electrochemical cell connected to a reciprocating ball-on-plate tribometer (CETR-UMT-2). The experiments were performed in saline (9 g/l NaCl) solution at 37 ± 2 °C temperature using Gamry Potentiostat/Galvanostat/ZRA (model Reference 600) with the same electrode configurations used in the electrochemical tests. A 10 mm diameter alumina ball (Ceratec) was used as the counter-body. The tests were carried out both under continuous and intermittent sliding at OCP, and under continuous sliding at an anodic applied potential (AP) of +0.5 V_{SCE} (Fig. 5.1). Intermittent tests were included in order to provide an extra information on the mechanism of the periodic removal and re-growth of surface oxide film [21]. During intermittent sliding, linear polarization (LPR) scans were performed 3 min before each sliding step, and 7 min after the final sliding step, at ± 20 mV_{OCP} with 0.5 mVs^{-1} scanning rate, in order to investigate the effect of sliding damage on the polarization resistance

(R_p extracted from LPR tests by using Gamry Echem Analyst software version 7.1). Each 6 sliding steps were employed for 5 minutes, giving 30 min of total sliding time such as continuous sliding. All tribocorrosion tests were performed at 1 Hz of frequency, 3 mm of amplitude, and 1 N of normal load (corresponds to 0.41 and 0.37 GPa maximum Hertzian contact pressure for Ti-6Al-4V and both Ti-12Nb alloys, respectively [22]). After each test, samples were cleaned in propanol and distilled water in ultrasonic bath for 10 min and 5 min, respectively, and the surfaces were analyzed by using FEG-SEM/EDS (FEI Nova 200/EDAX). Wear volume loss was calculated for all conditions following the method described before by Doni *et al.* [23], through wear track profiles taken by a profilometer (Veeco, Dektak 150).

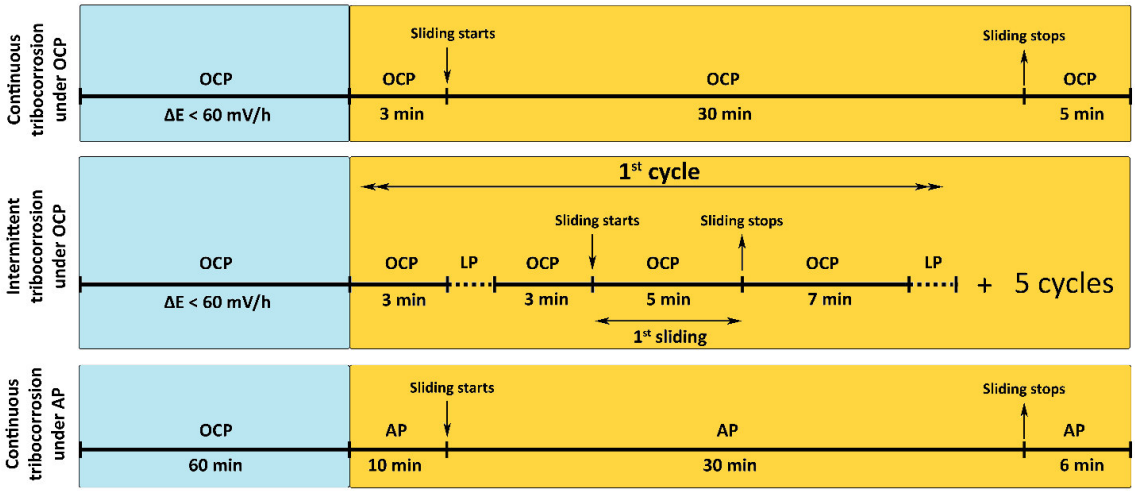

Fig. 5.1. Schematic representation of the tribocorrosion protocol.

5.2.5. Statistical analysis

The results are presented as the average ± standard deviation values from tests run in triplicates on three independent samples. Statistical analysis was evaluated by one-way ANOVA followed by Tukey's test for multiple comparisons, considering $p < 0.05$ as significant.

5.3. Results

5.3.1. Physical and structural properties

The microstructures and XRD pattern of the Ti-6Al-4V and Ti-12Nb alloys are given in Fig. 5.2. The optical microscope images evidence microstructures constituted by a mixture of α+β phases for all alloys. The Ti-6Al-4V alloy showed the small-sized homogenous distribution of grains with equiaxial α phase and β phase in grain boundaries (Fig. 5.2a). The light-colored (Nb rich area) and dark-colored (Ti-rich area) regions on Ti-Nb alloys represent β and α phases, respectively. The cast (Fig. 5.2b) and sintered (Fig. 5.2c) Ti-12Nb alloys are composed of lamellar α+β phases, however, the cast Ti-12Nb

alloy showed a thicker and relatively inhomogeneously distributed β phase, that may be explained by the hot deformation during processing resulting in the change of microstructures and phase transformations on two-phase titanium alloys as pointed by Banumathy *et al.* [24]. The sintered Ti-12Nb alloy exhibited smaller grain size and a more homogenous distribution of lamellar α and β phases with the presence of small pores. The XRD patterns of the Ti-12Nb alloys were composed of α (ICDD 00-044-1294) and β (ICDD 00-044-1288) phases which are in accordance with the observed microstructure. The phase percentages of the cast and the sintered alloys were 81% α, 19% β and 84% α, 16% β, respectively. These changes in the microstructure affected the mechanical properties (Table 5.1). The sintered Ti-12Nb alloy was harder than the cast one, whereas the commercial Ti-6Al-4V was significantly harder than the both Ti-Nb alloys ($p < 0.05$). Young's modulus of the sintered alloy was slightly higher than that of the cast one that may be linked to the relatively lower concentration of β phase and smaller grains obtained on the sintered alloy. Even though, the values were noticeably lower than that of the commercial Ti-6Al-4V alloy, that is reported in the literature as 112 GPa [1]. The R_a value of the Ti-6Al-4V was considerably lower than the both Ti-12Nb alloys, while the average value of sintered alloy was slightly higher than the cast alloy.

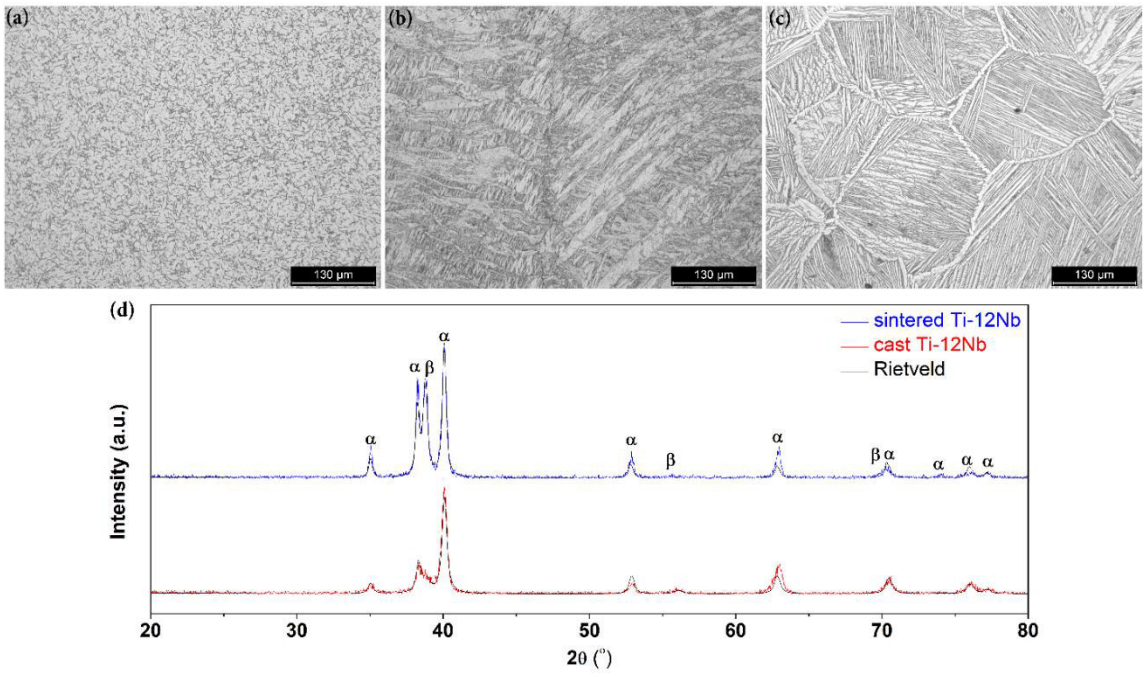

Fig. 5.2. Microstructural images of a) Ti-6Al-4V, b) Cast Ti-12Nb, and c) sintered Ti-12Nb alloys, and d) XRD patterns of the cast and sintered Ti-12-Nb alloys.

Table 5.1. Hardness, Young's modulus and R_a values.

Samples	*Hardness ($HV_{0.5}$)*	*Young's Modulus (GPa)*	*Average surface roughness-R_a (μm)*
Ti-6Al-4V	350 ± 3	112 [1]	0.19 ± 0.02
Cast Ti-12Nb	252 ± 4	92.6 ± 0.4	0.25 ± 0.02
Sintered Ti-12Nb	267 ± 5	94.6 ± 0.2	0.27 ± 0.01

5.3.2. Corrosion results

Representative results of the electrochemical tests are given in Fig. 5.3. Regarding the potentiodynamic polarization curves (Fig. 5.3a), all samples presented passivation plateau started at −41 ± 6 mV_{SCE}, 200 ± 103 mV_{SCE}, and 374 ± 29 mV_{SCE} for the cast Ti-12Nb, Ti-6Al-4V, and sintered Ti-12Nb, respectively. The sintered Ti-12Nb presented statistically significant higher corrosion potential ($E_{(i=0)}$) than the other alloys. While the cast Ti-12Nb sample presented higher passivation current density (i_{pass}) than the other alloys, the statistically significant difference was only observed with the Ti-6Al-4V alloy ($p < 0.05$).

In order to obtain further information on the protective character of passive films formed on the samples, EIS was carried out. Representative Bode diagrams are shown in Fig. 5.3b. The fitted EIS parameters for tested alloys were computed by Gamry Echem Analyst software (version 7.05) and summarized in Table 5.2. The quality of the suggested electrical equivalent circuit (EEC, Fig. 5.3c) was evaluated through the goodness of fitting where the EEC presented values below 10^{-4}. The EEC included R_e, R_{ox}, and Q_{ox} corresponding to the resistance of the electrolyte, the resistance of the oxide layer, and a constant phase angle element (CPE) of the oxide layer, respectively. The CPE indicating a non-ideal behavior of capacitive elements due to surface heterogeneity results from impurities, roughness, and dislocations. The impedance of CPE is expressed as $Z_{CPE} = [Y_0(jw)^n]^{-1}$, where Y_0 is the CPE constant, w is the angular frequency in rad/s, $j^2 = -1$ is the imaginary number, and n is the exponential factor, $-1 \leq n \leq 1$. When the n value is 1, 0, and −1, the CPE response is an ideal capacitor, a resistor, and an inductor, respectively. The n value is associated with the roughness of the surface and its heterogeneities [25]. The capacitance (C_{ox}) values of a single oxide layer parallel to its resistance result from its dielectric properties converted from Q_{ox} values through Eq. (3) derived from Brug's equation [25];

$$C_{ox} = \left[Q_{ox}R_e^{(1-n)}\right]^{\frac{1}{n}} \quad (1)$$

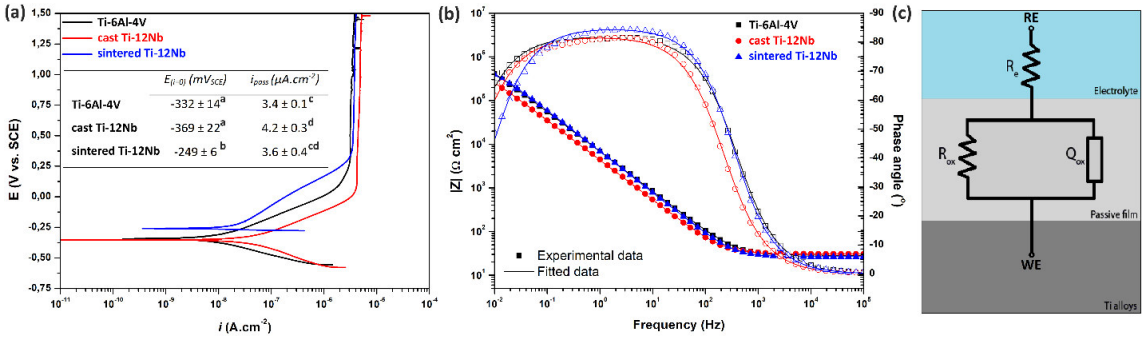

Fig. 5.3. a) Potentiodynamic polarization curves including $E_{(i=0)}$ and i_{pass} values (statistically homogenous groups are indicated by the same letters), b) Bode diagrams, and (c) representative EEC for fitted EIS data.

Table 5.2. Electrochemical parameters obtained from the proposed EEC (statistically homogenous groups are indicated by the same letters).

Samples	R_{ox} ($M\Omega.cm^2$)	C_{ox} ($\mu F.cm^{-2}$)	n
Ti-6Al-4V	1.30 ± 0.42^{a}	15.2 ± 1.7^{b}	0.92 ± 0.01^{d}
Cast Ti-12Nb	0.65 ± 0.05^{a}	25.4 ± 4.1^{c}	0.92 ± 0.01^{d}
Sintered Ti-12Nb	0.69 ± 0.27^{a}	17.0 ± 2.1^{b}	0.94 ± 0.01^{e}

All alloys presented a one-time constant indicating a passive film in contact with the electrolyte. In the low-frequency range, very similar |Z| (impedance modulus) values were observed for the sintered Ti-12Nb and the Ti-6Al-4V alloys, and it was higher than the values of the cast Ti-12Nb alloy. The increased phase angle values at the middle-frequency range for alloys were close to −90° showing the capacitive behavior of a compact passive oxide layer. The phase angle values of the sintered Ti-12Nb sample were higher in the medium frequency range whereas the phase angle values of both Ti-12Nb alloys were slightly lower than the Ti-6Al-4V alloy in the low-frequency range. As can be seen in Table 5.1, the average R_{ox} value of the Ti-6Al-4V was higher than the values of the cast Ti-12Nb and the sintered Ti-12Nb alloys, however, the difference was not statistically significant. The C_{ox} of Ti-6Al-4V and sintered Ti-12Nb were similar and significantly lower than the values of cast Ti-12Nb ($p < 0.05$). Moreover, the cast Ti-12Nb and Ti-6Al-4V alloys presented the same n values whereas the value was statistically higher on the sintered Ti-12Nb alloy.

5.3.3. Tribocorrosion results

5.3.3.1. Continuous and intermittent tribocorrosion under OCP

The evolution of OCP and coefficient of friction (COF) both for continuous and intermittent sliding are given in Fig. 5.4, together with the evolution of R_p (obtained from LPR), and k_1 (calculated repassivation rate) for intermittent sliding. Before sliding, all alloys showed stable potential values because of the presence of a passive oxide film on alloy surfaces. When sliding started, an instant drop in OCP values was observed for all alloys indicating the partial or total destruction of the oxide film at the contact region. During sliding, all tested alloys presented relatively large OCP oscillations resulting from passivation/repassivation actions during both continuous and intermittent sliding. After sliding, all alloys recovered their potentials close to the ones recorded before sliding, due to the repassivation of the worn areas. Regarding the COF evolution, all alloys presented a similar trend under continuous and intermittent sliding where the Ti-6Al-4V alloy showed statistically significant lower COF values while the other alloys presented very similar values. Also, non-destructive linear polarization tests were performed at 7 mins after stopping each sliding cycle to study the influence of intermittency on the polarization resistance. The sintered Ti-12Nb presented higher average R_p values than the other alloys, however, statistically, the difference was not significant between the tested groups. The repassivation rate after sliding was calculated according to Hanawa *et al.* [26] by using the following equation:

$$\Delta E = k_1 log t + k_2 \ (2)$$

where ΔE is the potential variation, t *(s)* is the time after stopping sliding, k_1 is the slope and k_2 is a constant defined by the solution where the sliding took place. k_1 values demonstrating the repassivation rate are showed in Fig. 5.4. No statistically significant difference was found on the k_1 values between the sliding cycles. Regarding the comparison of the alloys, although the average values of the cast Ti-12Nb alloy were higher than the sintered Ti-12Nb and the Ti-6Al-4V alloys, the difference between the groups was not statistically significant.

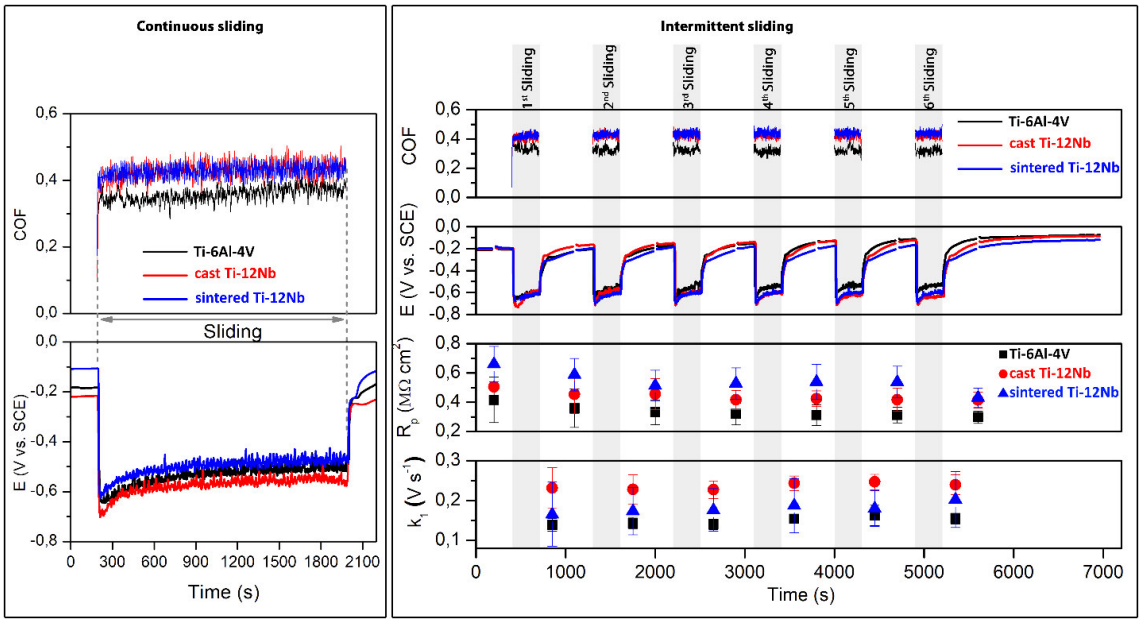

Fig. 5.4. a) Evolution of COF and potential during continuous sliding, b) evolution of COF, potential, R_p, and repassivation rate (k_1) during intermittent sliding.

5.3.3.2. Continuous tribocorrosion under anodic applied potential

The current and COF evolution at +0.5 V_{SCE} anodic applied potential (AP), against an alumina ball, in saline solution are presented in Fig. 5.5. The current was stable and close to zero before sliding, in agreement with passive current (i_{pass}) values from the potentiodynamic polarization curves (Fig. 5.3a). When sliding started, sudden current increases were caused by the mechanical destruction of the passive film (depassivation). This abrupt increase was observed for the Ti-6Al-4V as soon as the sliding started, while an approx. 100 s delay was observed for the both Ti-12Nb alloys. During sliding, local current increments corresponded to decrements on COF values; were observed for all alloys, and it was more evident for the cast Ti-12Nb. Moreover, COF values at the AP condition were significantly higher than the ones recorded under the OCP condition ($p < 0.05$). The charge values obtained during sliding were calculated by $Q = \int_0^t Idt$ the equation as 0.022 ± 0.007, 0.026 ± 0.010, and 0.021 ± 0.004 C for the Ti-6Al-4V, cast Ti-12Nb, and sintered Ti-12Nb, respectively, where no statistically significant difference was found between the alloys.

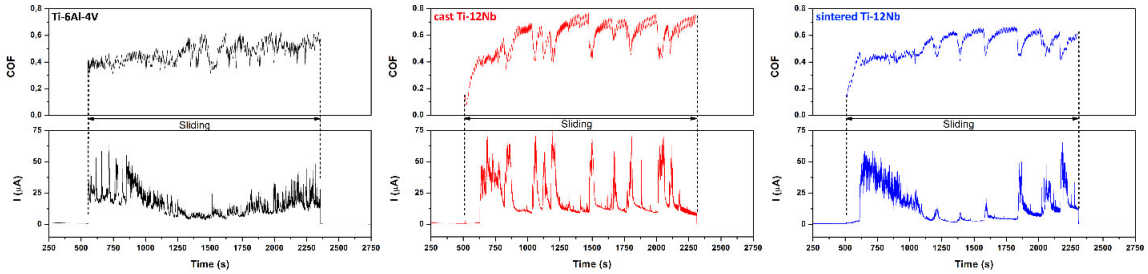

Fig. 5.5. The current evolution together with COF evolution for Ti-6Al-4V, cast and sintered Ti-12Nb alloys under applied anodic potential.

5.3.3.3. Wear morphology

The wear morphologies after continuous and intermittent sliding at OCP, as well, after continuous sliding at AP were analyzed by using secondary electron (SE) and backscattered electron (BSE) mode SEM to understand the wear mechanism (Fig. 5.6). Parallel sliding grooves, adhered oxidized particles, and plastic deformations were observed on all worn surfaces as usual wear surface features for Ti and its alloys. Regarding the testing conditions, while there were no clear differences in wear features between continuous and intermittent sliding at OCP, discontinuous tribolayer was observed on both Ti-12Nb alloys under AP condition as evidenced by the darker regions on the BSE images. Accordingly, existence of more tribolayer was observed on the BSE images of the cast Ti-12Nb alloy surfaces as compared to the sintered alloy for all testing conditions.

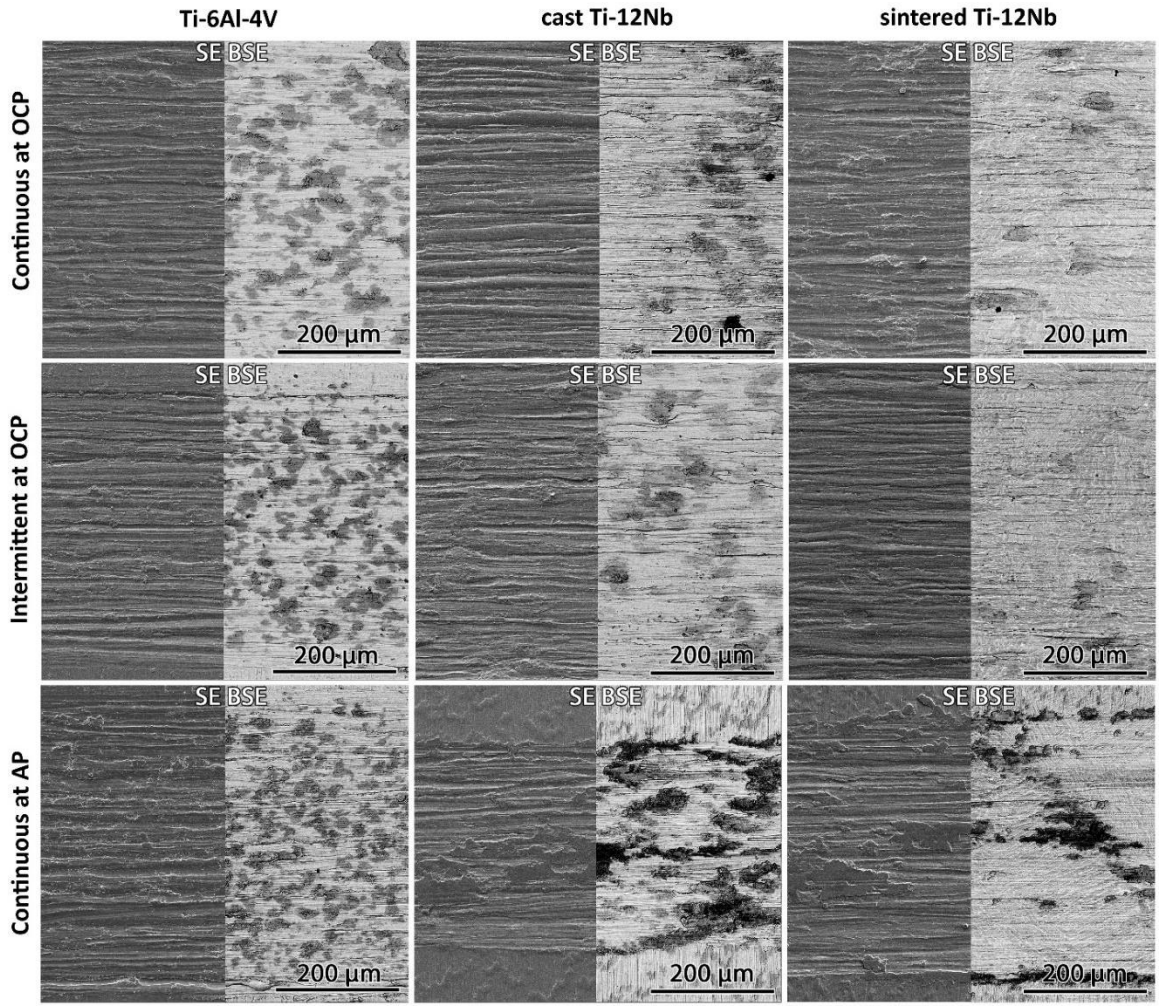

Fig. 5.6. SEM images of the worn alloy surfaces.

Fig. 5.7 shows the SE/SEM images and EDS spectra of wear scar on alumina ball surfaces taken from the wear scars after the tribocorrosion tests. Transferred material from samples to the alumina ball was confirmed by EDS spectra for all alloys in all tested conditions. Nevertheless, the transferred material at AP condition seemed to be drastically decreased while the intensity of the oxygen peaks was increased for all alloys.

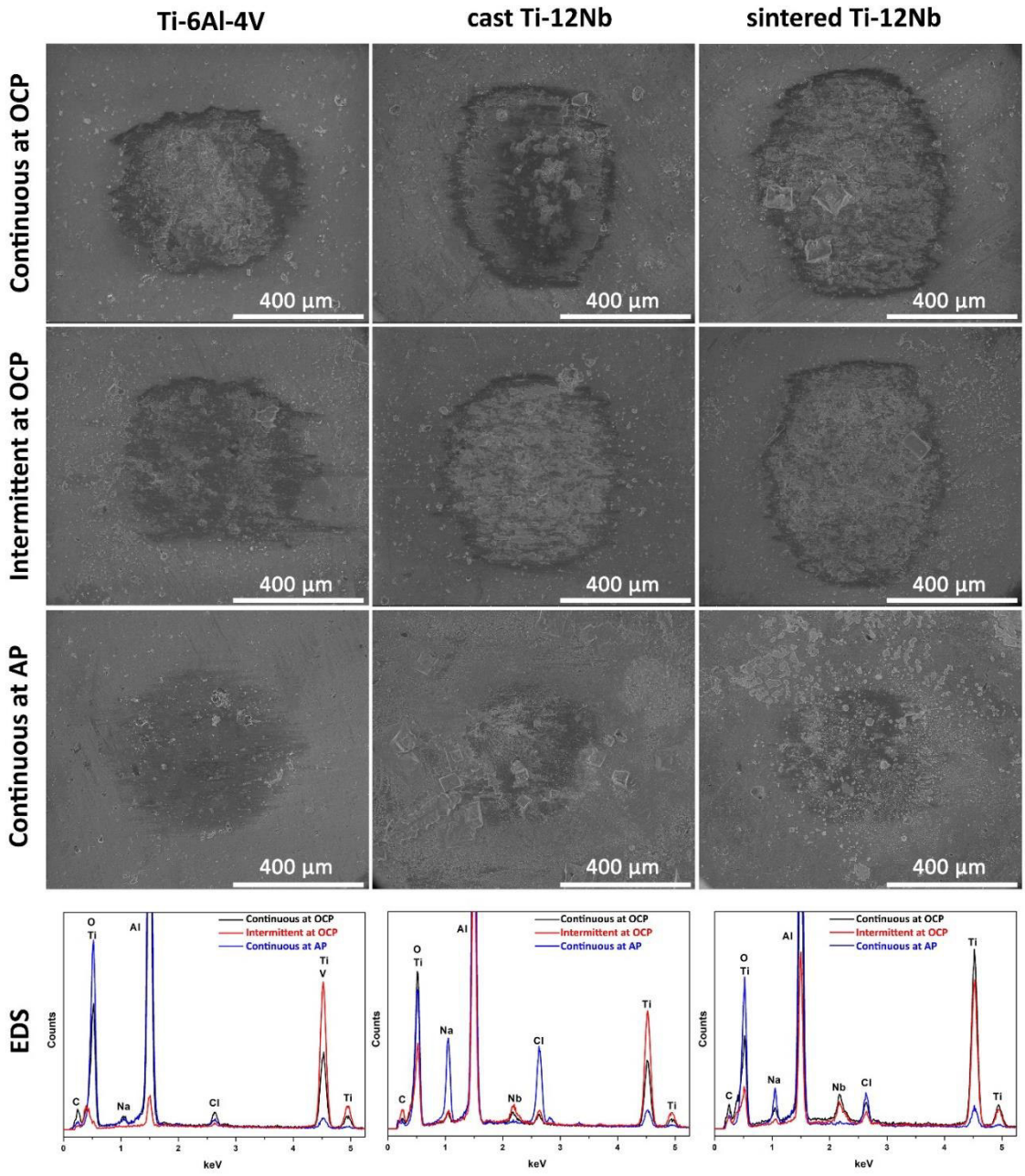

Fig. 5.7. SEM image of the wear scars on alumina balls and corresponding EDS spectra.

5.3.3.4. Wear loss

Fig. 5.8 presents the wear volume loss after each testing condition. Wear volume loss on the Ti-6Al-4V alloy was lower than the ones obtained for the both Ti-12Nb alloys, except for the AP condition ($p < 0.05$). Intermittency did not significantly affect the wear volume loss values of all alloys ($p < 0.05$). While wear volume loss of the Ti-6Al-4V was not significantly affected by the testing conditions, values of the both Ti-12Nb alloys tested at AP were significantly lower as compared to the other testing conditions ($p < 0.05$).

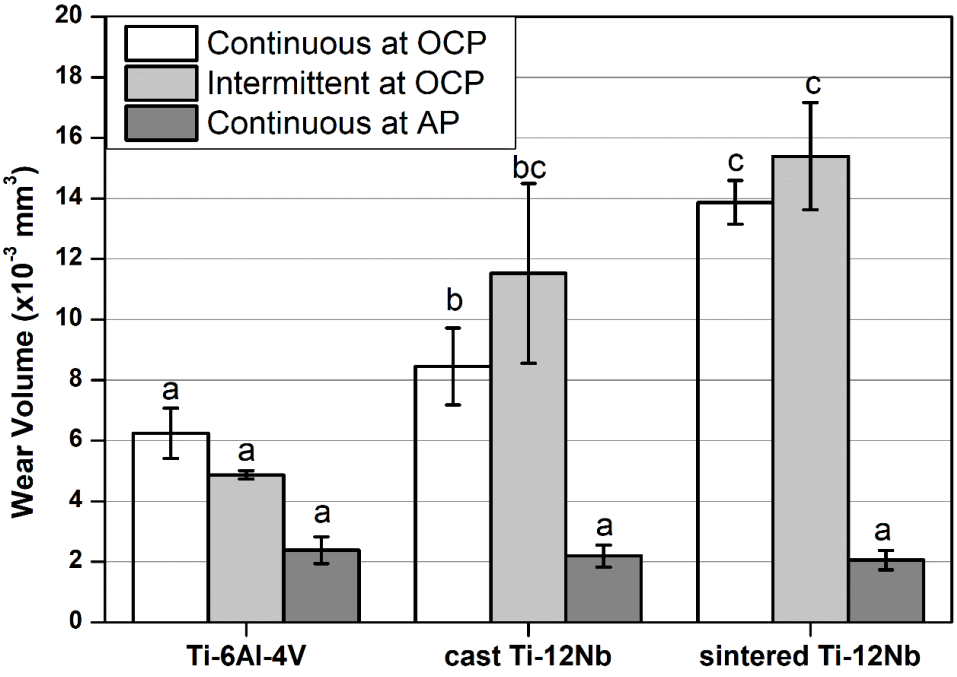

Fig. 5.8. Total wear volume loss after continuous and intermittent tribocorrosion under OCP, and after continuous tribocorrosion under anodic (AP) applied potential (statistically homogenous groups are indicated by the same letters).

5.4. Discussion

The processing method influenced the corrosion behavior of Ti alloys in 9 g/l NaCl solution; this was attributed to the differences in the microstructures. Significantly nobler $E_{(i=0)}$ values (Fig. 5.3a) obtained for the sintered alloy indicated a lower tendency to corrosion ($p < 0.05$). Furthermore, significantly lower C_{ox} values and n_{ox} closer to 1 (Table 5.2) observed for the sintered alloy suggested a higher quality of the native oxide film ($p < 0.05$). The effect of the processing route on the corrosion behavior of various Ti alloys has been investigated in the literature. Within those, Toptan *et al.* [27] compared the corrosion and tribocorrosion behavior of Ti-6Al-4V alloys processed by selective laser melting (SLM), hot pressing, and casting and forging, in saline (9 g/l NaCl) solution. The authors reported that samples processed by SLM presented lower quality of passive film due to the lower amount of the β phase and the presence of martensite (α′) phase. Dalmau *et al.* [9] studied the corrosion behavior of Ti-6Al-4V alloys in PBS electrolyte and reported higher corrosion resistance for the sintered alloy as compared to the rolled alloy due to its microstructure presenting smaller grain size, including pores, and having higher surface roughness. The relationship of microstructure and corrosion behavior on Ti-30Nb-Zr alloy was investigated by Martins *et al.* [28]. The authors pointed that the alloy having a more uniform phase distribution presented better corrosion resistance due to the formation of a more

homogeneous oxide film. Regarding phase volume fractions, Yang *et al.* [29] reported that the α phase had higher resistance to corrosion than the β phase. Therefore, the relatively better corrosion behavior of the sintered Ti-12Nb compared to the cast alloy may be linked with its higher volume fraction of α phase and more uniform phase distribution along smaller grains that possibly led to a more homogeneous oxide film.

Tribocorrosion tests were performed both at OCP (continuous and intermittent) and at potentiostatic conditions by applying a potential corresponding to the passive region of the tested alloys. As reviewed by Cao and Mischler [30], tribocorrosion tests at OCP are closer to the simulation of a real implant system. But these tests do not provide information on the electrochemical kinetics. On the other hand, as pointed by López-Ortega *et al.* [31], tests performed at the anodic applied potential result in degradation by the combined effect of wear and corrosion, which provide information on electrochemical kinetics offering a better understanding to the prevailing wear mechanisms.

Several studies showed that Ti-6Al-4V presents better wear resistance than the α+β Ti-15Nb [15], near β Ti-13Nb-13Zr [16], β Ti-12Mo-6Zr-2Fe [17], and β Ti-29Nb-13Ta-4.6Zr [18] mainly due to its higher hardness resulting from its microstructure. Under OCP conditions, the Ti-6Al-4V alloy presented lower wear volume loss that may be linked to its higher hardness values compared to the Ti-12Nb alloys. However, among the Ti-12Nb alloys, although cast alloy has relatively lower hardness value, it exhibited lower wear volume loss that may be linked with the characteristics of the tribolayer generated during sliding. SEM observations of the worn surfaces suggested that the discontinuous tribolayer covered a larger area on wear tracks of the cast alloy, which may be connected with the lower quality of its oxide layer (evidenced by significantly higher C_{ox} value from the EIS test) that requires further investigation. The total wear volume loss of both Ti-12Nb alloys in AP condition was significantly lower than that of the wear volume loss obtained at OCP condition ($p < 0.05$). It is known that applied potential can affect the material loss under tribocorrosion [20]. On one hand, a lower amount of wear-enhanced corrosion is expected at passive domain (such as AP condition in the present study), compared to OCP domains, as a consequence of the continuous repassivation of damaged oxide film imposed by the potentiostat. On the other hand, a larger amount of corrosion-enhanced wear (in particular, mechanical wear of repassivated material) is expected at passive domain than in OCP conditions, due to the third body wear arising from the removed oxide particles whose formation was increased under applied potential [32–36]. In the case of Ti-12Nb alloys, the worn area covered by the discontinuous tribolayer was substantially increased under AP and it apparently played a protective role against tribocorrosion (Fig. 5.6). Some of the present

authors had recently reported a similar behavior also for β type Ti-40Nb alloy tested under continuous sliding at +0.5 V_{SCE} (passive region) in 9 g/l NaCl electrolyte, due to the formation of a tribolayer [37]. The elevated formation of the discontinuous tribolayer on the worn Ti-12Nb alloy surfaces at AP condition may be influenced by the fast repassivation of Nb [1]. However, after reaching a certain thickness, this discontinuous layer may be removed by the counter-material resulting in a rapid increase in the current density values (Fig. 5.5).

Intermittent sliding tests enabled studying the mechanism of the regular removal and regrowth of surface oxide films through the sliding cycle followed by a pause time. There was no visible influence of intermittency on the wear track features, as well as on the evolution of COF, OCP, R_p, and k_1 values. The higher average k_1 values of the cast alloy may be linked with its passivation plateau that started to be formed at relatively lower potentials (Fig. 5.3a), though it needs further studies to reveal clearly the correlations. Finally, intermittency did not play a statistically significant difference on the wear volume loss for any alloy.

Although the degradation behavior of alloys was systematically studied, some limitations have been encountered. In order to have a better understanding to the corrosion mechanism, long-term corrosion behavior should be studied in more complex solutions and the released ions into the testing solution should to be quantified. Furthermore, future works should also take into consideration the effect of bone-forming cells on the corrosion and tribocorrosion mechanisms.

5.5. Conclusions

The corrosion and tribocorrosion behavior of the Ti-12Nb alloy processed by different processing techniques (casting and P/M) was investigated in 9 g/l NaCl at 37 ± 2 °C, in comparison with the commercial Ti-6Al-4V alloy. Results revealed better overall degradation resistance for the commercial Ti-6Al-4V alloy as compared to the both Ti-12Nb alloys. The corrosion behavior of the sintered Ti-12Nb alloy was better than the cast alloy; this could be attributed to its more uniform microstructure. Both Ti-12Nb alloys showed significantly lower wear volume loss at AP condition than in OCP conditions; this was attributed to the formation of discontinuous tribolayer, which was prevalently observed on the worn surfaces after AP tests. The intermittency did not affect significantly the wear volume loss in tested conditions.

Acknowledgments

This work was supported by FCT national funds, under the national support to R&D units grant, through the reference project UIDB/04436/2020 and UIDP/04436/2020, together with M-ERA-NET/0001/2015, and co-supported by Brazilian agencies CNPq [grants #308.204/2017-4 and #125.954/2018-2] and FAPESP M-ERA-NET [grant #2015/50.280-5], also by MINECO (Spain) through the program PCIN-2016-123 and the Ramón y Cajal project RYC-2014-15014. I. Çaha is grateful for a PhD grant under the NORTE-08-5369-FSE-000012 project.

References

[1] M. Geetha, A.K. Singh, R. Asokamani, A.K. Gogia, Ti based biomaterials, the ultimate choice for orthopaedic implants - A review, Prog. Mater. Sci. 54 (2009) 397–425. doi:10.1016/j.pmatsci.2008.06.004.

[2] M. Niinomi, M. Nakai, Titanium-based biomaterials for preventing stress shielding between implant devices and bone, Int. J. Biomater. (2011) 1–10. doi:10.1155/2011/836587.

[3] M.A. Gepreel, M. Niinomi, Biocompatibility of Ti-alloys for long-term implantation, J. Mech. Behav. Biomed. Mater. 20 (2013) 407–415. doi:10.1016/j.jmbbm.2012.11.014.

[4] S. Abdi, M.S. Khoshkhoo, O. Shuleshova, M. Bönisch, M. Calin, L. Schultz, J. Eckert, M.D. Baró, J. Sort, A. Gebert, Effect of Nb addition on microstructure evolution and nanomechanical properties of a glass-forming Ti-Zr-Si alloy, Intermetallics. 46 (2014) 156–163. doi:10.1016/j.intermet.2013.11.010.

[5] Y. Bai, Y. Deng, Y. Zheng, Y. Li, R. Zhang, Y. Lv, Q. Zhao, S. Wei, Characterization, corrosion behavior, cellular response and in vivo bone tissue compatibility of titanium-niobium alloy with low Young's modulus, Mater. Sci. Eng. C. 59 (2016) 565–576. doi:10.1016/j.msec.2015.10.062.

[6] H. Matsuno, A. Yokoyama, F. Watari, M. Uo, T. Kawasaki, Biocompatibility and osteogenesis of refractory metal implants, titanium, hafnium, niobium, tantalum and rhenium, Biomaterials. 22 (2001) 1253–1262. doi:10.1016/S0142-9612(00)00275-1.

[7] E. Yılmaz, A. Gökçe, F. Findik, Ho.O. Gulsoy, Metallurgical properties and biomimetic HA deposition performance of Ti-Nb PIM alloys, J. Alloys Compd. 746 (2018) 301–313. doi:10.1016/j.jallcom.2018.02.274.

[8] M. Geetha, U. Kamachi Mudali, A.K. Gogia, R. Asokamani, B. Raj, Influence of microstructure and alloying elements on corrosion behavior of Ti-13Nb-13Zr alloy, Corros. Sci. 46 (2004) 877–892. doi:10.1016/S0010-938X(03)00186-0.

[9] A. Dalmau, V. Guiñón Pina, F. Devesa, V. Amigó, A. Igual Muñoz, Influence of fabrication process on electrochemical and surface properties of Ti-6Al-4V alloy for medical applications, Electrochim. Acta. 95 (2013) 102–111. doi:10.1016/j.electacta.2013.01.155.

[10] P.A. Revell, The combined role of wear particles, macrophages and lymphocytes in the loosening of total joint prostheses, J. R. Soc. Interface. 5 (2008) 1263–1278. doi:10.1098/rsif.2008.0142.

[11] M.K. Dimah, F. Devesa Albeza, V. Amigó Borrás, A. Igual Muñoz, Study of the biotribocorrosion behaviour of titanium biomedical alloys in simulated body fluids by electrochemical techniques, Wear. 294–295 (2012) 409–418. doi:10.1016/j.wear.2012.04.014.

[12] M.P. Licausi, A. Igual Muñoz, V. Amigó Borrás, Influence of the fabrication process and fluoride content on the tribocorrosion behaviour of Ti6Al4V biomedical alloy in artificial saliva, J. Mech. Behav. Biomed. Mater. 20 (2013) 137–148. doi:10.1016/j.jmbbm.2013.01.019.

[13] M.F. Semlitsch, H. Weber, R.M. Streicher, R. Schön, Joint replacement components made of hot-forged and surface-treated Ti-6Al-7Nb alloy, Biomaterials. 13 (1992) 781–788. doi:10.1016/0142-9612(92)90018-J.

[14] X. Yang, H. Pan, J. Zhang, H. Gao, B. Shu, Y. Gong, X. Zhu, Progress in mechanical properties of gradient structured metallic materials induced by surface mechanical attrition treatment, Mater. Trans. 60 (2019) 1543–1552. doi:10.2320/matertrans.MF201911.

[15] I. Çaha, A.C. Alves, P.A.B. Kuroda, C.R. Grandini, A.M.P. Pinto, L.A. Rocha, F. Toptan, Degradation behavior of Ti-Nb alloys: Corrosion behavior through 21 days of immersion and tribocorrosion behavior against alumina, Corros. Sci. 167 (2020) 108488. doi:10.1016/j.corsci.2020.108488.

[16] I. Cvijović-Alagić, Z. Cvijović, S. Mitrović, V. Panić, M. Rakin, Wear and corrosion behaviour of Ti-13Nb-13Zr and Ti-6Al-4V alloys in simulated physiological solution, Corros. Sci. 53 (2011) 796–808. doi:10.1016/j.corsci.2010.11.014.

[17] X. Yang, C.R. Hutchinson, Corrosion-wear of β-Ti alloy alloy TMZF (Ti-12Mo-6Zr-2Fe) in simulated body fluid, Acta Biomater. 42 (2016) 429–439. doi:10.1016/j.actbio.2016.07.008.

[18] Y.S. Lee, M. Niinomi, M. Nakai, K. Narita, K. Cho, Predominant factor determining wear properties of β-type and (α+β)-type titanium alloys in metal-to-metal contact for biomedical applications, J. Mech. Behav. Biomed. Mater. 41 (2015) 208–220. doi:10.1016/j.jmbbm.2014.10.005.

[19] C. Chirico, S. Tsipas, F. Toptan, E. Gordo, Development of Ti–Nb and Ti–Nb–Fe beta alloys from TiH2 powders, Powder Metall. 62 (2019) 44–53. doi:10.1080/00325899.2018.1563953.

[20] P. Ponthiaux, F. Wenger, J. Pierre, Tribocorrosion: material behaviour under combined conditions of corrosion and mechanical loading, in: Corros. Resist., IntechOpen, 2012. doi:10.5772/35634.

[21] P. Ponthiaux, R. Bayon, F. Wenger, J.-P. Celis, Testing protocol for the study of bio-tribocorrosion, Woodhead Publishing Limited, 2013. doi:10.1533/9780857098603.3.372.

[22] G.W. Stachowiak, A.W. Batchelor, Engineering Tribology, 2000. http://www.ncbi.nlm.nih.gov/pubmed/22068761.

[23] Z. Doni, A.C. Alves, F. Toptan, J.R. Gomes, A. Ramalho, M. Buciumeanu, L. Palaghian, F.S. Silva, Dry sliding and tribocorrosion behaviour of hot pressed CoCrMo biomedical alloy as compared with the cast CoCrMo and Ti6Al4V alloys, Mater. Des. 52 (2013) 47–57. doi:10.1016/j.matdes.2013.05.032.

[24] S. Banumathy, R.K. Mandal, A.K. Singh, Phase transformation textures in hot-rolled binary Ti-Nb alloys, Metall. Mater. Trans. A Phys. Metall. Mater. Sci. 44 (2013) 2499–2511. doi:10.1007/s11661-013-1634-x.

[25] M.E. Orazem, B. Tribollet, Electrochemical Impedance Spectroscopy, 2008. doi:10.1002/9780470381588.

[26] T. Hanawa, K. Asami, K. Asaoka, Repassivation of titanium and surface oxide film regeneration in simulated bioliquid, J Biomed Mater Res1. 40 (1998) 530–538. doi:10.1002/(SICI)1097-4636(19980615)40:4<530::AID-JBM3>3.0.CO;2-.

[27] F. Toptan, A.C. Alves, Ó. Carvalho, F. Bartolomeu, A.M.P. Pinto, F. Silva, G. Miranda, Corrosion and tribocorrosion behaviour of Ti6Al4V produced by selective laser melting and hot pressing in comparison with the commercial alloy, J. Mater. Process. Technol. 266 (2019) 239–245. doi:10.1016/j.jmatprotec.2018.11.008.

[28] D.Q. Martins, W.R. Osório, M.E.P. Souza, R. Caram, A. Garcia, Effects of Zr content on

microstructure and corrosion resistance of Ti-30Nb-Zr casting alloys for biomedical applications, Electrochim. Acta. 53 (2008) 2809–2817. doi:10.1016/j.electacta.2007.10.060.

[29] Y. Yang, C. Xia, Z. Feng, X. Jiang, B. Pan, X. Zhang, M. Ma, R. Liu, Corrosion and passivation of annealed Ti-20Zr-6.5Al-4V alloy, Corros. Sci. 101 (2015) 56–65. doi:10.1016/j.corsci.2015.08.038.

[30] S. Cao, S. Mischler, Modeling tribocorrosion of passive metals – A review, Curr. Opin. Solid State Mater. Sci. (2018) 1–15. doi:10.1016/j.cossms.2018.06.001.

[31] A. López-Ortega, J.L. Arana, R. Bayón, Tribocorrosion of Passive Materials: A Review on Test Procedures and Standards, Int. J. Corros. (2018) 24. doi:10.1155/2018/7345346.

[32] Y. Sun, V. Rana, Tribocorrosion behaviour of AISI 304 stainless steel in 0.5 M NaCl solution, Mater. Chem. Phys. 129 (2011) 138–147. doi:10.1016/j.matchemphys.2011.03.063.

[33] C. Jun, Corrosion wear characteristics of TC4, 316 stainless steel, and Monel K500 in artificial seawater, RSC Adv. 7 (2017) 23835–23845. doi:10.1039/c7ra03065g.

[34] A. Igual Muñoz, L. Casabán Julián, Influence of electrochemical potential on the tribocorrosion behaviour of high carbon CoCrMo biomedical alloy in simulated body fluids by electrochemical impedance spectroscopy, Electrochim. Acta. 55 (2010) 5428–5439. doi:10.1016/j.electacta.2010.04.093.

[35] P. Henry, J. Takadoum, P. Berçot, Tribocorrosion of 316L stainless steel and TA6V4 alloy in H2SO4 media, Corros. Sci. 51 (2009) 1308–1314. doi:10.1016/j.corsci.2009.03.015.

[36] S. Barril, S. Mischler, D. Landolt, Electrochemical effects on the fretting corrosion behaviour of Ti6Al4V in 0.9% sodium chloride solution, in: Wear, 2005: pp. 282–291. doi:10.1016/j.wear.2004.12.012.

[37] I. Çaha, A. Alves, C. Chirico, A. Pinto, S. Tsipas, E. Gordo, F. Toptan, Corrosion and Tribocorrosion Behavior of Ti-40Nb and Ti-25Nb-5Fe Alloys Processed by Powder Metallurgy, Metall. Mater. Trans. A Phys. Metall. Mater. Sci. 51 (2020) 3256–3267. doi:10.1007/s11661-020-05757-6.

Chapter 6: A promising method to develop TiO_2-based nanotubular surfaces on Ti-40Nb alloy with enhanced adhesion and improved tribocorrosion resistance

Published in Applied surface science, 542 (2021) 148658

A promising method to develop TiO_2-based nanotubular surfaces on Ti-40Nb alloy with enhanced adhesion and improved tribocorrosion resistance

Ihsan Çaha[a], Alexandra C. Alves[a], Caterina Chirico[b], Ana M.P. Pinto[a,c], Sophia Tsipas[b,d], Elena Gordo[b,d], and Fatih Toptan[a,e]

[a] CMEMS-UMinho - Center for MicroElectroMechanical Systems, Universidade do Minho, Azurém, 4800-058 Guimarães, Portugal

[b] Universidad Carlos III de Madrid, Avda. Universidad, 30, 28911 Leganés, Spain

[c] Universidade do Minho, Dept. Eng. Mecânica, Azurém, 4800-058 Guimarães, Portugal

[d] Instituto "Álvaro Alonso Barba", 30, 28911 Leganés, Madrid

[e] IBTN/Euro – European Branch of the Institute of Biomaterials, Tribocorrosion and Nanomedicine, Dept. Eng. Mecânica, Universidade do Minho, Azurém, 4800-058 Guimarães, Portugal

* Corresponding author at: CMEMS-Uminho – Center for MicroElectroMechanical Systems, Universidade do Minho, Azurém, 4800-058 Guimarães, Portugal. Tel.: +351 253 510 220; fax: +351 253 516 007. E-mail: ihsancaha@gmail.com (Ihsan Çaha).

Abstract

Although TiO_2 nanotubes have unique properties making them attractive for variety of applications, their poor adhesion to the substrate is a major limitation. In order to overcome this limitation, a facile route, combination of a two-step anodic treatment and heat treatment was applied in order to develop a well-adhered TiO_2-based nanotubular surface on Ti-40Nb alloy. The adhesion of the nanotubular layer was evaluated by Daimler-Benz Rockwell C test. Corrosion and tribocorrosion behavior was investigated in phosphate-buffered saline solution (PBS) at body temperature. Corrosion behavior was examined by potentiodynamic polarization and electrochemical impedance spectroscopy whereas tribocorrosion behavior was evaluated by reciprocating sliding against an alumina ball at open circuit potential. Results showed that the adhesion, corrosion, and tribocorrosion behavior of the nanotubular layer was drastically improved with the combination of a two-step anodic treatment and heat treatment.

Keywords: Adhesion; TiO_2 nanotubes; Beta Titanium alloys; corrosion; tribocorrosion

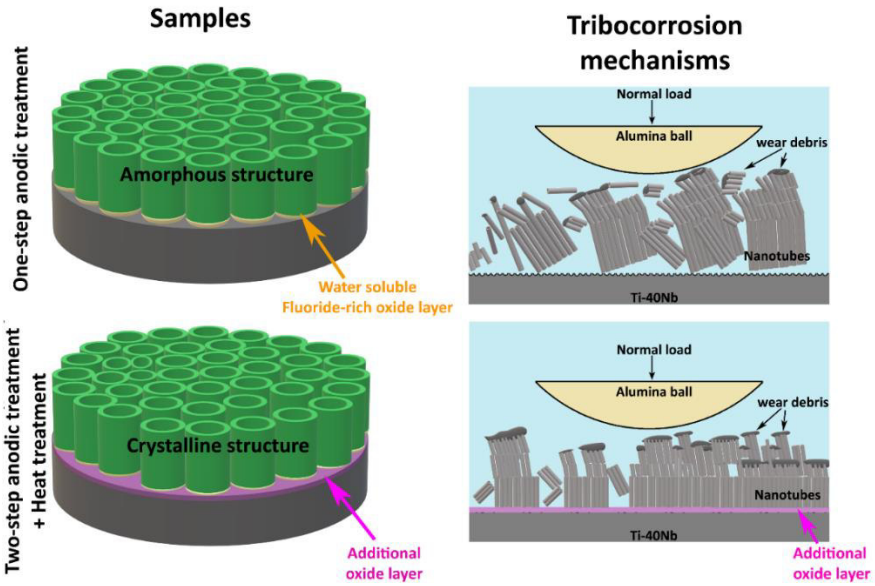

Graphical abstract

6.1. Introduction

Titanium (Ti) and its alloys have attracted attention for biomedical applications because of their combination of unique properties as compared to 316L stainless steel and Co-Cr alloys [1]. However, it is well documented that Ti and its alloys possess poor wear resistance that limits their usage in biomedical applications due to releasing of wear debris and metallic ions that may result in adverse local tissue reactions [2,3]. In addition, some clinical concerns exist about widely used Ti-6Al-4V alloy not only due to the toxicity of vanadium but also due to the presence of aluminum that is suspected to be associated with Alzheimer's disease [4,5]. Moreover, the Young's modulus of Ti and Ti-6Al-4V is significantly higher than that of the bone, leading to bone resorption and eventually revision surgeries [6,7]. Therefore, new β-type Ti alloys have been developed, containing non-toxic elements (Nb, Ta, Mo, Zr, etc.) and presenting significantly lower Young's modulus [8]. Among these new alloys, Ti-Nb based alloys gained a considerable attention for load-bearing implants not only due to their low Young's modulus but also due to their good corrosion behavior and biocompatibility [8].

Ti-based alloys are bioinert materials, however, their bioactivity can be improved with suitable surface modifications. TiO_2-based nanotubular (TNT) surfaces formed by anodic treatment presents self-organized, well-aligned, and controllable morphologies and they have been widely investigated for various applications to be used in several fields, such as solar cells [9,10], photocatalysis [11], water splitting [12,13], supercapacitors [14], and biomaterials [15]. Regarding biomaterials, TNT surfaces grown on Ti and its alloys exhibited better apatite formation, osteoblast adhesion, proliferation, and differentiation compared to their untreated substrates [16–18].

Corrosion is one of the main factors for a metallic material to be used in the human body since body fluids are corrosive environments. Ti and its alloys present excellent corrosion resistance because they spontaneously form a passive oxide layer on their surface, however, it may not be protective enough in an aggressive environment [19]. Yu *et al.* [20] studied the corrosion behavior of TNT surface on Ti in Hank's solution and reported that TNT surfaces exhibited higher corrosion resistance than the untreated Ti due to a thicker barrier layer supplied by the TNT layer. Similar behavior was reported for TNT formed on β-type Ti-35Nb-4Zr alloy tested in 9 g/l NaCl solution [21]. Nevertheless, the integrity of the TNT layer strongly influences the corrosion behavior. For instance, comparing to its bare alloy, Saji *et al.* [22] reported lower corrosion resistance for the TNT layer developed on the β-type Ti-35Nb-5Ta-7Zr alloy due to the presence of open spaces between the bottom of the tubes and the substrate. On the other hand, studies showed that the corrosion resistance of the TNT was significantly improved with heat treatment owing to the transformation of amorphous nanotubular structure to crystalline structure [20,23,24].

While some authors reported better biocompatibility for β-type Ti alloys over the Ti-6Al-4V alloy [25–27], lower wear resistance was reported for several β-type Ti alloys tested in 9 g/l NaCl solution [28], Ringer's solution [29], simulated body solution [30], and under dry sliding condition [31], mainly due to low strain hardening behavior of the β phase. To improve the wear resistance of Ti and its alloys, TNT surfaces have been proposed and investigated in the literature. Rodrigues *et al.* [32] showed that the tribocorrosion behavior of TNT grown on Ti-6Al-4V alloy by anodic treatment in H_2SO_4 based electrolyte during 1 h presented promising results as significantly lower tendency to corrosion under sliding compared to the untreated alloy. However, after tribocorrosion tests, Alves *et al.* [33,34] reported an easy detachment of the TNT layer, formed by anodic treatment in ethylene glocol based electrolyte, while the tribocorrosion behavior of TNT layer grown on Ti was significantly improved by the formation of a thick oxide layer at the interface formed during an additional cycle of reverse polarization anodic treatment. Then, Luz *et al.* [35] showed a lower wear rate for TNT formed on Ti-35Nb alloy by anodic treatment in H_3PO_4 based electrolyte during 160 min following by heat treatment, tested under dry sliding with 1 N of normal load against alumina ball, but tribocorrosion behavior is yet to be known.

Among the developed β-type Ti alloys, one of the most studied and proposed alloy for load-bearing implant aplications is Ti-40Nb alloy due to an appropriate combination of promising properties [36–42]. Recently, some of the present authors reported that the cast Ti-40Nb alloy has significantly lower tribocorrosion resistance compared to commercial Ti-6Al-4V in a physiological solution at body temperature, pointing the necessity of an appropriate modification for long term implantation [28]. The

tribocorrosion resistance may be improved by the formation of an oxide nanotubular structure [32,34], however, it has been reported that the nanotubes grown on Ti have significantly poor adhesion to the substrate [43–45]. In this study, in order to overcome the poor adhesion of the TNT layer to the bare metal, an additional anodic treatment was performed in fluoride-free electrolyte after the formation of the nanotubes in the conventional fluoride-containing electrolyte in order to form an additional oxide layer at the interface between the bare metal and the nanotubes. Additionally, a heat treatment was performed to investigate the effect of the crystallization of the nanotubular layer. The adhesion of TNT layers was studied by Daimler-Benz Rockwell C adhesion test whereas the corrosion and tribocorrosion behavior were investigated in PBS solution at body temperature.

6.2. Materials and methods

6.2.1. Sample preparation

Ti-40Nb (% wt.) alloy was processed by powder metallurgy (P/M) from TiH_2 (D_{50} 27 μm, GfE) and Nb (D_{50} 15 μm, Alfa Aesar) powders. Cylinder samples of 14 mm diameter and 3 mm thickness were obtained by sintering at 1250 °C for 4 h. Other details of the processing procedure are given elsewhere [46]. The samples were ground with SiC papers up to 2400 mesh and polished with colloidal silica suspension (Buehler, 0.02 μm) until obtaining mirror-finished surface. Microstructural analysis was carried out after etching with Kroll's reagent (%3 vol. HF + %6 vol. HNO_3 + %91vol. H_2O). Then, the samples were ultrasonically cleaned in propanol and distilled water for 10 min and 5 min, respectively, and dried with hot air. Both anodic treatments were carried out using a DC power supply (Agilent Technologies N5772A) and multimeter (Agilent Technologies 34410A) connected to a two-electrode electrochemical cell set-up. A platinum sheet was used as a cathode having an exposed area of 5.3 cm^2 whereas 1.1 cm^2 of Ti-40Nb surfaces were exposed to the electrolyte, working as anode. The distance between the working and the counter electrode was 8 cm. The nanotubular layer was obtained using an aqueous solution of 1.0 M H_3PO_4 (orthophosphoric acid, Fluka, ≥ %85) and 0.8 wt% NaF (Panreac, %99) as 180 ml volume of electrolyte, at a constant voltage of 20 V for 1 h under continuous magnetic stirring (500 rpm). In order to fabricate an additional oxide layer between the nanotubular layer and the substrate, the as-obtained nanotubular surfaces were immersed in a fluoride-free electrolyte of 1.0 M H_3PO_4 and then a second anodic treatment was carried out under constant 20 V for 5 min. After the second anodic treatment, the samples were rinsed with propanol and distilled water. The heat treatment was performed at 500 °C for 3 h with a heating and cooling rate of 5 °C min^{-1}. Groupings of surfaces are given in Table 6.1.

Table 6.1. Groupings of surfaces.

Sample	Description
S	Polished surface
A	One-step anodic treatment
AH	One-step Anodic treatment + Heat treatment
2A	Two-step anodic treatment
2AH	Two-step anodic treatment + Heat treatment

6.2.2. Corrosion and tribocorrosion experiments

Corrosion and tribocorrosion behavior were investigated in PBS solution (0.2 g/l KCl, 0.24 g/l KH_2PO_4, 8 g/l NaCl, 1.44 g/l Na_2HPO_4) at body temperature (37 ± 2 °C). Corrosion tests were performed on 0.38 cm^2 of exposed area in 180 ml by means of open circuit potential (OCP) monitoring, electrochemical impedance spectroscopy (EIS), and potentiodynamic polarization. Conventional three-electrode set up was utilized where a Pt electrode was used as counter electrode (CE), saturated calomel electrode (SCE) was used as reference electrode (RE), and samples were used as working electrode (WE), connected to a Potentiostat/Galvanostat/ZRA (Gamry Reference-600®). After stabilization of samples at OCP (ΔE<60 mV/h), EIS measurements were performed at OCP and the spectra were acquired over a frequency range of 10 mHz to 100 kHz with a 10 mV of AC signal and 7 points per decade. Gamry Echem Analyst (version 7.05) was used for fitting the EIS experimental data. The potentiodynamic polarization scan was performed starting at −0.25 V_{OCP} up to 1.5 V_{SCE} in anodic direction with a scan rate of 0.5 mV/s.

Tribocorrosion tests were performed at OCP with a tribometer (CETR-UMT-2) of pin-on-plate reciprocating sliding configuration. A two-electrode set-up was used where the samples were placed as WE against an alumina ball (10 mm in diameter, Ceratec) using a Potentiostat/Galvanostat/ZRA (Gamry Reference-600). The tests were carried out under a frequency of 1 Hz, a normal load of 0.5 N, and an amplitude of 2 mm. 30 min of sliding started after the stabilization of OCP at least for 2 h and ΔE was below 60 mV/h. After sliding, the counter material was removed and OCP continued to be recorded for 30 min.

All corrosion and tribocorrosion tests were at least triplicated on three different samples and all results were presented as the arithmetic mean ± standard deviation.

6.2.3. Characterization

Surfaces, cross-sections, and wear tracks were analyzed by field emission gun scanning electron microscope (FEG-SEM, FEI Nova 200). The structural characterization was employed by X-ray diffraction (XRD, Bruker D8 Discover diffractometer) by grazing incidence mode, scanning from an angle (2θ) 20° to 80° at 3° with a 0.03°/s step size. The phase percentages were calculated by following Eq. (1), where I is the intensity.

$$\%\, phase_{\alpha} = \frac{\sum I_{\alpha\, peaks}}{\sum I_{all\, peaks}} \quad \text{Eq. (1)}$$

The TNT grown samples were broken by three-point bending set up (Instron 8874) in order to analyze the cross-section of TNT layers. The distance between the two parallel supports was 10 mm. After, the indenter was driven down to the specimens at a speed of 8.33×10^{-6} m/s until the fracture of the sample. Vickers microhardness was determined using Emcotest Durascan tester by 10 indentations performed randomly per 3 different samples with a load of 0.98 N (0.1 kgf). The average surface roughness (R_a) was evaluated by 3D profilometry (Profilm3D). Adhesion of the nanotubular layer was evaluated by Daimler-Benz Rockwell C test, using a load of 150 kg with 200 μm tip radius conical Rockwell C indenter for at least three indentions per sample on Officine Galileo Mod. D200 tester. The damage around indentation scars were analyzed by FEG-SEM (FEI Quanta 650) and the quality of the adhesion layer was evaluated by comparing with quality maps from VDI 3198 standard [47]. Surface wettability was accessed by contact angle measurements through a sessile drop method using an optical tensiometer (Theta Lite) controlled by OneAttension software. A 5 μl droplet of ultra-pure water was dropped on the surface of the samples and the contact angle was considered after 10 s at room temperature. Three different samples per group were analyzed and the drop image was recorded by using a video camera.

6.3. Results

6.3.1. Characterization of the nanotubular films

SEM image of the Ti-40Nb alloy etched surface, representative anodic current evolution of first-step and second-step anodic treatments, and the resulting nanotubular surfaces are shown in Fig. 6.1, together with the insets showing the images of the contact angles of the corresponding samples. Ti-40Nb alloy presented an equiaxial β grain microstructure (Fig. 6.1a). The representative anodic current evolution of first-step anodic treatment is considered to show the formation process of TNT, where three different stages were observed from the curve. First stage is the growth of a barrier oxide layer resulted

in an exponential decline of the current, second one is the starting of the nucleation of nanotubes causing an increase on current after reaching a minimum, and the final one is the formation of TNT where current remains stable with time. The current evolution of the second-step anodic treatment suggests the formation of a compact oxide layer, considering its values approaching to zero [48]. The difference between the current evolutions of one-and two-step anodic treatment may be due to the compacted oxide layer between the nanotubular layer and the substrate for 2A and 2AH groups. Uniformly distributed and vertically well-aligned nanotubes were obtained on all sample surfaces. No visible influence of the second-step anodic treatment and heat treatment was observed on the surface morphology where nanotubes exhibited an average outer diameter of ~ 95 nm. The nanotubular surface modification drastically changed wettability behavior of the alloy, where no visible difference observed among the TNT formed groups. XRD pattern of all samples are shown in Fig. 6.1g. Group S was mainly composed of β-Ti phase (ICDD 00-044-1288) with some minor α-Ti phase (ICDD 00-044-1294). The A and 2A groups presented the same peaks of group S indicating that the TNT were formed as amorphous structures, whereas both heat-treated groups (AH and 2AH) showed anatase (ICCD 00-021-1272) and rutile (ICCD 01-070-7347) phases. The nanotubular layer on group AH was composed of 71% anatase and 29% rutile phases, while group 2AH presented 59% anatase and 41% rutile phases.

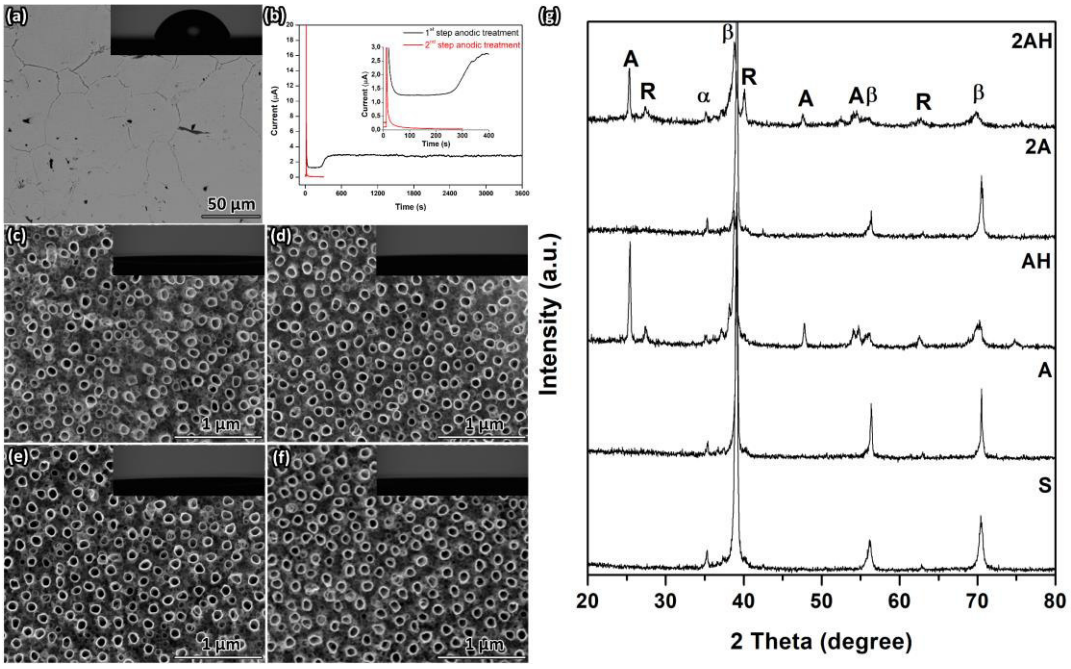

Fig. 6.1. Characterization of the nanotubular films: a) back-scattered electron (BSE) SEM image of S; b) current evolution of one and two-step anodic treatment; secondary electron (SE) SEM images of c) A, d) AH, e) 2A, and f) 2AH (the inset images present the wettability of the corresponding group of samples); g) XRD pattern of the substrate and the treated groups.

Fig. 6.2 presents SEM images of the TNT formed samples, broken to observe the cross-sections. All functionalized samples presented bamboo-like structure nanotube arrays having similar length of ~ 1.6 μm. The hollow spaces observed between the TNT layers and the substrates for group A, 2A, and AH suggested poor adhesion of the nanotubes. The hemispherical bottom of nanotubes was clearly observed for these samples; however, they were embedded in the additional oxide layer in the case of 2AH groups. Interastingly, the TNT layer appears to be non-embedded in additional oxide layer for group 2A (Fig. 6.2c). For a further insight to the additional oxide layer and the TNT layer, further SEM images were given in Figs. 6.2d and e. As observed, the additional oxide layer on group 2A presented poor integration to the nanotubular layer with many large cracks resulted from mechanical bending process.

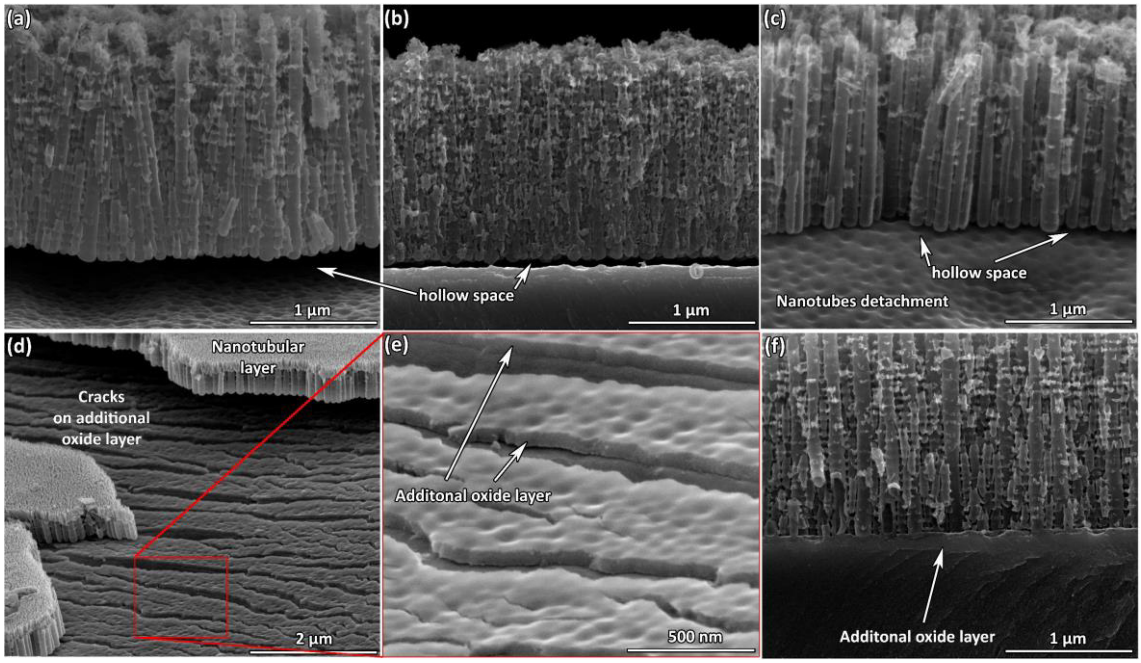

Fig. 6.2. Cross-section SE/SEM images of nanotubes grown on Ti-40Nb alloy for a) A; b) AH; c, d, and e) 2A; and f) 2AH groups.

Table 6.2. displays the hardness and R_a values of samples. The hardness value of the untreated group was notably lower than the anodic treated groups. The second anodic treatment and heat treatment also led to an increase of hardness, where the highest value was observed for group 2AH. Concerning the R_a values, all treated groups exhibited similar values that were obviously higher than the untreated group.

Table 6.2. The hardness and R_a values of the substrate and the treated groups.

Samples	Hardness $HV_{0.1}$	Average surface roughness-R_a (nm)
S	243 ± 6	20 ± 3
A	298 ± 7	130 ± 17
AH	330 ± 15	129 ± 11
2A	340 ± 19	135 ± 15
2AH	349 ± 17	130 ± 15

6.3.2. Adhesion behavior of nanotubular films

The Daimler-Benz Rockwell C adhesion test is a fast and easy method that has been studied to evaluate the adhesion of hard coatings [49,50] that can also be used for TNT layers [51]. The Daimler-Benz Rockwell-C adhesion test results are shown in Fig. 6.3. According to VDI 3198 standard [47], HF1 to HF4 represent acceptable adhesion where the minor cracks and delamination are observed, unlike, HF5 and HF6 correspond to poor adhesion with a large area of delamination around the indentation. A large amount of delamination area was observed around the Rockwell-C indentation scar for the single-step anodic treated groups indicating poor adhesion of the nanotubular layer corresponding to HF6 (Fig. 6.3a). On the contrary, there was no delamination of the nanotubular layer around the indentation scar of groups AH, 2A, and 2AH, although the radial cracks were observed on their indentation scars. It can be stated that groups AH, 2A and 2AH indicated acceptable adhesion of nanotubular layer with quality of HF1.

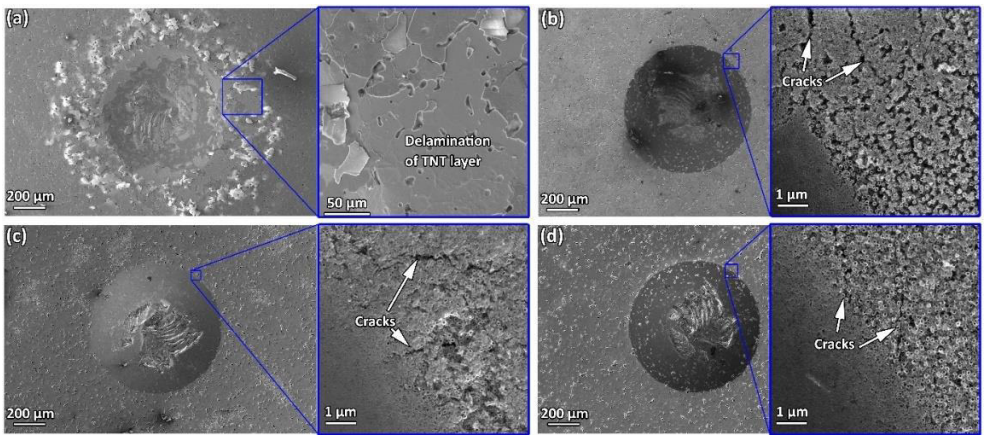

Fig. 6.3. SE/SEM images of Daimler-Benz Rockwell C adhesion test for a) A, b) AH, c) 2A, and d) 2AH groups.

6.3.3. Corrosion behavior

The corrosion kinetics was studied by potentiodynamic polarization in PBS solution at body temperature and the results are given in Fig. 6.4a, together with the obtained corrosion potential ($E_{(i=0)}$) and passivation current density (i_{pass}) (taken at 0.5 V vs. SCE for all groups). Groups S and A presented considerably lower corrosion potential as compared to groups AH and 2A, which presented significantly lower than group 2AH. The untreated group and both single-step anodic treated groups showed well-defined passivation plateau, while the current density of the two-step anodic treated groups tended to increase (more evidenced for group 2A) on the anodic domain. As can be seen in table on Fig. 6.4a, both groups A and AH showed higher i_{pass} values than the untreated group, groups 2A and 2AH presented lower values. Also, it is important to pointed out, group 2AH is showed two orders of magnitude lower i_{pass} values from group A.

The EIS results in the form of Bode diagrams and the electrical equivalent circuits (EECs) used for fitting experimental data are given in Fig. 6.4. The EEC parameters are given in Table 6.3. All samples presented the goodness of fitting below 10^{-4} pointed out an adequate quality of fitting of the proposed EECs. The Bode diagrams showed one-time, two-time and three-time constants for group S; group A; and groups AH, 2A, and 2AH, respectively, that were fitted with EECs composed with resistances and constant phase elements (CPE). The R_e represents the resistance of electrolyte for all EECs. Regarding the untreated alloy (S group), R_1/Q_1 pair corresponds to the resistance and CPE of the natural passive film. On the other hand, R_1/Q_1 pair corresponds to the resistance and CPE of the outer porous layer for nanotubes formed samples. The R_2/Q_2 pair indicates the resistance and CPE of the inner-tube layer. Although the R_3/Q_3 pair presents the same physical meaning for groups AH, 2A, and 2AH, it corresponds to different nature of the additional oxide layer formed through heat treatment, second-step anodic treatment, and combination of second-step anodic treatment and heat treatment, respectively. The Q shows the CPE that represents a non-ideal capacitor, and the impedance is defined as $Z_{CPE} = [Y_o(jw)^n]^{-1}$, where Y_o is a frequency-independent parameter, j is an imaginary number, n the CPE exponent ($-1 \leq n \leq 1$; $n = -1, 0, and\ 1$ presenting an inductor, a resistor, and an ideal capacitor, respectively), and $w = 2\pi f$ is the angular frequency.

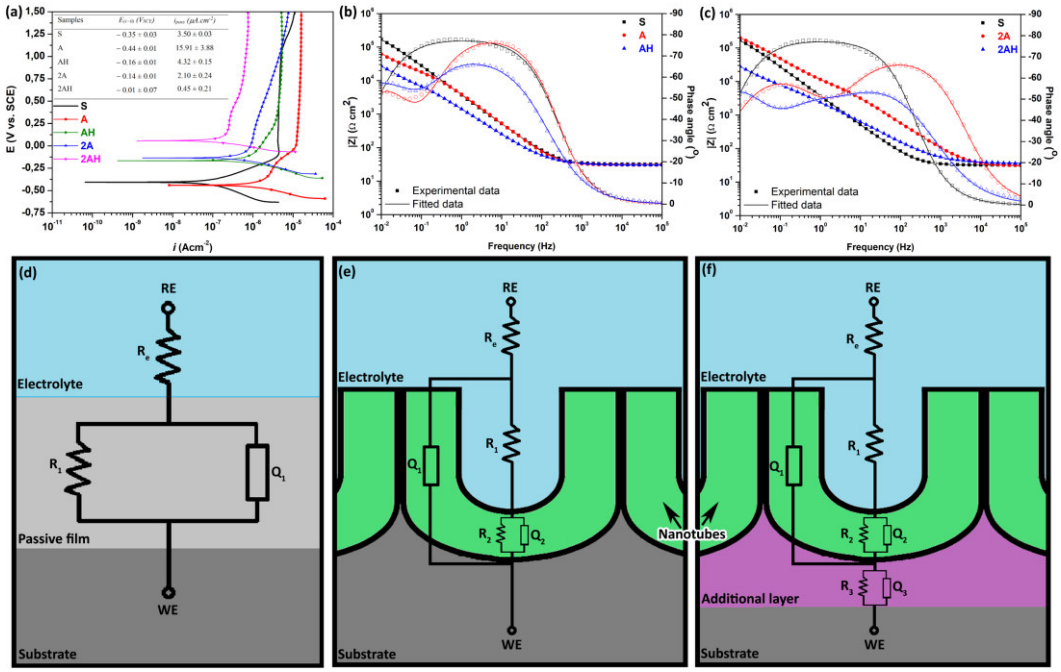

Fig. 6.4. Corrosion behavior of the TNT surfaces: a) Potentiodynamic polarization curves including $E_{(i=0)}$ and i_{pass} values; Bode diagrams of b) S, A, and AH (substrate with single-step anodic treated groups), c) S, 2A, and 2AH (substrate with two-step anodic treated samples); EECs proposed for d) group S, e) group A, and f) groups AH, 2A, and 2AH.

Table 6.3. EIS parameters obtained by fitting with corresponding EECs.

Groups	R_1 (kΩ cm²)	Q_1 (x10⁻⁵ S sⁿ cm⁻²)	R_2 (kΩ cm²)	Q_2 (x10⁻⁵ S sⁿ cm⁻²)	R_3 (kΩ cm²)	Q_3 (x10⁻⁵ S sⁿ cm⁻²)
S	351 ± 39	6 ± 1	-	-	-	-
A	3 ± 2	11 ± 7	34 ± 9	18 ± 5	-	-
AH	4 ± 3	26 ± 6	111 ± 26	51 ± 6	3 ± 1	63 ± 14
2A	4 ± 1	10 ± 2	33 ± 4	16 ± 3	378 ± 87	16 ± 3
2AH	5 ± 2	1 ± 1	100 ± 30	2 ± 1	1932 ± 47	1 ± 1

6.3.4. Tribocorrosion behavior

Representative curves of the evolution of the OCP before, during and after sliding in PBS at body temperature, together with recorded coefficient of friction (COF) values are shown in Fig. 6.5a. Before sliding, all samples presented stable OCP values due to the presence of a passive oxide layer in contact

with the electrolyte. As soon as sliding started, an abrupt drop was observed for group S from around −0.4 to approximately −0.9 V. Oscillations were observed during the sliding due to depassivation and repassivation mechanisms resulted from the periodic removal and growth of the passive film [52]. At the end of the sliding, the OCP immediately increased up to values close to the ones recorded before sliding, and remained stable due to repassivation of the worn area. As soon as the sliding started on groups A and 2A, smaller OCP drops were recorded and then a gradual decrease observed. After certain times, sharp OCP drops were observed on groups A and 2A then they gained their OCP. It is important to point out that this behavior happened at different times during sliding, and the most representative curves are shown in Fig. 6.5a. After sliding, both groups (A and 2A) presented progressively increase on OCP values, and the values did not reach to the initial level within the observation period. On the other hand, a distinct behavior was recorded on both heat-treated groups (AH and 2AH), where almost no influence of sliding was observed on the OCP values.

Regarding COF, the untreated group presented the highest values (0.7 ± 0.1) followed by A and 2A groups (0.6 ± 0.1), and AH and 2AH groups (0.5 ± 0.1). Besides, the COF evaluation of both heat treated groups tended to decrease during sliding.

The representative SEM images of wear tracks are also given in Fig. 6.5. Group S presented parallel ploughing grooves, adhered/oxidized patches, and plastic deformations. As compared to the other samples, relatively irregular wear track shapes were observed for both groups A and 2A, resulted from the detachment of the nanotubular layer. Comparing the center of the wear tracks, both groups A and 2A presented similar wear features to the substrate, being more evident on group A. Both heat treated groups (AH and 2AH) presented dissimilar behavior, where no evidence of detachment at the border of wear tracks nor sliding grooves were observed. Among the both heat treated group, group 2AH presented smaller wear track width and relatively darker wear track compared to group AH.

Higher magnification SEM images taken from the zones indicated with the red rectangles on the wear tracks of the TNT surfaces (Fig. 6.5). Detachment of the nanotubular layers on groups A and 2A can be seen more clearly on higher magnification images, whereas intact nanotubes covered by compacted wear products can be seen on groups AH and 2AH (Figs. 6.5d-f).

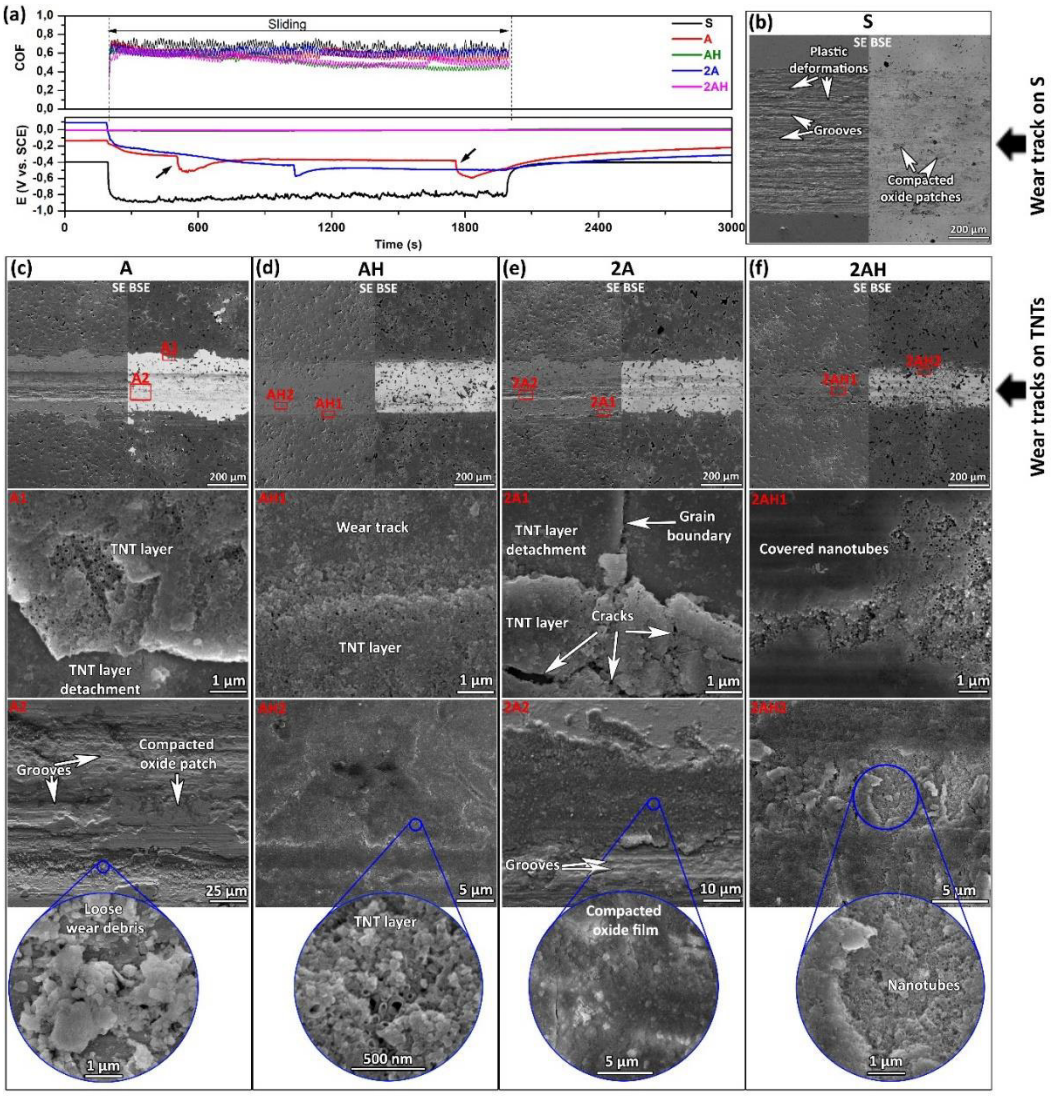

Fig. 6.5. Triboorrosion behavior of the TNT surfaces: a) Evolution of COF together with OCP before, during, and after sliding in PBS solution; b) representative low magnification SE and BSE wear track images of group S; lower and higher magnification SEM images of c) group A, d) group AH, e) group 2A, and f) group 2AH.

6.4. Discussion

6.4.1. Physical properties of TNT layers

The TiO_2 nanotubular formation mechanism is well reported in the literature [17–19]. Generally, TiO_2 nanotubes formed by anodic treatment present an amorphous structure that can be transformed to anatase starting at around 300 °C and to rutile starting at around 450 °C [20,21]. Sarraf *et al.* [53] reported that temperatures above 700 °C leads to a complete collapse of nanotubes. For this reason, in the present work, heat treatment temperature was selected as 500 °C in order to avoid the collapsing

of TNT layer and also to obtain a mixture of anatase and rutile phases. All anodic treated samples presented drastically higher hardness values as compared to the substrate due to the formation of a thicker oxide layer [22]. The high hardness value of group 2AH can be explained by its increased amount of rutile phase, having typical hardness value of 17 GPa, which has significantly higher hardness and Young's modulus properties than anatase phase, having typical hardness value of 8 GPa [54]. Regarding both amorphous groups (A and 2A) the higher hardness values of group 2A was possibly due to an additional oxide layer (Fig. 62e-f).

Contact angle assays revealed that the solution completely spread over the anodic treated samples while no visible difference was observed between them. TNT surfaces presented drastically lower values as compared to the substrate possibly due to increased surface roughness [55]. This behavior indicates that the hydrophobic behavior of the substrate is turned to hydrophilic behavior after the formation of nanotubes [24]. It has been well reported that the cell attachment, spreading, and cytoskeletal organization is better on hydrophilic surfaces than on hydrophobic ones [25–27]. Therefore, one can expect that the TNT layer on Ti-Nb alloy may lead to improved osteointegration, as higher cell adhesion and cell viability, that had already been reported for TNT grown Ti-Zr-Nb alloy [18].

Adhesion test indicated that the TNT formed by conventional anodic treatment presented significantly poor adhesion suggesting the need of additional treatments (Fig. 6.4a and Fig. 6.5a). While the presence of the additional oxide layer improved the adhesion of the nanotubular layer, the main improvement came from the heat treatment resulted in the transition of amorphous structure to crystalline structure. Xiong *et al.* [13] reported that heat treatment improved the adhesion of the TiO_2 nanotubular layer due to the formation of an oxide layer at the interface with the substrate, that might be a reason for the improved adhesion of group AH. However, as reported by Albu *et al.* [28], when TNT formed in a fluoride-containing electrolyte, an additional fluoride-rich interface layer formed between the bottom of nanotubes and the substrate and it can easily dissolve due to its water solubility. The fluoride species are not only present in the interface layer but also they are formed through all nanotubes, where the fluoride concentration decreases from bottom to upper part of nanotubes [56]. According to Regonini *et al.* [29], the significant reduction of fluoride concentration from 3.8 at% to 0.3 at% after heat treatment at 400 °C indicates that the fluorine species are expelled from the anodic film. This chemical dissolution may lead to the formation of voids and/or gaps at the interface, that may be the main reason for the weak adhesion of nanotubes [28,30]. In order to reduce the effect of these defects on adhesion of nanotubes, an additional oxide layer was formed at the interface by anodic treatment in the fluoride-free

electrolyte and a significant improvement was achieved due to fluoride-rich layer surrounded by an additional fluoride-free layer. Similar results were reported by Yu *et al.* [31] for cp-Ti anodic treated in ethylene glycol-based solution. However, as observed in Figs. 6.2d and 6.2e, the adhesion of the additional oxide layer and nanotubes were weak, and it is supposed that the adhesion was improved in the case of group 2AH due to the transformation of amorphous structure to crystalline structure with the heat treatment.

6.4.2. Corrosion behavior

Ti and its alloys present excellent corrosion resistance due to spontaneously formed 2 - 6 nm thick passive film [57], and their corrosion behavior is further improved with an anodic nanotubular layer [15,23,58]. The specific surface area calculation model for TiO_2 nanotubes has been reported in the literature [59–61]. Hilario *et al.* [62] calculated the specific surface area of TiO_2 nanotubes, formed at 20 V during 1 h, and it was reported that the treated surfaces presented 60 times larger surface area than the geometric area. In this study, the i_{pass} values were calculated by the geometric exposed area (0.38 cm^2). It was found that groups A and AH presented lower i_{pass} values than group S. However, it may be speculated that if the real exposure area of the nanotubes formed samples could precisely determined, all nanotubes formed samples might present lower i_{pass} values than the substrate. Nevertheless, among all tested groups, group 2AH had significantly lower i_{pass} values indicating a significantly lower corrosion rate. The decrement of i_{pass} values with heat treatment attributed to the stable behavior of anatase and rutile phases as compared to the amorphous phase [24]. Also, the increasing i_{pass} on group 2A may be attributed to lesser stability of passivation layer due to poor integration of the additional oxide layer resulted in the oxygen evolution and change in the electrical characteristics [62].

As abovementioned, while oxide layers formed at the nanotubes/substrate interface on groups AH, 2A, and 2AH played the similar physical barrier role against corrosion, they have different nature of the oxide layers. The formed oxide layer on group AH was resulted from thermal oxidation of substrate in oxygen containing atmospheres through heat treatment. The one formed on group 2A was due to electrochemical oxidation of substrate in H_3PO_4 solution by applying anodic potential. Finally, the one formed on group 2AH was consequence of the combination of electrochemical oxidation and thermal oxidation through a second-step anodic treatment and heat treatment, respectively. In order to further investigate the effect of these oxide layers on corrosion behavior, EIS was performed in PBS solution at body temperature, and the results were simulated by EECs. In the literature, similar EECs have been proposed for group S [27,63–65], group A [21,66,67], and groups AH, 2A, and 2AH [66–68]. Bode

diagrams revealed that only 2A group presented higher |Z| values than group S at low frequency range. Nevertheless, since the |Z| modulus was calculated by the geometric exposure area for all groups, as also discussed above for i_{pass} values, a precise determination of the real exposed area might shift the modulus of the anodic treated groups to higher |Z| modulus. On the other hand, R_2 values of all groups were higher than the corresponding R_1 values (Table 6.3) indicating that the bottom of the tubes played the main protective role against corrosion as also reported in the literature [20,66,67,69]. Although group AH presented higher R_2 values compared to group A, the increased Q_1 and Q_2 values of group AH suggests lower quality of TNT layer indicating that the heat treatment was exacerbated the corrosion behavior of the sample. The lower quality of TNT layer after heat treatment may be explained by the abovementioned defects in the interface of nanotube/substrate, as a consequence of the penetration of the electrolyte to the substrate through the voids among the fluoride-rich layer. The R_3 value of group AH was drastically lower than the ones recorded for group 2A suggesting that the oxide layers formed by the second-step anodic treatment presented significantly better protective properties than that the one formed after the heat treatment. Similarly, the Q_3 values of group AH was visibly higher than group 2A indicating that the quality of the oxide layer formed by the second-step anodic treatment was better than the one formed by the heat treatment. Regarding the two-step anodic treatment samples, the main protective role against corrosion was presented by an additional oxide layer, where the R_3 values of both groups 2A and 2AH were drasticaly higher than their R_1 and R_2 values. Furthermore, the resistance and quality of the oxide layer formed at the interface of group 2AH were significantly improved resulted from combination of the two-step anodic treatment and heat treatment, as expressed by drastically higher R_3 and lower Q_3 values, respectively. Also, it is worth note that since the R_2 values of both heat treated groups (AH and 2AH) were similar, the observed significantly lower Q_2 values for group 2AH may be related to the formed oxide layer after combination two-step anodic treatment and heat treatment prevented the formation of defects in the bottom/inner of tubes.

6.4.3. Tribocorrosion behavior

In this study, the tribocorrosion behavior was investigated at OCP condition, which is closer to the real implant system since no potential is applied [70]. When the sliding started, the recorded OCP drop for group S is attributed to the mechanical deformation of passive oxide layer and the exposure of the bare alloy to the fresh electrolyte. The observed large oscillations during sliding were resulted from fast depassivation and passivation phenomena, and regaining of its potential after sliding was due to the repassivation of the worn area, being a typical behavior for Ti and its alloys [28,71,72]. Regarding both amorphous nanotubes formed groups (A and 2A), as soon as sliding started, gradual decreases in OCP

values were observed, suggesting a gradual mechanical damage given to the nanotubular layer. After a certain time, the observed sharp drop on OCP may be explained by the partial detachments of the nanotubular layer as also confirmed by wear track images. As discussed above, groups A and 2A presented poor adhesion of nanotubular layers, thus, the wear debris coming out from detachment of nanotubular layers may acted as third body or got pressed between the contacting surfaces resulting in formation of a discontinuous tribolayer. Similar behavior reported by Alves *et al.* [34] for TNT formed on cp-Ti, tested in artificial saliva against alumina ball under 1 N normal load. This discontinuous tribolayer may give a limited protection against wear and corrosion, however, after reaching a certain thickness, it may be removed by the counter material resulting in a rapid drop on the OCP as observed for group A (indicated by arrows on Fig. 6.5a).

In the case of both heat-treated groups (AH and 2AH), once sliding started, the OCP was almost not affected by sliding, indicating thermodynamically an excellent protection against sliding alumina counter body under the testing conditions. Gradually decreased COF values for these groups may also be attributed to the stronger TNT layers, i.e. lesser formation of hard third-bodies due to lesser damage on the TNT layers and formation of a tribolayer (compacted oxides) on a smoother wear surface. Overall, the improved protection for these two groups against alumina may be explained by good adhesion and formation of harder anatase/rutile nanotubular layers. The anatase/rutile crystalline nanotubes showed better tribological behavior as compared to the amorphous surfaces, resulted from the improvement of mechanical properties [35,53,73,74]. As mentioned above, rutile phase presents higher hardness and Young's modulus than anatase phase. According to the literature [48,75,76], within the processing conditions of the present work, rutile phase can be expected to form mainly at the TNT/substrate interface and anatase is in the TNT layer. The higher concentration of the rutile phase in group 2AH may be attributed to the transformation of the amorphous additional oxide layer formed by the second-step anodic treatment to rutile phase. Thus, the improved tribocorrosion behavior of group 2AH may be explained by the improved adhesion of the nanotubular layer and higher hardness due to the increased amount of the rutile phase.

Fig. 6.6 shows a schematic illustration of wear mechanisms for nanotubes formed samples. Wear mechanisms of Ti-40Nb alloy were schematically reported elsewhere, where it presented dominantly abrasive and adhesive wear [28,71]. Regarding nanotubes formed samples, as observed on SEM images (Figs. 6.5c and 6.5e), both A and 2A groups showed similar wear mechanisms, mainly smashing and densification of the nanotubes, affiliated by full delamination of nanotubular layer most

probably due to their amorphous structure and relatively poor adhesion. Similar full delamination mechanisms through cracks formation and propagation from surface to bottom regions of film have already reported by Alves *et al.* for TNT formed on cp-Ti [33,34]. In case of both heat-treated groups (AH and 2AH), the smashing and densification of tubes on the top region took place, however, instead of gross delamination of nanotubes, partial crack formation and delamination are occurred from top to bottom as can be seen from their wear track SEM images (Fig. 6.5d and 6.5f), attributed to their crystalline (anatase and rutile) structure, together with enhanced adhesion.

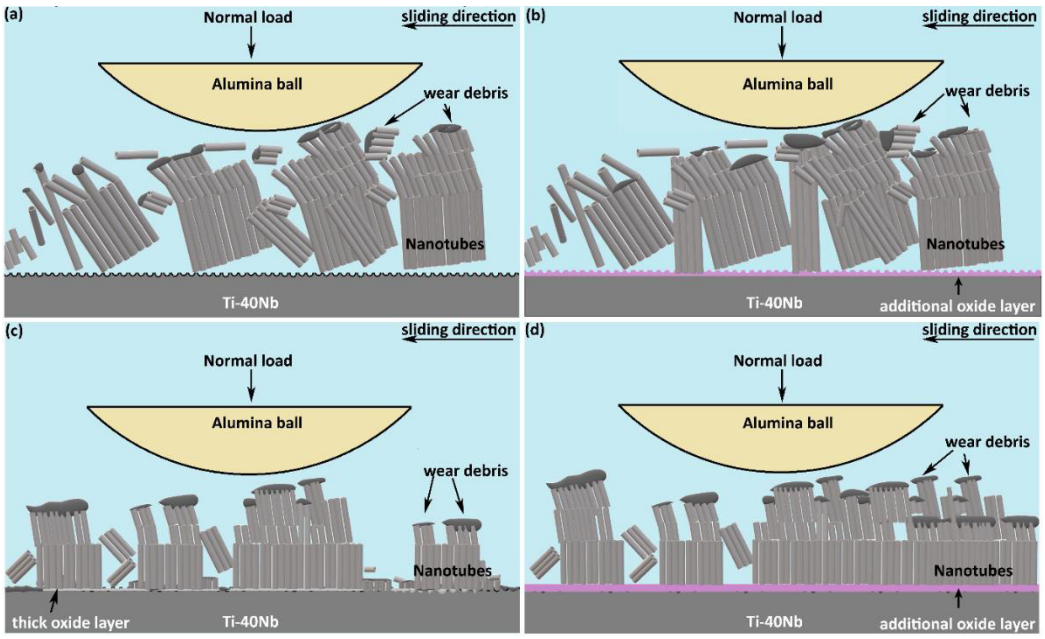

Fig. 6.6. Schematic illustration of wear mechanism of (a) A, (b) 2A, (c) AH, and (d) 2AH samples (inspired from [34]).

6.5. Conclusion

TNT surfaces formed conventionally on Ti-40Nb by anodic treatment presented poor adhesion. The adhesion of nanotubes was improved drastically by a combined route, where a second-step anodic treatment in fluoride-free electrolyte resulted in formation of an additional oxide layer in the interface, and a following heat treatment yielded with a crystalline transformation. While heat treatment mainly played a role on improving the tribocorrosion behavior due to formation of crystalline structure, the combination of formation of an additional oxide layer in the interface and heat treatment mainly played a role on improving the corrosion behavior by preventing the formation of defects at the interface thus blocking the penetration of electrolyte to the substrate. Therefore, within the limitations of this work, it can be stated that this facile and low-cost nanoscale surface modification technique seems to be a promising method to overcome the poor tribocorrosion behavior of β-type Ti-40Nb alloy processed by powder metallurgy.

Acknowledgments

This work was supported by FCT national funds, under the national support to R&D units grant, through the reference project UIDB/04436/2020 and UIDP/04436/2020, together with M-ERA-NET/0001/2015 and PCIN-2016-123 project. I. Çaha is grateful for the financial support through a Ph.D. grant under the NORTE-08-5369-FSE-000012 project.

References

[1] J.M. Cordeiro, V.A.R. Barão, Is there scientific evidence favoring the substitution of commercially pure titanium with titanium alloys for the manufacture of dental implants?, Mater. Sci. Eng. C. 71 (2016) 1201–1215. doi:10.1016/j.msec.2016.10.025.

[2] S. Rashdan, L.S. Roselin, R. Selvin, O.M. Lemine, M. Bououdina, 1 - Nanoparticles for biomedical applications: current status, trends and future challenges, in: J.P.B.T.-B. and M.T. Davim (Ed.), Woodhead Publ. Ser. Biomater., Woodhead Publishing, 2013: pp. 1–132. doi:https://doi.org/10.1533/9780857092205.1.

[3] F. Eltit, Q. Wang, R. Wang, Mechanisms of adverse local tissue reactions to hip implants, Front. Bioeng. Biotechnol. 7 (2019) 1–17. doi:10.3389/fbioe.2019.00176.

[4] X. Yang, H. Pan, J. Zhang, H. Gao, B. Shu, Y. Gong, X. Zhu, Progress in mechanical properties of gradient structured metallic materials induced by surface mechanical attrition treatment, Mater. Trans. 60 (2019) 1543–1552. doi:10.2320/matertrans.MF201911.

[5] M. Geetha, A.K. Singh, R. Asokamani, A.K. Gogia, Ti based biomaterials, the ultimate choice for orthopaedic implants - A review, Prog. Mater. Sci. 54 (2009) 397–425. doi:10.1016/j.pmatsci.2008.06.004.

[6] A. Panigrahi, B. Sulkowski, T. Waitz, K. Ozaltin, W. Chrominski, A. Pukenas, J. Horky, M. Lewandowska, W. Skrotzki, M. Zehetbauer, Mechanical properties, structural and texture evolution of biocompatible Ti–45Nb alloy processed by severe plastic deformation, J. Mech. Behav. Biomed. Mater. 62 (2016) 93–105. doi:10.1016/j.jmbbm.2016.04.042.

[7] Y. Okazaki, E. Gotoh, Comparison of metal release from various metallic biomaterials in vitro, Biomaterials. 26 (2005) 11–21. doi:10.1016/j.biomaterials.2004.02.005.

[8] M. Niinomi, M. Nakai, J. Hieda, Development of new metallic alloys for biomedical applications, Acta Biomater. 8 (2012) 3888–3903. doi:10.1016/j.actbio.2012.06.037.

[9] J. Yan, F. Zhou, TiO2 nanotubes: Structure optimization for solar cells, J. Mater. Chem. 21 (2011) 9406–9418. doi:10.1039/c1jm10274e.

[10] G. Liu, K. Wang, N. Hoivik, H. Jakobsen, Progress on free-standing and flow-through TiO 2 nanotube membranes, Sol. Energy Mater. Sol. Cells. 98 (2012) 24–38. doi:10.1016/j.solmat.2011.11.004.

[11] J. Zhou, L. Yin, K. Zha, H. Li, Z. Liu, J. Wang, K. Duan, B. Feng, Hierarchical fabrication of heterojunctioned SrTiO3/TiO2 nanotubes on 3D microporous Ti substrate with enhanced photocatalytic activity and adhesive strength, Appl. Surf. Sci. 367 (2016) 118–125. doi:10.1016/j.apsusc.2016.01.096.

[12] Q. Gui, Z. Xu, H. Zhang, C. Cheng, X. Zhu, M. Yin, Y. Song, L. Lu, X. Chen, D. Li, Enhanced photoelectrochemical water splitting performance of anodic TiO2 Nanotube arrays by surface passivation, ACS Appl. Mater. Interfaces. 6 (2014) 17053–17058. doi:10.1021/am504662w.

[13] Y.H. Chiu, T.H. Lai, C.Y. Chen, P.Y. Hsieh, K. Ozasa, M. Niinomi, K. Okada, T.F.M. Chang, N. Matsushita, M. Sone, Y.J. Hsu, Fully Depleted Ti-Nb-Ta-Zr-O Nanotubes: Interfacial Charge Dynamics and Solar Hydrogen Production, ACS Appl. Mater. Interfaces. 10 (2018) 22997–23008. doi:10.1021/acsami.8b00727.

[14] L. Zheng, Y. Dong, H. Bian, C. Lee, J. Lu, Y.Y. Li, Self-ordered Nanotubular TiO2 Multilayers for High-Performance Photocatalysts and Supercapacitors, Electrochim. Acta. 203 (2016) 257–264. doi:10.1016/j.electacta.2016.04.049.

[15] S. Minagar, C.C. Berndt, J. Wang, E. Ivanova, C. Wen, A review of the application of anodization for the fabrication of nanotubes on metal implant surfaces, Acta Biomater. 8 (2012) 2875–2888. doi:10.1016/j.actbio.2012.04.005.

[16] A.W. Tan, B. Pingguan-Murphy, R. Ahmad, S.A. Akbar, Review of titania nanotubes: Fabrication and cellular response, Ceram. Int. 38 (2012) 4421–4435. doi:10.1016/j.ceramint.2012.03.002.

[17] D. Ding, C. Ning, L. Huang, F. Jin, Y. Hao, S. Bai, Y. Li, M. Li, D. Mao, Anodic fabrication and bioactivity of Nb-doped TiO2 nanotubes, Nanotechnology. 20 (2009) 2–8. doi:10.1088/0957-4484/20/30/305103.

[18] M. Qadir, J. Lin, A. Biesiekierski, Y. Li, C. Wen, Effect of Anodized TiO2-Nb2O5-ZrO2 Nanotubes

with Different Nanoscale Dimensions on the Biocompatibility of a Ti35Zr28Nb Alloy, ACS Appl. Mater. Interfaces. 12 (2020) 6776–6787. doi:10.1021/acsami.9b21878.

[19] M.C. García-Alonso, L. Saldaña, G. Vallés, J.L. González-Carrasco, J. González-Cabrero, M.E. Martínez, E. Gil-Garay, L. Munuera, In vitro corrosion behaviour and osteoblast response of thermally oxidised Ti6Al4V alloy, Biomaterials. 24 (2003) 19–26. doi:https://doi.org/10.1016/S0142-9612(02)00237-5.

[20] W. Yu, J. Qiu, L. Xu, F. Zhang, Corrosion behaviors of TiO2 nanotube layers on titanium in Hank' s solution, Biomed. Mater. 4 (2009) 0–5. doi:10.1088/1748-6041/4/6/065012.

[21] A.Z. Fatichi, M.G. Mello, R. Caram, A. Cremasco, Self-organized TiO2 nanotube layer on Ti–Nb–Zr alloys: growth, characterization, and effect on corrosion behavior, J. Appl. Electrochem. 49 (2019) 1079–1089. doi:10.1007/s10800-019-01345-8.

[22] V.S. Saji, H.C. Choe, W.A. Brantley, An electrochemical study on self-ordered nanoporous and nanotubular oxide on Ti-35Nb-5Ta-7Zr alloy for biomedical applications, Acta Biomater. 5 (2009) 2303–2310. doi:10.1016/j.actbio.2009.02.017.

[23] W. Jiang, H. Cui, Y. Song, Electrochemical corrosion behaviors of titanium covered by various TiO2 nanotube films in artificial saliva, J. Mater. Sci. 53 (2018) 15130–15141. doi:10.1007/s10853-018-2706-5.

[24] A. Mazare, G. Totea, C. Burnei, P. Schmuki, I. Demetrescu, D. Ionita, Corrosion, antibacterial activity and haemocompatibility of TiO2 nanotubes as a function of their annealing temperature, Corros. Sci. 103 (2016) 215–222.

[25] M. Niinomi, T. Hattori, K. Morikawa, T. Kasuga, A. Suzuki, H. Fukui, S. Niwa, Development of Low Rigidity β-type Titanium Alloy for Biomedical Applications, Mater. Trans. 43 (2002) 2970 to 2977. doi:10.2320/matertrans.43.2970.

[26] Y.L. Zhou, M. Niinomi, T. Akahori, H. Fukui, H. Toda, Corrosion resistance and biocompatibility of Ti-Ta alloys for biomedical applications, Mater. Sci. Eng. A. 398 (2005) 28–36. doi:10.1016/j.msea.2005.03.032.

[27] J.M. Cordeiro, T. Beline, A.L.R. Ribeiro, E.C. Rangel, N.C. da Cruz, R. Landers, L.P. Faverani, L.G. Vaz, L.M.G. Fais, F.B. Vicente, C.R. Grandini, M.T. Mathew, C. Sukotjo, V.A.R. Barão, Development of binary and ternary titanium alloys for dental implants, Dent. Mater. 33 (2017)

1244–1257. doi:10.1016/j.dental.2017.07.013.

[28] I. Çaha, A.C. Alves, P.A.B. Kuroda, C.R. Grandini, A.M.P. Pinto, L.A. Rocha, F. Toptan, Degradation behavior of Ti-Nb alloys: Corrosion behavior through 21 days of immersion and tribocorrosion behavior against alumina, Corros. Sci. 167 (2020) 108488. doi:10.1016/j.corsci.2020.108488.

[29] I. Cvijović-Alagić, Z. Cvijović, S. Mitrović, V. Panić, M. Rakin, Wear and corrosion behaviour of Ti-13Nb-13Zr and Ti-6Al-4V alloys in simulated physiological solution, Corros. Sci. 53 (2011) 796–808. doi:10.1016/j.corsci.2010.11.014.

[30] X. Yang, C.R. Hutchinson, Corrosion-wear of β-Ti alloy alloy TMZF (Ti-12Mo-6Zr-2Fe) in simulated body fluid, Acta Biomater. 42 (2016) 429–439. doi:10.1016/j.actbio.2016.07.008.

[31] Y.S. Lee, M. Niinomi, M. Nakai, K. Narita, K. Cho, Predominant factor determining wear properties of β-type and (α+β)-type titanium alloys in metal-to-metal contact for biomedical applications, J. Mech. Behav. Biomed. Mater. 41 (2015) 208–220. doi:10.1016/j.jmbbm.2014.10.005.

[32] N.R. Rodrigues, A.C. Alves, F. Toptan, L.A. Rocha, Preliminary investigation on the tribocorrosion behaviour of nanotubular structured Ti6Al4V surfaces, Mater. Lett. 213 (2018) 214–217. doi:10.1016/j.matlet.2017.11.067.

[33] S.A. Alves, A.L. Rossi, A.R. Ribeiro, F. Toptan, A.M. Pinto, T. Shokuhfar, J.P. Celis, L.A. Rocha, Improved tribocorrosion performance of bio-functionalized TiO2 nanotubes under two-cycle sliding actions in artificial saliva, J. Mech. Behav. Biomed. Mater. 80 (2018) 143–154. doi:10.1016/j.jmbbm.2018.01.038.

[34] S.A. Alves, A.L. Rossi, A.R. Ribeiro, F. Toptan, A.M. Pinto, J.P. Celis, T. Shokuhfar, L.A. Rocha, Tribo-electrochemical behavior of bio-functionalized TiO2 nanotubes in artificial saliva: Understanding of degradation mechanisms, Wear. 384–385 (2017) 28–42. doi:10.1016/j.wear.2017.05.005.

[35] A.R. Luz, G.B. De Souza, C.M. Lepienski, N.K. Kuromoto, C.J.M. Siqueira, Tribological properties of nanotubes grown on Ti-35Nb alloy by anodization, Thin Solid Films. 660 (2018) 529–537. doi:10.1016/j.tsf.2018.06.050.

[36] K. Zhuravleva, A. Chivu, A. Teresiak, S. Scudino, M. Calin, L. Schultz, J. Eckert, A. Gebert, Porous low modulus Ti40Nb compacts with electrodeposited hydroxyapatite coating for biomedical

applications, Mater. Sci. Eng. C. 33 (2013) 2280–2287. doi:10.1016/j.msec.2013.01.049.

[37] M. Calin, A. Helth, J.J. Gutierrez Moreno, M. Bönisch, V. Brackmann, L. Giebeler, T. Gemming, C.E. Lekka, A. Gebert, R. Schnettler, J. Eckert, Elastic softening of β-type Ti-Nb alloys by indium (In) additions, J. Mech. Behav. Biomed. Mater. 39 (2014) 162–174. doi:10.1016/j.jmbbm.2014.07.010.

[38] A. Gebert, D. Eigel, P.F. Gostin, V. Hoffmann, M. Uhlemann, A. Helth, S. Pilz, R. Schmidt, M. Calin, M. Göttlicher, M. Rohnke, J. Janek, Oxidation treatments of beta-type Ti-40Nb for biomedical use, Surf. Coatings Technol. 302 (2016) 88–99. doi:10.1016/j.surfcoat.2016.05.036.

[39] A. Helth, S. Pilz, T. Kirsten, L. Giebeler, J. Freudenberger, M. Calin, J. Eckert, A. Gebert, Effect of thermomechanical processing on the mechanical biofunctionality of a low modulus Ti-40Nb alloy, J. Mech. Behav. Biomed. Mater. 65 (2017) 137–150. doi:10.1016/j.jmbbm.2016.08.017.

[40] R. Schmidt, V. Hoffmann, A. Helth, P.F. Gostin, M. Calin, J. Eckert, A. Gebert, Electrochemical deposition of hydroxyapatite on beta-Ti-40Nb, Surf. Coatings Technol. 294 (2016) 186–193. doi:10.1016/j.surfcoat.2016.03.063.

[41] M. Göttlicher, M. Rohnke, A. Helth, T. Leichtweiß, T. Gemming, A. Gebert, J. Eckert, J. Janek, Controlled surface modification of Ti-40Nb implant alloy by electrochemically assisted inductively coupled RF plasma oxidation, Acta Biomater. 9 (2013) 9201–9210. doi:10.1016/j.actbio.2013.07.015.

[42] S. Pilz, A. Gebert, A. Voss, S. Oswald, M. Göttlicher, U. Hempel, J. Eckert, M. Rohnke, J. Janek, M. Calin, Metal release and cell biological compatibility of beta-type Ti-40Nb containing indium, J. Biomed. Mater. Res. - Part B Appl. Biomater. 106B (2017) 1686–1697. doi:10.1002/jbm.b.33976.

[43] M. Sun, D. Yu, L. Lu, W. Ma, Y. Song, X. Zhu, Effective approach to strengthening TiO2 nanotube arrays by using double or triple reinforcements, Appl. Surf. Sci. 346 (2015) 172–176. doi:10.1016/j.apsusc.2015.04.004.

[44] D. Yu, X. Zhu, Z. Xu, X. Zhong, Q. Gui, Y. Song, S. Zhang, X. Chen, D. Li, Facile method to enhance the adhesion of TiO2 nanotube arrays to Ti substrate, ACS Appl. Mater. Interfaces. 6 (2014) 8001–8005. doi:10.1021/am5015716.

[45] H.M. Ouyang, G.T. Fei, Y. Zhang, H. Su, Z. Jin, S.H. Xu, L. De Zhang, Large scale free-standing open-ended TiO2 nanotube arrays: Stress-induced self-detachment and in situ pore opening, J. Mater. Chem. C. 1 (2013) 7498–7506. doi:10.1039/c3tc31642d.

[46] C. Chirico, S. Tsipas, F. Toptan, E. Gordo, Development of Ti–Nb and Ti–Nb–Fe beta alloys from TiH2 powders, Powder Metall. 62 (2019) 44–53. doi:10.1080/00325899.2018.1563953.

[47] Verein Deutscher Ingenieure Normen, VDI 3198, VDI-Handbuch Betriebstechnik, 1991.

[48] P. Roy, S. Berger, P. Schmuki, TiO2 nanotubes: Synthesis and applications, Angew. Chemie - Int. Ed. 50 (2011) 2904–2939. doi:10.1002/anie.201001374.

[49] Ł. Łapaj, J. Wendland, J. Markuszewski, A. Mróz, T. Wiśniewski, Retrieval analysis of titanium nitride (TiN) coated prosthetic femoral heads articulating with polyethylene, J. Mech. Behav. Biomed. Mater. 55 (2016) 127–139. doi:10.1016/j.jmbbm.2015.10.012.

[50] I. Çaha, A.C. Alves, L.J. Affonço, P.N. Lisboa-Filho, J.H.D. da Silva, L.A. Rocha, A.M.P. Pinto, F. Toptan, Corrosion and tribocorrosion behaviour of titanium nitride thin films grown on titanium under different deposition times, Surf. Coatings Technol. 374 (2019) 878–888. doi:10.1016/j.surfcoat.2019.06.073.

[51] J. Xiong, X. Wang, Y. Li, P.D. Hodgson, Interfacial chemistry and adhesion between titanium dioxide nanotube layers and titanium substrates, J. Phys. Chem. C. 115 (2011) 4768–4772. doi:10.1021/jp111651d.

[52] V.G. Pina, A. Dalmau, F. Devesa, V. Amigó, A.I. Muñoz, Tribocorrosion behavior of beta titanium biomedical alloys in phosphate buffer saline solution, J. Mech. Behav. Biomed. Mater. 46 (2015) 59–68. doi:10.1016/j.jmbbm.2015.02.016.

[53] M. Sarraf, E. Zalnezhad, A.R. Bushroa, A.M.S. Hamouda, A.R. Rafieerad, B. Nasiri-Tabrizi, Effect of microstructural evolution on wettability and tribological behavior of TiO2 nanotubular arrays coated on Ti–6Al–4V, Ceram. Int. 41 (2015) 7952–7962. doi:10.1016/j.ceramint.2015.02.136.

[54] O. Zywitzki, T. Modes, H. Sahm, P. Frach, K. Goedicke, D. Glöß, Structure and properties of crystalline titanium oxide layers deposited by reactive pulse magnetron sputtering, Surf. Coatings Technol. 180–181 (2004) 538–543. doi:10.1016/j.surfcoat.2003.10.115.

[55] M. Qadir, Y. Li, A. Biesiekierski, C. Wen, Optimized Fabrication and Characterization of TiO2-

Nb2O5-ZrO2 Nanotubes on β-Phase TiZr35Nb28 Alloy for Biomedical Applications via the Taguchi Method, ACS Biomater. Sci. Eng. 5 (2019) 2750–2761. doi:10.1021/acsbiomaterials.9b00356.

[56] S. Berger, S.P. Albu, F. Schmidt-Stein, H. Hildebrand, P. Schmuki, J.S. Hammond, D.F. Paul, S. Reichlmaier, The origin for tubular growth of TiO2 nanotubes: A fluoride rich layer between tube-walls, Surf. Sci. 605 (2011) L57–L60. doi:10.1016/j.susc.2011.06.019.

[57] L. Yang, V. Chinthapenta, Q. Li, D. Stout, A. Liang, B.W. Sheldon, T.J. Webster, Understanding osteoblast responses to stiff nanotopographies through experiments and computational simulations, J. Biomed. Mater. Res. - Part A. 97 A (2011) 375–382. doi:10.1002/jbm.a.33094.

[58] A. Mazare, M. Dilea, D. Ionita, I. Titorencu, V. Trusca, E. Vasile, Changing bioperformance of TiO2 amorphous nanotubes as an effect of inducing crystallinity, Bioelectrochemistry. 87 (2012) 124–131. doi:10.1016/j.bioelechem.2012.01.002.

[59] B. Munirathinam, L. Neelakantan, Titania nanotubes from weak organic acid electrolyte: Fabrication, characterization and oxide film properties, Mater. Sci. Eng. C. 49 (2015) 567–578. doi:10.1016/j.msec.2015.01.045.

[60] S.A. Ali Yahia, L. Hamadou, A. Kadri, N. Benbrahim, E.M.M. Sutter, Effect of Anodizing Potential on the Formation and EIS Characteristics of TiO2 Nanotube Arrays, J. Electrochem. Soc. 159 (2012) K83–K92. doi:10.1149/2.077204jes.

[61] A.G. Kontos, A.I. Kontos, D.S. Tsoukleris, V. Likodimos, J. Kunze, P. Schmuki, P. Falaras, Photo-induced effects on self-organized TiO2 nanotube arrays: The influence of surface morphology, Nanotechnology. 20 (2009) 045603. doi:10.1088/0957-4484/20/4/045603.

[62] F. Hilario, V. Roche, R.P. Nogueira, A.M.J. Junior, Influence of morphology and crystalline structure of TiO2 nanotubes on their electrochemical properties and apatite-forming ability, Electrochim. Acta. 245 (2017) 337–349. doi:10.1016/j.electacta.2017.05.160.

[63] M.T. Woldemedhin, D. Raabe, A.W. Hassel, Characterization of thin anodic oxides of Ti-Nb alloys by electrochemical impedance spectroscopy, Electrochim. Acta. 82 (2012) 324–332. doi:10.1016/j.electacta.2012.06.029.

[64] Y. Tsutsumi, S. Bartakova, P. Prachar, Suyalatu, S. Migita, H. Doi, N. Nomura, T. Hanawa, Long-Term Corrosion Behavior of Biocompatible β-Type Ti Alloy in Simulated Body Fluid, J. Electrochem. Soc. 159 (2012) C435–C440. doi:10.1149/2.045210jes.

[65] B.L. Wang, Y.F. Zheng, L.C. Zhao, Effects of Hf content and immersion time on electrochemical behavior of biomedical Ti-22Nb-xHf alloys in 0.9% NaCl solution, Mater. Corros. 60 (2009) 330–335. doi:10.1002/maco.200805120.

[66] P. Córdoba-Torres, N.T.C. Oliveira, C. Bolfarini, V. Roche, R.P. Nogueira, Electrochemical impedance analysis of TiO2 nanotube porous layers based on an alternative representation of impedance data, J. Electroanal. Chem. 737 (2015) 54–64. doi:10.1016/j.jelechem.2014.06.034.

[67] L. Mohan, C. Anandan, N. Rajendran, Electrochemical behaviour and bioactivity of self-organized TiO2 nanotube arrays on Ti-6Al-4V in Hanks' solution for biomedical applications, Electrochim. Acta. 155 (2015) 411–420.

[68] L. Mohan, C. Anandan, N. Rajendran, Electrochemical behavior and effect of heat treatment on morphology, crystalline structure of self-organized TiO2 nanotube arrays on Ti – 6Al – 7Nb for biomedical applications, Mater. Sci. Eng. C. 50 (2015) 394–401.

[69] W. Yu, J. Qiu, F. Zhang, In vitro corrosion study of different TiO2 nanotube layers on titanium in solution with serum proteins, Colloids Surfaces B Biointerfaces. 84 (2011) 400–405. doi:10.1016/j.colsurfb.2011.01.033.

[70] N.S. More, N. Diomidis, S.N. Paul, M. Roy, S. Mischler, Tribocorrosion behavior of β titanium alloys in physiological solutions containing synovial components, Mater. Sci. Eng. C. 31 (2011) 400–408. doi:10.1016/j.msec.2010.10.021.

[71] I. Çaha, A. Alves, C. Chirico, A. Pinto, S. Tsipas, E. Gordo, F. Toptan, Corrosion and Tribocorrosion Behavior of Ti-40Nb and Ti-25Nb-5Fe Alloys Processed by Powder Metallurgy, Metall. Mater. Trans. A Phys. Metall. Mater. Sci. 51 (2020) 3256–3267. doi:10.1007/s11661-020-05757-6.

[72] J. Ureña, S. Tsipas, A.M. Pinto, F. Toptan, E. Gordo, A. Jiménez-Morales, Corrosion and tribocorrosion behaviour of β-type Ti-Nb and Ti-Mo surfaces designed by diffusion treatments for biomedical applications, Corros. Sci. (2018) 0–1. doi:10.1016/j.corsci.2018.06.024.

[73] D. Khudhair, A. Bhatti, Y. Li, H.A. Hamedani, H. Garmestani, P. Hodgson, S. Nahavandi, Anodization parameters influencing the morphology and electrical properties of TiO2 nanotubes for living cell interfacing and investigations, Mater. Sci. Eng. C. 59 (2016) 1125–1142. doi:10.1016/j.msec.2015.10.042.

[74] B. Han, E.Z. Nezhad, F. Musharavati, F. Jaber, S. Bae, Tribo-mechanical properties and corrosion behavior investigation of anodized Ti-V alloy, Coatings. 8 (2018) 1–22. doi:10.3390/COATINGS8120459.

[75] D. Fang, Z. Luo, K. Huang, D.C. Lagoudas, Effect of heat treatment on morphology, crystalline structure and photocatalysis properties of TiO2 nanotubes on Ti substrate and freestanding membrane, Appl. Surf. Sci. 257 (2011) 6451–6461. doi:10.1016/j.apsusc.2011.02.037.

[76] O.K. Varghese, D. Gong, M. Paulose, C.A. Grimes, E.C. Dickey, Crystallization and high-temperature structural stability of titanium oxide nanotube arrays, J. Mater. Res. 18 (2003) 156–165. doi:10.1557/JMR.2003.0022.

Chapter 7: Corrosion and tribocorrosion behavior of titanium nitride thin films grown on titanium under different deposition times

Published in Surf. Coatings Technol. 374 (2019) 878–888.

Corrosion and tribocorrosion behaviour of titanium nitride thin films grown on titanium under different deposition times

I. Çaha[a,*], A.C. Alves[a], L.J. Affonço[b,c], P.N. Lisboa-Filho[b,c], J.H.D. da Silva[b,c] L.A. Rocha[a,b,c], A.M.P. Pinto[a,d], F. Toptan[a,b,d]

[a] CMEMS-Uminho – Center for MicroElectroMechanical Systems, Universidade do Minho, Azurém, 4800-058 Guimarães, Portugal

[b] IBTN/Br – Brazilan Branch of the Institute of Biomaterials, Tribocorrosion and Nanomedicine, Bauru, SP, Brazil

[c] UNESP—Univ. Estadual Paulista, Faculdade de Ciências de Bauru, Dep. Física, 17033-360 Bauru, SP, Brazil

[d] Universidade do Minho, Dept. Eng. Mecânica, Azurém, 4800-058 Guimarães, Portugal

[*] Corresponding author at: CMEMS-Uminho – Center for MicroElectroMechanical Systems, Universidade do Minho, Azurém, 4800-058 Guimarães, Portugal. Tel.: +351 253 510 220; fax: +351 253 516 007. E-mail: ihsancaha@gmail.com (I. Çaha).

Abstract

Ti and its alloys exhibit combination of unique properties for biomedical applications, however their poor tribo-electrochemical behaviour is a major concern. Therefore, TiN coatings were deposited on cp-Ti (grade 4) by sputtering technique aiming the improvement of its tribocorrosion behaviour. The properties of the coated samples, using different TiN deposition times, were characterized by using grazing incidence X-ray diffraction, FIB-SEM, and nanoindentation. The corrosion behaviour was studied by electrochemical impedance spectroscopy and potentiodynamic polarization in 9 g/L NaCl solution at body temperature. Tribocorrosion tests were employed under open circuit potential by using a ball-on-plate tribometer with 1 N normal load, 3 mm total stroke length, 1 Hz frequency, and 1800 s sliding duration. The results suggested that the TiN coatings deposited during 80 min presented better corrosion and tribocorrosion behaviour as compared to the bare metal and TiN coatings deposited during 30 min.

Keywords: TiN; Corrosion; Tribocorrosion

7.1. Introduction

Titanium and its alloys are widely used in a variety of fields including chemical, automotive, aerospace, ocean engineering, and biomedical industries due to their high strength, low Young's modulus, excellent corrosion resistance, and biocompatibility [1–4]. However, one of the major disadvantages of Ti and its alloys is their poor tribological properties [5,6] raising a particular concern for biomedical load bearing implants since they are in contact with corrosive body fluids and being subjected to relative movements resulting in the subsequent release of metallic ions and wear debris to the body. In order to overcome the low tribological resistance of titanium and its alloys, several surface modification techniques have been applied such as organic and inorganic coatings [7], thermal oxidation [8], acid etching [9], electrochemical processes [10], plasma spraying [11] and laser nitriding [12]. On the other hand, physical vapour deposition (PVD), especially sputtering is an attractive method for coating biomedical implant surfaces with tailorable coating conditions giving properties such as high hardness, high corrosion resistance, chemical stability, biocompatibility, hemocompatibility, high wear and abrasion resistance [13–17]. Thus, TiN coatings have been tested on various implant materials such as dental implants, orthopaedic implants (hip, knee, ankle joint), cardiac and cardiovascular applications [18–21].

Although some studies are available on the corrosion and tribocorrosion behaviour of nitrided Ti or Ti alloy surfaces [10,22–28], investigations on the corrosion and tribocorrosion behaviour of TiN thin films sputtered on Ti surfaces are still scarce. Rizwan *et al.* [29] studied the electrochemical behaviour of nitrogen implanted cp-Ti in Ringer´s lactate solution and found that the corrosion behaviour is improved as compared to untreated Ti. Savonov *et al.* [30] showed a better electrochemical behaviour of plasma immersed nitrogen implanted Ti-6Al-4V alloy compared to the untreated alloy, as concluded from potentiodynamic polarization and electrochemical impedance spectroscopy tests in a 35 g/L NaCl solution at room temperature. El-Hossary *et al.* [31] observed an improved corrosion resistance of RF (radio frequency) plasma nitrided cp-Ti in Ringer's solution, as well, an enhancement on wear resistance after dry sliding were tests performed against 6 mm diameter alumina ball under a sliding speed of 2 mm/s and a normal load of 1 N. Pohrelyuk *et al.* [32] investigated the corrosion behaviour of nitrided Ti-6Al-4V alloy in Ringer's solution at 36 and 40 °C and indicated that nitrided alloy presented better behaviour, and also the corrosion resistance of Ti-6Al-4V was decreased with increased solution temperature. Galliano *et al.* [22] studied the tribocorrosion behaviour of plasma nitrided Ti-6Al-4V alloy treated at 700 and 900 °C by performing tests under a normal load of 2 N, frequency of 2 Hz and stroke length of 3.2 mm during 30 min in 52.6 g/L NaCl solution. The authors reported better wear resistance,

together with lower change on open circuit potential (OCP) and lower galvanic current under sliding for the nitrided alloy, particularly for the ones treated at 900 °C.

Furthermore, in the literature, most of TiN coatings have been performed at high deposition temperatures (500-1100 °C) [6,22,28,31,33–38], which may cause mechanical, microstructural and chemical damage to the substrate [39–41]. Therefore, sputtering is a promising route due to easy control of deposition rate, high ionization rate, creation of high-density plasma, and preferable energy of deposition material improving the adhesion of coating layer [42]. The present study was aimed at studying the corrosion and tribocorrosion behaviour of TiN thin films produced by RF sputtering on Ti grade 4 in a 9 g/L NaCl solution at body temperature, as well as to have a preliminary understanding to the influence of the deposition time on the tribocorrosion mechanisms by characterizing worn surfaces and sub-surfaces.

7.2. Experimental procedure

7.2.1. Materials and processing

ASTM F67 grade 4 pure titanium (ACNIS) was used as substrate material and grinded with SiC paper down to 800 mesh size (R_a=0.20 ± 0.01 μm) by an automatic polishing machine. After grinding, samples were cleaned in an ultrasonic bath in deionized water, acetone and propanol for 10 minutes, respectively. TiN hard ceramic coatings were deposited on the substrate by RF sputtering technique (13.6 MHz power supply). Before TiN deposition, the residual pressure was below 10^{-6} Torr and substrate surface was sputtered in pure argon plasma in order to minimize the surface impurities. A resistance heater was used to keep the temperature at 400 °C and all samples were sputtered under 240W RF power. The TiN layer was deposited with 40 sccm (standard cubic centimetres per minute) Ar and 4 sccm N_2 flow at constant total pressure of 5×10^{-3} Torr for 30 and 80 minutes deposition time and labeled as TiN-30min and TiN-80min, respectively.

7.2.2. Corrosion and tribocorrosion tests

Prior to the corrosion and tribocorrosion tests the samples were cleaned ultrasonically in propanol and distilled water for 10 and 5 min, respectively. Uncoated samples were metallographically prepared down to 1200 mesh SiC papers and kept in desiccator for 24 h before being tested. Corrosion behaviour was evaluated by means of electrochemical impedance spectroscopy (EIS) and potentiodynamic polarization in 9 g/L sodium chloride (NaCl) solution at body temperature (37 ± 2 °C) using Gamry Potentiostat/Galvanostat/ZRA (Reference 600+). All corrosion tests were performed in a

conventional three-electrode electrochemical cell where samples were kept as a working electrode with an exposed area of 0.2 cm^2, a Pt and saturated calomel electrode (SCE) were used as counter and reference electrode, respectively. Before EIS measurements, the surfaces were stabilized at OCP till ΔE was below 60 mV h^{-1}, EIS data were employed at OCP by scanning a range of frequencies from 10^{-2} to 10^5 Hz with 7 points per frequency decade where the amplitude of the sinusoidal was set as 10 mV. After the EIS measurements, potentiodynamic polarization measurements were carried out after 10 min of delay at OCP, with 0.5 mV/s scan rate, starting at −0.25 V vs. OCP and moving in the anodic direction up to 1.0 V_{SCE}.

Tribocorrosion tests were performed using a pin-on-plate reciprocating sliding configuration. The testing samples were used as the working electrode with 0.8 cm^2 exposed area against a hard and inert counter-body, a 10 mm diameter alumina ball (Ceratec), and a SCE was used as the counter electrode, connected to a Gamry Potentiostat/Galvanostat/ZRA (Reference 600). The sliding tests were performed at a normal load of 1 N, a reciprocating sliding frequency of 1 Hz, and linear displacement amplitude of 3 mm using a tribometer (CETR-UMT-2) coupled to the UMT test viewer software to monitor the coefficient of friction (COF). Tribocorrosion tests carried out under OCP, in 30 ml of 9 g/L NaCl solution at body temperature (37 ± 2 °C), and consisted of three steps: (i) stabilization at OCP (ΔE < 60 mV h^{-1}) (ii) sliding for 30 min; (ii) removing the load and recording the recovering of OCP during 30 min. All tests were repeated at least three times in order to assure the reproducibility and the results were presented as the arithmetic mean ± standard deviation.

7.2.3. Characterization

The crystalline structure of the coatings were analysed using grazing incidence X-ray diffraction (XRD, Bruker D8 Discover diffractometer equipped with a Cu-Kα radiation (λ = 0.1544 nm) at 40 kV and 20 mA) scanned from angle (2θ) 30° to 65° with a 0.03°/s step size by grazing incidence mode at 3°. The phase percentage was calculated through relative intensity of each peak by following Eq. (1).

$$\%\, phase_{\alpha} = \frac{\sum I_{\alpha\, peaks}}{\sum I_{all\, peaks}} \qquad (1)$$

Nanoindentation studies were performed to obtain complementary hardness data as well as information on Young's modulus (*E*) (Micro Materials NanoTest). Data were obtained from 8 indentations on different locations using a depth-controlled test as maximum depth of 120 nm, 0.2 m N/s loading/unloading rate, and 5 s dwell time. The average surface roughness (R_a) were measured on three different sample by profilometry (Veeco, Dektak 150). The Daimler-Benz Rockwell-C adhesion test has

been used in literature [43–46] as a fast and easy method to evaluate the adhesion of various coatings. This test was performed by using a Rockwell 'C' indenter with a load of 150 kg for at least three indentions by using Officine Galileo Mod. D200 tester.

After each tribocorrosion test, samples were ultrasonically cleaned for 10 min in propanol and 5 min in distilled water, respectively. The wear tracks and worn counter-body surfaces were characterized by SEM using FEI Nova 200 field emission gun scanning electron microscope (FEG-SEM) equipped with energy dispersive X-Ray spectroscopy (EDS). All worn surface images were taken parallel to the sliding direction by using backscattered (BSE) and secondary electron (SE) detector whereas sub-worn surface images were taken perpendicular to the sliding direction. The 2D wear track profiles were obtained by a surface profiler (Veeco, Dektak 150), and total wear volume loss was determined following the model and calculation procedure given elsewhere [47].

The cross-sections of the TiN coatings and subsurface of wear tracks were prepared and characterized by using FEI Helios NanoLab 450S DualBeam – FIB (focused ion beam) with UHREM FEG-SEM. To protect the films, first a few hundred nm of Pt protection was deposited on 15 × 2 μm^2 area with the electron beam using 6.4 nA current accelerated at 3 kV. Afterwards, 1-3 µm of Pt protective strap was deposited with 80 pA Ga^+ ion at 30 kV. Bulk milling was performed with 9.3 nA, and fine milling (polishing) was performed on the edge of the trenches with 2.5 nA, both at 30 kV. Finally, cross-sectional images were taken with SE mode at the accelerating voltage of 10 kV.

7.3. Results

7.3.1. Surface characterization

The XRD pattern obtained on the TiN-30min and TiN-80min samples are presented in Fig. 7.1. TiN-30min samples exhibited high-intensity peaks characteristics of the hexagonal α-Ti phase (ICDD 00-044-1294) from the substrate. Regarding the thin film, the tetragonal Ti_2N phase (ICDD 00-017-0386), and rhombohedral $Ti_4N_{2.33}$ phase (ICDD 01-089-5210) could be identified. The identified diffraction peaks were well matched to corresponding cards, however, a slight shift occurred on $Ti_4N_{2.33}$ and Ti_2N peaks for TiN-80min which may be due to the residual stresses in the coating [38]. By increasing the deposition time to 80 min, the XRD pattern revealed the same phases, however, the relative intensities of $Ti_4N_{2.33}$ and Ti_2N phases were higher, indicating that a thicker film was present, as expected from the longer deposition time. Relative intensity of Ti_2N phase was observed to be increased on TiN-80min samples. Also, the phase percentages (phase distribution) regarding TiN coatings were

calculated by Eq. (1), and the results showed that the coating film on TiN-30min was a combination of 75% $Ti_4N_{2.33}$ and 25% Ti_2N, while the coating film on TiN-80min was a combination of 46% $Ti_4N_{2.33}$ and 54% Ti_2N. Thus, in addition to obtaining a relatively thicker and rougher surface, increased deposition time also seems to promote the formation of Ti_2N phase on the coating layer, which may contribute to obtain harder and more mechanically-resistant surfaces on TiN-80min samples [48].

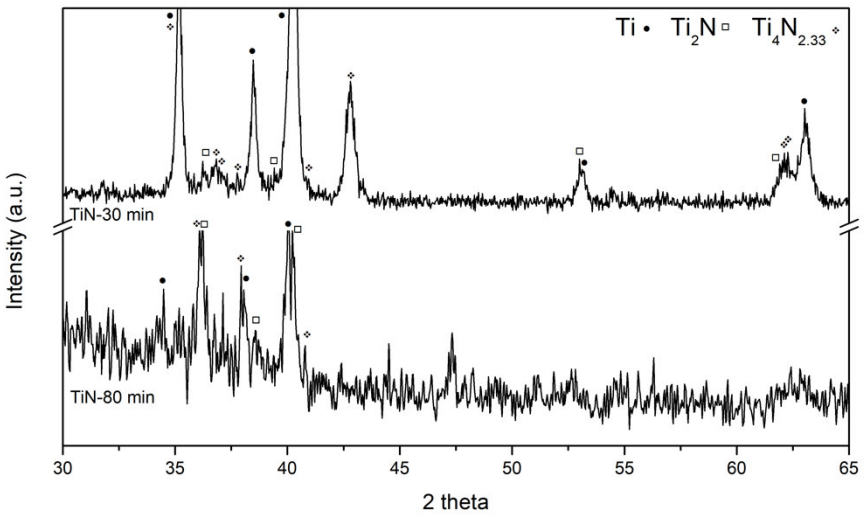

Fig. 7.1. XRD patterns of TiN coated samples.

Fig. 7.2 presents the cross-sectional FIB-SEM micrographs of TiN coated samples showing the continuous coating layer. Thickness of the films were estimated to be of 148 ± 13 nm and 209 ± 6 nm for TiN-30min and TiN-80min, respectively.

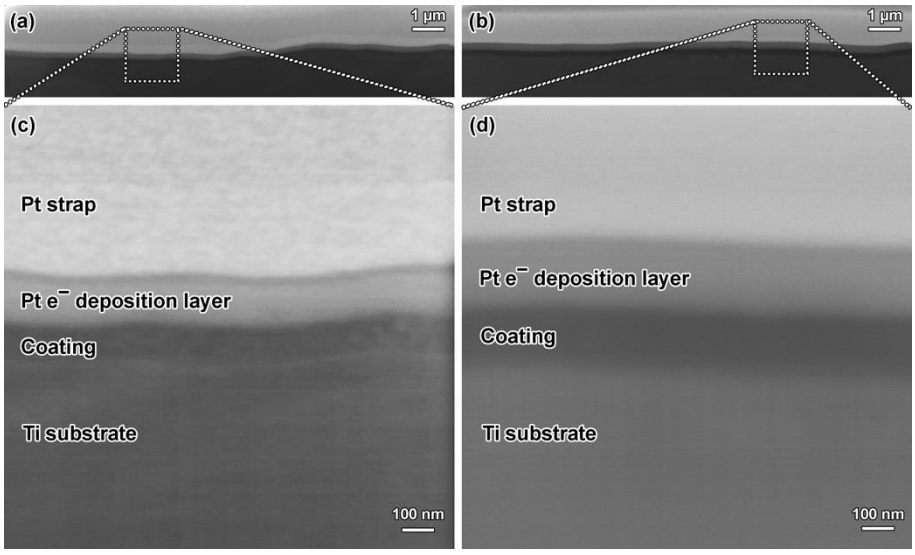

Fig. 7.2. Lower (a, b) and higher (c,d) magnification SEM cross-section images of TiN-30min and TiN-80min samples, respectively.

The hardness and Young's modulus of uncoated Ti and TiN coated samples calculated from the nanoindentation tests are given in Table 7.1 together with the average roughness (R_a) values. As can be seen in Table 7.1, the hardness values were significantly higher on the coated samples as compared to the values calculated for the bare metal. Besides, average values of Young's modulus were close to those observed in the substrate for the TiN-30min samples. However, a noticeable increase was observed for the TiN-80min samples. On the other hand, it was also observed that both hardness and Young's modulus increased on the coated samples with increasing the deposition time. The R_a value of TiN coated samples was higher than uncoated sample, while the R_a values was significantly increased with increasing deposition time that is known to be influenced by the atomic shadowing effect [49], structural orientation of the coating [50], and change of coating density [49].

Table 7.1. Hardness, Young's modulus, and R_a values.

Sample	*Hardness (GPa)*	*Young's Modulus (GPa)*	*Average surface roughness-Ra (μm)*
Ti	2.9 ± 0.7	104.4 ± 18	0.19 ± 0.02
TiN-30min	5.0 ± 1.0	109.6 ± 17.5	0.22 ± 0.01
TiN-80min	7.1 ± 0.6	149.5 ± 9.8	0.58 ± 0.05

Fig. 7.3 shows Rockwell 'C' indentations on the coating samples. There was no evidence of coating delamination for both samples although micro cracks were observed on TiN-30min samples (insert on Fig. 7.3a) and relatively larger radial cracks were observed on TiN-80min samples. According to the Daimler-Benz Rockwell-C method, the layer damage adjacent to the boundary of the Rockwell indentation can be evaluated by microscopy and classifying the adhesion as HF1 to HF6 according to the level of cracking and coating delamination around the indentation. The indentations classified as HF1 and HF2 correspond to sufficient adhesion where only cracks are observed, whereas both cracks and deleminations are observed for HF3 to HF5, and finally, only deleminations are observed for HF6 [51]. Thus, it can be stated that TiN-30min and TiN-80min samples presented acceptable interfacial adhesion corresponding to HF1 and HF2, respectively.

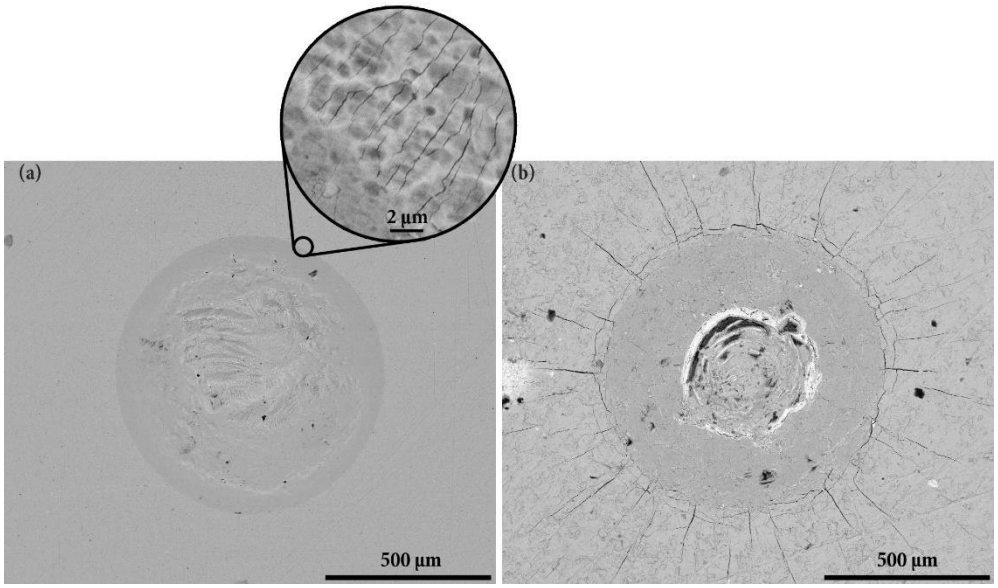

Fig. 7.3. BSE SEM images of Daimler-Benz adhesion test on (a) TiN-30min and (b) TiN-80min samples.

7.3.2. Corrosion behaviour

Fig. 7.4 shows representative potentiodynamic polarization curves of the uncoated and TiN coated samples obtained in 9 g/L NaCl solution at body temperature. The uncoated samples exhibited a well-defined passivation plateau above around 150 mV, whereas the TiN coated samples did not present an evident passivation plateau, even though they exhibited lower current densities on the anodic domain in the potential range tested. Moreover, the current densities recorded for the TiN coating deposited for 80 min were always lower than the ones recorded for the coatings with shorter deposition time, indicating higher corrosion resistance for TiN-80 min samples. The corrosion potentials ($E_{(i=0)}$) and the passivation current densities (i_{pass}) derived from the polarization curves are given in Table 7.2, and i_{pass} values for all samples were taken at 0.5 V vs. SCE.

As can be seen in Table 7.2, $E_{(i=0)}$ values of TiN coated samples were significantly higher than that of the uncoated samples, confirming a lower tendency to corrosion for coated samples. On the other hand, i_{pass} of both TiN coated samples were significantly lower as compared to the uncoated samples, while, the i_{pass} value of the TiN-80min was observed lower than the TiN-30min sample.

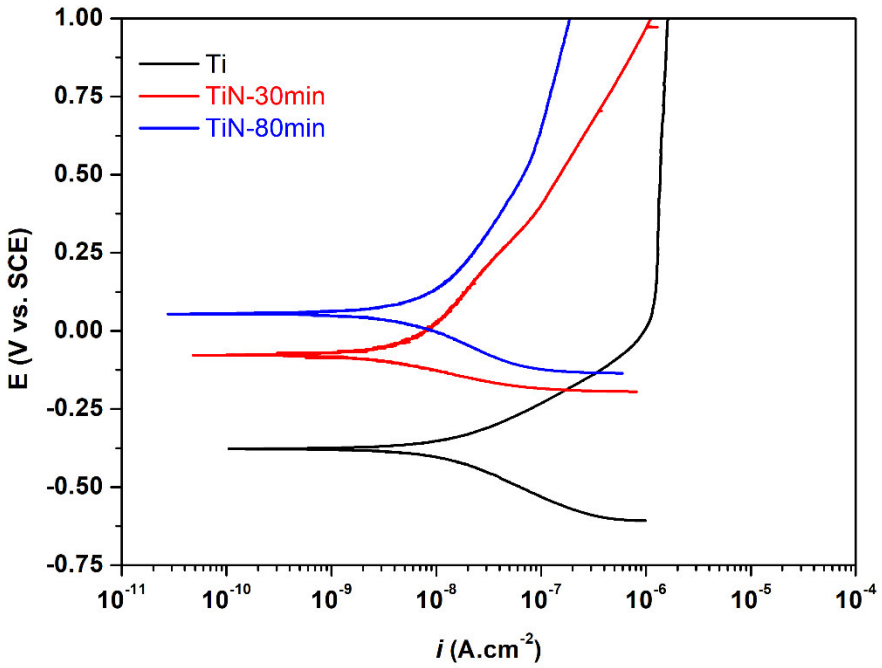

Fig. 7.4. Potentiodynamic polarization curves.

Table 7.2. Electrochemical parameters derived from the potentiodynamic polarization curves.

Sample	$E_{(i=0)}$ (V_{SCE})	i_{pass} ($\mu A\ cm^{-2}$)
Ti	−0.371 ± 0.018	1.37 ± 0.04
TiN-30min	−0.065 ± 0.022	0.11 ± 0.03
TiN-80min	0.009 ± 0.046	0.07 ± 0.02

Representative electrochemical impedance spectra of the uncoated and TiN coated samples are presented in Fig. 7.5 (Nyquist and Bode diagrams). It can be observed from the Nyquist diagram (Fig. 7.5a) that TiN coated samples presented a larger diameter of semi-circle indicating a higher corrosion resistance when compared to the uncoated samples. The improved corrosion resistance was also reflected by a slight increase on total impedance values (|Z|) represented in the Bode diagram (Fig. 7.5b). Comparing the TiN coated samples, it was possible to observe that the semi-circle diameter was slightly larger for TiN-80min as compared to TiN-30min. The constant values of |Z| observed in Bode diagram (Fig. 7.5b) at high frequencies for all samples, where the phase angle was near 0°, as the typical response of electrolyte resistance. In low and middle frequency ranges, the phase angle values approached values close to −90° for both substrate and coated samples. In the case of the substrate, this behaviour indicates a typical capacitive response of the native oxide film formed on the substrate

surface. Regarding the coated samples, the phase angle values were kept almost constant (approaching –90°) till the lowest frequencies, indicating the protector character of the TiN coatings.

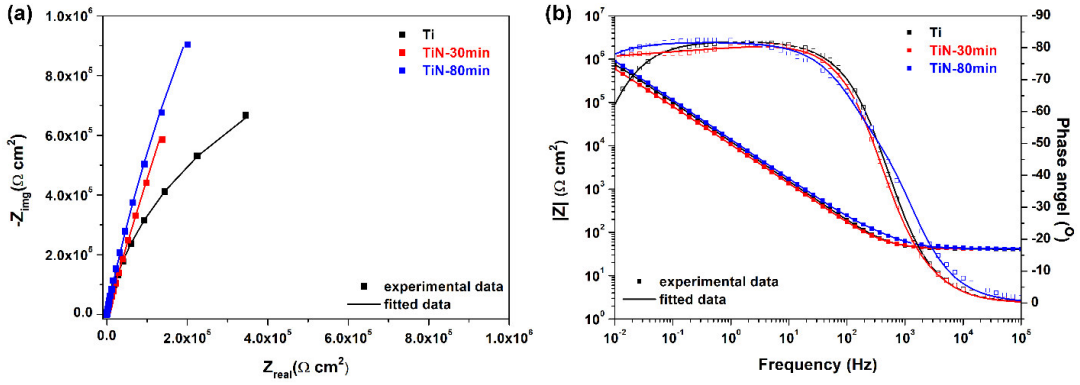

Fig. 7.5. (a) Nyquist and (b) Bode diagrams of EIS spectra

The electrical equivalent circuits (EECs) presented in Fig. 7.6 were used to fit experimental EIS data by using Gamry Echem Analyst software (version 5.61). The EIS experimental data of the uncoated samples was fitted by using a modified Randle's circuit (Fig. 7.6a) containing elements representing the electrolyte resistance (R_e), the native oxide film resistance (R_{nox}) and constant phase element (CPE) considering a non-ideal capacitance of the native oxide film (Q_{nox}). In fact, the impedance of the CPE is defined as:

$$Z_{CPE} = [Y_0(jw)^n]^{-1} \qquad (2)$$

where Y_0 is a frequency-independent constant, $j = \sqrt{(-1)}$, w is the angular frequency, and n is the fractional exponent which is in the $-1 \leq n \leq 1$ range. When $n = 1$, the CPE response is that of a pure capacitor, while $n = 0$ and $n = -1$ corresponds to a resistor and inductor response, respectively. The n value is influenced by surface heterogeneities and its roughness, thus this element may be described as a non-ideal capacitor, when n value is close to 1 [52].

Fig. 7.6b represents the EEC used for TiN coated samples. Elements of this circuit includes electrolyte resistance (R_e), while a pair R_{coat}/Q_{coat} should be added to represent the contribution of the resistance and capacitance of the TiN coating. However, since the R_{coat} tends to be extremely high due to the strong insulating properties of the TiN film, this element was removed from the EEC. Furthermore, in order to represent the corrosion process that takes place inside the defects of the TiN coating, a pair of R_{bl}/Q_{bl} was added in series with the additional electrolyte resistance inside those defects. The barrier

layer resistance (R_{bl}) represents the preferential sites for corrosion in the defects and the Q_{bl} regards the defect layer effect.

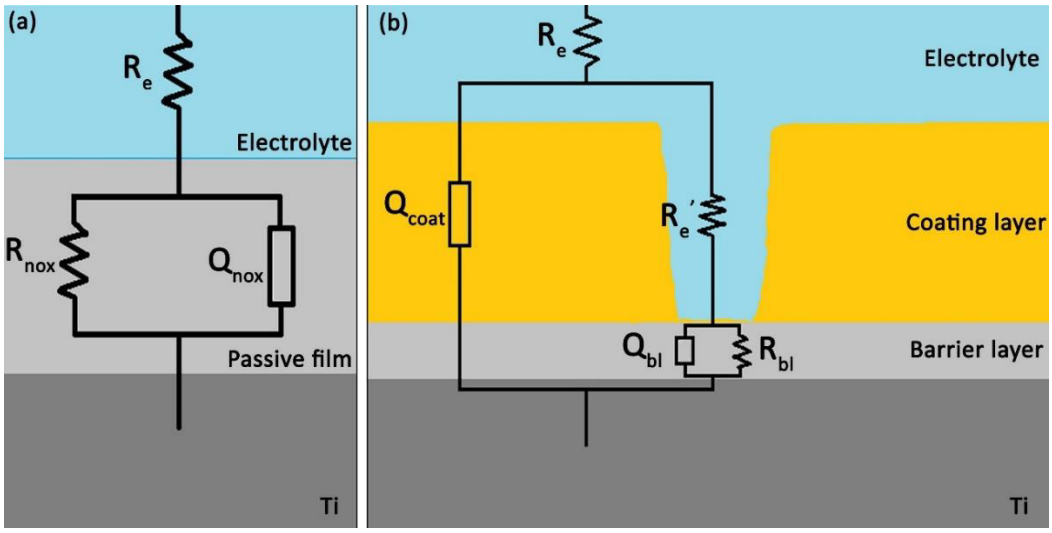

Fig. 7.6. EECs used for fitting EIS experimental data for a) the uncoated and b) TiN coated samples.

The quality of the equivalent circuits used for fitting was evaluated by the goodness of fitting (χ^2). All samples presented a good fitting to the corresponded EECs exhibiting χ^2 values below 10^{-3}. Q_{coat}, Q_{nox} and Q_{bl} values were converted to C_{coat} (capacitance of TiN coating) and C_{bl} (capacitance of the barrier layer) by using Eq. (3) and Eq. (4), respectively, derived from Brug's equation [53].

$$C_{nox/coat} = \left[Q_{nox/coat} R_e^{(1-n)}\right]^{\frac{1}{n}} \qquad (3)$$

$$C_{bl} = \left[Q_{bl}(R_e + R_{e'})^{(1-n)}\right]^{\frac{1}{n}} \qquad (4)$$

7.3.3. Tribocorrosion behaviour

The evolution of OCP before, during and after sliding in 9 g/L NaCl solution is shown in Fig. 7.7 together with the COF values recorded during sliding. Before sliding, all samples presented stable OCP values due to the presence of a passive film on the uncoated samples and a stable nitride layer on the coated samples.

In case of uncoated Ti, when sliding started, a sudden decrease in OCP was detected, that confirmed the removal of passive film due to mechanical damage and pointing an increased tendency to corrosion in the wear track region [54]. For the TiN-30min samples, after sliding started, the OCP values gradually decreased till approximately −0.35 V_{SCE} then suddenly dropped to lower values, around −0.7 V_{SCE}, similar to those observed on the uncoated samples at the beginning of sliding. After this, local

increments were recorded during sliding. The first gradual drop in the OCP observed at the beginning of sliding can be linked to a local damage of TiN coating, and the second sharp drop shows the destruction of the TiN coating on the contact region with the alumina ball resulting on the exposure of the bare Ti substrate to the solution (indicated by arrows on Fig. 7.7). Regarding TiN-80min samples, a very small drop on the OCP values (around 40 mV) was suddenly recorded at the beginning of sliding. Then the OCP values gradually decreased till approximately −0.30 V_{SCE} and remained relatively constant at this value till the end of sliding. After sliding, the OCP values of all samples increased near to the values recorded before sliding due to recovering of the passive oxide film on the damaged Ti area [22].

Evolution of COF can be also seen on Fig. 7.7. Once sliding started, COF value of the uncoated samples reached values around 0.4, in a short period. As sliding continued, COF of the uncoated samples kept relatively constant till around 650 s and after that an increment was recorded with a correspondence with a slight increase on OCP values. Regarding the TiN-30min samples, the initial decrease of OCP corresponded to an increase on COF values till around 0.7, after this, a sharp drop to around 0.45 was observed that can be due to removal and/or wear out of the TiN coating. Afterwards, local increments were observed during sliding, similar to the behaviour observed on the uncoated samples. Regarding the TiN-80min samples, COF values increased up to approximately 0.6 and then stayed relatively stable with minor oscillations till the end of sliding.

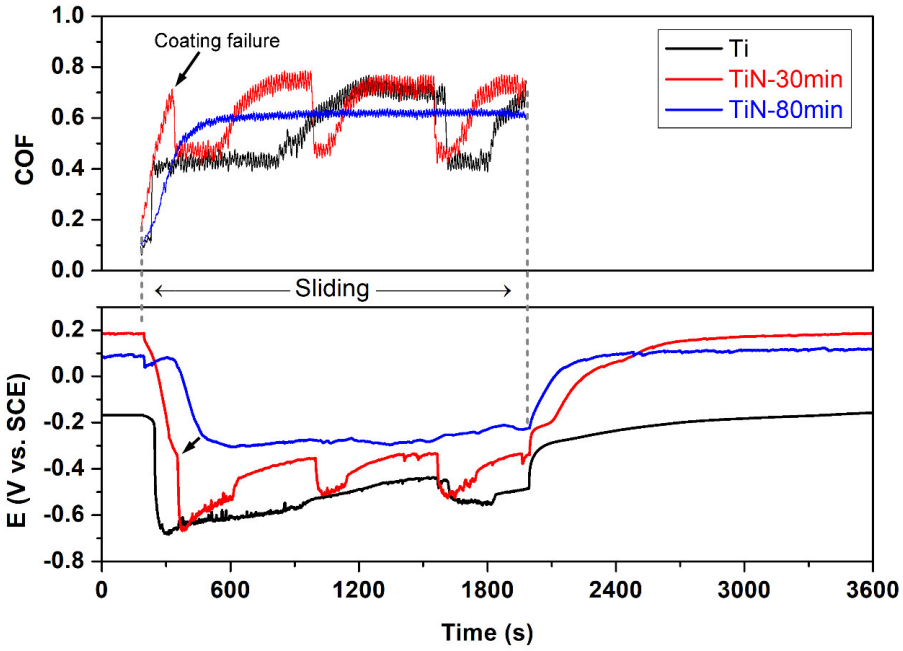

Fig. 7.7. The representative evolution of OCP before, during, and after sliding, together with evolution of COF under sliding for the uncoated and TiN coated samples in 9 g/L NaCl.

Representative lower magnification SEM images of wear tracks are shown in Figs. 7.8a-c. TiN-80min samples presented significantly lower wear damage compared to the other samples. Worn surface features can be seen in more detail on the representative higher magnification SEM images given in Figs. 7.8d-f. The uncoated Ti and TiN-30min sample surfaces exhibited typical worn surface features for Ti, namely parallel sliding grooves, adhered/oxidized patches (verified by the presence of oxygen on the EDS spectra presented in Figs. 7.8g and 7.8h), and plastic deformation. However, the worn surfaces of TiN-80min samples were dissimilar to other two samples. It can be seen that the damage of the surface of the TiN-80min samples was much less severe, and denser oxidized patches (black areas on Fig. 7.8f and corresponding EDS spectrum on Fig. 7.8i) were observed.

Hertzian contact pressures were calculated by using the measured Young's modulus values for TiN-30min and TiN-80min. The Young's modulus and Poisson ratio of cp Ti grade 4 [55] and alumina ball [56], as well, the Poisson ratio of TiN [57] were taken from the literature. The chosen normal load (1 N) corresponds to a maximum Hertzian contact pressure of approx. 390 MPa for Ti and TiN-30min, and approx. 460 MPa for TiN-80 min, being lower than the reported yield strength of cp Ti grade 4, that is 480 MPa [55].

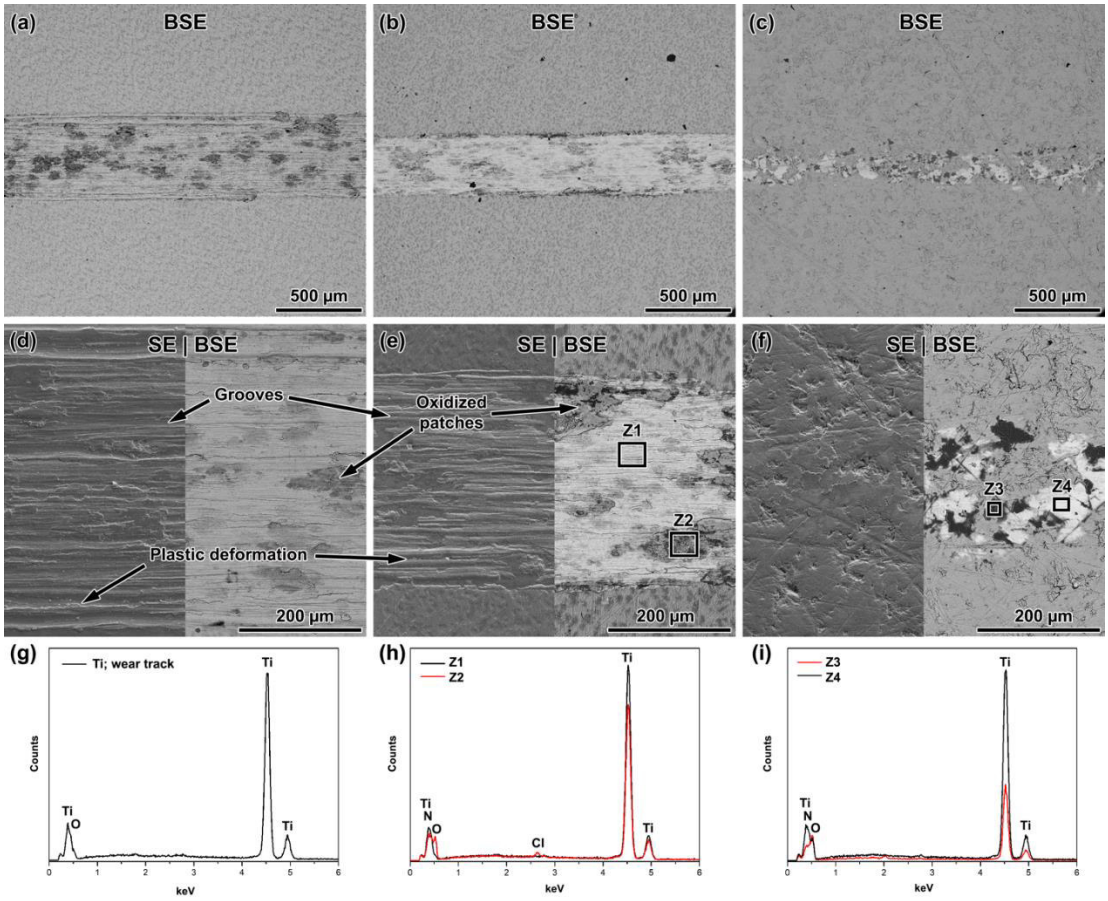

Fig. 7.8. Lower (a, b, c) and higher (d, e, f) magnification SEM images of the worn surfaces of Ti, TiN-30min, and TiN-80min, respectively, together with the EDS spectrum of the Ti worn surface (g) and EDS spectra taken from the marked zones of the coated samples (h, i).

In order to have a further understanding on the wear mechanism, FIB prepared cross-sectional SEM images of the worn sub-surfaces, taken as perpendicular to the sliding direction, were observed (Fig. 7.9). As it can be seen in Figs. 7.9a and 7.9d, relatively thick adhered/oxidized patches were found on the uncoated Ti samples. As oppose to the other samples, some cracks were observed on the worn areas of the TiN-80min samples. The coating layer was not observed under most of the patches, grooves (TiN-30min) or damaged areas (TiN-80min, represented by Z4 on Fig. 7.9f), due to the damage given by abrasive and adhesive wear actions.

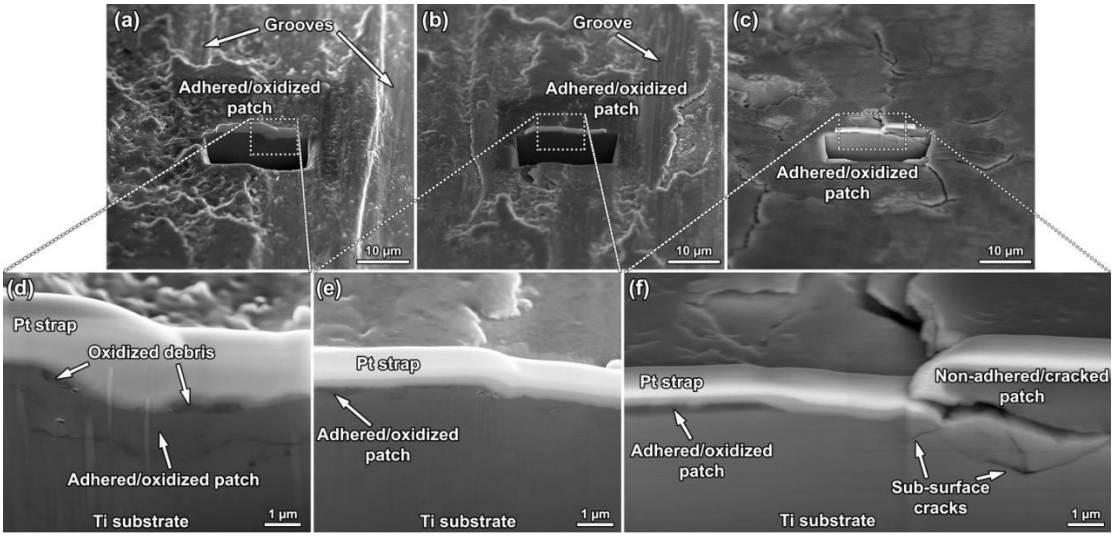

Fig. 7.9. Lower magnification SE/SEM images (a, b, c) showing FIB milling zones on the wear tracks, and higher (d, e, f) magnification SE/SEM images of the worn sub-surfaces of Ti, TiN-30min, and TiN-80min, respectively.

The SEM images and respective EDS spectra taken from the wear scars on the alumina balls used as counter-material are presented in Fig. 7.10. The wear scars on the balls that slid against the uncoated samples were much larger than that observed on the balls used to test the coated samples, which is in accordance with the dimensions of the wear tracks shown in Fig. 7.8. Transference of Ti to the alumina counter-body was detected in all surfaces by EDS analysis, indicating adhesive wear. However, that phenomenon was much pronounced in the uncoated samples.

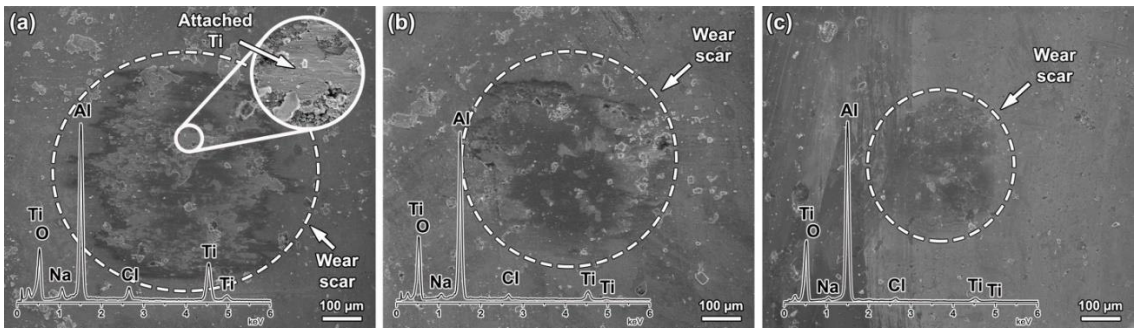

Fig. 7.10. SE/SEM images of the wear scars on the counter-material surfaces slid against Ti (a), TiN-30min (b), and TiN-80min (c), together with EDS spectra taken from each wear scar.

The representative 2D wear track profiles taken from centre of the wear tracks are presented in Fig. 7.11. The uncoated Ti and TiN-30min samples presented similar wear track profiles, whereas much lower volume loss was observed on the TiN-80min samples. The wear volume loss values were calculated

as (2.8 ± 0.5) $\times 10^{-3}$ mm^3, (3.3 ± 1.0) $\times 10^{-3}$ mm^3, and (0.4 ± 0.2) $\times 10^{-3}$ mm^3 for the uncoated Ti, TiN-30min, and TiN-80min, respectively.

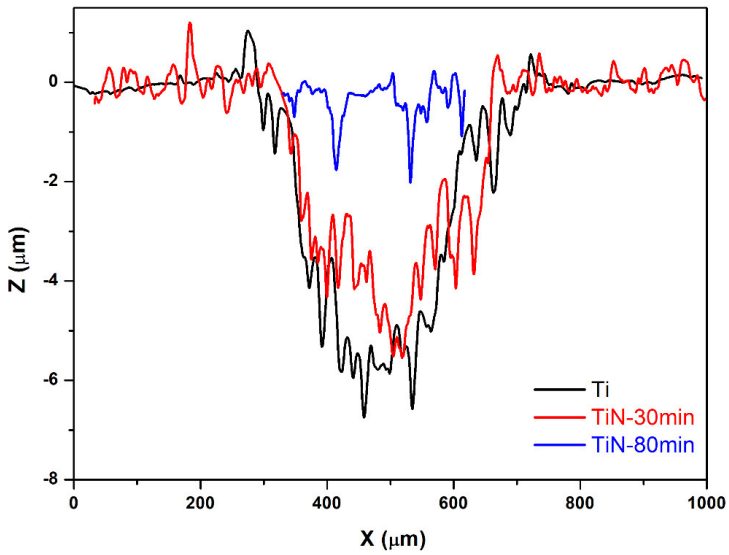

Fig. 7.11. Representative 2D wear track profiles.

7.4. Discussion

7.4.1. Corrosion behaviour

TiN coatings are commonly used to increase the corrosion resistance of metallic biomaterials [58]. Corrosion tests showed that the TiN coated samples presented lower tendency to corrosion and lower corrosion rate due to nobler potential and lower passive current density (Figs. 7.3 and 7.4) as also previously been reported for TiN coated on Ti [59], Ti-6Al-4V [60], Ti-6Al-7Nb [61], Ti-35Nb-7Zr-5Ta [25], and Ti-25Ta-25Nb alloy [62]. On the other hand, TiN-80min samples presented higher corrosion resistance as compared to TiN-30min. That may be related to the differences on the TiN coating thickness, that was not linearly proportional to the deposition time possibly due to the sub-stoichiometric phase transformation resulted in changing of crystalline structure and lattice parameters [63], together with the increase on the amount of the Ti_2N phase that is known for its more stable behaviour and good electrochemical response [35,60]. Nevertheless, the increase on the passive current densities of the TiN coated samples during the potentiodynamic polarization tests (less pronounced for the TiN-80min samples) might be attributed to the oxidation of the Ti_2N and $Ti_4N_{2.33}$ phases [22,64], by a process similar to that reported by Pohrelyuk *et al.* [32] for the oxidation of the TiN phase, according to the reaction (1),

$$2TiN + 2yH_2O \longrightarrow 2TiN_xO_y + (1\text{-}x)N_2 + 4yH^+ + 4ye^- \qquad (1)$$

The EEC parameters deducted from the fitting of the EIS data for the uncoated and TiN coated samples are presented in Table 7.3. The values of the resistance and capacitance of native oxide film formed on the uncoated samples were around 2.06 MΩ cm^2 and 7.73 μF cm^{-2}, respectively, suggesting a high corrosion resistance of the typical passive films formed on Ti surfaces. Regarding the coated samples, when the deposition time increased from 30 min to 80 min, a slight decrease on the capacitance values of the TiN coatings (C_{coat}) was observed, indicating an improvement on the corrosion resistance. Furthermore, the capacitance values of TiN coatings were lower when compared with the capacitance of the native oxide film formed on the substrate, indicating better corrosion protection characteristics of these coatings.

Table 7.3. Equivalent circuit parameters obtained from EIS data.

	Ti	TiN-30min	TiN-80min
R_{nox} (MΩ cm^2)	2.06 ± 0.33	–	–
C_{nox} (μF cm^{-2})	7.73 ± 0.36	–	–
n_{nox}	0.92 ± 0.01	–	–
C_{coat} (μF cm^{-2})	–	4.87 ± 1.43	3.08 ± 1.07
n_{coat}	–	0.94 ± 0.03	0.90 ± 0.02
R_{bl} (MΩ cm^2)	–	16.31 ± 2.67	11.75 ± 2.94
C_{bl} (μF cm^{-2})	–	2.63 ± 0.84	1.73 ± 0.86
n_{bl}	–	0.84 ± 0.02	0.86 ± 0.07
χ^2	<1.80 x 10^{-4}	<7.77 x 10^{-5}	<1.06 x 10^{-3}

7.4.2. Tribocorrosion behaviour

Evolution of OCP and COF during sliding, as well, the analysis of the worn surfaces after tribocorrosion tests revealed that the relative amount of phases presented in the coatings together with the deposition time significantly affected the tribocorrosion behaviour. The behaviour of the uncoated samples was observed to be in accordance with the tests made in the same conditions in the literature [65]. The relative increase in the potential up to around 1600 s during sliding was due to the thickening of the adhered/oxidized patches that may provide a limited protection against corrosion, as also reported by Silva *et al.* [65] for cp-Ti (grade 2) tested under similar conditions. After around 1600 s, the thickened adhered/oxidized patches might be removed, thus a decrease was observed on the potential values.

The evolution of OCP and COF was relatively similar on TiN-30min and uncoated Ti, probably due to the damage of the TiN coating at the beginning of the sliding (indicated by arrows on Fig. 7.7). After the failure of the coating layer, oxidized patches were formed, and the thickening and breaking of these patches caused increases and decreases both in OCP and COF values. The more positive increments on the OCP values during sliding for TiN-30min samples compared to uncoated Ti may be due to the incorporation of TiN debris in oxide patches which may provide a relatively higher protection against tribocorrosion. The samples coated with longer deposition time presented a significantly different behaviour as compared to the uncoated and TiN-30min samples where coating layer was not completely damaged during tribocorrosion thus less negative OCP values were observed, indicating lower tendency to corrosion under sliding.

Adhesive wear is characterized by elevated wear rates and larger, unstable COF resulting with a severe wear damage. During adhesive wear, strong adhesion formed between the asperities of the sliding surfaces causes elevated frictional forces, and the asperities may be removed leading to formation of wear debris, transfer layers, or adhered/oxidized patches. On the other hand, sliding movement leads to plastic deformation of the adhered asperities that may also result on work hardening of the adhered and deformed metallic surfaces eventually resulting in formation of grooves and abrasion scratches on the worn sample surface, which was clearly observed on the worn uncoated Ti and TiN-30min surfaces (Figs. 7.8 and 7.9) [66]. During this action, brittle materials produce less wear debris since they break easier than the ductile materials. As a result, detached pieces from the sample surfaces may attach to the counter material surface (insert on Fig. 7.10a), may repeatedly move from one sliding surface to the other one, or may attach to the worn sample surface in the form of a transfer film, or adhered/oxidized patch (Figs. 7.8d-f and 7.9) being another typical feature of adhesive wear [66] as also reported in the literature for Ti [65,67] and Ti-6Al-4V [47,68]. Besides, sub-surface cracks mainly observed under the patches on TiN-80min samples can be related with both the decreased ductility, as well, locally increased contact stresses due to higher roughness. As a result, during reciprocating sliding, fatigue may lead to nucleation and propagation of sub-surfaces cracks on the protruded surfaces [66].

It is known that increasing surface roughness, hardness, and Young's modulus, as well, the presence of contaminants such as oxides and nitrides reduces the influence of adhesive wear [66]. Accordingly, increased hardness, Young's modulus and surface roughness from the uncoated samples to the coated samples resulted with the decreased damage given by adhesive wear to the coated samples, which was confirmed by formation of relatively lesser and shallower adhered/oxidized patches,

sliding grooves (Figs. 7.8 and 7.9), and lesser amount of transferred material on the counter material surface (Fig. 7.10), eventually affecting the material loss during tribocorrosion (Fig. 7.11). Therefore, TiN-80min samples having the thickest TiN coating, highest hardness and highest Young's modulus exhibited highest resistance to abrasive wear, maintaining its barrier role between the substrate and the counter material thus minimizing the influence of adhesive wear.

Fig. 7.12 shows schematically the wear mechanisms proposed for the materials tested in this work. The uncoated and TiN-30min samples presented mainly a combination of abrasive and adhesive wear governed by parallel grooves, discontinuous tribolayers (patches), plastic deformation, and transferred material, whereas the features of abrasive and adhesive was only occurred on the protruded surfaces on TiN-80min samples. However, TiN-80min samples also suffered to fatigue wear, that was evident on the worn sub-surfaces.

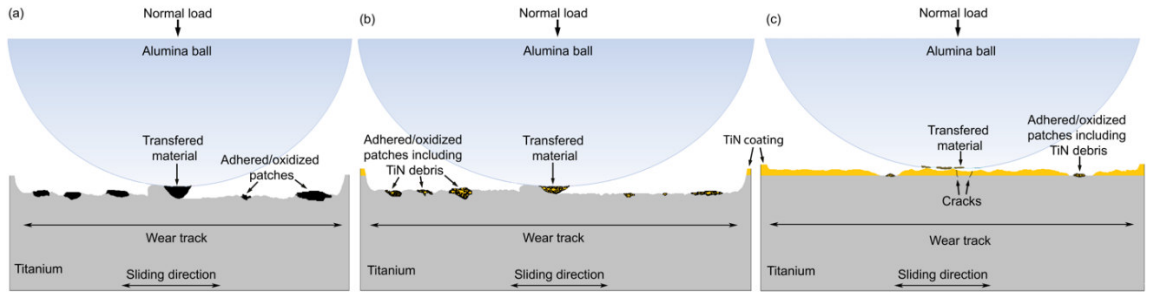

Fig. 7.12. Schematic tribocorrosion mechanisms of uncoated Ti (a), TiN-30min (b) and c) TiN-80min.

Although this work showed that the deposition time can have a noticeable influence on the tribocorrosion mechanisms, the correlation between the deposition time and tribocorrosion mechanism is worth to be explored more in detail. Besides, since different implants, even in different implant parts over same implants are required different surface characteristics, further studies should consider the effect of the topographical factors, together with the biological factors, on the tribocorrosion mechanisms.

7.5. Conclusions

The corrosion and tribocorrosion behaviour of TiN coating on cp-Ti (grade 4) obtained by reactive sputtering with longer deposition time (80 min) presented lower corrosion rate and better capacitive behaviour due to increased thickness of the coating layer and increased percentage of Ti_2N phase on the coating layer. Increased coating thickness and promotion of the formation of Ti_2N phase also gave a resistance against abrasive wear, adhesive wear, and plastic deformation, thus, led to obtain a clear improvement on the tribocorrosion resistance. Therefore, these results pointed that deposition time should be carefully adjusted according to the contact conditions of the targeted applications.

Acknowledgements

This work is supported by FCT with the reference project UID/EEA/04436/2013, COMPETE 2020 with the code POCI-01-0145-FEDER-006941, and M-ERA-NET/0001/2015 (FAPESP proc. #2015/50.280-5) project. I. Caha grateful for financial support through PhD grant under NORTE-08-5369-FSE-000012 project. The authors would also like to acknowledge Dr. Paulo Ferreira and Dr. Enrique Carbó-Argibay (International Iberian Nanotechnology Laboratory) for the provision of FIB facilities, and Prof. Graça Minas (Universidade do Minho) for the provision of profilometry.

References

[1] I. V. Okulov, H. Wendrock, A.S. Volegov, H. Attar, U. Kühn, W. Skrotzki, J. Eckert, High strength beta titanium alloys: New design approach, Mater. Sci. Eng. A. 628 (2015) 297–302. doi:10.1016/j.msea.2015.01.073.

[2] Q. Wang, Q. Li, X. Li, R. Zhang, X. Gao, C. Dong, P.K. Liaw, Microstructures and Stability Origins of β-(Ti,Zr)-(Mo,Sn)-Nb Alloys with Low Young's Modulus, Metall. Mater. Trans. A Phys. Metall. Mater. Sci. 46 (2015) 3924–3931. doi:10.1007/s11661-015-3011-4.

[3] D.W. Shoesmith, J.J. Noël, Corrosion of titanium and its alloys, in: Shreir's Corros., 2010: pp. 2042–2052. doi:10.1016/B978-044452787-5.00097-4.

[4] M. Niinomi, Biologically and Mechanically Biocompatible Titanium Alloys, Mater. Trans. 49 (2008) 2170–2178. doi:10.2320/matertrans.L-MRA2008828.

[5] M.J. Runa, M.T. Mathew, L.A. Rocha, Tribocorrosion response of the Ti6Al4V alloys commonly used in femoral stems, Tribol. Int. 68 (2013) 85–93. doi:10.1016/j.triboint.2013.09.022.

[6] A. Samanta, M. Bhattacharya, I. Ratha, H. Chakraborty, S. Datta, J. Ghosh, S. Bysakh, M. Sreemany, R. Rane, A. Joseph, S. Mukherjee, B. Kundu, M. Das, A.K. Mukhopadhyay, Nano- and micro-tribological behaviours of plasma nitrided Ti6Al4V alloys, J. Mech. Behav. Biomed. Mater. 77 (2018) 267–294. doi:10.1016/j.jmbbm.2017.09.013.

[7] E. Arslan, Y. Totik, I. Efeoglu, The investigation of the tribocorrosion properties of DLC coatings deposited on Ti6Al4V alloys by CFUBMS, in: Prog. Org. Coatings, 2012: pp. 768–771. doi:10.1016/j.porgcoat.2011.10.023.

[8] S. Wang, Y. Liu, C. Zhang, Z. Liao, W. Liu, The improvement of wettability, biotribological behavior and corrosion resistance of titanium alloy pretreated by thermal oxidation, Tribol. Int. 79 (2014) 174–182. doi:10.1016/j.triboint.2014.06.008.

[9] J. Geringer, N. Demanget, J. Pellier, From acid etching treatments to tribocorrosive properties of dental implants: Do some experimental results on surface treatments have an influence on the tribocorrosion behaviour of dental implants?, J. Phys. D. Appl. Phys. 46 (2013). doi:10.1088/0022-3727/46/40/404005.

[10] M. Azzi, J.A. Szpunar, Tribo-electrochemical technique for studying tribocorrosion behavior of biomaterials, Biomol. Eng. 24 (2007) 443–446. doi:10.1016/j.bioeng.2007.07.015.

[11] M. Annunziata, A. Oliva, M.A. Basile, M. Giordano, N. Mazzola, A. Rizzo, A. Lanza, L. Guida, The effects of titanium nitride-coating on the topographic and biological features of TPS implant surfaces, J. Dent. 39 (2011) 720–728. doi:10.1016/j.jdent.2011.08.003.

[12] S. Sathish, M. Geetha, N.D. Pandey, C. Richard, R. Asokamani, Studies on the corrosion and wear behavior of the laser nitrided biomedical titanium and its alloys, Mater. Sci. Eng. C. 30 (2010) 376–382. doi:10.1016/j.msec.2009.12.004.

[13] A. Scarano, M. Piattelli, G. Vrespa, G. Petrone, G. Iezzi, A. Piattelli, Bone healing around titanium and titanium nitride-coated dental implants with three surfaces: an experimental study in rats., Clin. Implant Dent. Relat. Res. 5 (2003) 103–11. http://www.ncbi.nlm.nih.gov/pubmed/14536045.

[14] J.A. Hendry, R.M. Pilliar, The fretting corrosion resistance of PVD surface-modified orthopedic implant alloys, J. Biomed. Mater. Res. 58 (2001) 156–166. doi:10.1002/1097-4636(2001)58:2<156::AID-JBM1002>3.0.CO;2-H.

[15] J. Bolton, X. Hu, In vitro corrosion testing of PVD coatings applied to a surgical grade Co-Cr-Mo alloy, J. Mater. Sci. Mater. Med. 13 (2002) 567–574. doi:10.1023/A:1015126810485.

[16] J. Zhao, X.M. Cai, H.Q. Tang, T. Liu, H.Q. Gu, R.Z. Cui, Bactericidal and biocompatible properties of TiN/Ag multilayered films by ion beam assisted deposition, in: J. Mater. Sci. Mater. Med., 2009. doi:10.1007/s10856-008-3491-5.

[17] G.K. Hyde, S.D. McCullen, S. Jeon, S.M. Stewart, H. Jeon, E.G. Loboa, G.N. Parsons, Atomic layer deposition and biocompatibility of titanium nitride nano-coatings on cellulose fiber

substrates, Biomed. Mater. 4 (2009) 025001. doi:10.1088/1748-6041/4/2/025001.

[18] Y.S. Al Jabbari, J. Fehrman, A.C. Barnes, A.M. Zapf, S. Zinelis, D.W. Berzins, Titanium Nitride and Nitrogen Ion Implanted Coated Dental Materials, Coatings. 2 (2012) 160–178. doi:10.3390/coatings2030160.

[19] S. Piscanec, L.C. Ciacchi, E. Vesselli, G. Comelli, O. Sbaizero, S. Meriani, A. De Vita, Bioactivity of TiN-coated titanium implants, Acta Mater. 52 (2004) 1237–1245. doi:10.1016/j.actamat.2003.11.020.

[20] M.A. Pellman, Overview of PVD coating development for Co-based alloys, ASTM Spec. Tech. Publ. (1999) 169–178. doi:Doi 10.1520/Stp14272s.

[21] D.-C. Sin, H.-L. Kei, X. Miao, Surface coatings for ventricular assist devices, Expert Rev. Med. Devices. 6 (2009) 51–60. doi:10.1586/17434440.6.1.51.

[22] F. Galliano, E. Galvanetto, S. Mischler, D. Landolt, Tribocorrosion behavior of plasma nitrided Ti-6Al-4V alloy in neutral NaCl solution, Surf. Coatings Technol. 145 (2001) 121–131. doi:10.1016/S0257-8972(01)01309-3.

[23] A.C. Fernandes, F. Vaz, E. Ariza, L.A. Rocha, A.R.L. Ribeiro, A.C. Vieira, J.P. Rivière, L. Pichon, Tribocorrosion behaviour of plasma nitrided and plasma nitrided + oxidised Ti6Al4V alloy, Surf. Coatings Technol. 200 (2006) 6218–6224. doi:10.1016/j.surfcoat.2005.11.069.

[24] T.M. Manhabosco, S.M. Tamborim, C.B. dos Santos, I.L. Müller, Tribological, electrochemical and tribo-electrochemical characterization of bare and nitrided Ti6Al4V in simulated body fluid solution, Corros. Sci. 53 (2011) 1786–1793. doi:10.1016/j.corsci.2011.01.057.

[25] X. Zhao, P. Zhang, X. Wang, Y. Chen, H. Liu, L. Chen, Y. Sheng, W. Li, In-situ formation of textured TiN coatings on biomedical titanium alloy by laser irradiation, J. Mech. Behav. Biomed. Mater. 78 (2018) 143–153. doi:10.1016/j.jmbbm.2017.11.019.

[26] Ç. Albayrak, I. Hacisalihoğlu, S. Yenal vangölü, A. Alsaran, Tribocorrosion behavior of duplex treated pure titanium in Simulated Body Fluid, Wear. 302 (2013) 1642–1648. doi:10.1016/j.wear.2013.01.064.

[27] G.H. Zhao, R.E. Aune, N. Espallargas, Tribocorrosion studies of metallic biomaterials: The effect of plasma nitriding and DLC surface modifications, J. Mech. Behav. Biomed. Mater. 63 (2016)

100–114. doi:10.1016/j.jmbbm.2016.06.014.

[28] A. Shenhar, I. Gotman, S. Radin, P. Ducheyne, E.Y. Gutmanas, Titanium nitride coatings on surgical titanium alloys produced by a powder immersion reaction assisted coating method: Residual stresses and fretting behavior, Surf. Coatings Technol. 126 (2000) 210–218. doi:10.1016/S0257-8972(00)00524-7.

[29] M. Rizwan, A. Ahmad, K.M. Deen, W. Haider, Electrochemical behavior and biological response of Mesenchymal Stem Cells on cp-Ti after N-ions implantation, Appl. Surf. Sci. 320 (2014) 718–724. doi:10.1016/j.apsusc.2014.09.169.

[30] G.S. Savonov, M. Ueda, R.M. Oliveira, C. Otani, Electrochemical behavior of the Ti6Al4V alloy implanted by nitrogen PIII, Surf. Coatings Technol. 206 (2011) 2017–2020. doi:10.1016/j.surfcoat.2011.09.007.

[31] F.M. El-Hossary, N.Z. Negm, A.M. Abd El-Rahman, M. Raaif, A.A. Seleem, A.A. Abd El-Moula, Tribo-mechanical and electrochemical properties of plasma nitriding titanium, Surf. Coatings Technol. 276 (2015) 658–667. doi:10.1016/j.surfcoat.2015.06.003.

[32] I.M. Pohrelyuk, V.M. Fedirko, O.V. Tkachuk, R.V. Proskurnyak, Corrosion resistance of Ti–6Al–4V alloy with nitride coatings in Ringer's solution, Corros. Sci. 66 (2013) 392–398. doi:10.1016/j.corsci.2012.10.005.

[33] C. Mendoza, Z. Gonzalez, E. Gordo, B. Ferrari, Y. Castro, Protective nature of nano-TiN coatings shaped by EPD on Ti substrates, J. Eur. Ceram. Soc. 38 (2017) 495–500. doi:10.1016/j.jeurceramsoc.2017.09.046.

[34] E. Galvanetto, F.P. Galliano, A. Fossati, F. Borgioli, S. Marta, Corrosion resistance properties of plasma nitrided Ti – 6Al – 4V alloy in hydrochloric acid solutions, 44 (2002) 1593–1606.

[35] A. Fossati, F. Borgioli, E. Galvanetto, T. Bacci, Corrosion resistance properties of plasma nitrided Ti-6Al-4V alloy in nitric acid solutions, Corros. Sci. 46 (2004) 917–927. doi:10.1016/S0010-938X(03)00188-4.

[36] F. Yildiz, A.F. Yetim, A. Alsaran, A. Çelik, Plasma nitriding behavior of Ti6Al4V orthopedic alloy, Surf. Coatings Technol. 202 (2008) 2471–2476. doi:10.1016/j.surfcoat.2007.08.004.

[37] T. Wierzchoń, E. Czarnowska, J. Grzonka, A. Sowińska, M. Tarnowski, J. Kamiński, K. Kulikowski,

T. Borowski, K.J. Kurzydłowski, Glow discharge assisted oxynitriding process of titanium for medical application, Appl. Surf. Sci. 334 (2015) 74–79. doi:10.1016/j.apsusc.2014.08.071.

[38] V. Fouquet, L. Pichon, M. Drouet, A. Straboni, Plasma assisted nitridation of Ti-6Al-4V, Appl. Surf. Sci. 221 (2004) 248–258. doi:10.1016/S0169-4332(03)00889-4.

[39] D. Nolan, S.W. Huang, V. Leskovsek, S. Braun, Sliding wear of titanium nitride thin films deposited on Ti-6Al-4V alloy by PVD and plasma nitriding processes, Surf. Coatings Technol. 200 (2006) 5698–5705. doi:10.1016/j.surfcoat.2005.08.110.

[40] D. Goldbaum, P. Manimuda, G. Kamath, S. Descartes, J.E. Klemberg-Sapieha, R.R. Chromik, Tribological behavior of TiN and Ti (Si,C)N coatings on cold sprayed Ti substrates, Surf. Coatings Technol. 291 (2016) 264–275. doi:10.1016/j.surfcoat.2016.02.044.

[41] J. Wagner, V. Edlmayr, M. Penoy, C. Michotte, C. Mitterer, M. Kathrein, Deposition of Ti-Al-N coatings by thermal CVD, Int. J. Refract. Met. Hard Mater. 26 (2008) 563–568. doi:10.1016/j.ijrmhm.2008.01.003.

[42] J. Bohlmark, M. Östbye, M. Lattemann, H. Ljungcrantz, T. Rosell, U. Helmersson, Guiding the deposition flux in an ionized magnetron discharge, Thin Solid Films. 515 (2006) 1928–1931. doi:10.1016/j.tsf.2006.07.183.

[43] S.G. Harris, E.D. Doyle, Y.C. Wong, P.R. Munroe, J.M. Cairney, J.M. Long, Reducing the macroparticle content of cathodic arc evaporated TiN coatings, Surf. Coatings Technol. 183 (2004) 283–294. doi:10.1016/j.surfcoat.2003.08.086.

[44] G.A. Rodríguez-Castro, L.F. Jiménez-Tinoco, J.V. Méndez-Méndez, I. Arzate-Vázquez, A. Meneses-Amador, H. Martínez-Gutiérrez, I. Campos-Silva, Damage Mechanisms in AISI 304 Borided Steel: Scratch and Daimler-Benz Adhesion Tests, Mater. Res. 18 (2015) 1346–1353. doi:10.1590/1516-1439.025515.

[45] E. Gemelli, A. Scariot, N.H.A. Camargo, Thermal characterization of commercially pure titanium for dental applications, Mater. Res. 10 (2007) 241–246. doi:10.1590/s1516-14392007000300004.

[46] H. Ollendorf, D. Schneider, A comparative study of adhesion test methods for hard coatings, Surf. Coatings Technol. 113 (1999) 86–102. doi:10.1016/S0257-8972(98)00827-5.

[47] Z. Doni, A.C. Alves, F. Toptan, J.R. Gomes, A. Ramalho, M. Buciumeanu, L. Palaghian, F.S. Silva, Dry sliding and tribocorrosion behaviour of hot pressed CoCrMo biomedical alloy as compared with the cast CoCrMo and Ti6Al4V alloys, Mater. Des. 52 (2013) 47–57. doi:10.1016/j.matdes.2013.05.032.

[48] V. Poulek, J. Musil, V. Valvoda, R. Černý, Microhardness of Ti-N films containing the ε -Ti2N phase, J. Phys. D. Appl. Phys. 21 (1988). doi:10.1088/0022-3727/21/11/020.

[49] I. Petrov, P.B. Barna, L. Hultman, J.E. Greene, Microstructural evolution during film growth, J. Vac. Sci. Technol. A Vacuum, Surfaces, Film. (2003). doi:10.1116/1.1601610.

[50] N.K. Ponon, D.J.R. Appleby, E. Arac, P.J. King, S. Ganti, K.S.K. Kwa, A. O'Neill, Effect of deposition conditions and post deposition anneal on reactively sputtered titanium nitride thin films, Thin Solid Films. 578 (2015) 31–37. doi:10.1016/j.tsf.2015.02.009.

[51] E. Broitman, L. Hultman, Adhesion improvement of carbon-based coatings through a high ionization deposition technique, J. Phys. Conf. Ser. 370 (2012). doi:10.1088/1742-6596/370/1/012009.

[52] N. Figueira, T.M. Silva, M.J. Carmezim, J.C.S. Fernandes, Corrosion behaviour of NiTi alloy, Electrochim. Acta. 54 (2009) 921–926. doi:10.1016/j.electacta.2008.08.001.

[53] M.E. Orazem, B. Tribollet, Electrochemical Impedance Spectroscopy, Jonh Wiley & Sons, New Jersey, 2008.

[54] N. Diomidis, S. Mischler, N.S. More, M. Roy, Tribo-electrochemical characterization of metallic biomaterials for total joint replacement, Acta Biomater. 8 (2012) 852–859. doi:10.1016/j.actbio.2011.09.034.

[55] E.L. Rooy, J.H.L. Van Linden, ASM Metals Handbook, Vol 02 Properties and Selection: Nonferrous Alloys and Special-Purpose Materials, Metals Park, Ohio, 1990. doi:10.1016/S0026-0576(03)90166-8.

[56] A. Iwabuchi, J.W. Lee, M. Uchidate, Synergistic effect of fretting wear and sliding wear of Co-alloy and Ti-alloy in Hanks' solution, Wear. 263 (2007) 492–500. doi:10.1016/j.wear.2007.01.102.

[57] S. Yu, Q. Zeng, A.R. Oganov, G. Frapper, L. Zhang, Phase stability, chemical bonding and mechanical properties of titanium nitrides: A first-principles study, Phys. Chem. Chem. Phys. 17

(2015) 11763–11769. doi:10.1039/c5cp00156k.

[58] R.P. Van Hove, I.N. Sierevelt, B.J. Van Royen, P.A. Nolte, Titanium-Nitride Coating of Orthopaedic Implants: A Review of the Literature, Biomed Res. Int. 2015 (2015). doi:10.1155/2015/485975.

[59] H. Aghajani, M.S. Motlagh, Effect of temperature on surface characteristics of nitrogen ion implanted biocompatible titanium, J. Mater. Sci. Mater. Med. 28 (2017) 29. doi:10.1007/s10856-016-5843-x.

[60] A. Scerri, J. Buhagiar, S. Banfield, J.C. Avelar-Batista Wilson, J. Housden, A. Leyland, A. Matthews, G. Cassar, Corrosion behaviour of triode plasma diffusion treated and PVD TiN-coated Ti-6Al-4V in acidified aqueous chloride environments, Surf. Coatings Technol. 280 (2015) 185–193. doi:10.1016/j.surfcoat.2015.08.040.

[61] L. Thair, U.K. Mudali, N. Bhuvaneswaran, K.G.M. Nair, R. Asokamani, B. Raj, Nitrogen ion implantation and in vitro corrosion behavior of as-cast Ti-6Al-7Nb alloy, Corros. Sci. 44 (2002) 2439–2457. doi:10.1016/S0010-938X(02)00034-3.

[62] S.I. Drob, C. Vasilescu, P. Drob, E. Vasilescu, D.M. Gordin, T. Gloriant, Corrosion Behaviour of Nitrogen-Implantation Ti-Ta-Nb Alloy in Physiological Solutions Simulating Real Conditions from Human Body, Jom. 67 (2015) 818–829. doi:10.1007/s11837-015-1351-6.

[63] D. Zhou, H. Liang, S. Chu, J. Xu, Y. Bai, X. Sun, Thickness dependent microstructural and electrical properties of TiN thin films prepared by DC reactive magnetron sputtering, Ceram. Int. 42 (2015) 2642–2647. doi:10.1016/j.ceramint.2015.10.070.

[64] N. Heide, J.W. Schultze, Corrosion stability of TiN prepared by ion implantation and PVD, Nucl. Inst. Methods Phys. Res. B. 80–81 (1993) 467–471. doi:10.1016/0168-583X(93)96162-6.

[65] J.I. Silva, A.C. Alves, A.M. Pinto, F. Toptan, Corrosion and tribocorrosion behavior of Ti–TiB–TiNx in-situ hybrid composite synthesized by reactive hot pressing, J. Mech. Behav. Biomed. Mater. 74 (2017) 195–203. doi:10.1016/j.jmbbm.2017.05.041.

[66] G.W. Stachowiak, A.W. Batchelor, Engineering Tribology, Butterworth Heinemann, 2005.

[67] F. Toptan, A. Rego, A.C. Alves, A. Guedes, Corrosion and tribocorrosion behavior of Ti–B4C composite intended for orthopaedic implants, J. Mech. Behav. Biomed. Mater. 61 (2016) 152–163. doi:10.1016/j.jmbbm.2016.01.024.

[68] W.H. Kao, Y.L. Su, Y.T. Hsieh, Effects of Duplex Nitriding and TiN Coating Treatment on Wear Resistance, Corrosion Resistance and Biocompatibility of Ti6Al4V Alloy, J. Mater. Eng. Perform. 26 (2017) 3686–3697. doi:10.1007/s11665-017-2815-3.

Chapter 8: Improved tribocorrosion behavior on bio-functionalized β-type titanium alloy by the pillar effect given by TiN reinforcements

Published in Surf. Coat. Technol. 415 (2021) 127122

Improved tribocorrosion behaviour on bio-functionalized β-type titanium alloy by the pillar effect given by TiN reinforcements

Ihsan Çaha[a], Alexandra C. Alves[a], Caterina Chirico[b], Ana Maria Pinto[a,c], Sophia Tsipas[b,d], Elena Gordo[b,d], and Fatih Toptan[a,e,f]

[a] CMEMS-UMinho - Center for MicroElectroMechanical Systems, Universidade do Minho, Azurém, 4800-058 Guimarães, Portugal

[b] Universidad Carlos III de Madrid, Avda. Universidad, 30, 28911 Leganés, Spain

[c] Universidade do Minho, Dept. Eng. Mecânica, Azurém, 4800-058 Guimarães, Portugal

[d] Instituto "Álvaro Alonso Barba", 30, 28911 Leganés, Madrid

[e] Department of Materials Science and Engineering, Izmir Institute of Technology, 35430, Urla, Izmir, Turkey

[f] IBTN/Euro – European Branch of the Institute of Biomaterials, Tribocorrosion and Nanomedicine, Dept. Eng. Mecânica, Universidade do Minho, Azurém, 4800-058 Guimarães, Portugal

[*] Corresponding author at: CMEMS-Uminho – Center for MicroElectroMechanical Systems, Universidade do Minho, Azurém, 4800-058 Guimarães, Portugal. Tel.: +351 253 510 220; fax: +351 253 516 007. E-mail: ihsancaha@gmail.com (Ihsan Çaha).

Abstract

A novel multi-functional material was developed by hard TiN particle reinforcement addition to a β-type Ti alloy, following by bio-functionalization of its surface through Ca and P rich oxide layer. Corrosion and tribocorrosion behavior of this multi-functional material was investigated in phosphate buffer solution at body temperature. Bio-functionalization drastically improved the corrosion and tribocorrosion behavior of the unreinforced and reinforced samples, where the bio-functionalized β-type titanium alloy matrix composite presented the best tribocorrosion behavior due to the load-carrying role of the hard reinforcement phase that gave a support to the functionalized surface layer.

Keywords: Metal matrix composites, β-type Ti alloys, Micro-arc oxidation, Corrosion, Tribocorrosion

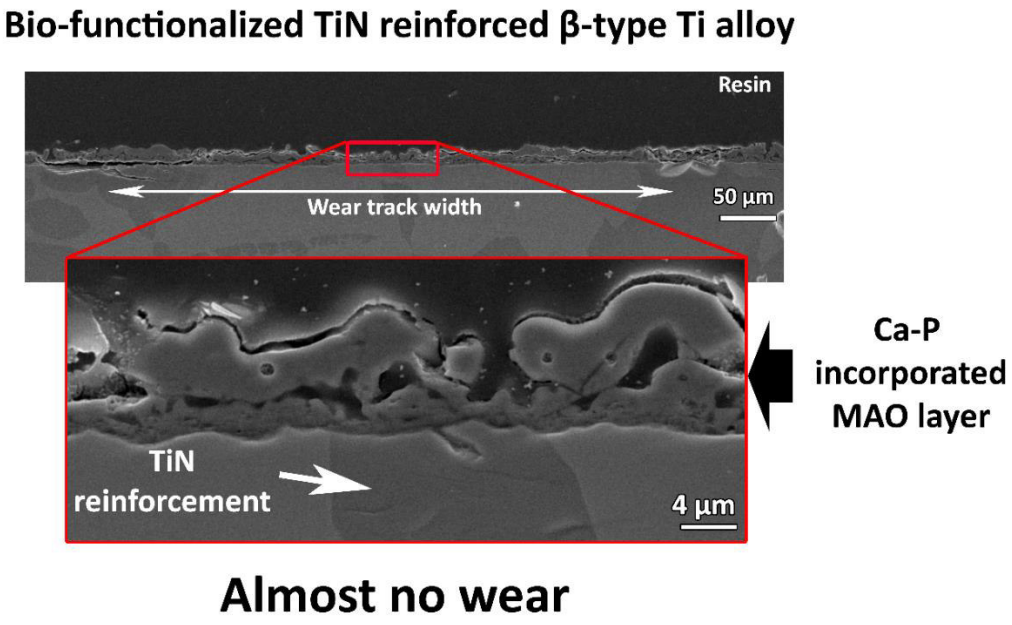

Graphical abstract

8.1. Introduction

β-Type Ti alloys have been the focus of research among metallic based biomaterials particularly for load-bearing applications, hard tis- sue replacement, and fracture healing, mainly due to their two important properties [1,2]: First, they show excellent mechanical compatibility resulted from their low Young's modulus values and appropriate strength which is crucial for reducing stress shielding effect that hinders bone ingrowth [3,4]. Second, they are mostly composed of non-toxic elements, thus, expected to be a good alternative to the most widely employed Ti alloy, α + β type Ti-6Al-4V alloy, which has great concerns due to the release of harmful Al and V ions to cells and tissues [5–7]. However, recently it has been reported that β-type Ti alloys present poor wear resistance compared to Ti-6Al-4V alloy under different tribological conditions, mainly due to the low strain hardening behavior of the β phase [8–11]. The generated wear debris cause osteolysis and eventually implant failure may occur [12]. Hard coatings have been extensively proposed to overcome the poor wear resistance of Ti and its alloys [13–18]. One of the most studied hard coatings for load- bearing applications is TiN coatings due to its high hardness [19], superior wear resistance [20], excellent corrosion resistance [21], and good biocompatibility [22]. However, their inherent brittleness and low fracture toughness are still a major concern for load-bearing applications [23,24].

Metal matrix composites (MMCs) reinforced with hard particles have been well studied in order to overcome the possible low fracture toughness of hard coatings and also to improve the wear resistance

[25]. Ti and its alloys reinforced with TiN particles might potentially over- come the problems related to TiN coatings applied on monolithic metal. Romero *et al.* [26] studied mechanical and microstructural behavior of Ti matrix composites (TMCs) reinforced by TiN particles and reported a significant improvement in hardness not only due to load carrying effect of hard TiN particles, but also the modifications on the matrix micro- structure. Similarly, mechanical and microstructural properties of spark plasma sintered Ti-6Al-4V reinforced with nano TiN particles were studied by Maja *et al.* [27]. The authors reported that the addition of nanosized TiN led to the transformation of α and β phases to a bimodal structure together with drastic increase of hardness and Young's modulus. Furthermore, the fracture toughness of Ti-6Al-4V alloy was improved with reinforced nano TiN particles [28]. Kundu *et al.* [29] studied the effect of volume fraction of TiN on hardness and wear behavior of Ti-6Al-4V alloy and it was reported a direct proportional ratio between volume fraction, hardness, and wear behavior. Regarding corrosion, the main determining parameter is the formation of defects or discontinuities at the matrix/reinforcement interface, which can lead to localized corrosion or galvanic coupling [30–32]. Toptan *et al.* [31] studied the corrosion and tribocorrosion behavior of Ti-B_4C composite in 9 g/l NaCl solution and reported increased corrosion kinetics resulted from localized corrosion due to the formation of porosity around agglomerated B_4C particles. However, Silva *et al.* [33] demonstrated that the defect-free interface between matrix and reinforcement of hybrid in-situ Ti-TiB-TiN_x composite did not deteriorate the corrosion behavior, but significantly improved the tribocorrosion behavior under 1 N normal load in 9 g/l NaCl solution.

While Ti and its alloys are one of the best biocompatible metallic materials, their bioinert behavior cannot lead to bone growth. Micro-arc oxidation (MAO) technique is well studied in the literature not only to improve the bioactivity of Ti and its alloys but also to improve the corrosion and tribocorrosion behavior through a formation of desired surface characteristics [34–40]. Also, the MAO treatment allows incorporating the bioactive agents such as Ca and P allowing to obtain a Ca/P ratio that similar to hydroxyapatite. As a consequence of improved surface roughness, better wettability, and bioactivity, the MAO treated β-type Ti alloys present better adhesion, proliferation, and differentia- tion of cells [41–45].

Poor tribocorrosion resistance and lack of bioactivity are major limiting factors for non-toxic and low Young's modulus β-type Ti alloys to be used in load-bearing biomedical applications. Therefore, the pre- sent work aimed to develop a novel multi-functional material not only to improve the tribocorrosion behavior of β-type Ti alloys, but also to improve their biological behavior. For this reason, a β-type Ti-25Nb-5Fe alloy was reinforced with hard TiN particles by powder metallurgy route, and bio-

functionalized through MAO treatment with incorporation of Ca and P. The corrosion and tribocorrosion behavior was investigated in a physiological solution at body temperature.

8.2. Materials and methods

8.2.1. Materials and sample preparation

The raw material used in this study for obtaining Ti-25Nb-5Fe in wt% alloy was commercial TiH_2 powder (GfE, D_{50} < 63 μm), Nb powder (Sat-Nano, D_{50}: 18 μm), and Fe powder (H.C. Starck, D_{50}: 5 μm). The alloy was reinforced with 5% vol. of TiN powder (Sigma-Aldrich, D_{50}: 1–5 μm). Mixtures of samples were prepared by wet planetary milling to improve the dispersion of powders with milling for 2 h at 150 rpm in isopropanol at a ball-powder ratio of 10:1 in weight. Then, mixtures were dried in a rotary evaporator and green compacts were pressed at 700 MPa (16 mm in diameter and about 4 mm in height), then sintered under 1450 °C for 4 h with a high vacuum (10^{-5} mbar). The Ti-25Nb- 5Fe alloy and its composites were labeled as Alloy and MMC, respectively. Samples were grounded with SiC papers down to 2400 mesh size and mirror-finished by using colloidal silica suspension (Buehler, 0.02 μm), following by ultrasonically cleaning in propanol and distilled water for 10 min and 5 min, respectively. Before tests, samples were held up in a desiccator for a day before starting each test.

8.2.2. Bio-functionalization by micro-arc oxidation

Mirror finished samples were subjected to MAO in an aqueous electrolyte including a mixture of 0.35 M calcium acetate monohydrate (CA, Fluka) and 0.02 M β-glycerophosphate disodium salt pentahydrate (β-GP, Alfa Aesar) in order to obtain Ca and P-rich bio-functionalized surface. The MAO treatment was performed under potentiostatic regime at 300 V by DC power supply (Agilent N5772A) under a limiting current of 2.5 A during 1 min at room temperature under 500 rpm of magnetic stirrer conditions. A platinum foil was used as a cathode with a 7.0 cm^2 exposure area, and distance between Pt foil and samples (anode, with 1.5 cm^2 exposure area) was kept in 8 cm. After the bio-functionalization, all samples were cleaned by propanol and distilled water and dried with warm air. The MAO treated Alloy and MMC samples were labeled as MAO-Alloy and MAO-MMC, respectively.

8.2.3. Corrosion and tribocorrosion tests

Degradation behavior was investigated by corrosion and tribocorrosion tests in phosphate buffer solution (PBS; 0.2 g/l KCl, 0.24 g/l KH_2PO_4, 8 g/l NaCl, 1.44 g/l Na_2HPO_4) at body temperature (37 °C). The Corrosion behavior was studied by open circuit potential (OCP), electrochemical impedance spectroscopy (EIS), and potentiodynamic polarization measurements on 0.38 cm^2 exposure area in

180 ml electrolyte (adapted from ASTM: G3-89) placed using Gamry Potentiostat/ Galvanostat/ZRA (model Reference-600+). An Ag/AgCl (KCl saturated) electrode was used as a reference electrode (RE), a platinum net was used as the counter electrode (CE), and the samples were used as a working electrode (WE). EIS was performed after stabilization of samples of OCP ($\Delta E < 60$ mV for last hour) by scanning a frequency range from 10^{5} to 10^{-2} Hz with an AC signal of 10 mV and counting 7 points per frequency decade. Afterward, the potentiodynamic polarization measurement was performed with a 0.5 mV/s scan rate, starting to scan at $-0.25\ V_{OCP}$ up to $1.5\ V_{Ag/AgCl}$.

Tribocorrosion behavior was studied in a triboelectrochemical cell installed on a reciprocating tribometer (CETR-UMT-2). The tests were carried out against the alumina ball (10 mm in diameter, Ceratec) in 30 ml PBS electrolyte by using a Gamry Potentiostat/Galvanostat (model Reference-600) together with same electrodes that used in the corrosion tests. OCP was monitored before, during, and after sliding. The sliding started under 1 N of normal load, 5 mm of displacement amplitude, 1 Hz of frequency, and 30 min of sliding time.

8.2.4. Characterizations

The microstructure of the bare alloy and composite, and wear scars of counter material were analyzed by optical microscope (OM, Leica- DM2500) after etching in Kroll's reagent (%3 vol HF + %6 vol HNO3 + %91 vol H2O). Surface morphology of the bare (alloy and composite) samples (FEI Quanta 650), MAO treated samples, and wear tracks was analyzed by secondary electron (SE) and backscattered electron (BSE) mode of scanning electron microscopy (SEM) equipped with energy dispersive spectroscopy (EDS) for elemental analysis (FEI Nova 200). The volume fraction of each phase in the MMC sample was calculated using ImageJ 1.51j8 software. Vickers micro-hardness and macro- hardness values were studied by using Emcotest Durascan tester and Officine Galileo Mod. D200 tester, respectively, by a mean of 10 indentations performed randomly per 3 different samples with a load of 0.5 kgf (micro-hardness) and 15 kgf (macro-hardness) during 15 s. The electron backscattering diffraction (EBSD) coupled with the EDS-SEM (FEI Quanta 400) operating at 15 kV was used in order to evaluate the phase mapping, Kikuchi patterns, and crystallographic orientation of each phase in MMC sample. The MAO treated samples were embedded in a hard resin, cut with a diamond disc, ground with SiC papers up to 2400 mesh, and polished with colloidal silica suspension (Buehler, 0.02 μm) to analyze the cross-section. The phase analysis was employed by X-ray diffraction (XRD, Bruker D8 Discover diffractometer) scanning from an angle of (2θ) 20° to 80° with a 0.02°/s step size. Surface wettability was accessed by contact angle measurements through a sessile drop method using an optical

tensiometer (dataphysics, OCA 15 plus). A 5 μl droplet of ultra-pure water was dropped on the surface of the samples and the contact angle was considered after 10 s at room temperature. Three different samples per group were analyzed and the drop image was recorded by using a video camera. The wear track profiles and total wear volume loss was evaluated by 3D profilometry (Profilm3D) over three different samples.

8.3. Results

Figs. 8.1a and b show SE and BSE SEM images together with an insert OM microstructure images of Ti-25Nb-5Fe alloy and its composite. As can be seen in Fig. 8.1a, the alloy presented single phase microstructure included pores. The MMC samples showed two well-differentiated phases, where the bright zones on SEM images correspond to the matrix, and dark one corresponding to the TiN reinforced phase with a 45.6% volume fraction. Also, the MMC samples exhibited smaller grain size and homogeneous dispersion of reinforcing phase through matrix, free from any gross defects such as porosity and cracks. Regarding hardness, the TiN reinforcement was significantly improved the Vickers macro hardness of Alloy as 449 ± 17 HV_{15}, 275 ± 4 HV_{15}, respectively. Also, the reinforced phase was presented drastically higher micro hardness values as compared to its matrix in the MMC sample by 846 ± 65 $HV_{0.5}$ and 421 ± 25 $HV_{0.5}$, respectively.

To identify each phase, EBSD analysis was performed on the MMC sample operating at 15 kV. The BSE image of both phases and its phase mapping image is given in Fig. 8.1c and Fig. 8.1d, respectively. The red regions correspond to the body-centered cubic (bcc) β-Ti phase as given its Kikuchi pattern and index (ICCD 00-044-1288) in Fig. 8.1f. The green regions presented the hexagonal close-packed (hcp) $TiN_{0.3}$ phases as identified by its Kikuchi pattern and index (ICCD 00-041-1352) in Fig. 8.1g. Also, the EBSD crystallographic orientation color map image is shown in Fig. 8.1e. Specifically, most of the areas of the matrix are green corresponding to the bcc (101) indices in the normal direction. The reinforced hcp $TiN_{0.3}$ phase indicated different crystallographic orientations in the β-Ti matrix.

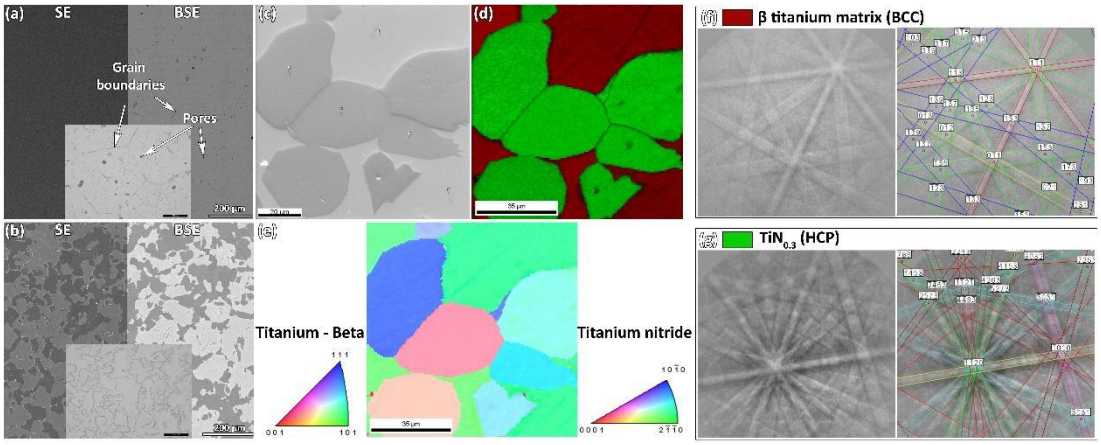

Fig. 8.1. SE and BSE SEM images together with an insert OM images of microstructure of a) Alloy and b) MMC samples. The EBSD results of the MMC sample; c) BSE image of both phases, d) its phase mapping image, e) the crystallographic orientation map and the corresponding inverse pole figure of MMC sample f) Kikuchi pattern of the matrix, g) Kikuchi pattern of reinforced phase.

The top view and cross-section images together with EDS and XRD pattern of MAO treated samples are shown in Fig. 8.2. As can be seen in SE and BSE SEM images, MAO-Alloy and MAO-MMC samples presented a uniform micro-porous volcano-like structure. Similar morphologies observed on the matrix and reinforcing phase of MAO-MMC samples. Regarding cross-sections, both samples presented a triplex anodic layer structure; barrier film formed at metal-anodic layer interface, inner porous layer with small pores, and outer porous layer with larger pores [35]. The average overall thickness of anodic layers for MAO-Alloy and MAO-MMC samples was the approximately 6 and 8 μm, respectively. Moreover, the anodic layer formed on both phases of MAO-MMC samples showed the same triplex structure, where no visible differences were observed. The EDS spectra indicating the incorporation of Ca and P for both samples. The Ca/P atomic ratio was 2.65 and 2.75 for overall MAO-Alloy and overall MAO-MMC samples, respectively. Also, the Ca/P atomic ratio was 2.17 and 2.91 for Z1 and Z2, respectively, showing higher the Ca/P atomic ratio on the reinforcement phase. Nitrogen (N) was not detected by EDS most probably due to relatively high thickness of the MAO layer. Regarding XRD results, while the XRD pattern of Alloy presented fully β-Ti phase (ICCD 00-044-1288), the MMC composed of β-Ti phase (ICCD 00-044-1288) and $TiN_{0.3}$ phase (ICCD 00-041-1352) as in accordance with the EBSD results. In the case of bio-functionalized samples, in addition to their substrate peaks, both MAO treated samples presented anatase (ICCD 00-021-1272) and rutile (ICCD 01-070-7347) TiO_2 peaks.

The surface properties of the material are the first key affecting the biological response of a biomaterial. Being one of the most important parameter, the wettability of samples was investigated

through contact angle measurements and the results are given in Fig. 8.2i, together with the representative optical images. Both bio-functionalized samples presented similar and drastically lower contact angle values compared to their untreated substrate. Among untreated samples, MMC showed a lower contact angle compared to Alloy.

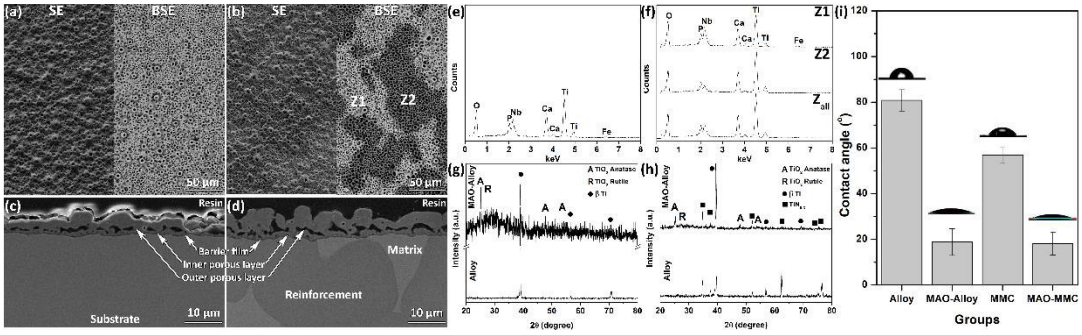

Fig. 8.2. Top view SE/BSE SEM, SE cross-section image, EDS spectra, and XRD pattern of MAO-Alloy in (a), (c), (e), and (g), and MAO-MMC in (b), (d), (f), and (h), respectively. Contact angle values and representative optical images given in (i).

The corrosion behavior was studied by potentiodynamic polarization measurement in PBS solution at 37 °C and the results are given in Fig. 8.3a. Corrosion potential ($E_{(i=0)}$) and passivation current density (i_{pass}) taken at 0.5 $V_{Ag/AgCl}$ were obtained from potentiodynamic polarization curves are shown in Table 8.1, together with recorded OCP values during last 10 min. Alloy and MMC showed similar E_{OCP}, $E_{(i=0)}$, and i_{pass} values and a well-defined passivation plateau. Both bio-functionalized groups presented a passive region but a slight increase of current above approximately 0.75 V that may be explained by the dissolution of Ca and P on the MAO layer. Significant increase of E_{OCP}, $E_{(i=0)}$ and significant decrease of the i_{pass} were observed from untreated groups to MAO treated groups.

Table 8.1. Corrosion potential ($E_{(i=0)}$) and passivation current density (i_{pass}) values obtained from poytentiodynamic polarization curves.

Groups	E_{OCP} (V_{SCE})	$E_{(i=0)}$ (V_{SCE})	i_{pass} ($\mu A.cm^2$)
Alloy	− 0.30 ± 0.03	− 0.25 ± 0.02	2.73 ± 0.33
MMC	− 0.29 ± 0.04	− 0.25 ± 0.04	2.62 ± 0.02
MAO-Alloy	0.54 ± 0.04	0.28 ± 0.03	0.12 ± 0.02
MAO-MMC	0.50 ± 0.10	0.26 ± 0.07	0.12 ± 0.04

Fig. 8.3b and c present the EIS for untreated and bio-functionalized samples in the form of Bode diagram. At the high-frequency range, the constant values of |Z| and phase angles close to 0° were obtained for Alloy and MMC showing a typical response of the electrolyte resistance. Both untreated groups showed one time constant, and their phase angle approaching −90° in low and middle-frequency range suggesting the capacitive behavior of a compact oxide film. The MMC presented a higher phase angle at the middle and low-frequency range and higher |Z| values at low-frequency range. Regarding the MAO-Alloy and MAO-MMC samples, both groups presented three-time constants and their phase angle approached to −60° values. Both groups showed relatively similar |Z| and phase angle values. Figs. 8.3d and e show the schematic representation of the electrical equivalent circuit (EEC) used for fitting the EIS experimental data of the untreated and bio-functionalized groups, respectively. The R_e, R_{ox}, and Q_{ox} are the electrolyte resistance, the resistance of natural passive oxide film, and a constant phase element (CPE), respectively, the CPE considering a non-ideal capacitance of passive oxide film. The R_{bf} and Q_{bf} are showing resistance and a CPE of the barrier film, respectively. Regarding the porous layer, since the thickness of corresponding layers were too high leading poor electronic conductivity, only the CPE of the outer porous layer and the inner porous layer was considered as representing the Q_{wall} and $Q_{1/2wall}$, respectively. The R_e' is additional resistance of the electrolyte inside the outer pores and the R_e'' is additional resistance of the electrolyte inside the inner pores.

The CPE showing a shift from an ideal capacitor used in EECs. The impedance of CPE is defined as: $Z_{CPE} = [Y_0(jw)^n]^{-1}$, where $-1 \leq n \leq 1$. A non-ideal capacitor may be described by a CPE if $n \cong 1$. The EEC parameters obtained from EIS experimental data for untreated and bio-functionalized groups are given in Table 8.2. The quality of fitting on the proposed EECs was evaluated by the χ^2 (goodness of fitting) where the proposed models showed values below 10^{-4}.

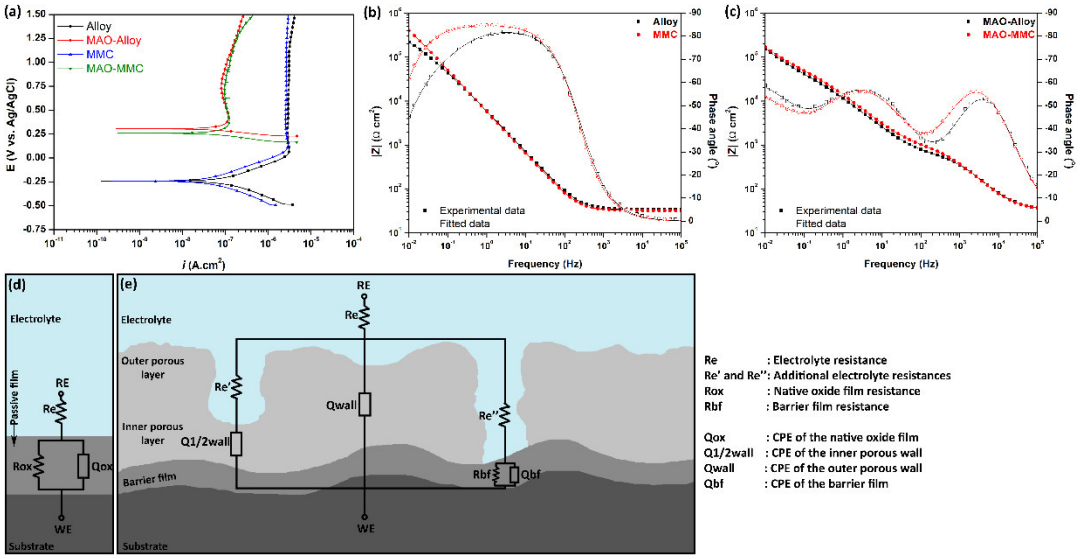

Fig. 8.3. Corrosion behavior: a) Representative potentiodynamic polarization curves of untreated and treated groups; Bode diagrams of b) Alloy and MMC, c) MAO-Alloy and MAO-MMC; EEC proposed for d) Alloy and MMC, and e MAO-Alloy and MAO-MMC (adapted from [46]).

Table 8.2. EEC parameters obtained from EIS data for all groups of samples.

Parameters	Alloy	MMC	MAO-Alloy	MAO-MMC
R_{ox} (MΩ cm²)	0.32 ± 0.06	0.99 ± 0.57	–	–
Q_{ox} (x10⁻⁵ F cm⁻² s^{n-1})	3.35 ± 0.46	3.20 ± 0.13	–	–
n_{ox}	0.91 ± 0.01	0.94 ± 0.01	–	–
Q_{bf} (x10⁻⁵ F cm⁻² s^{n-1})	–	–	3.12 ± 0.06	2.33 ± 0.54
n_{bf}	–	–	0.71 ± 0.01	0.64 ± 0.04
$Q_{1/2wall}$ (x10⁻⁵ F cm⁻² s^{n-1})	–	–	1.97 ± 0.26	1.52 ± 0.53
$n_{1/2wall}$	–	–	0.72 ± 0.01	0.73 ± 0.02
Q_{wall} (x10⁻⁵ F cm⁻² s^{n-1})	–	–	0.17 ± 0.03	0.19 ± 0.03
n_{wall}	–	–	0.83 ± 0.01	0.82 ± 0.01
χ^2 (x 10⁻⁴)	1.0 ± 0.2	1.4 ± 0.3	1.3 ± 0.2	0.3 ± 0.2

The evolution of OCP before, during, and after sliding together with the evolution of coefficient of friction (COF) are given in Fig. 8.4a. Before sliding, bio-functionalized samples showed significantly higher OCP values and all samples presented stable OCP values in agreement with E_{OCP} values shown in Table 8.1. As soon as sliding started, a sudden drop on OCP was recorded for Alloy and MMC samples due to

mechanical destruction of the passive film eventually exposing the corrosive electrolyte to the bare material. Alloy exhibited relatively large oscillations attributed to depassivation/repassivation mechanisms, whereas local increments of OCP were observed for MMC during sliding. After sliding, the OCP of both groups immediately increased close to the values observed before sliding as a consequence of repassivation of the worn area [47]. Regarding both bio-functionalized groups, there was no evidence of drop, an almost constant OCP value was recorded during the entire test.

The evolution of COF can be also seen in Fig. 8.4a. When sliding started, the COF value of Alloy reached values around 0.7 and evolved around this value during sliding with larger oscillations. Regarding MMC samples, once sliding started, COF values were recorded around 0.5 and evolved similar to Alloy till around 750 s and after that, local decrements and increments were observed corresponding to an increments and decrements, respectively, on OCP values. Both bio-functionalized samples presented relatively stable COF values around 0.4 with minor oscillations till the end of sliding.

The representative SEM images of wear tracks, the 2D and 3D wear track profile images together with cross-section SEM images of bio-functionalized groups are also shown in Fig. 8.4. Alloy presented significantly larger wear track width and more wear damage compared to other groups. Bio-functionalization clearly reduced the wear damage on both Alloy and MMC samples (Figs. 8.5d and e, respectively). Among bio-functionalized groups, although both groups presented relatively similar wear track width, the MAO-Alloy showed irregular wear track borders.

Worn surface features can be seen in more detail on the representative higher magnification SEM images shown in Figs. 8.5f-i. Both Alloy and MMC worn surfaces presented parallel sliding grooves and discontinuous tribolayer formation where MMC exhibited smoother surface. Among bio-functionalized samples, distinct worn features clearly observed in Figs. 8.5h and i. While the worn surface of MAO-Alloy sample exhibited mainly partially damaged MAO layer (removed outer MAO layer), worn MAO-MMC surfaces mainly presented a mixture of smashed outer MAO layer and unaffected zones.

The OM images taken from the wear scars on the alumina balls used as counter-material are presented in Figs. 8.4j-m. The wear scars on the balls that slid against the untreated samples were much larger than that observed on the balls used to test the MAO treated samples, which is in accordance with the dimensions of the wear tracks. Gross material transfer to the alumina counter-body was observed for Alloy.

Since no well-distinguishable wear loss occurred on bio-functionalized samples, the representative 2D and 3D worn surface profiles are only given for the untreated groups and presented together with the measured total wear volume loss in Figs. 8.4n and o. The alloy presented drastically deeper and larger wear track in agreement with the wear track SEM images. As can be seen from the profiles, while MMC sample presented rougher wear track, Alloy showed a smooth and uniform wear track. Regarding total wear volume loss values, Alloy presented almost 6 times higher wear volume loss. Cross-sectional SEM image of wear tracks perpendicular to the sliding direction of bio-functionalized samples are given in Figs. 8.5p and q. A partially damaged MAO layer, after the removal of the outer MAO layer, was observed on worn MAO-Alloy, whereas very less damage was observed on worn MAO-MMC, as in agreement with the top view SEM images of wear tracks.

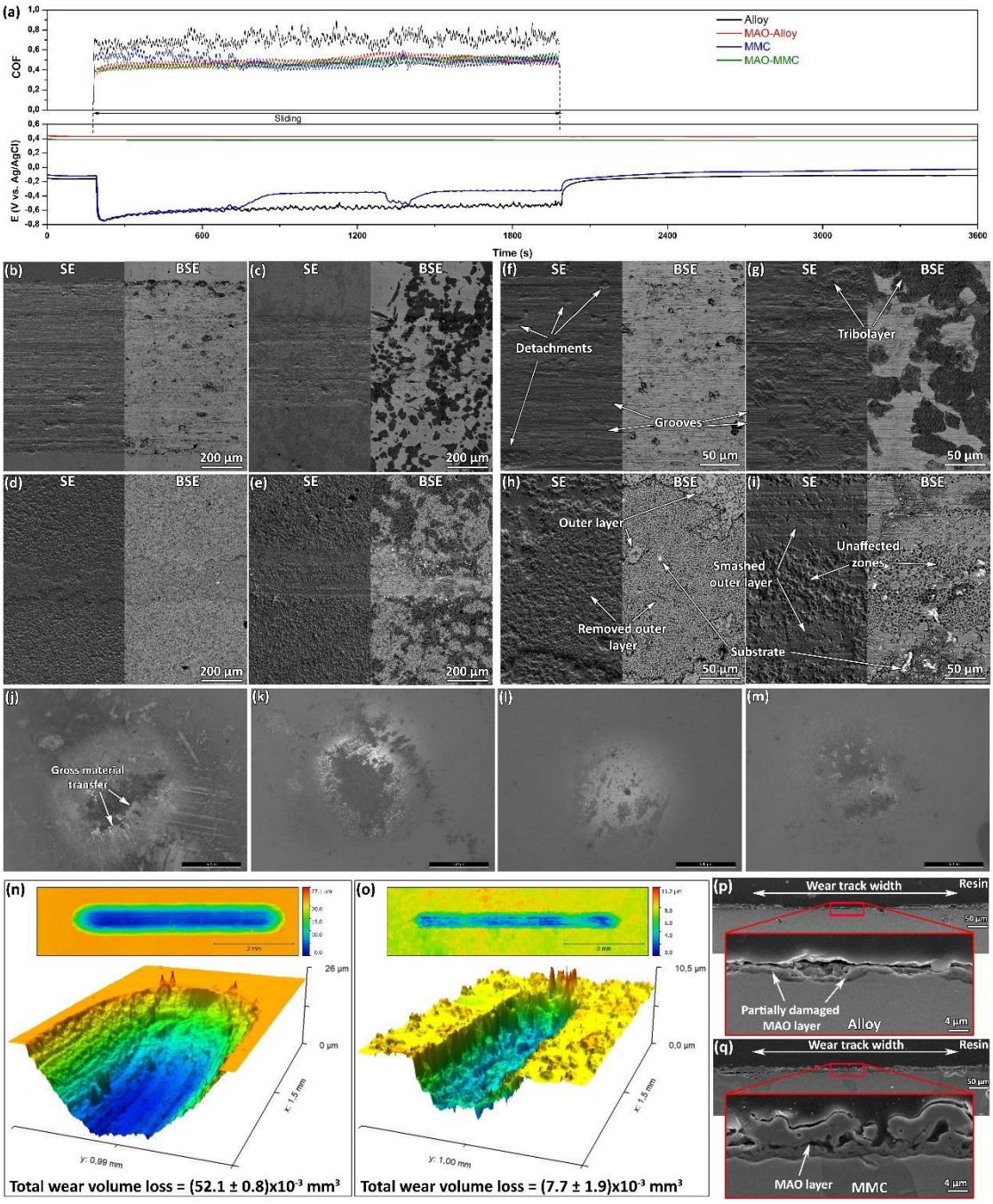

Fig. 8.4. Tribocorrosion behavior: a) The representative evolution of OCP before, during, and after sliding, together with the evolution of COF under sliding; lower magnification SE and BSE SEM images of wear tracks for b) Alloy, c) MMC, d) MAO-Alloy, and e) MAO-MMC; higher magnification SE and BSE images of worn surfaces for f) Alloy, g) MMC, h) MAO-Alloy, and i) MAO-MMC; wear scar OM images of counter material for j) Alloy, k) MMC, l) MAO-Alloy, and m) MAO-MMC; representative 2D and 3D (taken from the border of the wear tracks) wear track images, and measured total wear volume loss for n) Alloy and o) MMC; cross-section SEM images of wear tracks perpendicular to the sliding direction for (p) MAO-Alloy and (q) MAO-MMC.

8.4. Discussion

8.4.1. Microstructure

The size of TiN reinforcement was bigger than the raw TiN powder (1-5 μm) suggesting that the chemical reaction took place during sintering. The XRD and EBSD Kikuchi patterns revealed the reinforced phase as $TiN_{0.3}$, which was uniformly distributed. Also, the top view microstructures (Fig. 8.1b and c) and the cross-sectional microstructures of MMC (Fig. 8.2d) showed no evidence of interfacial defects suggesting excellent bonding at the matrix/reinforcement interface resulted from in-situ chemical reaction. It is known that on MMCs, in addition to the direct strengthening by the effect of the reinforcement, indirect strengthening resulted from the alterations on matrix structure such as strain hardening, dislocations and grain refinement is occurred. Consequently, a significant increase was obtained on hardness values from 275 ± 4 HV_{15} to 449 ± 17 HV_{15}, as also previously been reported for 5% vol. TiN reinforced pure Ti [26], thanks to thermodynamic compatibility and contamination-free matrix-reinforcement interface, along with classical composite strengthening mechanisms [48].

MAO is one of the most effective surface modification techniques for the bio-functionalization of valve metals and their alloys due to its simplicity, high efficiency, and low cost [49]. The incorporation of Ca and P bioactive elements were successfully achieved, that are reported to improve the biological behavior of implant materials since they are naturally presented in bones [50]. Also, the created higher surface roughness is known to be suitable for cell adhesion [51]. Moreover, the XRD results showed the formation of anatase and rutile phases in the MAO layer suggesting better osteointegration compared to bare materials [39]. Apart from its thickness, no visible differences on the microstructure of the MAO layer was observed after the incorporation of the reinforcement, while both bio-functionalized groups presented the same Ca/P ratio and crystalline anatase and rutile phases on the MAO layer. Concerning wettability, although both bio-functionalized groups showed the same and drastically lower contact angle (18 ± 2), MMC group (57 ± 3) presented lower values than the values of Alloy (81 ± 5), indicating improvement of hydrophilicity of the surface. The decreament of contact angle with MAO layer formation is mainly due to formation of higher surface porosity and rougher topography [38]. The decrement on contact angle with reinforcement has been also reported for laser processed TiN reinforced Ti-6Al-4V due to their higher surface energy as compared to the unreinforced alloy [51]. Hydrophilic surfaces are more prone to adhesion of proteins, molecules, cells, and tissue interactions, and improving osteointegration rate [52]. Therefore, the bio-functionalization may improve bioactivity in a biological environment by

transforming the surfaces from hydrophobic to hydrophilic together with other factors such as Ca/Pa ratio, surface roughness, and crystal structure, as discussed above.

8.4.2. Corrosion behavior

The defects at matrix/reinforcement interface such as cracks, porosity, discontinuities, and gaps are known as a determining factor on the corrosion behavior of MMCs, may be resulted in localized corrosion and galvanic coupling between the matrix and the reinforcement [32,33,53,54]. Based on the results, a clean and compatible interface was obtained for MMC samples resulted from the chemical reaction. Also, the corrosion results did not suggest any localized corrosion and galvanic coupling between the matrix and the reinforcement. Thus, the same EEC was used for both untreated groups that consider a native oxide film was formed on the surface of the samples exposed to PBS solution without any discontinuities on the matrix/reinforcement interface. As can be seen in Table 8.2, both Alloy and MMC samples showed similar $E_{OCP}, E_{(i=0)}, i_{pass}$ and Q_{ox} values, but the MMC presented higher R_{ox} values suggesting better corrosion resistance, which is in accordance with its higher $|Z|_{f\to 0}$ and higher phase angles at middle and lower frequency. Also, since surface heterogeneities influence the n values, lower n_{ox} values obtained for Alloy points higher surface heterogeneities resulted from its porosity as observed in Fig. 8.1a. This better corrosion behavior of MMC may be explained by the contribution of the $TiN_{0.3}$ reinforcing phase acting as inert physical barrier, similar to several MMC systems reported in the literature [55].

It is well reported that MAO treatment improves the corrosion behavior of Ti and its alloys [34,35,56,57]. Both bio-functionalized groups presented significantly higher E_{OCP} and $E_{(i=0)}$, and lower i_{pass} values compared to the untreated groups indicating their lower tendency to corrosion and corrosion rate in PBS solution. Regarding EIS, the same EEC had proposed before by some of the present authors to fit the results of MAO treated cp-Ti under the same conditions [35,46]. According to the EEC parameters given in Table 8.2, there was no significant difference between Q and n values of both bio-functionalized groups. The observed lower n values of bio-functionalized groups compared to the n_{ox} may be due to increased roughness and heterogeneities. The bio-functionalized groups presented similar n values except for n_{bf}, that might be due to chemical heterogeneities on barrier film formed on MAO-MMC sample. The lower Q_{wall} values compared with their $Q_{1/2wall}$ results from the higher thickness of the pores walls, since the thickness is inversely proportional to capacitance. Also, the Q_{bf}

values of bio-functionalized groups were lower than the Q_{ox} values of untreated groups suggesting improvement of corrosion behavior with MAO treatment.

8.4.3. Tribocorrosion behavior

The suggested tribocorrosion mechanisms are schematically illustrated in Fig. 8.5. The observed larger and unstable COF values with severe wear damage of Alloy resulted in higher wear volume loss revealed a dominantly adhesive wear mechanism as also evidenced on gross transfer of the substrate to the counter material slid against Alloy (Fig. 8.4j). Also, the parallel grooves on wear track of Alloy suggested abrasive wear mechanism, which can be explained by the ploughing action of the transferred material on the counter body. Similar dominant abrasive/adhesive mechanisms were reported for different β type Ti alloys under different testing conditions [8,10,11,58,59].

Similar wear mechanism was also observed for MMC, but with less visible wear damage and drastically lower wear volume loss, mainly due to the load-carrying effect of harder reinforcement phase, together with the contribution of the indirect strengthening resulted in the drastically increased hardness. Moreover, the formation of a tribolayer may also play a role for lower wear volume loss (Fig. 8.5g). The formation of tribolayer particularly observed on the reinforcement phase that may be explained by its the higher hardness, since, as reported by Cvijović-Alagić *et al.* [8], the harder material is able to hold a thicker oxide layer more uniformly as compared to a softer material. Likewise, β-Ti matrix does not have sufficient ability to hold an oxide patch during sliding due to its low plastic shear resistance [9]. As can be seen from Fig. 8.4, while MMC presented lower overall COF values, it presented relatively similar OCP and COF evolution up to around 750 s. After that time, the gradual increment on the OCP and decrement on the COF, followed by a relatively stable behavior suggested formation of a tribolyer. As observed in Fig. 8.5g, this tribolayer was in a discontinuous form. Also, this tribolayer might got thicker with sliding time, and due to its physical protection role, it may cause a local increment on OCP values. However, after reaching a certain thickness, it might be swept away by the counter body. Therefore, the repetitive thickening and breaking of this tribolayer can induce the decrements and increments both in OCP and COF values. Similar mechanisms were reported by Silva *et al.* [33] for Ti-TiB-TiN_x hybrid composite on reciprocating sliding under 1 N of normal load and 1 Hz of frequency in 9 g/l NaCl solution, where a continuous and compacted tribolayer played a dominant role on the wear mechanism.

Bio-functionalization drastically improved the tribocorrosion behavior of both alloy and MMC as evidenced by nobler OCP values, lower and more stable COF values, and less visible damage on the surfaces. The tribocorrosion mechanisms of the MAO layers formed on cp-Ti (grade 2) already reported

in the literature [34,36,64]. Oliveira *et al.* [34] studied a MAO layer composed of an amorphous outer layer followed by a gradient rutile to anatase structure formed due to a very high cooling rate during MAO treatment. As soon as sliding started, this amorphous layer easily worn out due to high contact pressure resulted from its high surface roughness. The rutile-anatase crystalline barrier layer played a main protective role against wear due to better mechanical behavior of the crystalline phases, especially the higher hardness of the rutile phase [36]. The observed irregular shape of wear track in the case of MAO-Alloy was due to the detachment of the outer porous layer during sliding. While small local damages of the MAO layer were observed on the worn surface of the Alloy, as can be seen more clearly in Fig. 8.4p, a partially damaged MAO layer was still survived against the counter body. In the case of MAO-MMC samples, since they presented relatively less damage of the MAO layer, most of the wear track composed of unaffected (intact) surfaces and/or smashed outer MAO layer. The better wear behavior of MAO-MMC samples compared to the MAO-Alloy samples may be explained by the pillar effect of the $TiN_{0.3}$ reinforcing phases under the TiO_2 MAO surface. The MAO layer formed on hard $TiN_{0.3}$ phase seems to carry efficiently the applied load, and thus its wear track presented less overall damage (Fig. 8.4q).

This is a novel consept for the bio-functionalization of β type Ti alloy matrix composites through MAO treatment for load-bearing implants. Although the MAO-MMC group presented promising behavior under the studied conditions, several studies need to be performed such as a detailed mechanical characterization (especially Young's modulus), the investigation of corrosion, and tribocorrosion behavior in more complex electrolytes, and finally the analysis of biological behavior *in vitro* and *in vivo*. Finally, in order to minimize the increase on Young's modulus after the addition of TiN particles, instead of bulk MMCs, functionally graded metal matrix composite concept can be considered.

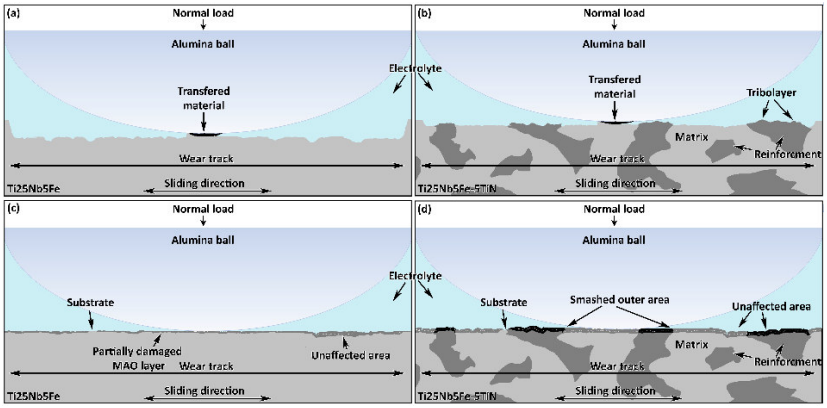

Fig. 8.5. Schematic illustrations of tribocorrosion mechanisms for a) Alloy, b) MMC, c) MAO-Alloy, and d) MAO-MMC samples.

8.5. Conclusion

The β type Ti-25Nb-5Fe alloy was reinforced with 5 vol% TiN particles and both alloy and composites were bio-functionalized with incorporation Ca and P through MAO treatment. The Alloy and MMC showed similar corrosion behavior and their corrosion behavior was significantly improved by the bio-functionalization treatment, mostly due to the formation of thicker oxide layer compared to their passive film. While the tribocorrosion behavior of Alloy improved with TiN reinforcement resulted from drastically improved hardness and microstructure, it was further improved by the bio-functionalization treatment due to obtaining a thick rutile-anatase TiO_2 layer. The MAO layer formed on the composites stayed mostly intact after tribocorrosion due to the pillar effect given by the reinforcements.

Acknowledgments

This work is supported by FCT with the reference project UID/EEA/04436/2019, together with M-ERA-NET/0001/2015, as well, by MINECO (Spain) through the program PCIN-2016-123 and the Ramón y Cajal project RYC-2014-15014. I. Çaha is grateful for the financial support through a Ph.D. grant under the NORTE-08-5369-FSE-000012 project, and mobility program under INTERREG VA España Portugal (POCTEP) territorial cooperation programme (Project ref: 0300_NANOGATEWAY_6_P). The authors would also like to acknowledge Dr. Andrea Zille for the provision of the contact angle measurements.

References

[1] M. Niinomi, M. Nakai, J. Hieda, Development of new metallic alloys for biomedical applications, Acta Biomater. 8 (2012) 3888–3903. doi:10.1016/j.actbio.2012.06.037.

[2] M. Geetha, A.K. Singh, R. Asokamani, A.K. Gogia, Ti based biomaterials, the ultimate choice for orthopaedic implants - A review, Prog. Mater. Sci. 54 (2009) 397–425. doi:10.1016/j.pmatsci.2008.06.004.

[3] Y. Bai, Y. Deng, Y. Zheng, Y. Li, R. Zhang, Y. Lv, Q. Zhao, S. Wei, Characterization, corrosion behavior, cellular response and in vivo bone tissue compatibility of titanium-niobium alloy with low Young's modulus, Mater. Sci. Eng. C. 59 (2016) 565–576. doi:10.1016/j.msec.2015.10.062.

[4] A.H. Glassman, J.D. Bobyn, M. Tanzer, New Femoral Designs: Do They Influence Stress Shielding?, Clin. Orthop. Relat. Res. 453 (2006) 64–74. https://journals.lww.com/clinorthop/Fulltext/2006/12000/New_Femoral_Designs__Do_They

_Influence_Stress.12.aspx.

[5] M. Niinomi, Recent metallic materials for biomedical applications, Metall. Mater. Trans. A. 33 (2002) 477–486. doi:10.1007/s11661-002-0109-2.

[6] E. Eisenbarth, D. Velten, M. Müller, R. Thull, J. Breme, Biocompatibility of β-stabilizing elements of titanium alloys, Biomaterials. 25 (2004) 5705–5713. doi:10.1016/j.biomaterials.2004.01.021.

[7] P.R. Walker, J. LeBlanc, M. Sikorska, Effects of aluminum and other cations on the structure of brain and liver chromatin, Biochemistry. 28 (1989) 3911–3915. doi:10.1021/bi00435a043.

[8] Z. Cvijovic, S. Mitrovic, V. Panic, Wear and corrosion behaviour of Ti – 13Nb – 13Zr and Ti – 6Al – 4V alloys in simulated physiological solution, Corros. Sci. 53 (2011) 796–808. doi:10.1016/j.corsci.2010.11.014.

[9] Y.S. Lee, M. Niinomi, M. Nakai, K. Narita, K. Cho, Predominant factor determining wear properties of β-type and (α+β)-type titanium alloys in metal-to-metal contact for biomedical applications, J. Mech. Behav. Biomed. Mater. 41 (2015) 208–220. doi:10.1016/j.jmbbm.2014.10.005.

[10] X. Yang, C.R. Hutchinson, Corrosion-wear of β-Ti alloy alloy TMZF (Ti-12Mo-6Zr-2Fe) in simulated body fluid, Acta Biomater. 42 (2016) 429–439. doi:10.1016/j.actbio.2016.07.008.

[11] I. Çaha, A.C. Alves, P.A.B. Kuroda, C.R. Grandini, A.M.P. Pinto, L.A. Rocha, F. Toptan, Degradation behavior of Ti-Nb alloys: Corrosion behavior through 21 days of immersion and tribocorrosion behavior against alumina, Corros. Sci. 167 (2020) 108488. doi:10.1016/j.corsci.2020.108488.

[12] D. Bitar, Biological response to prosthetic debris, World J. Orthop. 6 (2015) 172. doi:10.5312/wjo.v6.i2.172.

[13] F. Galliano, E. Galvanetto, S. Mischler, D. Landolt, Tribocorrosion behavior of plasma nitrided Ti-6Al-4V alloy in neutral NaCl solution, Surf. Coatings Technol. 145 (2001) 121–131. doi:10.1016/S0257-8972(01)01309-3.

[14] D. Nolan, S.W. Huang, V. Leskovsek, S. Braun, Sliding wear of titanium nitride thin films deposited on Ti-6Al-4V alloy by PVD and plasma nitriding processes, Surf. Coatings Technol. 200 (2006) 5698–5705. doi:10.1016/j.surfcoat.2005.08.110.

[15] Ł. Łapaj, J. Wendland, J. Markuszewski, A. Mróz, T. Wiśniewski, Retrieval analysis of titanium nitride (TiN) coated prosthetic femoral heads articulating with polyethylene, J. Mech. Behav. Biomed. Mater. 55 (2016) 127–139. doi:10.1016/j.jmbbm.2015.10.012.

[16] A. Vadiraj, M. Kamaraj, Effect of surface treatments on fretting fatigue damage of biomedical titanium alloys, Tribol. Int. 40 (2007) 82–88. doi:10.1016/j.triboint.2006.02.064.

[17] A. Samanta, M. Bhattacharya, I. Ratha, H. Chakraborty, S. Datta, J. Ghosh, S. Bysakh, M. Sreemany, R. Rane, A. Joseph, S. Mukherjee, B. Kundu, M. Das, A.K. Mukhopadhyay, Nano- and micro-tribological behaviours of plasma nitrided Ti6Al4V alloys, J. Mech. Behav. Biomed. Mater. 77 (2018) 267–294. doi:10.1016/j.jmbbm.2017.09.013.

[18] W. Cui, G. Qin, J. Duan, H. Wang, A graded nano-TiN coating on biomedical Ti alloy: Low friction coefficient, good bonding and biocompatibility, Mater. Sci. Eng. C. 71 (2017) 520–528. doi:10.1016/j.msec.2016.10.033.

[19] E. Santecchia, A.M.S. Hamouda, F. Musharavati, E. Zalnezhad, M. Cabibbo, S. Spigarelli, Wear resistance investigation of titanium nitride-based coatings, Ceram. Int. 41 (2015) 10349–10379. doi:10.1016/j.ceramint.2015.04.152.

[20] I. Çaha, A.C. Alves, L.J. Affonço, P.N. Lisboa-Filho, J.H.D. da Silva, L.A. Rocha, A.M.P. Pinto, F. Toptan, Corrosion and tribocorrosion behaviour of titanium nitride thin films grown on titanium under different deposition times, Surf. Coatings Technol. 374 (2019) 878–888. doi:10.1016/j.surfcoat.2019.06.073.

[21] T.M. Manhabosco, S.M. Tamborim, C.B. dos Santos, I.L. Müller, Tribological, electrochemical and tribo-electrochemical characterization of bare and nitrided Ti6Al4V in simulated body fluid solution, Corros. Sci. 53 (2011) 1786–1793. doi:10.1016/j.corsci.2011.01.057.

[22] M. Annunziata, A. Oliva, M.A. Basile, M. Giordano, N. Mazzola, A. Rizzo, A. Lanza, L. Guida, The effects of titanium nitride-coating on the topographic and biological features of TPS implant surfaces, J. Dent. 39 (2011) 720–728. doi:10.1016/j.jdent.2011.08.003.

[23] M.T. Mathew, P. Srinivasa Pai, R. Pourzal, A. Fischer, M.A. Wimmer, Significance of tribocorrosion in biomedical applications: Overview and current status, Adv. Tribol. (2009) 12. doi:10.1155/2009/250986.

[24] R.J.K. Wood, Tribo-corrosion of coatings: a review, J. Phys. D. Appl. Phys. 40 (2007) 5502–5521.

doi:10.1088/0022-3727/40/18/S10.

[25] M. Rosso, Ceramic and metal matrix composites: Routes and properties, J. Mater. Process. Technol. 175 (2006) 364–375. doi:https://doi.org/10.1016/j.jmatprotec.2005.04.038.

[26] F. Romero, V. Amigó, M.D. Salvador, A. Vicente, Interactions in Titanium Matrix Composites Reinforced by Titanium Compounds by Conventional PM Route, Mater. Sci. Forum. 534–536 (2007) 817–820. doi:10.4028/www.scientific.net/msf.534-536.817.

[27] M.E. Maja, O.E. Falodun, B.A. Obadele, S.R. Oke, P.A. Olubambi, Nanoindentation studies on TiN nanoceramic reinforced Ti–6Al–4V matrix composite, Ceram. Int. 44 (2018) 4419–4425. doi:10.1016/j.ceramint.2017.12.042.

[28] O.E. Falodun, B.A. Obadele, S.R. Oke, M.E. Maja, P.A. Olubambi, Effect of sintering parameters on densification and microstructural evolution of nano-sized titanium nitride reinforced titanium alloys, J. Alloys Compd. 736 (2018) 202–210. doi:10.1016/j.jallcom.2017.11.140.

[29] S. Kundu, M. Hussain, V. Kumar, S. Kumar, A.K. Das, Direct metal laser sintering of TiN reinforced Ti6Al4V alloy based metal matrix composite: Fabrication and characterization, Int. J. Adv. Manuf. Technol. 97 (2018) 2635–2646. doi:10.1007/s00170-018-2159-7.

[30] A.M. Ribeiro, A.C. Alves, F.S. Silva, F. Toptan, Electrochemical characterization of hot pressed CoCrMo–HAP biocomposite in a physiological solution, Mater. Corros. 66 (2015) 790–795. doi:10.1002/maco.201407885.

[31] F. Toptan, A. Rego, A.C. Alves, A. Guedes, Corrosion and tribocorrosion behavior of Ti–B4C composite intended for orthopaedic implants, J. Mech. Behav. Biomed. Mater. 61 (2016) 152–163. doi:10.1016/j.jmbbm.2016.01.024.

[32] B. Bobić, S. Mitrovic, M. Babic, I. Bobić, Corrosion of aluminium and zinc-aluminium alloys based metal-matrix composites, Tribol. Ind. 31 (2009) 44–53. https://www.scopus.com/inward/record.uri?eid=2-s2.0-73949137681&partnerID=40&md5=e6b16abb35b092f2435644231ff63e75.

[33] J.I. Silva, A.C. Alves, A.M. Pinto, F. Toptan, Corrosion and tribocorrosion behavior of Ti–TiB–TiNx in-situ hybrid composite synthesized by reactive hot pressing, J. Mech. Behav. Biomed. Mater. 74 (2017) 195–203. doi:10.1016/j.jmbbm.2017.05.041.

[34] F.G. Oliveira, A.R. Ribeiro, G. Perez, B.S. Archanjo, C.P. Gouvea, J.R. Araújo, A.P.C. Campos, A. Kuznetsov, C.M. Almeida, M.M. Maru, C.A. Achete, P. Ponthiaux, J. Celis, L.A. Rocha, Understanding growth mechanisms and tribocorrosion behaviour of porous TiO2 anodic films containing calcium , phosphorous and magnesium, Appl. Surf. Sci. 341 (2015) 1–12. doi:10.1016/j.apsusc.2015.02.163.

[35] A.C. Alves, F. Wenger, P. Ponthiaux, J.P. Celis, A.M. Pinto, L.A. Rocha, J.C.S. Fernandes, Corrosion mechanisms in titanium oxide-based films produced by anodic treatment, Electrochim. Acta. 234 (2017) 16–27. doi:10.1016/j.electacta.2017.03.011.

[36] A.C. Alves, F. Oliveira, F. Wenger, P. Ponthiaux, J.-P. Celis, L.A. Rocha, Tribocorrosion behaviour of anodic treated titanium surfaces intended for dental implants, J. Phys. D Appl. Phys. 46 (2013) 404001–9. doi:10.1088/0022-3727/46/40/404001.

[37] D.R.N. Correa, L.A. Rocha, A.R. Ribeiro, S. Gemini-Piperni, B.S. Archanjo, C.A. Achete, J. Werckmann, C.R.M. Afonso, M. Shimabukuro, H. Doi, Y. Tsutsumi, T. Hanawa, Growth mechanisms of Ca- and P-rich MAO films in Ti-15Zr-xMo alloys for osseointegrative implants, Surf. Coatings Technol. 344 (2018) 373–382. doi:10.1016/j.surfcoat.2018.02.099.

[38] M.B. Sedelnikova, E.G. Komarova, Y.P. Sharkeev, A. V. Ugodchikova, L.S. Mushtovatova, M.R. Karpova, V. V. Sheikin, L.S. Litvinova, I.A. Khlusov, Zn-, Cu- or Ag-incorporated micro-arc coatings on titanium alloys: Properties and behavior in synthetic biological media, Surf. Coatings Technol. 369 (2019) 52–68. doi:10.1016/j.surfcoat.2019.04.021.

[39] H. Te Chen, C.J. Chung, T.C. Yang, C.H. Tang, J.L. He, Microscopic observations of osteoblast growth on micro-arc oxidized β titanium, Appl. Surf. Sci. 266 (2013) 73–80. doi:10.1016/j.apsusc.2012.11.087.

[40] L. Zhao, Y. Wei, J. Li, Y. Han, R. Ye, Y. Zhang, Initial osteoblast functions on Ti-5Zr-3Sn-5Mo-15Nb titanium alloy surfaces modified by microarc oxidation, J. Biomed. Mater. Res. - Part A. 92 (2010) 432–440. doi:10.1002/jbm.a.32348.

[41] S. Yu, Z. Yu, G. Wang, J. Han, X. Ma, M.S. Dargusch, Biocompatibility and osteoconduction of active porous calcium-phosphate films on a novel Ti-3Zr-2Sn-3Mo-25Nb biomedical alloy, Colloids Surfaces B Biointerfaces. 85 (2011) 103–115. doi:10.1016/j.colsurfb.2011.02.025.

[42] S.J. CLi, C.Y. Zheng, J. Fu, Z. Guo, Y.L. Hao, R. Yang, Z.X. Guo, Synthesis of a porous oxide layer

on a multifunctional biomedical titanium by micro-arc oxidation, Mater. Sci. Eng. C. 29 (2009) 1923–1934. doi:10.1016/j.msec.2009.03.004.

[43] S. Yu, Z.T. Yu, G. Wang, J.Y. Han, X.Q. Ma, M.S. Dargusch, Preparation and osteoinduction of active micro-arc oxidation films on Ti-3Zr-2Sn-3Mo-25Nb alloy, Trans. Nonferrous Met. Soc. China (English Ed. 21 (2011) 573–580. doi:10.1016/S1003-6326(11)60753-X.

[44] M.B. Sedelnikova, Y.P. Sharkeev, E.G. Komarova, I.A. Khlusov, V. V. Chebodaeva, Structure and properties of the wollastonite–calcium phosphate coatings deposited on titanium and titanium–niobium alloy using microarc oxidation method, Surf. Coatings Technol. 307 (2016) 1274–1283. doi:10.1016/j.surfcoat.2016.08.062.

[45] A. Kazek-Kęsik, M. Krok-Borkowicz, G. Dercz, A. Donesz-Sikorska, E. Pamuła, W. Simka, Multilayer coatings formed on titanium alloy surfaces by plasma electrolytic oxidation-electrophoretic deposition methods, Electrochim. Acta. 204 (2016) 294–306. doi:10.1016/j.electacta.2016.02.193.

[46] A.C. Alves, A.I. Costa, F. Toptan, J.L. Alves, I. Leonor, E. Ribeiro, R.L. Reis, A.M.P. Pinto, J.C.S. Fernandes, Effect of bio-functional MAO layers on the electrochemical behaviour of highly porous Ti, Surf. Coatings Technol. 386 (2020) 125487. doi:10.1016/j.surfcoat.2020.125487.

[47] T. Hanawa, K. Asami, K. Asaoka, Repassivation of titanium and surface oxide film regenerated in simulated bioliquid, J. Biomed. Mater. Res. 40 (1998) 530–538. doi:10.1002/(SICI)1097-4636(19980615)40:4<530::AID-JBM3>3.0.CO;2-G.

[48] W.J. Lu, D. Zhang, R.J. Wu, H. Mori, Solidification paths and reinforcement morphologies in melt-processed (TiB + TiC)/Ti in situ composites, Metall. Mater. Trans. A Phys. Metall. Mater. Sci. 33 (2002) 3055–3063. doi:10.1007/s11661-002-0290-3.

[49] Y. Wang, H. Yu, C. Chen, Z. Zhao, Review of the biocompatibility of micro-arc oxidation coated titanium alloys, Mater. Des. 85 (2015) 640–652. doi:10.1016/j.matdes.2015.07.086.

[50] C.E. Tanase, M. Golozar, S.M. Best, R.A. Brooks, Cell response to plasma electrolytic oxidation surface-modified low-modulus β-type titanium alloys, Colloids Surfaces B Biointerfaces. 176 (2019) 176–184. doi:10.1016/j.colsurfb.2018.12.064.

[51] J.I. Rosales-Leal, M.A. Rodríguez-Valverde, G. Mazzaglia, P.J. Ramón-Torregrosa, L. Díaz-Rodríguez, O. García-Martínez, M. Vallecillo-Capilla, C. Ruiz, M.A. Cabrerizo-Vílchez, Effect of

roughness, wettability and morphology of engineered titanium surfaces on osteoblast-like cell adhesion, Colloids Surfaces A Physicochem. Eng. Asp. 365 (2010) 222–229. doi:10.1016/j.colsurfa.2009.12.017.

[52] R.A. Gittens, L. Scheideler, F. Rupp, S.L. Hyzy, J. Geis-Gerstorfer, Z. Schwartz, B.D. Boyan, A review on the wettability of dental implant surfaces II: Biological and clinical aspects, Acta Biomater. 10 (2014) 2907–2918. doi:10.1016/j.actbio.2014.03.032.

[53] F. Toptan, L.A. Rocha, Tribocorrosion in metal matrix composites, Mater. Sci. Eng. Concepts, Methodol. Tools, Appl. 2–3 (2017) 825–844. doi:10.4018/978-1-5225-1798-6.ch032.

[54] L.H. Hihara, R.M. Latanision, Corrosion of metal matrix composites, Int. Mater. Rev. 39 (1994) 245–264. doi:10.1179/imr.1994.39.6.245.

[55] K.H.W. Seah, M. Krishna, V.T. Vijayalakshmi, J. Uchil, Corrosion behaviour of garnet particulate reinforced LM13 Al alloy MMCs, Corros. Sci. 44 (2002) 917–925. doi:10.1016/S0010-938X(01)00099-3.

[56] A. Kazek-Kęsik, M. Krok-Borkowicz, E. Pamuła, W. Simka, Electrochemical and biological characterization of coatings formed on Ti-15Mo alloy by plasma electrolytic oxidation, Mater. Sci. Eng. C. 43 (2014) 172–181. doi:10.1016/j.msec.2014.07.021.

[57] C.F. Liu, T.H. Lee, J.F. Liu, W.T. Hou, S.J. Li, Y.L. Hao, H. Pan, H.H. Huang, A unique hybrid-structured surface produced by rapid electrochemical anodization enhances bio-corrosion resistance and bone cell responses of β-type Ti-24Nb-4Zr-8Sn alloy, Sci. Rep. 8 (2018) 1–14. doi:10.1038/s41598-018-24590-x.

[58] I. Çaha, A. Alves, C. Chirico, A. Pinto, S. Tsipas, E. Gordo, F. Toptan, Corrosion and Tribocorrosion Behavior of Ti-40Nb and Ti-25Nb-5Fe Alloys Processed by Powder Metallurgy, Metall. Mater. Trans. A Phys. Metall. Mater. Sci. 51 (2020) 3256–3267. doi:10.1007/s11661-020-05757-6.

[59] Y. Lee, M. Niinomi, M. Nakai, K. Narita, K. Cho, Differences in Wear Behaviors at Sliding Contacts for β-Type and (α + β)-Type Titanium Alloys in Ringer' s Solution and Air, Mater. Trans. 56 (2015) 317–326.

[60] F. Toptan, A.C. Alves, I. Kerti, E. Ariza, L.A. Rocha, Corrosion and tribocorrosion behaviour of Al-Si-Cu-Mg alloy and its composites reinforced with B4C particles in 0.05M NaCl solution, Wear. 306 (2013) 27–35. doi:10.1016/j.wear.2013.06.026.

[61] J.I. Silva, A.C. Alves, A.M. Pinto, F.S. Silva, F. Toptan, Dry sliding wear behaviour of Ti-TiB-TiN x in-situ composite synthesised by reactive hot pressing, Int. J. Surf. Sci. Eng. 10 (2016) 317–329. doi:10.1504/IJSURFSE.2016.077533.

[62] K. Soorya Prakash, P.M. Gopal, D. Anburose, V. Kavimani, Mechanical, corrosion and wear characteristics of powder metallurgy processed Ti-6Al-4V/B4C metal matrix composites, Ain Shams Eng. J. (2016) 0–7. doi:10.1016/j.asej.2016.11.003.

[63] A.M. Ribeiro, A.C. Alves, L.A. Rocha, F.S. Silva, F. Toptan, Synergism between corrosion and wear on CoCrMo–Al2O3biocomposites in a physiological solution, Tribol. Int. 91 (2015) 198–205. doi:10.1016/j.triboint.2015.01.018.

[64] A.F. Yetim, Investigation of wear behavior of titanium oxide films, produced by anodic oxidation, on commercially pure titanium in vacuum conditions, Surf. Coatings Technol. 205 (2010) 1757–1763. doi:10.1016/j.surfcoat.2010.08.079.

Chapter 9: Tribocorrosion resistant Ti40Nb-TiN composites having TiO_2-based nanotubular surfaces

Submitted for publication in Corrosion Science

Tribocorrosion resistant Ti40Nb-TiN composites having TiO_2-based nanotubular surfaces

Ihsan Çaha[a], Alexandra C. Alves[a], Caterina Chirico[b], Ana Maria Pinto[a,c], Sophia Tsipas[b,d], Elena Gordo[b,d], and Fatih Toptan[a,e,f]

[a] CMEMS-UMinho - Center for MicroElectroMechanical Systems, Universidade do Minho, Azurém, 4800-058 Guimarães, Portugal

[b] Universidad Carlos III de Madrid, Avda. Universidad, 30, 28911 Leganés, Spain

[c] Universidade do Minho, Dept. Eng. Mecânica, Azurém, 4800-058 Guimarães, Portugal

[d] Department of Materials Science and Engineering, Izmir Institute of Technology, 35430, Urla, Izmir, Turkey

[e] Instituto "Álvaro Alonso Barba", 30, 28911 Leganés, Madrid

[f] IBTN/Euro – European Branch of the Institute of Biomaterials, Tribocorrosion and Nanomedicine, Dept. Eng. Mecânica, Universidade do Minho, Azurém, 4800-058 Guimarães, Portugal

* Corresponding author at: CMEMS-Uminho – Center for MicroElectroMechanical Systems, Universidade do Minho, Azurém, 4800-058 Guimarães, Portugal. Tel.: +351 253 510 220; fax: +351 253 516 007. E-mail: ihsancaha@gmail.com (Ihsan Çaha).

Abstract

A novel multi-functional material was developed by hard TiN particle reinforcement addition to β-type Ti40Nb alloy, followed by surface functionalization, yielding with the formation of a nanotubular layer. Corrosion and tribocorrosion behavior were investigated in a PBS solution at body temperature. Results revealed that the TiN reinforcement did not jeopardize the corrosion behavior and drastically improved tribocorrosion resistance of Ti40Nb alloy as a consequence of the load-carrying effect given by the reinforcement phases. The corrosion and tribocorrosion behavior was further improved through surface functionalization due to the formation of a well-adhered anatase-rutile TiO_2-based nanotubular layer.

Keywords: Metal matrix composites, β-type Ti alloys, Nanotubes, Corrosion, Tribocorrosion

9.1. Introduction

Many new biocompatible Ti alloys were developed in the last decade to replace the Ti6Al4V alloy that is the most used Ti alloy for orthopedic applications. One reason was the clinical concern about V and Al, which were replaced with alloying elements such as Ta, Nb, Mo, or Zr that show better cytocompatibility [1,2]. Another concern is about higher Young's modulus of Ti and Ti6Al4V alloy (100-120 GPa) compared to Young's modulus of bone (varies in a range of 4–30 GPa) [3,4]. This mismatch leads to aseptic loosening of load-bearing implants due to bone resorption (known as a stress-shielding phenomenon) [5]. While newly developed biocompatible β-type Ti alloys have shown lower Young's modulus to reduce the stress-shielding effect, recently, their poor wear resistance has been reported in the literature [6–10]. Wear debris are generated in load-bearing implants due to poor wear resistance of Ti and its alloys, leading to implant loosening, as well, osteolysis [11]. In order to overcome the poor wear resistance of Ti and its alloys, hard coatings such as TiN, TiC, TiB, and TiAlN have been widely studied in the literature [12–19]. Among them, TiN has been the most proposed one due to its excellent corrosion and tribocorrosion resistance, and good biocompatibility [20–23]. Nevertheless, the inherent brittleness and low fracture toughness of monolithic hard coatings are still a major concern for load-bearing applications [23,24].

Metal matrix composites (MMCs) have been well-studied due to their potential to provide tailored mechanical properties such as high hardness, strength, and fracture toughness, compared to their matrix materials [24–26]. TiN particle reinforced Ti and its alloys have been processed by different techniques such as powder metallurgy, mechanical alloying and spark plasma sintering, and their mechanical, microstructural, and wear behavior were investigated. Romero *et al.* [27] studied the mechanical behavior of TiN reinforced Ti processed by conventional powder metallurgy route and reported a significant increase of hardness for composites due to good dispersion of the particles in the matrix and grain refinement. Falodun *et al.* [28] investigated the effect of spark plasma sintering parameters on the microstructure of TiN reinforced Ti6Al4V alloy and it was reported that the composite sintered for 30 min showed a significantly higher hardness and fracture toughness. Kundu *et al.* [29] reported that wear resistance of Ti6Al4V was improved with TiN reinforcement by direct laser sintering method due to a uniform dispersion and good metallurgical bonding of TiN particles in the matrix. According to the corrosion behavior of MMCs, localized corrosion is often observed in ex-situ MMCs due to the formation of discontinuities, defects, and gaps at the matrix/reinforcement interface [30,31]. Toptan *et al.* [26] studied the corrosion and tribocorrosion behavior of Ti-B_4C composite in 9 g/l NaCl solution and reported increased corrosion kinetics resulted from localized corrosion due to the formation of high porosity around

B_4C particles. Since the discontinuities at the interface are typically eliminated in the in-situ composites, localized corrosion that mainly resulted from these discontinuities has been minimized [32]. Accordingly, Silva *et al.* [32] demonstrated that the "clean", defect-free interface between the matrix and reinforcement of the hybrid in-situ Ti-TiB-TiN_x composite did not present any deterioration on the corrosion behavior while significantly improving the tribocorrosion behavior under 1 N normal load in 9 g/l NaCl solution.

In addition to the abovementioned issues, another common clinical concern is the bioinertness of Ti and its alloys, leading to poor osteointegration of implants. The surface topography and characteristics of the metallic implant surface has a significant influence on the biological response [33]. One of the most proposed surface modification in the literature to improve the biological response is the development of a nanotubular layer on Ti and its alloys [34,35]. The chemical composition of the nanotubular layer on Ti alloys is composed of the mixture of the oxides of the alloying elements, where mixed nanotubular structures have been reported to exhibit better biological response compared to single-phase structures due to a better surface stability [36–40]. Ding *et al.* [41] reported better bioactivity for mesenchymal stem cell adhesion and spreading on mixed nanotubular layer (TiO_2-based; TNT) formed on Ti35Nb compared to single-phase TNT grown on Ti. Regarding corrosion behavior, Fatichi *et al.* [42] studied the corrosion behavior of the TNT surface on β-type Ti35Nb4Zr alloy in 9 g/l NaCl solution and reported that TNT surfaces exhibited higher corrosion resistance than the untreated Ti due to a thicker barrier layer supplied by the TNT layer. On the other hand, there are limited number of studies in literature about the tribocorrosion or wear behavior of TNT formed on β-type Ti alloys. Luz *et al.* [43] reported that the TNT formed on Ti35Nb presented a significant increase of wear resistance in dry sliding condition.

One of the most studied β-type Ti alloys for load-bearing implants is Ti40Nb mainly due to its low Young's modulus and excellent biological response [6,44–46]. However, as previously reported by some of the present authors [6,10], Ti40Nb alloy presented significantly lower tribocorrosion resistance compared to Ti6Al4V in a simple physiological solution. In order to overcome on the poor tribocorrosion behavior of β-type Ti40Nb alloy, the present authors previously reported a low-cost and facile promising method through TNT formation resulted in drastically increased adhesion strength to substrate [47]. Accordingly, as a following study, the present work aimed to develop a novel multi-functional hybrid material not only to overcome the poor tribocorrosion behavior of the β-type Ti40Nb alloy but also give the first insight on surface functionalization through TNT formation to improve its biological response.

9.2. Materials and methods

9.2.1. Materials and sample preparation

The raw commercial TiH_2 powder (GfE, D_{50}< 63 μm) and Nb powder (Sat-Nano, D_{50}: 18 μm) were used to obtain Ti40Nb alloy (composition in wt%). The Ti40Nb alloy reinforced with 5% vol. of TiN powder (Sigma-Aldrich, D_{50}: 1-5 μm) for obtaining Ti40Nb-TiN composite. A planetary wet milling was used to prepare mixtures of samples under 150 rpm for 2 h in isopropanol together with a ball-powder ratio of 10:1 in weight. Afterwards, a rotary evaporator was used to dry the powder mixtures. The dried mixtures were pressed under a pressure of 700 MPa to form green compacts (cylindrical billets 10 mm in diameter and 4 mm in height), then subsequently sintered under a high vacuum (10^{-5} mbar) at 1450 °C temperature for 4 h holding time. The Ti40Nb alloy and its composite were labeled as Alloy and MMC, respectively. All characterizations, TNT layer formation, and tribocorrosion tests were employed on mirror-finished surfaces by grounded down to 2400 mesh SiC papers followed by polishing with silica colloidal suspension (Buehler, 0.02 μm), except for corrosion studies performed on the surfaces grounded down to 1200 mesh SiC papers. After the samples were cleaned by an ultrasonic bath in propanol and distilled water for 10 min and 5 min and dried with warm air, respectively, the samples were kept in a desiccator for 24 h before starting each test.

9.2.2. Nanotubular layer formation

The nanotubular layer was obtained by anodic treatment using a two-electrode electrochemical cell set up with samples (having an exposed area of 1.1 cm^2) and a Pt sheet (having an exposed area of 5.3 cm^2) as the working and counter electrodes, respectively. The distance between electrodes was kept constant as 8 cm, and the electrolyte was continually stirred at 500 rpm. A DC power supply (Agilent Technologies N5772A) and multimeter (Agilent Technologies 34410A) was connected to an electrochemical cell for the anodic treatments. Two-step anodic treatment and heat treatment was used to improve the adhesion and stability of nanotubes. The first anodic treatment was carried out in an aqueous solution of 1.0 M H_3PO_4 (orthophosphoric acid, Fluka, ≥ %85) and 0.8 wt% NaF (Panreac, %99) as 180 ml volume of electrolyte, at a constant voltage of 20 V for 1 h. The second step anodic treatment was performed in a fluoride-free electrolyte of 1.0 M H_3PO_4 (orthophosphoric acid, Fluka, ≥ %85) under constant 20 V for 5 min on nanotubes formed surfaces to create an additional oxide layer in nanotubes/substrate interface. After the second anodic treatment, the samples were rinsed with propanol and distilled water. Then, a heat treatment was carried out at 500 °C for 3 h with a heating and

cooling rate of 5 °C/min. The nanotubes formed Alloy and MMC samples were labeled as NT-Alloy and NT-MMC, respectively

9.2.3. Corrosion and tribocorrosion tests

The open-circuit potential (OCP), electrochemical impedance spectroscopy (EIS), and potentiodynamic polarization tests were performed in a 180 ml PBS solution (0.2 g/l KCl, 0.24 g/l KH_2PO_4, 8 g/l NaCl, 1.44 g/l Na_2HPO_4) at 37 °C on 0.38 cm^2 of the exposed area to evaluate the corrosion behavior. The conventional three-electrode electrochemical cell was used with a counter electrode (CE) of Pt net, a reference electrode (RE) of saturated Ag/AgCl, and samples as a working electrode (WE), connected to a Potentiostat/Galvanostat/ZRA (Gamry Reference-600+). After stabilization at OCP (ΔE<60 mV/h), EIS was performed at OCP with AC potential amplitude of 10 mV at frequencies between 10^2 Hz and 10^5 Hz. The results were fitted with proposed electrical equivalent circuits (EECs) using gamry Echem Analyst (7.05 version) software. After EIS, a potentiodynamic polarization scan was carried out starting at −0.25 V_{OCP} and up to 1.5 $V_{Ag/AgCl}$ in anodic direction with a scan rate of 0.5 mV/s.

The tribocorrosion behavior of samples was investigated at OCP with a tribometer (CETR-UMT-2) of pin-on-plate reciprocating sliding configuration. A two-electrode set-up was connected to a Potentiostat/Galvanostat/ZRA (Gamry Reference-600), using a reference electrode (RE) of saturated Ag/AgCl, and the samples were placed as WE against an alumina ball (10 mm in diameter, Ceratec). The tests were carried out under a normal load of 0.5 N during 2 h with a frequency of 1 Hz and an amplitude of 2 mm. Sliding motion started after the stabilization of OCP (ΔE<60 mV/h, min. 2 h), then the counter material was removed and OCP was recorded for 30 min.

All corrosion and tribocorrosion tests were at least triplicated on three different samples and all results were presented as the arithmetic mean ± standard deviation.

9.2.4. Characterization

The microstructure of untreated alloy and composite was analyzed by optical microscope (OM, Leica-DM2500) after etching in Kroll's reagent (%3 HF + %6 HNO_3 + %91 H_2O), the grain size was measured using the linear intercept method. Surface morphology of untreated samples (FEI Quanta 650), nanotubes formed samples, and wear tracks was analyzed by secondary electron (SE) and backscattered electron (BSE) mode of scanning electron microscopy (SEM) equipped with energy dispersive spectroscopy (EDS) for elemental analysis (FEI Nova 200). The volume fraction of each phase in the MMC sample was calculated by image analysis using ImageJ 1.51j8 software. The density of the

processed samples was measured by the Archimedes method, while the Vickers macro-hardness was studied by using Officine Galileo Mod. D200 tester by a mean of 10 indentations performed randomly per 3 different samples with a load of 15 kgf during 15 s. The electron backscattering diffraction (EBSD) coupled with the EDS-SEM (FEI Quanta 400) operating at 15 kV was used in order to evaluate the Kikuchi patterns of each phase in the MMC sample. In order to analyze the cross-section of NT layers, samples were broken by a three-point bending set up (Instron 8874), where the distance between the two parallel supports was 10 mm and the indenter was driven down to the specimens at a speed of 8.33×10^{-6} m/s. The structural characterization was employed by X-ray diffraction (XRD, Bruker D8 Discover diffractometer) scanning from an angle of (2θ) 20° to 80° with a 0.02°/s step size. Surface wettability was assessed by contact angle measurements through a sessile drop method using an optical tensiometer (dataphysics, OCA 15 plus). A 5 μl droplet of ultra-pure water was dropped on the surface of the samples and the contact angle was considered after 10 s at room temperature. Three different samples per group were analyzed and the drop image was recorded by using a video camera. The wear track profiles and total wear volume loss was evaluated by 3D profilometry (Profilm3D) over the three different samples.

9.3. Results

The SE and BSE-SEM images together with the insert OM microstructure images of as-processed Alloy and MMC samples are shown in Fig. 9.1. While Alloy presented single-phase (Fig. 9.1a), MMC sample showed three distinct phases (Figs. 9.1b and c). As can be seen from the higher magnification BSE image and insert EDS results in Fig. 9.1c, the bright zones correspond to the matrix and both darker regions depict the reinforcement phases with 24.6% total volume fraction, while the relatively darker region presents the higher concentration of N. The microstructure of MMC reveals the distribution of reinforcement mainly along grain boundaries. Furthermore, as can be seen from Figs. 9.1a and b, MMC clearly showed a smaller grain size compared to Alloy. Also, MMC presented lower porosity compared to Alloy, as in accordance with the relative density values, and significantly higher hardness values (Table 9.1).

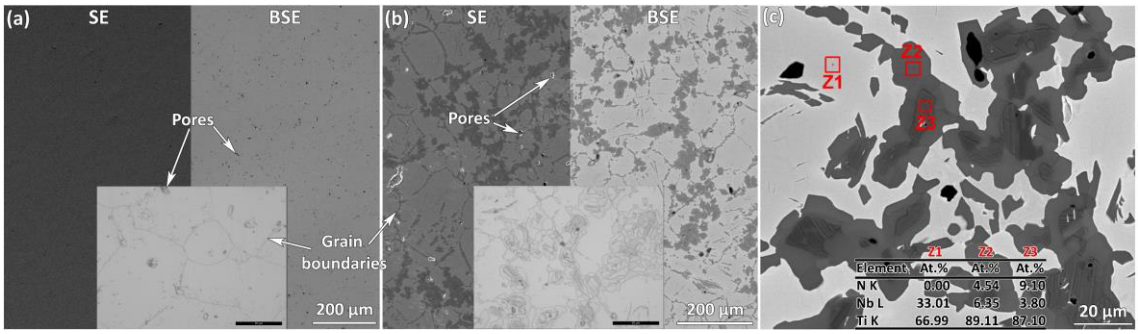

Fig. 9.1. SE, BSE, and OM (insert images) microstructure images of (a) Alloy, (b) MMC samples, and (c) higher magnification BSE image of MMC with EDS analysis results.

Table 9.1. Relative density and hardness values of Alloy and MMC.

Sample	Relative density (%)	Hardness (HV_{15})
Alloy	93.4 ± 1.6	208 ± 20
MMC	97.6 ± 1.6	362 ± 30

EBSD technique was used to identify the phases in the MMC sample (Fig. 9.2). Three distinct regions were clearly observed from the tilted BSE SEM image (Fig. 9.2a). The Kikuchi pattern and its index for matrix (Z1 zone) presented body-centered cubic (bcc) β phase (ICCD 00-044-1288) as shown in Fig. 9.2b. Z2 regions show a hexagonal closed-packed (hcp) $TiN_{0.3}$ phase (ICCD 00-041-1352) as given its Kikuchi patterns and index in Fig. 9.2c. Finally, Z3 regions included line-like features that were associated with the face-centered cubic (fcc) $NbTiN_2$ phases (ICCD 01-089-5134), where its Kikuchi patterns and index presented in Fig. 9.2d.

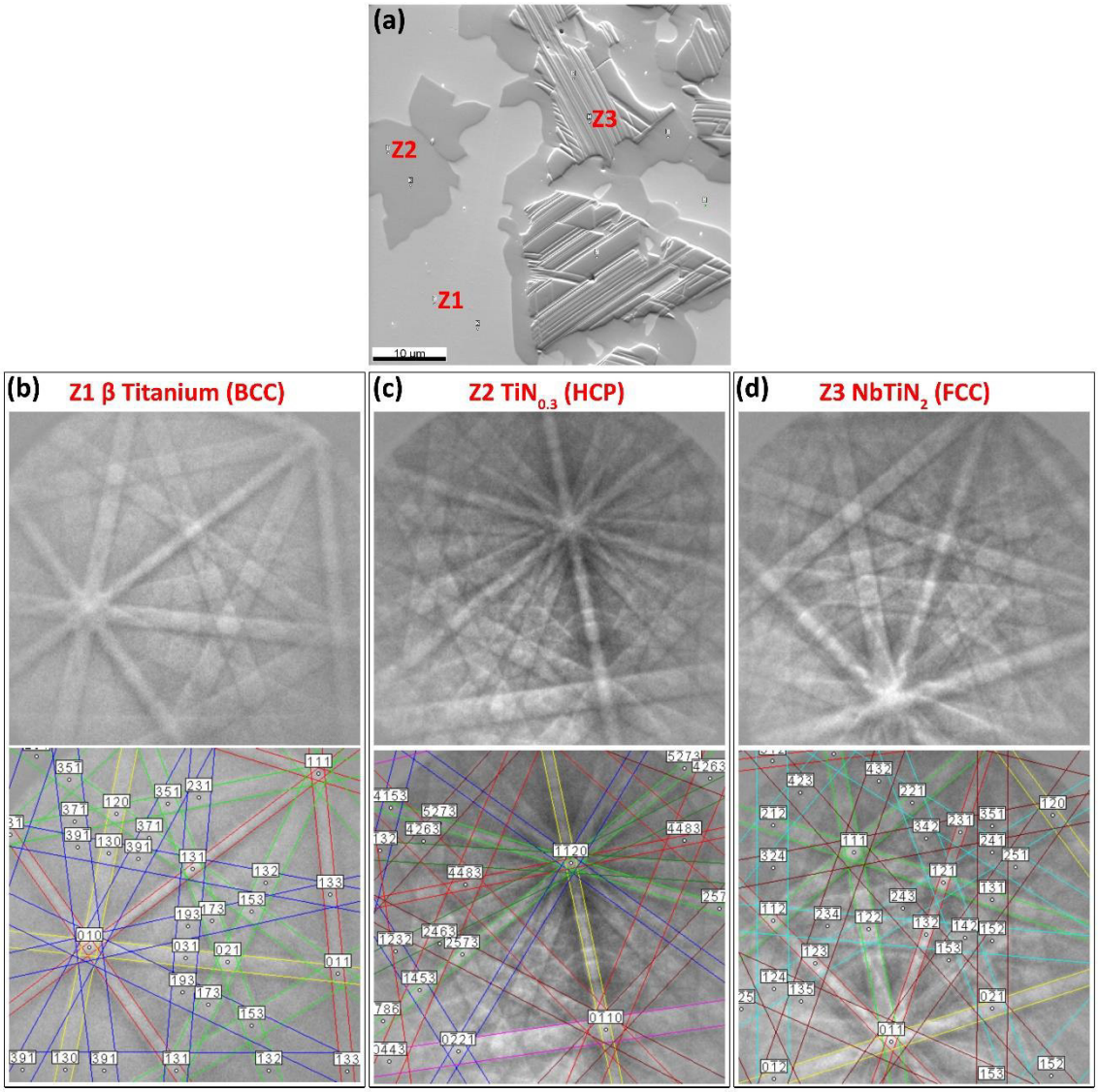

Fig. 9.2. (a) BSE image for three phases and corresponding EBSD Kikuchi patterns for (b) bcc β Ti matrix, (c) hcp $TiN_{0.3}$ phase, and (d) fcc $NbTiN_2$ phase with their index.

Fig. 9.3 shows the top view and cross-section SEM images of TNT formed samples together with the XRD pattern of untreated and treated samples. As can be seen from the top view and cross-section SEM images, a uniform and well-aligned TNT layer formed on NT-Alloy and matrix of NT-MMC sample. On the other hand, a nanostructure formation was obtained on reinforcement phases as given in Fig. 9.3f. According to cross-section analysis, both TNT layers were well embedded in the additional oxide layer, without any evidence of hollow space or gap between nanotubes and substrate. Table 9.2 shows the inner diameter (D_i) and length (L_n) of nanotubes. The nanotubes formed on NT-Alloy presented larger D_i and smaller L_n compared to ones formed on the matrix of the NT-MMC sample. The XRD results depict a single β phase (ICCD 00-044-1288) of Alloy and a mixture of the β phase, $TiN_{0.3}$ (ICCD 00-041-1352),

and $NbTiN_2$ phases (ICCD 01-089-5134) of MMC sample, which are in agreement with microstructure and EBSD results. Also, both TNT formed samples showed additional anatase (ICCD 00-021-1272) and rutile (ICCD 01-070-7347) crystalline phases.

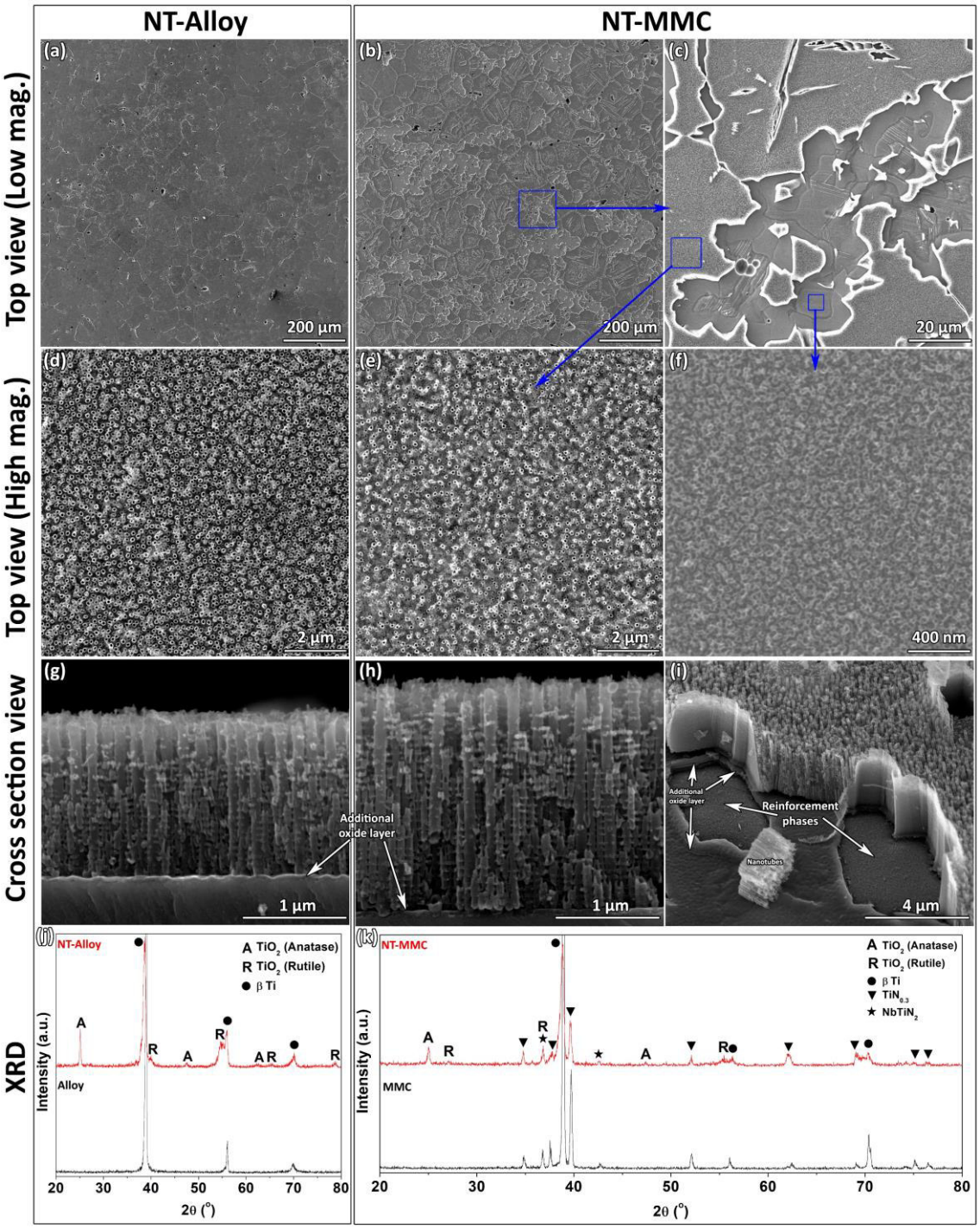

Fig. 9.3. Lower and higher magnification top view, cross-section view SEM images of NT layers, and XRD of untreated and NT formed samples.

Table 9.2. Inner diameter (D_i) and length (L_n) of nanotubes formed on NT-Alloy and NT-MMC samples.

Sample	D_i (nm)	L_n (µm)
NT-Alloy	95.9 ± 11.6	1.52 ± 0.03
NT-MMC	77.9 ± 12.8	2.12 ± 0.07

The wettability of surface is one of the most crucial parameter for early stage of implantation resulted in rejection or integration of implant materials [48]. Hence, the wettability was evaluated by contact angle measurements, where the contact angle values of the MMC (57 ± 4°) sample was lower than the values of Alloy (79 ± 6°) (Fig. 9.4). While the TNT formed samples presented drastically lower contact angle values than their untreated ones, the contact angle values of NT-Alloy (12 ± 4°) were lower than the values of NT-MMC (21 ± 2°).

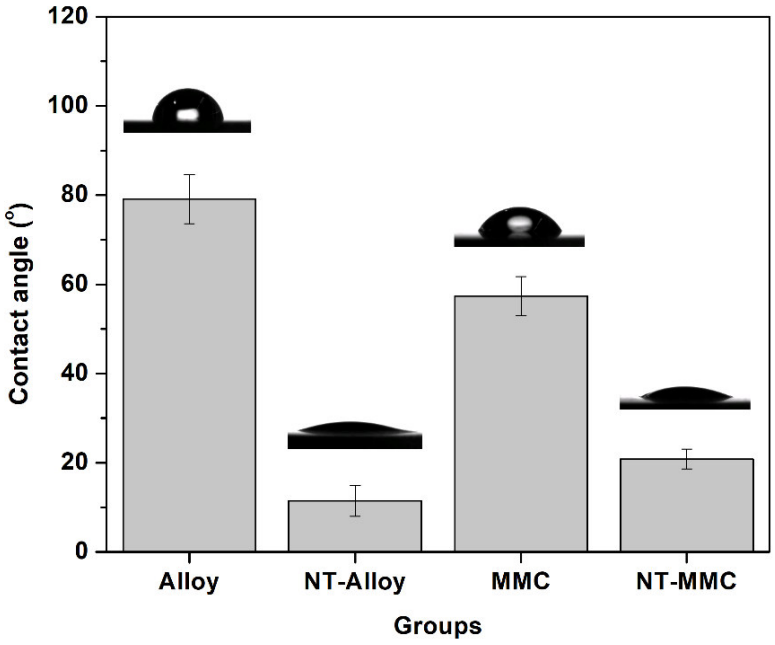

Fig. 9.4. Contact angle values and representative drop images of untreated and TNT formed samples.

Representative potentiodynamic polarization curves of samples in PBS solution are presented in Fig. 9.5a and extracted corrosion potential ($E_{(i=0)}$) and passivation current density (i_{pass}; taken at 0.5 V for all groups) values together with the average OCP (E_{OCP}) of the last 10 min are given in Table 9.3. While both untreated samples showed a well-defined passivation plateau, the current density of TNT formed samples were tended to increase slightly at the passive region. As can be seen from Table 9.3, the MMC sample presented similar E_{OCP}, $E_{(i=0)}$, and lower i_{pass} values compared to Alloy. Also, both samples presented drastically higher E_{OCP} and $E_{(i=0)}$ values, as well as lower i_{pass} values compared to their substrates.

Table 9.3. Corrosion potential ($E_{(i=0)}$) and passivation current density (i_{pass}) values obtained from potentiodynamic polarization curves together with the average E_{OCP} ($V_{Ag/AgCl}$) values at last 10 min of OCP.

Sample	E_{OCP} ($V_{Ag/AgCl}$)	$E_{(i=0)}$ ($V_{Ag/AgCl}$)	i_{pass} ($\mu A.cm^{-2}$)
Alloy	− 0.28 ± 0.02	− 0.20 ± 0.04	4.80 ± 0.34
MMC	− 0.26 ± 0.05	− 0.19 ± 0.02	4.13 ± 0.16
NT-Alloy	− 0.02 ± 0.06	− 0.12 ± 0.05	0.28 ± 0.22
NT-MMC	0.25 ± 0.06	0.15 ± 0.05	0.01 ± 0.01

Representative Nyquist and Bode diagrams of EIS results are shown in Fig. 9.5 together with the proposed EECs. It can be observed from Fig. 9.5b (Nyquist diagram) that the NT-MMC sample showed drastically larger diameter of incomplete semi-circle depicting higher corrosion resistance compared to other groups. Similar behavior can be observed on the total modulus of impedance values (|Z|) in the Bode diagram (Fig. 9.5c), where TNT formed groups presented higher the |Z| values than their untreated groups. It is also worth pointing out on the inserted graph of the Nyquist diagram, the TNT formed samples showed smaller semicircles diameter than their bare samples at the high-frequency range. Regarding the phase angle values on Fig. 9.5d, the values of all samples were near 0° at high frequencies, where corresponding constant |Z| values were observed in Fig. 9.5c, indicating a typical response of electrolyte resistance. One time constant recorded for both untreated groups, and samples presented similar phase angle values approached close to −90° at middle frequencies range. According to TNT formed samples, at least two times constant observed at middle and low frequencies range, where NT-MMC samples exhibited clearly higher values.

In order to deduce quantitative values from EIS experimental data, the EECs as given in Figs. 9.5e and f were used to fit for untreated groups and TNT formed groups, respectively. Similar EECs were proposed in the literature for untreated and TNT formed Ti and its alloys [6,49–51]. The quality of fitting was evaluated by the goodness of fitting values below10^{-4}, which indicates a good fitting to the proposed EECs. The physical significance of the EEC given in Fig. 9.5e assumes that the Alloy and MMC samples consist of a compact layer formation on substrate. In the case of TNT formed samples, the proposed model assumes that the nanotubes consist of a porous outer layer, a barrier-like inner layer (bottom of tubes), and an additional oxide layer at the interface (formed by second step anodic treatment and heat treatment) as illustrated in Fig. 9.5f. While both TNT formed groups has additional oxide layer at interface presented the same physical meaning, it corresponds to different nature formed through heat

treatment and combination of second-step anodic treatment and heat treatment as also previously discussed elsewhere [47]. The R_e, R_{ox}, and Q_{ox} corresponds to electrolyte resistance, resistance of passive oxide layer, and capacitance of oxide layer. The R'_e represents the additional resistance of electrolyte inside the pores. The R_{bl} and R_{al} element corresponds to the resistance of the barrier layers and additional oxide layer, respectively. The Q_{pl}, Q_{bl} and Q_{al} element corresponds to a constant phase element (CPE) of the porous layers, barrier layers, and additional oxide layer, respectively. The CPE was used instead of the ideal capacitor due to surface heterogeneities resulted from surface impurities and roughness. The impedance of CPE is defined as $Z_{CPE} = [Y_o(jw)^n]^{-1}$, where Y_o is the CPE constant, j is the imaginary number, w is the angular frequency, and n is the fractional exponent in the $-1 \leq n \leq 1$ range. When $n = -1, 0$ and 1, the CPE depicts an inductor, resistor, and a pure capacitor, respectively. The obtained EECs simulation parameters are presented in Table 9.4. As can be seen, with consideration of standard deviation, both untreated samples presented similar R_{ox} and lower Q_{ox} values. Regarding the TNT formed samples, NT-MMC sample presented higher R and lower Q values compared to NT-Alloy suggesting better protection for NT-MMC, which agree with potentiodynamic polarization results.

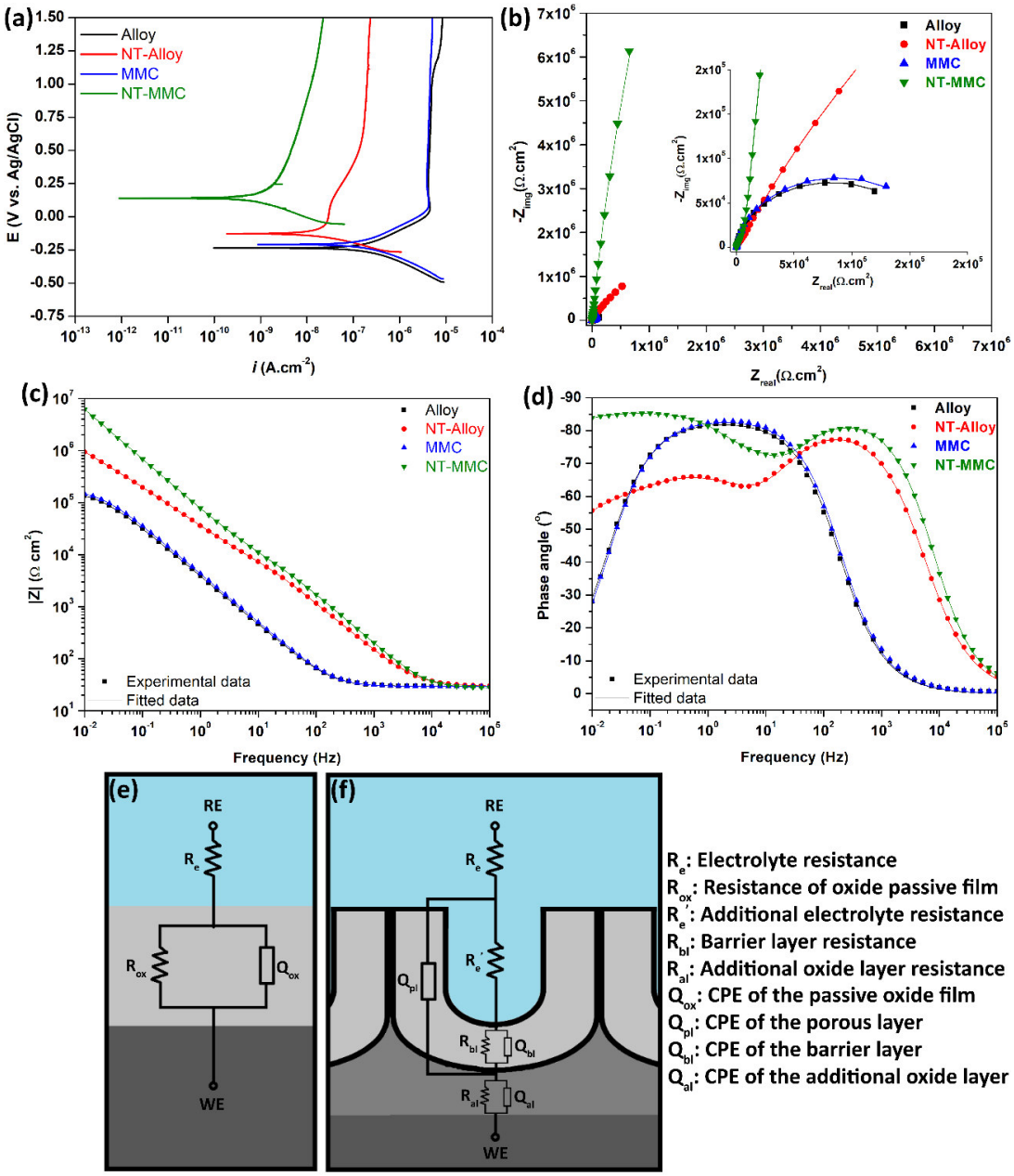

Fig. 9.5. Corrosion results: (a) Representative potentiodynamic polarization curves; representative EIS results in (b) Nyquist diagram, (c) Bode diagram of impedance, and (d) Bode diagram of phase angle; EECs for (e) untreated groups and (f) TNT formed groups.

Table 9.4. EECs parameters obtained from the simulation of EIS data.

Parameters	Alloy	MMC	NT-Alloy	NT-MMC
R_{ox} ($M\Omega$ cm^2	0.15 ± 0.02	0.28 ± 0.14	–	–
Q_{ox} ($x10^{-5}$ F cm^{-2} s^{n-1})	5.14 ± 0.51	4.89 ± 0.12		
R_{bl} ($M\Omega$ cm^2)	–	–	0.15 ± 0.05	0.31 ± 0.09
Q_{pl} ($x10^{-5}$ S s^n cm^{-2})	–	–	0.27 ± 0.03	0.27 ± 0.01
Q_{bl} ($x10^{-5}$ S s^n cm^{-2})	–	–	17.28 ± 0.57	4.67 ± 2.35
R_{al} ($M\Omega$ cm^2)	–	–	3.20 ± 1.45	134.80 ± 91.48
Q_{al} ($x10^{-5}$ S s^n cm^{-2})	–	–	15.82 ± 10.37	0.24 ± 0.01

The wear morphologies analyzed by SEM images are given in Fig. 9.6. A drastically larger wear track width was obtained on Alloy, where parallel sliding grooves and oxide patches were observed. Similarly, parallel sliding grooves were observed on the matrix of the MMC sample, together with reinforcing phases surrounded by compacted denser oxide patches. As shown in insert images, the reinforced regions were smooth and free from grooves. Regarding TNT formed samples, while NT-MMC demonstrated smaller wear track width, both samples were free from visible abrasion grooves.

Since no detectable wear volume loss obtained for the TNT formed samples, only the representative 2D and 3D wear track profiles (taken from the border) are presented in Figs. 9.6e and f together with the measured total wear volume loss for untreated groups. Alloy presented drastically deeper and larger wear track as in agreement with the wear damage observed on the SEM images. As can be seen from 2D and 3D profiles, MMC sample presented clearly rougher wear track (Alloy had R_a=95 ± 4 nm; MMC had R_a=143 ± 7 nm, measured along sliding direction). Regarding average total wear volume loss values, Alloy presented almost 15 times higher values.

The OCP evaluation was monitored before, during, and after sliding and it is shown in Fig. 9.6g, together with the evaluation of the coefficient of friction (COF). As soon as sliding started, both untreated samples presented a sharp decrease to ~–0.7 V due to mechanical damage given to the native passive oxide film. Afterward, while MMC rapidly regained its potential close to –0.3 V, Alloy showed large OCP oscillations for 20 min then regained its potential around –0.3 V. After that point, abrupt decrements were observed on OCP of both samples during sliding, that was more evident on Alloy. When unloaded, the OCP values immediately increased to the values recorded before sliding because of the repassivation

of the worn area [6]. Regarding both TNT formed samples, after a very small (around 0.05 V) gradual decrease on OCP values recorded on the onset of sliding, relatively stable values were observed during sliding and after sliding, the potential values were increased close to the initial values. Additionally, the NT-MMC sample presented slightly higher OCP values during sliding compared to NT-Alloy as −0.01 ± 0.06 V and −0.06 ± 0.06 V, respectively.

Concerning the COF evaluation, both untreated samples presented two different stages. At initial stage, the recorded COF values tended to gradually decrease, where their OCP were tended to increase up to around −0.3 V, after that relatively fewer oscillations and a slight tendency to increase were observed during sliding. While Alloy showed higher COF values at the initial stage, MMC presented higher values at the second stage. Also, the observed abrupt decrements on OCP of both untreated samples were accompanied by the decrements on their COF values. In the case of both TNT formed samples, lower COF evaluations were observed where NT-MMC presented the lowest COF values (0.46 ± 0.05 for NT-Alloy and 0.42 ± 0.01 for NT-MMC).

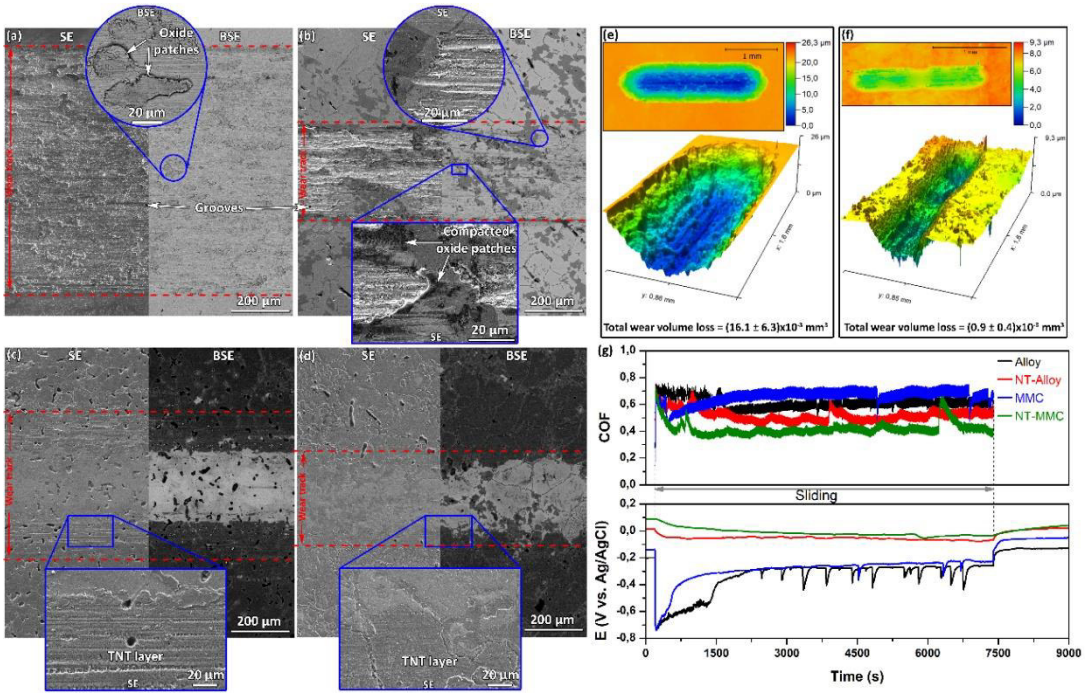

Fig. 9.6. Representative SE and BSE images of wear tracks for a) Alloy, b) MMC, c) NT-Alloy, and d) NT-MMC samples; representative 2D and 3D (taken from the border) wear track images for (e) Alloy and (f) MMC samples, together with their total wear volume loss values; (g) representative evolution of OCP and COF.

9.4. Discussion

9.4.1. Reinforcement and functionalization

The EBSD and XRD results indicated that the MMC composed of β Ti-Nb matrix, hcp $TiN_{0.3}$, and fcc $NbTiN_2$ reinforcement phases resulted from the in-situ reaction of TiH_2, Nb, and TiN powders. As can be observed from the microstructure images, the composites were homogenous and compact, with no evidence of cracks, gaps, and interfacial impurities suggesting good interfacial bonding between the phases [52–55]. The hardness of Alloy was increased from 208 ± 20 HV_{15} to 362 ± 30 HV_{15} with reinforcement, which also may be explained by good bonding of reinforcement phases resulting from thermodynamic compatibility and being free of contamination at the matrix/reinforcement interface [56]. However, since the porosity was higher for Alloy, it may diminish their mechanical properties such as fracture toughness and ultimate tensile strength [57]. Moreover, the observed line-like structures in the $NbTiN_2$ phase correspond to twining formation that might be resulted from interruption or change in the lattice parameters during formation or growth and stress formation on new crystal structure [58].

Nanotubular structures on β-Ti alloys have been reported to stimulate rapid cell proliferation and osteoblast differentiation as well as to accelerate osteointegration, facilitate the transport of nutrients and bone ingrowth [59,60]. The wettability of implants is also a crucial factor in their osteoconductivity because it influences the adsorption of cell-attached proteins onto the surface, where hydrophilic surfaces are more prone to improve osteointegration rate [48]. While MMC presented a lower contact angle among untreated samples, the hydrophilicity of both samples significantly increased with TNT formation. Also, increase on surface roughness and formation of anatase-rutile phases with TNT morphology may provide better osteointegration [61,62]. Among TNT formed samples, the nanotubes formed on NT-MMC sample presented smaller D_i and longer L_n values, which may have positive influence on its bioactivity considering the study of Park *et al.* [63] reported that the smaller D_i showed a better biological response, and Tsuchiya *et al.* [64] indicated that the longer L_n layers were more efficient for hydroxyapatite formation. Nevertheless, the NT-MMC sample had discontinuities on the TNT layer since this layer did not cover the reinforcing phases where, instead, a nanostructured morphology was observed. Thus, *in vitro* and *in vivo* biological studies need to be performed on NT-MMC sample to clarify the biological response of these complex hybrid surfaces.

9.4.2. Corrosion behavior

The corrosion behavior of particulate reinforced MMCs is mainly determined by impurities, gaps, and defects at the matrix/reinforcement interface leading to localized corrosion [65,66]. The

discontinuities at the interface are eliminated in the in-situ composites minimizing the risk of localized corrosion. As can be seen from the potentiodynamic polarization curves and EIS results, no evidence of localized corrosion was observed on MMC since in-situ chemical reactions resulted in smooth and good chemical bonding of reinforcement phases. Therefore, the same EEC was proposed for both untreated groups, which correspond to a formation of passive oxide film on sample surfaces contacted with PBS electrolyte, as considered in the literature for different passive metals [67–71]. Overall, the TiN reinforcement did not jeopardize the corrosion behavior of Alloy, reflected by similar electrochemical response.

Corrosion behavior of various β-type Ti alloys has been improved through the nanotubular formation by anodic treatment mainly due to formation of a thicker oxide layer resulted in a better physical barrier as compared to native passive oxide layer [42,72,73]. As can be seen from Table 9.3, NT-Alloy presented higher E_{OCP} and one order of magnitude lower i_{pass} values compared to the values of Alloy, suggesting significantly lower corrosion tendency and corrosion rate in PBS solution for NT-Alloy. Same improvement can be observed by higher R_{al} values of NT-Alloy than the R_{ox} values of the Alloy resulted in significantly improved its corrosion resistance. According to potentiodynamic polarization curves, lowest corrosion tendency and corrosion rate was observed on NT-MMC sample. Although the additional oxide layer between substrate and TNT layer plays the main protective role [47], NT-MMC sample presented drastically higher R_{al} values and lower Q_{al} values indicating higher corrosion resistance and better quality of oxide layer, respectively, which might be linked with the nanostructured reinforcement phases. Besides, the slight increase trend on the passive current density of NT-MMC sample on the potentiodynamic polarization curves might be associated with the oxidation of reinforcement phases, considering that the increase on the passive current density for monolithic TiN coating due to oxidation of TiN phases have already been reported in the literature [12,18,74]. Since the corrosion behaviors of bare samples were similar, the improved corrosion resistance observed on TNT formed MMC may be attributed to its hybrid oxide surface. Nevertheless, the electrochemical behavior of the nanostructured $TiN_{0.3}$ and $NbTiN_2$ phases needs to be well-understood by using micro-electrochemical techniques.

9.4.3. Tribocorrosion behavior

The tribocorrosion behavior of β-type Ti alloy was significantly influenced by the reinforcement and TNT formation, as can be seen by microstructural and profilometric analysis of the worn surfaces. The worn surface morphology of Alloy was observed to agree with the β-type Ti literature [6,10], including parallel sliding grooves and oxide patches on wear tracks. The wear resistance of Alloy was significantly

improved by TiN reinforcement as observed by lower total wear volume loss values mainly due to load-carrying effect of the reinforcement phases. Furthermore, the oxidized patches may provide limited protection against wear and corrosion as observed by the increase of OCP during sliding. When the thickening of these oxidized patches reached a critical point, they might be removed, thus decrements were recorded on the OCP values, as also reported in literature [18,32]. Regarding COF of the untreated samples, the higher COF values of Alloy at the initial stage may be attributed to its dominant adhesive wear mechanism resulted from higher contact area between metallic substrate and counter body [6]. Accordingly, the tendency of the COF values to decrease might be due to the formation of oxide patches consequently decreasing the metallic contact area [75]. At the second stage, COF values of both samples tended to increase due to the presence of freely moving third body particles at the sliding contact region [75] where the values of MMC was higher than the values of Alloy probably due to harder wear debris with the presence of hard reinforcing phases [32].

Taking consideration of wear track microstructure and OCP evolution, instead of fully detachments, as in accordance with the previous study [47], a gradual delamination occurred from top to bottom resulted in smashing and densification of tubes on the wear tracks. This dense compact oxide layer probably contributed to the decrease of COF values. Compared to the previous study [47] the sliding duration was increased from 0.5 h to 2 h in order to observe better the durability strength of the formed oxide layer. Although the wear volume loss of TNT formed samples was not measurable, NT-MMC samples presented smaller wear track width, lower COF and higher OCP values suggesting relatively better tribocorrosion behavior.

9.5. Conclusion

Ti40Nb-TiN composites were developed and bio-functionalized through the formation of nanotubular surfaces. Tests in simulated body environment showed that TiN reinforcement did not jeopardize the corrosion behavior of Ti40Nb alloy thanks to its uniform microstructure and the defect-free matrix/reinforcement interface. The tribocorrosion resistance drastically improved with reinforcement as a consequence of the load-carrying effect given by the reinforcement phases. The functionalization through TNT formation improved the tribocorrosion behavior due to well adhered and wear resistant anatase-rutile nanotubular layer. Compared to Alloy, TNT formation yielded with improved corrosion and tribocorrosion behavior on MMC due to presence of nanostructured reinforcement phases. Therefore, based on these results, bio-functionalized β type Ti matrix composites appear as an alternative material for load-bearing implant applications.

Acknowledgments

This work is supported by FCT with the reference project UID/EEA/04436/2019, together with M-ERA-NET/0001/2015, as well, by MINECO (Spain) through the program PCIN-2016-123 and the Ramón y Cajal project RYC-2014-15014. I. Caha is grateful for the financial support through a Ph.D. grant under the NORTE-08-5369-FSE-000012 project, and mobility program under INTERREG VA España Portugal (POCTEP) territorial cooperation programme (Project ref: 0300_NANOGATEWAY_6_P). The authors would also like to acknowledge Dr. Andrea Zille for the provision of the contact angle measurements.

References

[1] Y. Okazaki, Cytocompatibility of Various Metals and Development of New Titanium Alloy for Medical Implant., Mater. Sci. Eng. A. 243 (1988) 250–256. doi:10.2320/materia.37.838.

[2] P. Stenlund, O. Omar, U. Brohede, S. Norgren, B. Norlindh, A. Johansson, J. Lausmaa, P. Thomsen, A. Palmquist, Bone response to a novel Ti-Ta-Nb-Zr alloy, Acta Biomater. 20 (2015) 165–175. doi:10.1016/j.actbio.2015.03.038.

[3] M. Geetha, A.K. Singh, R. Asokamani, A.K. Gogia, Ti based biomaterials, the ultimate choice for orthopaedic implants - A review, Prog. Mater. Sci. 54 (2009) 397–425. doi:10.1016/j.pmatsci.2008.06.004.

[4] K. Miura, N. Yamada, S. Hanada, T.-K. Jung, E. Itoi, The bone tissue compatibility of a new Ti–Nb–Sn alloy with a low Young's modulus, Acta Biomater. 7 (2011) 2320–2326. doi:10.1016/j.actbio.2011.02.008.

[5] M.A. Gepreel, M. Niinomi, Biocompatibility of Ti-alloys for long-term implantation, J. Mech. Behav. Biomed. Mater. 20 (2013) 407–415. doi:10.1016/j.jmbbm.2012.11.014.

[6] I. Çaha, A.C. Alves, P.A.B. Kuroda, C.R. Grandini, A.M.P. Pinto, L.A. Rocha, F. Toptan, Degradation behavior of Ti-Nb alloys: Corrosion behavior through 21 days of immersion and tribocorrosion behavior against alumina, Corros. Sci. 167 (2020) 108488. doi:10.1016/j.corsci.2020.108488.

[7] Z. Cvijovic, S. Mitrovic, V. Panic, Wear and corrosion behaviour of Ti – 13Nb – 13Zr and Ti – 6Al – 4V alloys in simulated physiological solution, Corros. Sci. 53 (2011) 796–808. doi:10.1016/j.corsci.2010.11.014.

[8] X. Yang, C.R. Hutchinson, Corrosion-wear of β-Ti alloy alloy TMZF (Ti-12Mo-6Zr-2Fe) in simulated body fluid, Acta Biomater. 42 (2016) 429–439. doi:10.1016/j.actbio.2016.07.008.

[9] Y.S. Lee, M. Niinomi, M. Nakai, K. Narita, K. Cho, Predominant factor determining wear properties of β-type and (α+β)-type titanium alloys in metal-to-metal contact for biomedical applications, J. Mech. Behav. Biomed. Mater. 41 (2015) 208–220. doi:10.1016/j.jmbbm.2014.10.005.

[10] I. Çaha, A. Alves, C. Chirico, A. Pinto, S. Tsipas, E. Gordo, F. Toptan, Corrosion and Tribocorrosion Behavior of Ti-40Nb and Ti-25Nb-5Fe Alloys Processed by Powder Metallurgy, Metall. Mater. Trans. A Phys. Metall. Mater. Sci. 51 (2020) 3256–3267. doi:10.1007/s11661-020-05757-6.

[11] R. Khanna, T. Kokubo, T. Matsushita, H. Takadama, Fabrication of dense α-alumina layer on Ti-6Al-4V alloy hybrid for bearing surfaces of artificial hip joint, Mater. Sci. Eng. C. 69 (2016) 1229–1239. doi:10.1016/j.msec.2016.08.025.

[12] F. Galliano, E. Galvanetto, S. Mischler, D. Landolt, Tribocorrosion behavior of plasma nitrided Ti-6Al-4V alloy in neutral NaCl solution, Surf. Coatings Technol. 145 (2001) 121–131. doi:10.1016/S0257-8972(01)01309-3.

[13] D. Nolan, S.W. Huang, V. Leskovsek, S. Braun, Sliding wear of titanium nitride thin films deposited on Ti-6Al-4V alloy by PVD and plasma nitriding processes, Surf. Coatings Technol. 200 (2006) 5698–5705. doi:10.1016/j.surfcoat.2005.08.110.

[14] Ł. Łapaj, J. Wendland, J. Markuszewski, A. Mróz, T. Wiśniewski, Retrieval analysis of titanium nitride (TiN) coated prosthetic femoral heads articulating with polyethylene, J. Mech. Behav. Biomed. Mater. 55 (2016) 127–139. doi:10.1016/j.jmbbm.2015.10.012.

[15] A. Vadiraj, M. Kamaraj, Effect of surface treatments on fretting fatigue damage of biomedical titanium alloys, Tribol. Int. 40 (2007) 82–88. doi:10.1016/j.triboint.2006.02.064.

[16] A. Samanta, M. Bhattacharya, I. Ratha, H. Chakraborty, S. Datta, J. Ghosh, S. Bysakh, M. Sreemany, R. Rane, A. Joseph, S. Mukherjee, B. Kundu, M. Das, A.K. Mukhopadhyay, Nano- and micro-tribological behaviours of plasma nitrided Ti6Al4V alloys, J. Mech. Behav. Biomed. Mater. 77 (2018) 267–294. doi:10.1016/j.jmbbm.2017.09.013.

[17] W. Cui, G. Qin, J. Duan, H. Wang, A graded nano-TiN coating on biomedical Ti alloy: Low friction coefficient, good bonding and biocompatibility, Mater. Sci. Eng. C. 71 (2017) 520–528. doi:10.1016/j.msec.2016.10.033.

[18] I. Çaha, A.C. Alves, L.J. Affonço, P.N. Lisboa-Filho, J.H.D. da Silva, L.A. Rocha, A.M.P. Pinto, F. Toptan, Corrosion and tribocorrosion behaviour of titanium nitride thin films grown on titanium under different deposition times, Surf. Coatings Technol. 374 (2019) 878–888. doi:10.1016/j.surfcoat.2019.06.073.

[19] X. Huang, I. Etsion, T. Shao, Effects of elastic modulus mismatch between coating and substrate on the friction and wear properties of TiN and TiAlN coating systems, Wear. 338–339 (2015) 54–61. doi:10.1016/j.wear.2015.05.016.

[20] T.M. Manhabosco, S.M. Tamborim, C.B. dos Santos, I.L. Müller, Tribological, electrochemical and tribo-electrochemical characterization of bare and nitrided Ti6Al4V in simulated body fluid solution, Corros. Sci. 53 (2011) 1786–1793. doi:10.1016/j.corsci.2011.01.057.

[21] M. Annunziata, A. Oliva, M.A. Basile, M. Giordano, N. Mazzola, A. Rizzo, A. Lanza, L. Guida, The effects of titanium nitride-coating on the topographic and biological features of TPS implant surfaces, J. Dent. 39 (2011) 720–728. doi:10.1016/j.jdent.2011.08.003.

[22] N. Lin, X. Huang, J. Zou, X. Zhang, L. Qin, A. Fan, B. Tang, Effects of plasma nitriding and multiple arc ion plating TiN coating on bacterial adhesion of commercial pure titanium via in vitro investigations, Surf. Coatings Technol. 209 (2012) 212–215. doi:10.1016/j.surfcoat.2012.07.046.

[23] M. Rizwan, A. Ahmad, K.M. Deen, W. Haider, Electrochemical behavior and biological response of Mesenchymal Stem Cells on cp-Ti after N-ions implantation, Appl. Surf. Sci. 320 (2014) 718–724. doi:10.1016/j.apsusc.2014.09.169.

[24] H.Y. Wang, Q.C. Jiang, Y. Wang, B.X. Ma, F. Zhao, Fabrication of TiB2 participate reinforced magnesium matrix composites by powder metallurgy, Mater. Lett. 58 (2004) 3509–3513. doi:10.1016/j.matlet.2004.04.038.

[25] Z. Zhang, T. Topping, Y. Li, R. Vogt, Y. Zhou, C. Haines, J. Paras, D. Kapoor, J.M. Schoenung, E.J. Lavernia, Mechanical behavior of ultrafine-grained Al composites reinforced with B4C nanoparticles, Scr. Mater. 65 (2011) 652–655. doi:10.1016/j.scriptamat.2011.06.037.

[26] F. Toptan, A. Rego, A.C. Alves, A. Guedes, Corrosion and tribocorrosion behavior of Ti–B4C composite intended for orthopaedic implants, J. Mech. Behav. Biomed. Mater. 61 (2016) 152–163. doi:10.1016/j.jmbbm.2016.01.024.

[27] F. Romero, V. Amigó, M.D. Salvador, A. Vicente, Interactions in Titanium Matrix Composites Reinforced by Titanium Compounds by Conventional PM Route, Mater. Sci. Forum. 534–536 (2007) 817–820. doi:10.4028/www.scientific.net/msf.534-536.817.

[28] O.E. Falodun, B.A. Obadele, S.R. Oke, M.E. Maja, P.A. Olubambi, Effect of sintering parameters on densification and microstructural evolution of nano-sized titanium nitride reinforced titanium alloys, J. Alloys Compd. 736 (2018) 202–210. doi:10.1016/j.jallcom.2017.11.140.

[29] S. Kundu, M. Hussain, V. Kumar, S. Kumar, A.K. Das, Direct metal laser sintering of TiN reinforced Ti6Al4V alloy based metal matrix composite: Fabrication and characterization, Int. J. Adv. Manuf. Technol. 97 (2018) 2635–2646. doi:10.1007/s00170-018-2159-7.

[30] A.M. Ribeiro, A.C. Alves, F.S. Silva, F. Toptan, Electrochemical characterization of hot pressed CoCrMo–HAP biocomposite in a physiological solution, Mater. Corros. 66 (2015) 790–795. doi:10.1002/maco.201407885.

[31] B. Bobić, S. Mitrovic, M. Babic, I. Bobić, Corrosion of aluminium and zinc-aluminium alloys based metal-matrix composites, Tribol. Ind. 31 (2009) 44–53. https://www.scopus.com/inward/record.uri?eid=2-s2.0-73949137681&partnerID=40&md5=e6b16abb35b092f2435644231ff63e75.

[32] J.I. Silva, A.C. Alves, A.M. Pinto, F. Toptan, Corrosion and tribocorrosion behavior of Ti–TiB–TiNx in-situ hybrid composite synthesized by reactive hot pressing, J. Mech. Behav. Biomed. Mater. 74 (2017) 195–203. doi:10.1016/j.jmbbm.2017.05.041.

[33] D. Khudhair, A. Bhatti, Y. Li, H.A. Hamedani, H. Garmestani, P. Hodgson, S. Nahavandi, Anodization parameters influencing the morphology and electrical properties of TiO2 nanotubes for living cell interfacing and investigations, Mater. Sci. Eng. C. 59 (2016) 1125–1142. doi:10.1016/j.msec.2015.10.042.

[34] X. Liu, P.K. Chu, C. Ding, Surface modification of titanium, titanium alloys, and related materials for biomedical applications, Mater. Sci. Eng. R Reports. 47 (2004) 49–121. doi:10.1016/j.mser.2004.11.001.

[35] I. Çaha, A.C. Alves, L.A. Rocha, F. Toptan, A Review on Bio-functionalization of β-Ti Alloys, J. Bio-Tribo-Corrosion. 6 (2020) 1–31. doi:10.1007/s40735-020-00432-0.

[36] A. Stróż, B. Łosiewicz, M. Zubko, B. Chmiela, K. Balin, G. Dercz, M. Gawlikowski, T. Goryczka,

Production, structure and biocompatible properties of oxide nanotubes on Ti13Nb13Zr alloy for medical applications, Mater. Charact. 132 (2017) 363–372. doi:10.1016/j.matchar.2017.09.004.

[37] S. Minagar, Y. Li, C.C. Berndt, C. Wen, Cell response and bioactivity of titania-zirconia-zirconium titanate nanotubes with different nanoscale topographies fabricated in a non-aqueous electrolyte, Biomater. Sci. 3 (2015) 636–644. doi:10.1039/c5bm00007f.

[38] M. Qadir, Y. Li, A. Biesiekierski, C. Wen, Optimized Fabrication and Characterization of TiO2-Nb2O5-ZrO2 Nanotubes on β-Phase TiZr35Nb28 Alloy for Biomedical Applications via the Taguchi Method, ACS Biomater. Sci. Eng. 5 (2019) 2750–2761. doi:10.1021/acsbiomaterials.9b00356.

[39] P. Roy, S. Berger, P. Schmuki, TiO2 nanotubes: Synthesis and applications, Angew. Chemie - Int. Ed. 50 (2011) 2904–2939. doi:10.1002/anie.201001374.

[40] A. Ghicov, S. Aldabergenova, H. Tsuchiya, P. Schmuki, TiO2–Nb2O5 Nanotubes with Electrochemically Tunable Morphologies, Angew. Chemie - Int. Ed. 45 (2006) 6993–6996. doi:10.1002/anie.200601957.

[41] D. Ding, C. Ning, L. Huang, F. Jin, Y. Hao, S. Bai, Y. Li, M. Li, D. Mao, Anodic fabrication and bioactivity of Nb-doped TiO2 nanotubes, Nanotechnology. 20 (2009) 2–8. doi:10.1088/0957-4484/20/30/305103.

[42] A.Z. Fatichi, M.G. Mello, R. Caram, A. Cremasco, Self-organized TiO2 nanotube layer on Ti–Nb–Zr alloys: growth, characterization, and effect on corrosion behavior, J. Appl. Electrochem. 49 (2019) 1079–1089. doi:10.1007/s10800-019-01345-8.

[43] A.R. Luz, G.B. de Souza, C.M. Lepienski, C.J.M. Siqueira, N.K. Kuromoto, Tribological properties of nanotubes grown on Ti-35Nb alloy by anodization, Thin Solid Films. 660 (2018) 529–537. doi:10.1016/j.tsf.2018.06.050.

[44] R. Schmidt, V. Hoffmann, A. Helth, P.F. Gostin, M. Calin, J. Eckert, A. Gebert, Electrochemical deposition of hydroxyapatite on beta-Ti-40Nb, Surf. Coatings Technol. 294 (2016) 186–193. doi:10.1016/j.surfcoat.2016.03.063.

[45] A. Gebert, D. Eigel, P.F. Gostin, V. Hoffmann, M. Uhlemann, A. Helth, S. Pilz, R. Schmidt, M. Calin, M. Göttlicher, M. Rohnke, J. Janek, Oxidation treatments of beta-type Ti-40Nb for biomedical use, Surf. Coatings Technol. 302 (2016) 88–99.

doi:10.1016/j.surfcoat.2016.05.036.

[46] R. Medda, A. Helth, P. Herre, D. Pohl, B. Rellinghaus, N. Perschmann, S. Neubauer, H. Kessler, S. Oswald, J. Eckert, J.P. Spatz, A. Gebert, E.A. Cavalcanti-Adam, Investigation of early cell - Surface interactions of human mesenchymal stem cells on nanopatterned β-type titanium - Niobium alloy surfaces, Interface Focus. 4 (2014). doi:10.1098/rsfs.2013.0046.

[47] I. Çaha, A.C. Alves, C. Chirico, A.M.P. Pinto, S. Tsipas, E. Gordo, F. Toptan, A promising method to develop TiO2-based nanotubular surfaces on Ti-40Nb alloy with enhanced adhesion and improved tribocorrosion resistance, Appl. Surf. Sci. 542 (2021) 148658. doi:10.1016/j.apsusc.2020.148658.

[48] R.A. Gittens, L. Scheideler, F. Rupp, S.L. Hyzy, J. Geis-Gerstorfer, Z. Schwartz, B.D. Boyan, A review on the wettability of dental implant surfaces II: Biological and clinical aspects, Acta Biomater. 10 (2014) 2907–2918. doi:10.1016/j.actbio.2014.03.032.

[49] L. Mohan, C. Anandan, N. Rajendran, Electrochemical behaviour and bioactivity of self-organized TiO2 nanotube arrays on Ti-6Al-4V in Hanks' solution for biomedical applications, Electrochim. Acta. 155 (2015) 411–420.

[50] L. Mohan, C. Anandan, N. Rajendran, Electrochemical behavior and effect of heat treatment on morphology, crystalline structure of self-organized TiO2 nanotube arrays on Ti – 6Al – 7Nb for biomedical applications, Mater. Sci. Eng. C. 50 (2015) 394–401. http://dx.doi.org/10.1016/j.msec.2015.02.013.

[51] P. Córdoba-Torres, N.T.C. Oliveira, C. Bolfarini, V. Roche, R.P. Nogueira, Electrochemical impedance analysis of TiO2 nanotube porous layers based on an alternative representation of impedance data, J. Electroanal. Chem. 737 (2015) 54–64. doi:10.1016/j.jelechem.2014.06.034.

[52] K.K. Chawla, Composite materials, Third, Springer Science and Business Media LLC, New york, 2012. doi:10.1007/978-0-387-74365-3.

[53] P. Majumdar, S.B. Singh, M. Chakraborty, Wear properties of Ti-13Zr-13Nb (wt.%) near β titanium alloy containing 0.5 wt.% boron in dry condition, Hank's solution and bovine serum, Mater. Sci. Eng. C. 30 (2010) 1065–1075. doi:10.1016/j.msec.2010.05.011.

[54] C. Li, X. Lv, X. Wu, J. Chen, X. Liu, L. Pang, Nano-sized TiN-reinforced composites: Fabrication,

microstructure, and mechanical properties, J. Mater. Res. 34 (2019) 2582–2589. doi:10.1557/jmr.2019.200.

[55] M.E. Maja, O.E. Falodun, B.A. Obadele, S.R. Oke, P.A. Olubambi, Nanoindentation studies on TiN nanoceramic reinforced Ti–6Al–4V matrix composite, Ceram. Int. 44 (2018) 4419–4425. doi:10.1016/j.ceramint.2017.12.042.

[56] W.J. Lu, D. Zhang, R.J. Wu, H. Mori, Solidification paths and reinforcement morphologies in melt-processed (TiB + TiC)/Ti in situ composites, Metall. Mater. Trans. A Phys. Metall. Mater. Sci. 33 (2002) 3055–3063. doi:10.1007/s11661-002-0290-3.

[57] L. Bolzoni, E.M. Ruiz-Navas, E. Gordo, Evaluation of the mechanical properties of powder metallurgy Ti-6Al-7Nb alloy, J. Mech. Behav. Biomed. Mater. 67 (2017) 110–116. doi:10.1016/j.jmbbm.2016.12.005.

[58] O. Eso Falodun, B.A. Obadele, S. Ranti Oke, P. Apata Olubambi, J. Westraadt, Characterization of spark plasma sintered TiN nanoparticle strengthened titanium alloy using EBSD and TKD, Mater. Res. Bull. 117 (2019) 90–95. doi:10.1016/j.materresbull.2019.04.031.

[59] X. Li, T. Chen, J. Hu, S. Li, Q. Zou, Y. Li, N. Jiang, H. Li, J. Li, Modified surface morphology of a novel Ti-24Nb-4Zr-7.9Sn titanium alloy via anodic oxidation for enhanced interfacial biocompatibility and osseointegration, Colloids Surfaces B Biointerfaces. 144 (2016) 265–275. doi:10.1016/j.colsurfb.2016.04.020.

[60] Y.Q. Hao, S.J. Li, Y.L. Hao, Y.K. Zhao, H.J. Ai, Effect of nanotube diameters on bioactivity of a multifunctional titanium alloy, Appl. Surf. Sci. 268 (2013) 44–51. doi:10.1016/j.apsusc.2012.11.142.

[61] H. Te Chen, C.J. Chung, T.C. Yang, C.H. Tang, J.L. He, Microscopic observations of osteoblast growth on micro-arc oxidized β titanium, Appl. Surf. Sci. 266 (2013) 73–80. doi:10.1016/j.apsusc.2012.11.087.

[62] J.I. Rosales-Leal, M.A. Rodríguez-Valverde, G. Mazzaglia, P.J. Ramón-Torregrosa, L. Díaz-Rodríguez, O. García-Martínez, M. Vallecillo-Capilla, C. Ruiz, M.A. Cabrerizo-Vílchez, Effect of roughness, wettability and morphology of engineered titanium surfaces on osteoblast-like cell adhesion, Colloids Surfaces A Physicochem. Eng. Asp. 365 (2010) 222–229. doi:10.1016/j.colsurfa.2009.12.017.

[63] J. Park, S. Bauer, K.A. Schlegel, F.W. Neukam, K. Der Von Mark, P. Schmuki, TiO2 nanotube surfaces: 15 nm - an optimal length scale of surface topography for cell adhesion and differentiation, Small. 5 (2009) 666–671. doi:10.1002/smll.200801476.

[64] H. Tsuchiya, J.M. Macak, L. Müller, J. Kunze, F. Müller, P. Greil, S. Virtanen, P. Schmuki, Hydroxyapatite growth on anodic TiO2 nanotubes, J. Biomed. Mater. Res. - Part A. 77 (2006) 534–541. doi:10.1002/jbm.a.30677.

[65] L.H. Hihara, R.M. Latanision, Corrosion of metal matrix composites, Int. Mater. Rev. 39 (1994) 245–264. doi:10.1179/imr.1994.39.6.245.

[66] C. Lin, H. Ruan, S.Q. Shi, Phase field study of mechanico-electrochemical corrosion, Electrochim. Acta. 310 (2019) 240–255. doi:10.1016/j.electacta.2019.04.076.

[67] Y. Tsutsumi, S. Bartakova, P. Prachar, Suyalatu, S. Migita, H. Doi, N. Nomura, T. Hanawa, Long-Term Corrosion Behavior of Biocompatible β-Type Ti Alloy in Simulated Body Fluid, J. Electrochem. Soc. 159 (2012) C435–C440. doi:10.1149/2.045210jes.

[68] J. Fojt, L. Joska, J. Málek, Corrosion behaviour of porous Ti-39Nb alloy for biomedical applications, Corros. Sci. 71 (2013) 78–83. doi:10.1016/j.corsci.2013.03.007.

[69] H.M. Yehia, A. El-Tantawy, I.M. Ghayad, A.S. Eldesoky, O. El-kady, Effect of zirconia content and sintering temperature on the density, microstructure, corrosion, and biocompatibility of the Ti–12Mo matrix for dental applications, J. Mater. Res. Technol. 9 (2020) 8820–8833. doi:10.1016/j.jmrt.2020.05.109.

[70] A.M. Ribeiro, A.C. Alves, L.A. Rocha, F.S. Silva, F. Toptan, Synergism between corrosion and wear on CoCrMo–Al2O3biocomposites in a physiological solution, Tribol. Int. 91 (2015) 198–205. doi:10.1016/j.triboint.2015.01.018.

[71] I. Çaha, A.C. Alves, C. Chirico, S.A. Tsipas, I.R. Rodrigues, A.M.P. Pinto, C.R. Grandini, L.A. Rocha, E. Gordo, F. Toptan, Interactions between wear and corrosion on cast and sintered Ti-12Nb alloy in comparison with the commercial Ti-6Al-4V alloy, Corros. Sci. 176 (2020) 108925. doi:10.1016/j.corsci.2020.108925.

[72] W. Jiang, H. Cui, Y. Song, Electrochemical corrosion behaviors of titanium covered by various TiO2 nanotube films in artificial saliva, J. Mater. Sci. 53 (2018) 15130–15141. doi:10.1007/s10853-018-2706-5.

[73] V.S. Saji, H.C. Choe, W.A. Brantley, An electrochemical study on self-ordered nanoporous and nanotubular oxide on Ti-35Nb-5Ta-7Zr alloy for biomedical applications, Acta Biomater. 5 (2009) 2303–2310. doi:10.1016/j.actbio.2009.02.017.

[74] I.M. Pohrelyuk, V.M. Fedirko, O.V. Tkachuk, R.V. Proskurnyak, Corrosion resistance of Ti–6Al–4V alloy with nitride coatings in Ringer's solution, Corros. Sci. 66 (2013) 392–398. doi:10.1016/j.corsci.2012.10.005.

[75] Z. Doni, A.C. Alves, F. Toptan, J.R. Gomes, A. Ramalho, M. Buciumeanu, L. Palaghian, F.S. Silva, Dry sliding and tribocorrosion behaviour of hot pressed CoCrMo biomedical alloy as compared with the cast CoCrMo and Ti6Al4V alloys, Mater. Des. 52 (2013) 47–57. doi:10.1016/j.matdes.2013.05.032.

Chapter 10: Degradation behaviour of a Ti-12Nb alloy coated with ZnO/TiN double layer

Published in Surf. Coat. Technol. 413 (2021) 127104

Degradation behaviour of a Ti-12Nb alloy coated with ZnO/TiN double layer

I. Çaha[a,*], A.C. Alves[a], L.J. Affonço[b,c], J.H.D. da Silva[b,c], I.R. Rodrigues[b,c], C.R. Grandini[b,c], L.A. Rocha[b], A.M.P. Pinto[a,d], P.N. Lisboa-Filho[b,c], F. Toptan[a,e,f]

[a] CMEMS-Uminho – Center for MicroElectroMechanical Systems, Universidade do Minho, Azurém, 4800-058 Guimarães, Portugal

[b] IBTN/Br – Brazilan Branch of the Institute of Biomaterials, Tribocorrosion and Nanomedicine, Bauru, SP, Brazil

[c] UNESP—Univ. Estadual Paulista, Faculdade de Ciências de Bauru, Dep. Física, 17033-360 Bauru, SP, Brazil

[d] Universidade do Minho, Dept. Eng. Mecânica, Azurém, 4800-058 Guimarães, Portugal

[e] Department of Materials Science and Engineering, Izmir Institute of Technology, 35430, Urla, Izmir, Turkey

[f] IBTN/Euro – European Branch of the Institute of Biomaterials, Tribocorrosion and Nanomedicine, Dept. Eng. Mecânica, Universidade do Minho, Azurém, 4800-058 Guimarães, Portugal

[*] Corresponding author at: CMEMS-Uminho – Center for MicroElectroMechanical Systems, Universidade do Minho, Azurém, 4800-058 Guimarães, Portugal. Tel.: +351 253 510 220; fax: +351 253 516 007. E-mail: ihsancaha@gmail.com (I. Çaha).

Abstract

Ti and its alloys have attracted attention for biomedical applications, but their low tribocorrosion resistance, lack of bioactivity and antimicrobial properties are still major clinical concerns. In this study a ZnO coating, intended to act as an antibacterial agent, was deposited on a Ti-12Nb alloy, which was previously coated with a TiN hard coating, for improving tribocorrosion resistance. The idea behind is the proof-of -concept that ZnO is able to provide interesting tribological properties to the surface, thus inspiring new ZnO-containing surfaces that can combine antimicrobial properties and tribocorrosion resistance. Thus, the corrosion behaviour was studied by open circuit potential, electrochemical impedance spectroscopy, and potentiodynamic polarization tests in phosphate buffered solution at body

temperature. The tribocorrosion behaviour was employed at open circuit potential under 0.5 N of normal load, 1 Hz frequency, during 3600 s sliding in phosphate buffered solution at body temperature. The results indicated that duplex coating sample showed better corrosion resistance and drastically better tribocorrosion resistance compared to uncoated and single TiN coating samples.

Keywords: ZnO; TiN; Biofunctionalization; Corrosion; Tribocorrosion

10.1. Introduction

Ti and its alloys have been widely used for different biomedical applications due to their combination of unique properties. However, some major clinical concerns still exist for load bearing implants such as their low tribocorrosion resistance, lack of bioactivity, and risk of infection. In order to overcome low tribocorrosion resistance, hard coatings are one of the most proposed method mainly due to their excellent wear resistance. Among hard coatings, TiN has been presented good corrosion behaviour, tribocorrosion resistance, and biocompatibility [1]. The improvement of corrosion resistance with TiN coating have been reported for different Ti-based materials such as pure Ti [2,3], Ti-6Al-4V [4,5], Ti-6Al-7Nb [6,7], and Ti-25Ta-25Nb alloy [8]. Although wear behaviour significantly depends on tribological conditions, as general, the wear resistance of various Ti-based materials improved through TiN coating [9–14]. Regarding biocompatibility, Samanta et al. [15] studied tribological behaviour and biocompatibility of plasma nitrided Ti-6Al-4V alloy, and reported a drastically better wear resistance in simulated body fluid (SBF) together with better viability and proliferation of mouse embryonic fibroblast cells for nitrided sample. Also, Huang et al. [16] reported higher osteoblast-like cell adhesion onto TiN coated sample as compared to uncoated Ti.

The lack of bioactivity for Ti and its alloys is mainly due to their bioinert surface. Several surface bio-functionalization techniques have been proposed to overcome their lack of bioactivity through incorporated bioactive agents in metal oxide film such as micro-arc oxidation, hydroxyapatite coatings, nanotubular surfaces, and immobilization of bio-functional molecules [1]. Among these metal oxide coatings, zinc oxide (ZnO) suggests excellent proliferation and differentiation of osteoblast cells, and particularly it has gained attention to improve antibacterial activity [17–21]. Moreover, Zn is a vital main element found in the human bone and plays an extremely important role in physiological activities such as DNA synthesis, enzymatic activity, and biomineralization [22]. Although ZnO-incorporated coatings have been well explored for different industrial applications, the corrosion and tribocorrosion behaviour of ZnO film is rarely investigated. Ding et al. [20] studied the corrosion and antibacterial behaviour of ZnO doped tantalum oxide on Ti-6Al-4V alloy and reported better corrosion resistance and antibacterial

behaviour for the doped sample compared to the uncoated and undoped tantalum oxide coating samples. Song et al. [23] studied the tribological behaviour of ZnO doped polyurethane and reported significantly lower wear rate compared to the unreinforced polyurethane composite. Mbamara et al. [24] investigated the wear behaviour of nitrogen doped ZnO film deposited on 304 L stainless steel via metal organic chemical vapor deposition (MOCVD) method and reported that the crystallinity and thickness of coatings drastically influenced the wear resistance. Also, the ZnO film has strong ability to terminate its surface by hydroxyl groups, allowing further bio-functionalization through biomolecules such as carboxylic acids, esters, acid chlorides and other self-assembled monolayers [25]. Trino et al. [26] deposited ZnO films by sol-gel method onto Ti (grade 4) and functionalized with 3-(4aminophenyl)propionic acid (APPA), 3-aminopropyltrimetoxysilane (APTMS), 3-mercaptopropionic acid (MPA), and polyethylene glycol (PEG) organic bifunctional molecules and reported the corrosion behaviour improvement with surface functionalization.

Ti-6Al-4V alloy is one of the most employed implant materials and commercially available in market mainly due to its good mechanical strength and corrosion resistance. However, its high Young's modulus causes bone resorption and the concerns about the toxicity of its alloying elements are leading to the investigation of alternative materials. Recently, some of the present authors studied a non-toxic and promising Ti-12Nb alloy [27]. Although it presented lower Young's modulus, its tribocorrosion resistance and bioactivity needs to be further improved. Therefore, Ti-12Nb alloy was first coated with TiN hard coating, and then ZnO coating, in a way to develop new ZnO-containing surfaces that can combine antimicrobial properties and tribocorrosion resistance. As a first step to design such multi-functional hybrid material, the present work aimed to investigate its corrosion and tribocorrosion behaviour in phosphate buffered solution at body temperature.

10.2. Materials and methods

10.2.1. Materials and sample preparation

The raw materials used to produce cast Ti-12Nb alloy were Ti (99.7% purity, Sandinox Biometais, Brazil) and Nb (99.8 % purity, Brazilian Metallurgy and Mining Company). The raw metals were arc melted together to form an ingot. The ingot was re-melted five times and then it was submitted to a hot-rolling treatment carried out at 900 °C (complete details of the processing are given elsewhere [27]).

Before TiN coating, substrate was grinded with SiC paper down to 1500 mesh size and polished with alumina (1 μm) and colloidal silica (0.04 μm) by using an automatic polishing machine (Arotec,

Aropol2V). After polishing, samples were ultrasonically cleaned for 10 min in propanol followed by cleaning in distilled water for 5 min.

TiN hard thin films were deposited on the Ti-12Nb substrate by Radio Frequency (RF) sputtering technique (13.6 MHz power supply). A pure (99.999%) Ti target and an atmosphere composed of Ar and N_2 (both 99.9999% pure) were used on depositions. The residual pressures were below 10^{-6} Torr and target surface was sputtered in a pure argon plasma to avoid the surface impurities, before the TiN film deposition. A resistance heater was used to keep the substrate temperature at 400 °C. All TiN films were deposited under 240 W RF power, 40 sccm (standard cubic centimetres per minute) Ar and 10 sccm N_2 flows, at constant total pressure of 5×10^{-3} Torr, during 80 min, and labelled as TiN/Ti-12Nb.

TiN/Ti-12Nb sample surface was functionalized through the ZnO coating by employing a similar method to that of Trino et al. [26]. Firstly, the ZnO resin precursor was obtained by a modified sol-gel method as dissolving 72.05 g citric acid in 200 ml deionized water, and subsequently, 15.00 ml nitric acid was added to the mixture with 10.17 g zinc oxide (ZnO:citric acid molar ratio as 1:3). Then, the obtained solution heated to 90 °C during 15 min. Then, ethylene glycol was added to the solution considering the mass ratio 60:40 ratio between the citric acid and ethylene glycol, respectively. Afterwards, the temperature of plate was increased to 150 °C under magnetic stirring until reaching 100 ml solution. Subsequently, the solution was diluted in a ratio of 5:3 of deionized water and ZnO resin, respectively. The ZnO deposition was employed by three sequential spin coating (2000 rpm, 60 s) steps using 60 μl of ZnO solution for each step. After each coating, the samples were heated for 5 min on a hot plate at 70 °C. After all, an annealing heat treatment with two steps was performed: 150 °C during 2 h followed by 300 °C during 10 min at 1 °C/min heating and colling rates. After this procedure, samples were labelled as ZnO/TiN/Ti-12Nb.

10.2.2. Corrosion and tribocorrosion tests

Corrosion behaviour was accessed by means of open circuit potential (OCP), electrochemical impedance spectroscopy (EIS), and potentiodynamic polarization in phosphate buffer solution (PBS; 0.2 g/l KCl, 0.24 g/l KH_2PO_4, 8 g/l NaCl, 1.44 g/l Na_2HPO_4) at body temperature (37 °C) using Gamry Potentiostat/Galvanostat/ZRA (Reference 600+). The samples were kept as a working electrode (WE) with an exposed area of 0.2 cm^2 whereas a Pt and saturated calomel electrode (SCE) were used as counter (CE) and reference electrode (RE), respectively. Before EIS measurements, OCP was stabilized till ΔE was below 60 mVh^{-1}. EIS were performed at OCP by scanning a range of frequencies from 10^{-2} to 10^5 Hz with 7 points per frequency decade where the amplitude of the sinusoidal waveform was set as

10 mV. After the EIS measurements, potentiodynamic polarization measurements were carried out with 0.5 mV/s scan rate, starting at −0.25 V vs. OCP and moving in the anodic direction up to 1.0 VSCE.

Tribocorrosion behaviour was evaluated by using a pin-on-plate reciprocating sliding configuration at OCP condition using PBS solution at body temperature with 0.4 cm^2 exposed area against a hard and inert alumina ball (10 mm diameter, Ceratec). The samples were used as WE, a SCE was used as the RE connected to a Gamry Potentiostat/ Galvanostat/ZRA (Reference 600). Tribological parameters were chosen as 1 Hz frequency, 2 mm of amplitude, 3600 s sliding time, and 0.5 N normal load using a tribometer (CETR-UMT-2) coupled to the UMT test viewer software to monitor the coefficient of friction (COF). All tests were repeated at least three times in order to assure the reproducibility and the results were presented as the arithmetic mean ± standard deviation.

10.2.3. Characterizations

The morphological characterization of the thin films was employed by SEM using FEI Nova 200 field emission gun scanning electron microscope (FEG-SEM) equipped with energy dispersive X-Ray spectroscopy (EDS). The crystalline structure of the samples was analysed using X-ray diffraction (XRD, Bruker D8 Discover diffractometer equipped with a Cu-Kα radiation (λ = 0.1544 nm) at 40 kV and 20 mA, scanned from angle (2θ) 20° to 65° with a 0.02°/s step size. Surface wettability was assessed by contact angle measurements through sessile drop method using an optical tensiometer (dataphysics, OCA 15 plus). A 5 μl droplet of pure water was dropped on the surface of the samples and the contact angle was considered at room temperature. A video camera recorded for capture drop image over three different samples per group.

Nanoindentation studies were performed to obtain nano hardness data as well as information on samples Young's modulus (Micro Materials NanoTest). 8 indentations were made on different locations using a depth-controlled test as maximum depth of 120 nm, 0.2 m N/s loading/unloading rate, and 5 s dwell time was employed to obtain the nanoindentation data. Vickers microhardness was also employed to obtain the overall hardness of samples using Emcotest Durascan tester by 10 indentations performed randomly per 3 different samples with a load of 4.90 N (0.5 kgf). The ZnO/TiN coating sample was bended by three-point bending set up in order to analyze the cross-section of the coating layers. Adhesion of the coatings was evaluated by the scratch tests. The scratch tests were performed by Revetest scratch tester (CSM instruments) with 200 μm tip radius diamond conical Rockwell C indenter with 90° angle (perpendicular to samples surface) under progressively increasing load mode from 0.9 N to 15 N on a

2 mm scratch line with a speed of 1 mm/min. Scratch scars on coating surfaces were analyzed by optical microscope (Leica, DM2500).

After each tribocorrosion test, samples were cleaned by immersing in propanol and distilled water, respectively. The wear tracks and worn counter body surfaces were characterized by secondary electron (SE) and backscattered electron (BSE) mode of SEM using FEI Nova 200 FEG-SEM equipped with EDS. The wear track profiles and the average surface roughness (R_a) were obtained by a 3D profilometry (Profilm3D).

10.3. Results and discussion

10.3.1. Physical and structural properties

The SEM micrographs, EDS spectra, XRD pattern and surface wettability of sample surfaces are given in Fig. 10.1. The nanohardness, microhardness, and Young's modulus of samples are given in Table 10.1. The uniform surface morphologies for all groups can be seen on SEM images. Also, the surface roughness increased with TiN and ZnO film deposition, as it also can be seen on Table 10.1, which is expected to increase osteoblast-like cell adhesion [28]. The microstructure of cast Ti-12Nb alloy was reported elsewhere [27], which composed of lamellar $\alpha + \beta$ phase as presented on its XRD pattern given in Fig. 10.1e.

According to the XRD analysis of coated samples, presented in Fig. 10.1e, the TiN/Ti-12Nb presented a face-centered cubic (fcc) TiN phase (ICDD 03-065-5759) peaks, while only the most intense (111) peak of TiN coating and (101) peak of hexagonal (hcp) ZnO (ICDD 00-005-0664) was detected for ZnO/TiN/Ti-12Nb sample addition to substrate peaks. In order to achieve complete oxidation of ZnO and complete crystallization of the films, generally, heat treatment at higher temperatures are needed [26]. The main aim for applying relatively lower annealing temperature in this study was to avoid any possible defect formation in TiN film and also between substrate and TiN film. From the EDS results, it can be seen that only Zn, Ti, O and Nb, besides to C, probably on surface, were detected. The Nb detection, and part of the Ti, were due to the substrate, considering the long depth profile provided by the technique.

Wettability has been well established in the initial interaction of implants and aqueous biological ecosystem, as well as protein adsorption, cell-material contact, attachment and spreading [29]. Among samples, although all samples presented hydrophilic behaviour, TiN (69 ± 6 °) coated sample showed the highest and ZnO (24 ± 1 °) coated samples depicted the lowest contact angle. The lower contact angle values of ZnO/TiN/Ti-12Nb can be explained by its rougher surface and also their higher oxygen content which led to higher hydrogen bonding [29].

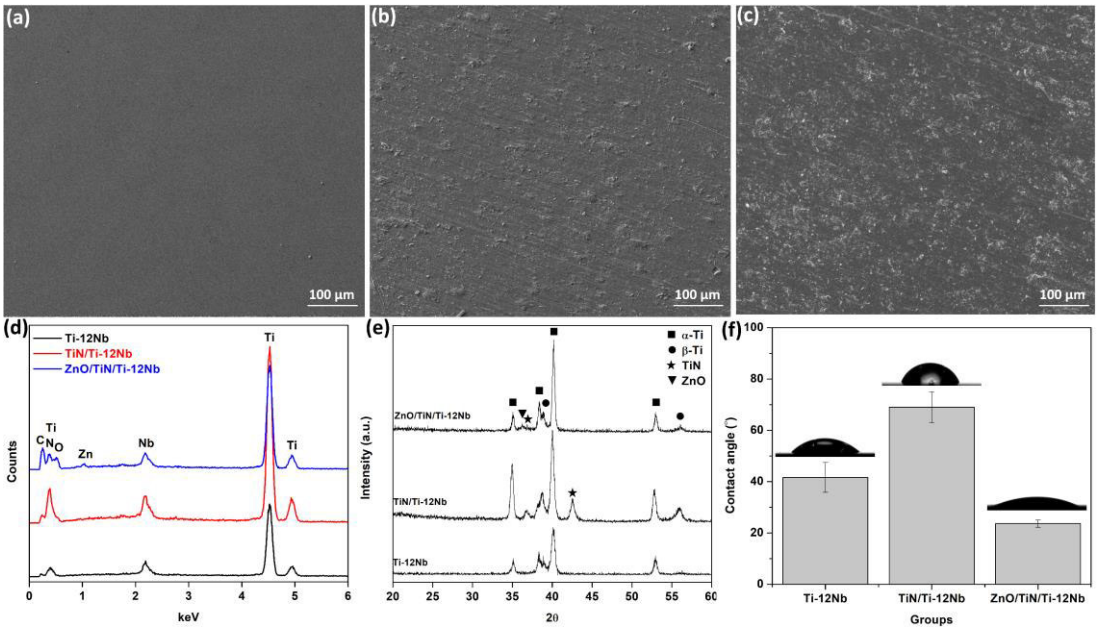

Fig. 10.1. Physical characterization: SEM images of (a) Ti-12Nb, (b) TiN/Ti-12Nb, (c) ZnO/TiN/Ti-12Nb, (d) EDS spectra, (e) XRD patterns, and (f) contact angle values.

Mechanical properties are another key factor for load-bearing implant materials. The TiN/Ti-12Nb sample presented higher nanohardness and Young's modulus compared to Ti-12Nb alloy which is attributed to the formation of hard TiN phases. As expected, ZnO film depicted drastically lower nanohardness and Young's modulus. However, the ZnO/TiN/Ti-12Nb presented significantly higher microhardness values compared to the other samples, that may be explained by the heat treatment resulted in improvement of hardness of TiN layer and substrate possibly resulted from alterations in their microstructure.

Table 10.1. Hardness, Young's modulus, and Ra values.

Sample	*Nano hardness (GPa)*	*Young's Modulus (GPa)*	*Micro hardness ($HV_{0.5}$)*	*Average surface roughness-Ra (nm)*
Ti-12Nb	3.6 ± 0.3	96.9 ± 5.9	246 ± 16	15.2 ± 0.3
TiN/Ti-12Nb	6.8 ± 0.3	131.8 ± 7.0	332 ± 7	89.1 ± 0.1
ZnO/TiN/Ti-12Nb	0.5 ± 0.1	13.6 ± 1.2	444 ± 17	110.0 ± 0.4

The SEM cross-section image and micro scratch test results of coatings are shown in Fig. 10.2. A continuous and uniform double layer of coatings can be seen clearly in Fig. 10.2a, where the thickness

of TiN and ZnO film was approximately 1 μm and 650 nm, respectively. Regarding the scratch test results, the acoustic emission signal and frictional force versus applied load together with optical microscopy images of scratch scars are presented in Figs. 10.2b and c. As marked on graphs, both samples were failed at very similar loads, which were 6.4 ± 0.4 N and 5.8 ± 0.8 N for TiN/Ti-12Nb and ZnO/TiN/Ti-12Nb sample, respectively. Slight decrement on average adhesion strength with relatively higher standard deviation for ZnO/TiN/Ti-12Nb sample may be explained by the mismatches of the coefficient of thermal expansion (CTE) between TiN and substrate, which led to excessive stresses at interface resulted from applied heat treatment [20].

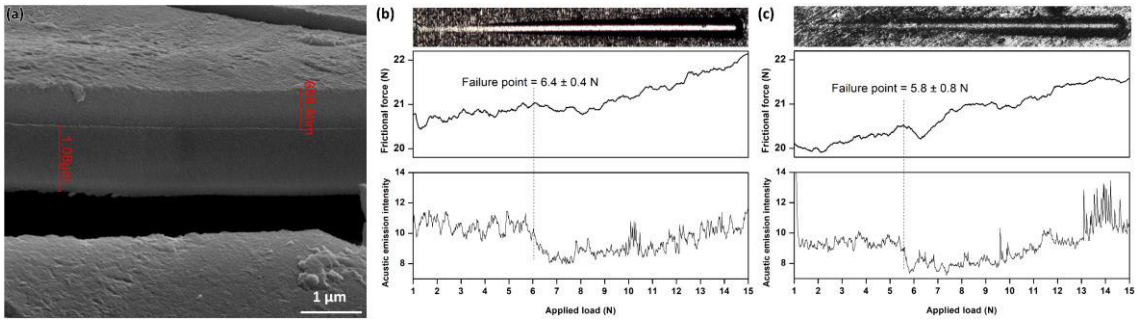

Fig. 10.2. The cross-section SEM image of (a) ZnO/TiN/Ti-12Nb sample, and scratch test results of (b) TiN/Ti-12Nb and (c) ZnO/TiN/Ti-12Nb samples.

10.3.2. Corrosion behaviour

Corrosion behaviour of an implant is one of the main factors that determine its service period. Lower corrosion resistance can lead to release of incompatible metal ions, that can cause infections around implants [30]. The results of the corrosion tests and the proposed electrical equivalent circuits (EECs) are given in Fig. 10.3; the E_{OCP}, extracted potentiodynamic polarization parameters, and electrochemical parameters obtained from the proposed EECs are shown in Table 10.2 and Table 10.3, respectively. Both coating samples presented drastically higher E_{OCP}, $E_{(i\sim0)}$ and lower i_{pass} (taken at 0.5 V) values compared to the uncoated sample pointing their lower tendency to corrosion and corrosion rate, respectively. While Ti-12Nb sample showed a well-defined passivation plateau, both coatings presented progressive increase of current density in the passive region, that can be explained by oxidation of coating surfaces as reported for oxidation of TiN phases [14,31].

Regarding the EIS results, both coating samples presented larger diameter of semi-circle in Nyquist diagram (Fig. 10.2b) compared to the uncoated substrate indicating their better corrosion resistance as in agreement with the potentiodynamic polarization results. In case of Bode diagram given in Fig. 10.3c, the constant values of |Z| and near to 0° of phase angle at high frequency range are the

response of electrolyte resistance. At the middle frequency range, the phase angle of all samples decreased near 90° suggesting capacitive behaviour of formed film on their surfaces. Since the phase angle of the substrate and TiN coated samples was slightly increased at low frequency range, ZnO/TiN/Ti-12Nb sample remained relatively constant owing to better quality of the coating. The improvement on corrosion behaviour of substrate can be observed by EECs simulated data in Table 10.3, where the R_1 and Q_1 represents resistance and constant phase element (CPE) of passive oxide film, TiN coating, ZnO coating on substrate, TiN/Ti-12Nb, and ZnO/TiN/Ti12Nb samples, respectively. The R_2 and Q_2 correspond to resistance and CPE of TiN layer for ZnO/TiN/Ti-12Nb sample. TiN/Ti-12Nb sample presented higher resistance (R_1) and lower CPE (Q_1) values than the values of the substrate, indicating improvement of corrosion resistance with TiN coating. TiN coatings are commonly used to increase the corrosion resistance of metallic biomaterials as well, as also similar improvement has been reported for TiN coated on Ti [2,14], Ti-6Al-4 V [5], Ti-6Al-7Nb [7], Ti-35Nb-7Zr-5Ta [13], and Ti-25Ta-25Nb alloy [8]. Regarding ZnO/TiN/Ti-12Nb sample, two series RQ circuits are proposed, where the first one represents (R_1Q_1) ZnO coating and the second one (R_2Q_2) represents TiN coating on substrate. According to the simulated data, lower R_1 value and higher Q_1 of ZnO/TiN/Ti-12Nb sample indicating drastically lower corrosion resistance of ZnO layer. The observed lower n_1 value for ZnO/TiN/Ti-12Nb sample may be explained by its surface roughness, where the n value is associated with surface heterogeneities and roughness [32]. The obtained higher R_2 and n_2 values indicate better protective resistance of TiN layer on ZnO/TiN/Ti-12Nb sample, which may be attributed to the closure of the surface irregularities by ZnO resin precursor through spin coating and also, the heat treatment of ZnO/TiN/Ti-12Nb sample may induce morphological alterations on TiN layer. Overall, since R_1 and R_2 are serial connected, the total resistance of ZnO/TiN/Ti-12Nb sample is defined as R_1+R_2, which is significantly higher than the resistance of other samples suggesting better corrosion resistance.

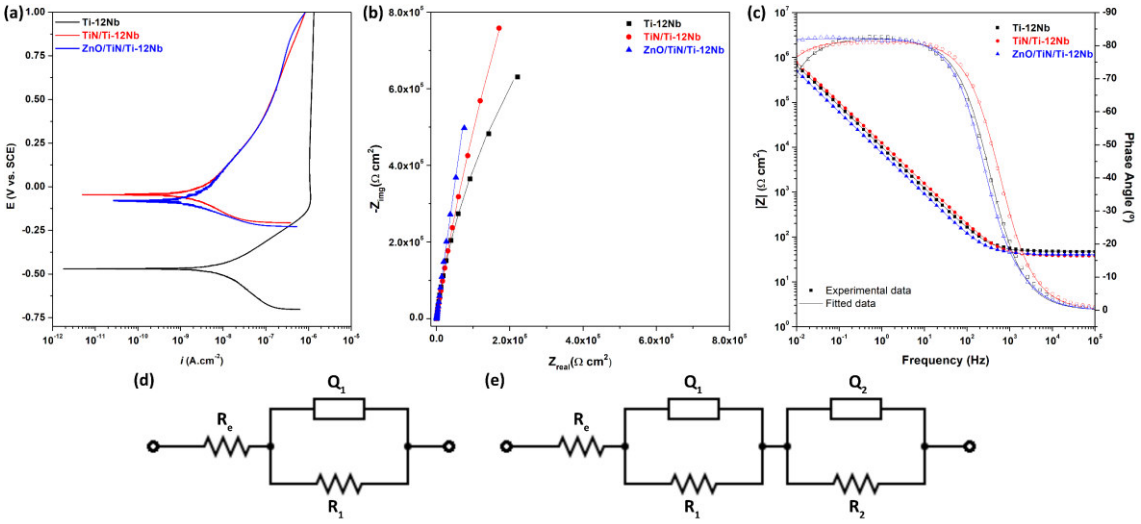

Fig. 10.3. Corrosion behaviour: (a) Representative potentiodynamic polarization curves, (b) Nyquist diagram, (c) Bode diagram, and EECs for (d) Ti-12Nb and TiN/Ti-12Nb, and (e) ZnO/TiN/Ti-12Nb.

Table 10.2. Corrosion potential ($E_{i=0}$) and passivation current density (i_{pass}) for for Ti-12Nb, TiN/Ti-12Nb and ZnO/TiN/Ti-12Nb samples.

Sample	E_{OCP} (V_{SCE})	$E_{i=0}$ (V_{SCE})	i_{pass} ($\mu A.cm^{-2}$)
Ti-12Nb	–0.48 ± 0.01	–0.47 ± 0.01	1.11 ± 0.08
TiN/Ti-12Nb	0.02 ± 0.02	–0.04 ± 0.01	0.12 ± 0.02
ZnO/TiN-12Nb	–0.01 ± 0.02	–0.11 ± 0.03	0.15 ± 0.01

Table 10.3. Electrochemical parameters obtained from the proposed EECs.

Parameters	Ti-12Nb	TiN/Ti-12Nb	ZnO/TiN-12Nb
R_1 ($x10^6$ $\Omega.cm^2$)	3.77 ± 0.68	7.67 ± 1.54	0.91 ± 0.11
Q_1 ($x10^{-5}$ $S\ s^n\ cm^{-2}$)	1.8 ± 0.2	1.4 ± 0.2	6.3 ± 0.9
n_1	0.91 ± 0.01	0.91 ± 0.01	0.75 ± 0.05
R_2 ($x10^6$ $\Omega.cm^2$)	–	–	15.3 ± 2.7
Q_2 ($x10^{-5}$ $S\ s^n\ cm^{-2}$)	–	–	1.5 ± 0.4
n_2	–	–	0.95 ± 0.02

10.3.3. Tribocorrosion behaviour

The load-bearing implants such as hip implant are subjected to tribocorrosion phenomena, which is described as material degradation resulted from the interaction between a mechanical load and corrosive media in tribological contact [33]. Tribocorrosion behaviour was studied at OCP condition that

is closer to simulation of a real implant system, and the results are given in Fig. 10.4. As can be seen from OCP-COF evolution graph, as soon as sliding started the OCP of Ti-12Nb suddenly dropped from −0.44 ± 0.03 V to −0.90 ± 0.03 V due to depassivation of wear track resulted from mechanical destruction of the formed passive film. Subsequently, the OCP slightly tended to increase, while its COF was around 0.4 until 10 mins of sliding. Afterwards, the COF and OCP of Ti-12Nb sample was increased to around 0.63 ± 0.02 and 0.48 ± 0.03 V, respectively, possibly due to formation of oxide patches in wear track giving a limited protection against corrosion [27,34]. These oxide formations can be clearly observed on SEM wear track images and also evidenced by detected oxygen element on its EDS spectra. While the oxide patches are giving a limited protection against corrosion and wear, they can detach after reaching a critical point resulted from getting thicker during sliding, as can be seen by observed local decrements on COF and OCP evolution. Immediately after sliding, the OCP increased close to the values before sliding due to repassivation of the worn area.

Regarding TiN coated sample, when sliding started the OCP was gradually decreased from 0.09 ± 0.04 V to −0.46 ± 0.01 V and then a sharp decrement observed on COF and OCP possibly resulted from local destruction of coating. As pointed on OCP graph, probably the TiN coating was totally removed roughly after 10 mins of sliding resulted in sharp drop of OCP values to the similar OCP values of substrate under sliding. Afterwards, compared to Ti-12Nb, relatively more and larger decrements were observed on OCP and COF due to contribution of hard TiN wear debris in contact as reported for TiN coated cp-Ti (grade 4) in NaCl solution under 1 N of normal load [14]. As can be seen on wear track images, TiN coated sample showed deeper grooves and less oxide patch formation that may be explained by the same manner, resulted from freely moved wear debris in contact which can act as extra abrasives on sliding surfaces. As it can be seen in Fig. 10.4, counter body against TiN coating sample presented more damage as compared to other groups due to hard TiN wear debris in tribological contact. Also, the transferred material on counter body for Ti-12Nb and TiN coated sample can be observed.

In case of ZnO coated sample, as soon as sliding started, instead of a sharp drop observed on the substrate or TiN coated sample, a gradual drop was recorded on OCP due to a progressive damage given to the coating. After around 900 s, unlike other groups of samples, both OCP and COF exhibited a relatively smoother evolution, that may be linked to the less overall damage given to the surface that can also be observed on the wear track image, where no evidence of abrasion grooves was detected. Also, higher amounts of N, Zn and O elements on its EDS spectra suggested that the coatings were not removed from the wear track. Similar to the worn sample surface, the corresponding counter body surface also presented a smoother surface as compared to other worn counter bodies. ZnO, as showed

by nanoindentation results, is a softer material, and smeared over contact region during sliding. Prasad and Zabinski [35] reported that the ZnO thin film coated on stainless steel drastically improved the wear resistance due to smearing of ZnO layer. Similarly, smearing of the ZnO film apparently played an important role on obtaining much smaller wear volume losses compared to the other groups of samples, as can be seen on their 3D wear track profiles and measured wear volume loss values given in Fig. 10.4.

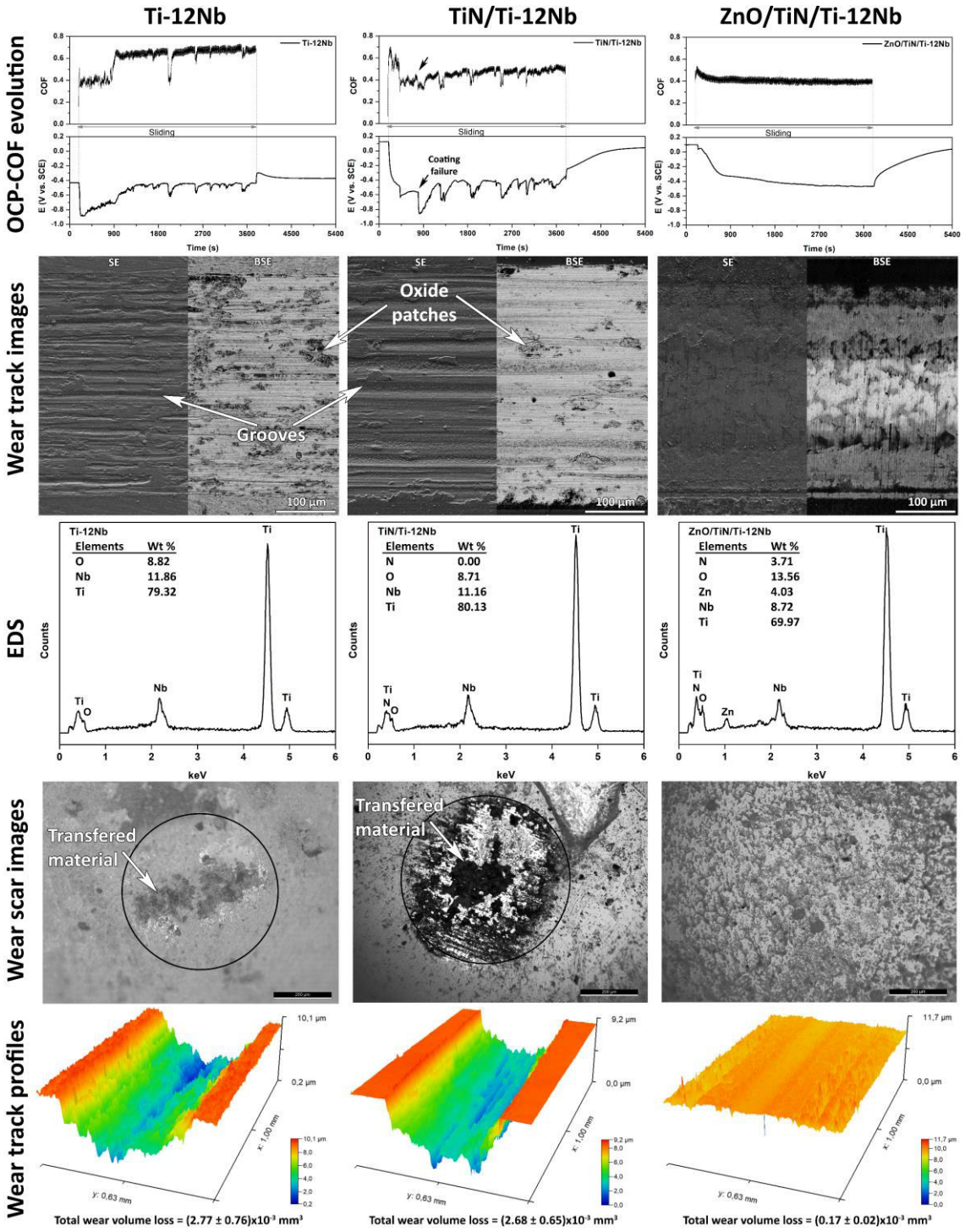

Fig. 10.4. The OCP-COF evolutions, SE and BSE wear track images, OM wear scar images on counter body, EDS spectra of wear tracks, and 3D wear track profiles taken at centre of Ti-12Nb, TiN/Ti-12Nb, and ZnO/TiN/Ti-12Nb samples.

The proposed tribocorrosion mechanisms for tested samples are schematically presented in Fig. 10.5. The uncoated and TiN coated samples showed dominantly combination of abrasive and adhesive wear evidenced by parallel grooves, adhered oxidised patches and transferred material. Similar

wear mechanism of Ti-12Nb was previously observed in 9 g/l NaCl solution under 1 N normal load [27]. The failure of TiN coating may be explained by its brittleness and surface defects such as pores and cavities [31]. Also, the mismatch between Young's modulus of substrate (96.9 ± 5.9) and TiN film (131.8 ± 7.0) may led to formation of cracks in hard TiN film under mechanical action. Totally different wear behaviour was observed in the case of ZnO coated sample, where no evidence of grooves, oxide patch, or significant amount of transferred material was observed probably due to the smearing of ZnO film that possible played a barrier role against wear. Besides the smearing of ZnO film, the higher microhardness of ZnO/TiN/Ti-12Nb sample is another reason for its better wear resistance behaviour.

Although this study showed that ZnO coatings can have a positive influence on the improvement of tribocorrosion resistance of TiN hard-coated lower Young's modulus Ti alloys, failure mechanisms of these coatings needs to be studied more in detail. Nevertheless, considering that the continuous release Zn ions may be toxic to the human cells, the composition of such coatings need to be carefully adjusted and their biological response should be investigated in vitro and in vivo.

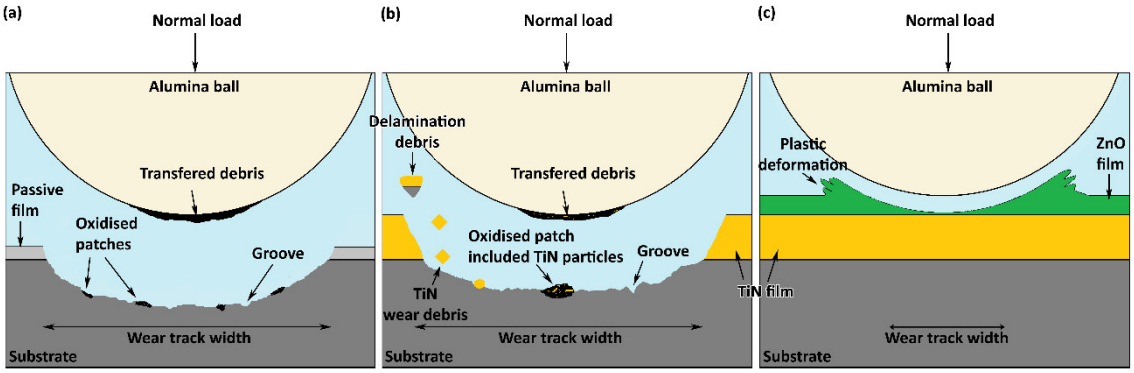

Fig. 10. 5. Schematic illustration of tribocorrosion mechanisms of uncoated Ti-12Nb (a), TiN/Ti-12Nb (b), and ZnO/TiN/Ti-12Nb (c) samples.

10.4. Conclusion

TiN coating presented lower tendency to corrosion, lower corrosion rate, higher corrosion resistance, and better capacitive behaviour compared to Ti-12Nb alloy due to nobler and thicker TiN layer compared to passive film formed on Ti-12Nb alloy. However, TiN coating did not improve the tribocorrosion resistance of Ti-12Nb alloy that was governed by failure of coating. The corrosion behaviour was further improved by ZnO coating possibly due to closure of surface defects such as pores and cavities on TiN film. ZnO coating also led to an improvement on the tribocorrosion resistance due to increased microhardness and physical barrier role of the smeared of ZnO film.

Acknowledgements

This work is supported by FCT with the reference project UID/EEA/04436/2019, together with M-ERA-NET/0001/2015. C.R. Grandini and I.R. Rodrigues are grateful to Brazilian agencies CNPq (grant 308.204/2017-4) and FAPESP-M-ERA-NET (grant 2015/50.280-5), for the financial support. I. Çaha is grateful for the financial support through a Ph.D. grant under the NORTE-08-5369-FSE-000012 project. The authors would also like to acknowledge Dr. Andrea Zille for the provision of the contact angle measurements.

References

[1] I. Çaha, A.C. Alves, L.A. Rocha, F. Toptan, A Review on Bio-functionalization of β-Ti Alloys, J. Bio-Tribo-Corrosion. 6 (2020) 1–31. doi:10.1007/s40735-020-00432-0.

[2] H. Aghajani, M.S. Motlagh, Effect of temperature on surface characteristics of nitrogen ion implanted biocompatible titanium, J. Mater. Sci. Mater. Med. 28 (2017) 29. doi:10.1007/s10856-016-5843-x.

[3] M.A. Arenas, T.J. Tate, A. Conde, J. De Damborenea, Corrosion behaviour of nitrogen implanted titanium in simulated body fluid, Br. Corros. J. 35 (2000) 232–236. doi:10.1179/000705900101501308.

[4] V.M.C.A. Oliveira, A.M. Vazquez, C. Aguiar, A. Robin, M.J.R. Barboza, Protective effect of plasma-assisted PVD deposited coatings on Ti-6Al-4V alloy in NaCl solutions, Mater. Des. 88 (2015) 1334–1341. doi:10.1016/j.matdes.2015.08.158.

[5] A. Scerri, J. Buhagiar, S. Banfield, J.C. Avelar-Batista Wilson, J. Housden, A. Leyland, A. Matthews, G. Cassar, Corrosion behaviour of triode plasma diffusion treated and PVD TiN-coated Ti-6Al-4V in acidified aqueous chloride environments, Surf. Coatings Technol. 280 (2015) 185–193. doi:10.1016/j.surfcoat.2015.08.040.

[6] J. Kim, W.J. Lee, H.W. Park, Mechanical properties and corrosion behavior of the nitriding surface layer of Ti-6Al-7Nb using large pulsed electron beam (LPEB), J. Alloys Compd. 679 (2016) 138–148. doi:10.1016/j.jallcom.2016.04.060.

[7] L. Thair, U.K. Mudali, N. Bhuvaneswaran, Nitrogen ion implantation and in vitro corrosion behavior of as-cast Ti – 6Al – 7Nb alloy, 44 (2002) 2439–2457.

[8] S.I. Drob, C. Vasilescu, P. Drob, E. Vasilescu, D.M. Gordin, T. Gloriant, Corrosion Behaviour of

Nitrogen-Implantation Ti-Ta-Nb Alloy in Physiological Solutions Simulating Real Conditions from Human Body, Jom. 67 (2015) 818–829. doi:10.1007/s11837-015-1351-6.

[9] F. Galliano, E. Galvanetto, S. Mischler, D. Landolt, Tribocorrosion behavior of plasma nitrided Ti-6Al-4V alloy in neutral NaCl solution, Surf. Coatings Technol. 145 (2001) 121–131. doi:10.1016/S0257-8972(01)01309-3.

[10] A. Shenhar, I. Gotman, S. Radin, P. Ducheyne, E.Y. Gutmanas, Titanium nitride coatings on surgical titanium alloys produced by a powder immersion reaction assisted coating method: Residual stresses and fretting behavior, Surf. Coatings Technol. 126 (2000) 210–218. doi:10.1016/S0257-8972(00)00524-7.

[11] M.V. Ermolenko, S.M. Zavadski, D.A. Golosov, S.N. Melnikov, E.G. Zamburg, Tribological behavior of TiN films depositid by reactive magnetron sputtering under low pressure, J. Frict. Wear. 37 (2016) 289–292. doi:10.3103/S1068366616030065.

[12] W. Cui, G. Qin, J. Duan, H. Wang, A graded nano-TiN coating on biomedical Ti alloy: Low friction coefficient, good bonding and biocompatibility, Mater. Sci. Eng. C. 71 (2017) 520–528. doi:10.1016/j.msec.2016.10.033.

[13] X. Zhao, P. Zhang, X. Wang, Y. Chen, H. Liu, L. Chen, Y. Sheng, W. Li, In-situ formation of textured TiN coatings on biomedical titanium alloy by laser irradiation, J. Mech. Behav. Biomed. Mater. 78 (2018) 143–153. doi:10.1016/j.jmbbm.2017.11.019.

[14] I. Çaha, A.C. Alves, L.J. Affonço, P.N. Lisboa-Filho, J.H.D. da Silva, L.A. Rocha, A.M.P. Pinto, F. Toptan, Corrosion and tribocorrosion behaviour of titanium nitride thin films grown on titanium under different deposition times, Surf. Coatings Technol. 374 (2019) 878–888. doi:10.1016/j.surfcoat.2019.06.073.

[15] A. Samanta, M. Bhattacharya, I. Ratha, H. Chakraborty, S. Datta, J. Ghosh, S. Bysakh, M. Sreemany, R. Rane, A. Joseph, S. Mukherjee, B. Kundu, M. Das, A.K. Mukhopadhyay, Nano- and micro-tribological behaviours of plasma nitrided Ti6Al4V alloys, J. Mech. Behav. Biomed. Mater. 77 (2018) 267–294. doi:10.1016/j.jmbbm.2017.09.013.

[16] H.H. Huang, C.H. Hsu, S.J. Pan, J.L. He, C.C. Chen, T.L. Lee, Corrosion and cell adhesion behavior of TiN-coated and ion-nitrided titanium for dental applications, in: Appl. Surf. Sci., 2005: pp. 252–256. doi:10.1016/j.apsusc.2004.10.144.

[17] J. Karbowniczek, L. Cordero-Arias, S. Virtanen, S.K. Misra, E. Valsami-Jones, L. Tuchscherr, B. Rutkowski, K. Górecki, P. Bała, A. Czyrska-Filemonowicz, A.R. Boccaccini, Electrophoretic deposition of organic/inorganic composite coatings containing ZnO nanoparticles exhibiting antibacterial properties, Mater. Sci. Eng. C. 77 (2017) 780–789. doi:10.1016/j.msec.2017.03.180.

[18] L. Zhang, Q. Gao, Y. Han, Zn and Ag Co-doped Anti-microbial TiO2 Coatings on Ti by Micro-arc Oxidation, J. Mater. Sci. Technol. 32 (2016) 919–924. doi:10.1016/j.jmst.2016.01.008.

[19] X. He, X. Zhang, X. Wang, L. Qin, Review of Antibacterial Activity of Titanium-Based Implants' Surfaces Fabricated by Micro-Arc Oxidation, Coatings. 7 (2017) 45. doi:10.3390/coatings7030045.

[20] Z. Ding, Q. He, Z. Ding, C. Liao, D. Chen, L. Ou, Fabrication and performance of ZnO doped tantalum oxide multilayer composite coatings on TI6AL4V for orthopedic application, Nanomaterials. 9 (2019). doi:10.3390/nano9050685.

[21] K. Yusa, O. Yamamoto, M. Fukuda, S. Koyota, Y. Koizumi, T. Sugiyama, In vitro prominent bone regeneration by release zinc ion from Zn-modified implant, Biochem. Biophys. Res. Commun. 412 (2011) 273–278. doi:10.1016/j.bbrc.2011.07.082.

[22] H. Hu, W. Zhang, Y. Qiao, X. Jiang, X. Liu, C. Ding, Antibacterial activity and increased bone marrow stem cell functions of Zn-incorporated TiO 2 coatings on titanium, Acta Biomater. 8 (2012) 904–915. doi:10.1016/j.actbio.2011.09.031.

[23] H.J. Song, Z.Z. Zhang, X.H. Men, Z.Z. Luo, A study of the tribological behavior of nano-ZnO-filled polyurethane composite coatings, Wear. 269 (2010) 79–85. doi:10.1016/j.wear.2010.03.011.

[24] U.S. Mbamara, B. Olofinjana, O.O. Ajayi, C. Lorenzo-Martin, E.I. Obiajunwa, E.O.B. Ajayi, Friction and wear behavior of nitrogen-doped ZnO thin films deposited via MOCVD under dry contact, Eng. Sci. Technol. an Int. J. 19 (2016) 956–963. doi:10.1016/j.jestch.2016.01.003.

[25] B. Zhang, T. Kong, W. Xu, R. Su, Y. Gao, G. Cheng, Surface functionalization of zinc oxide by carboxyalkylphosphonic acid self-assembled monolayers, Langmuir. 26 (2010) 4514–4522. doi:10.1021/la9042827.

[26] L.D. Trino, L.F.G. Dias, L.G.S. Albano, E.S. Bronze-Uhle, E.C. Rangel, C.F.O. Graeff, P.N. Lisboa-Filho, Zinc oxide surface functionalization and related effects on corrosion resistance of titanium

implants, Ceram. Int. 44 (2018) 4000–4008. doi:10.1016/j.ceramint.2017.11.195.

[27] I. Çaha, A.C. Alves, C. Chirico, S.A. Tsipas, I.R. Rodrigues, A.M.P. Pinto, C.R. Grandini, L.A. Rocha, E. Gordo, F. Toptan, Interactions between wear and corrosion on cast and sintered Ti-12Nb alloy in comparison with the commercial Ti-6Al-4V alloy, Corros. Sci. 176 (2020) 108925. doi:10.1016/j.corsci.2020.108925.

[28] J.I. Rosales-Leal, M.A. Rodríguez-Valverde, G. Mazzaglia, P.J. Ramón-Torregrosa, L. Díaz-Rodríguez, O. García-Martínez, M. Vallecillo-Capilla, C. Ruiz, M.A. Cabrerizo-Vílchez, Effect of roughness, wettability and morphology of engineered titanium surfaces on osteoblast-like cell adhesion, Colloids Surfaces A Physicochem. Eng. Asp. 365 (2010) 222–229. doi:10.1016/j.colsurfa.2009.12.017.

[29] X. Liu, J.Y. Lim, H.J. Donahue, R. Dhurjati, A.M. Mastro, E.A. Vogler, Influence of substratum surface chemistry/energy and topography on the human fetal osteoblastic cell line hFOB 1.19: Phenotypic and genotypic responses observed in vitro, Biomaterials. 28 (2007) 4535–4550. doi:10.1016/j.biomaterials.2007.06.016.

[30] L.C. Zhang, L.Y. Chen, A Review on Biomedical Titanium Alloys: Recent Progress and Prospect, Adv. Eng. Mater. 21 (2019) 1–29. doi:10.1002/adem.201801215.

[31] I.M. Pohrelyuk, V.M. Fedirko, O.V. Tkachuk, R.V. Proskurnyak, Corrosion resistance of Ti–6Al–4V alloy with nitride coatings in Ringer's solution, Corros. Sci. 66 (2013) 392–398. doi:10.1016/j.corsci.2012.10.005.

[32] L. Thair, U.K. Mudali, N. Bhuvaneswaran, K.G.M. Nair, R. Asokamani, B. Raj, Nitrogen ion implantation and in vitro corrosion behavior of as-cast Ti-6Al-7Nb alloy, Corros. Sci. 44 (2002) 2439–2457. doi:10.1016/S0010-938X(02)00034-3.

[33] M.E. Orazem, B. Tribollet, Electrochemical Impedance Spectroscopy, 2008. doi:10.1002/9780470381588.

[34] S. Cao, S. Mischler, Modeling tribocorrosion of passive metals – A review, Curr. Opin. Solid State Mater. Sci. (2018) 1–15. doi:10.1016/j.cossms.2018.06.001.

[35] I. Çaha, A.C. Alves, P.A.B. Kuroda, C.R. Grandini, A.M.P. Pinto, L.A. Rocha, F. Toptan, Degradation behavior of Ti-Nb alloys: Corrosion behavior through 21 days of immersion and tribocorrosion behavior against alumina, Corros. Sci. 167 (2020) 108488.

doi:10.1016/j.corsci.2020.108488.

[36] I. Çaha, A. Alves, C. Chirico, A. Pinto, S. Tsipas, E. Gordo, F. Toptan, Corrosion and Tribocorrosion Behavior of Ti-40Nb and Ti-25Nb-5Fe Alloys Processed by Powder Metallurgy, Metall. Mater. Trans. A Phys. Metall. Mater. Sci. 51 (2020) 3256–3267. doi:10.1007/s11661-020-05757-6.

[37] S. V. Prasad, J.J. Nainaparampil, J.S. Zabinski, Tribological behavior of alumina doped zinc oxide films grown by pulsed laser deposition, J. Vac. Sci. Technol. A Vacuum, Surfaces, Film. 20 (2002) 1738–1743. doi:10.1116/1.1501567.

[38] B. Liu, Z. Yang, J. Zhou, Tribological behavior of polyimide/zinc oxide hybrid films, Adv. Mater. Res. 105–106 (2010) 438–440. doi:10.4028/www.scientific.net/AMR.105-106.438.

[39] S. Wang, S. Ge, D. Zhang, Comparison of tribological behavior of nylon composites filled with zinc oxide particles and whiskers, Wear. 266 (2009) 248–254. doi:10.1016/j.wear.2008.06.019.

[40] H. Chakraborty, A. Sinha, N. Mukherjee, D. Ray, P. Protim Chattopadhyay, A study on nanoindentation and tribological behaviour of multifunctional ZnO/PMMA nanocomposite, Mater. Lett. 93 (2013) 137–140. doi:10.1016/j.matlet.2012.11.075.

Chapter 11: General discussion, conclusions and future works

General discussion, conclusions and future works

11.1. General discussion

The three main clinical concerns for load-bearing implants were addressed in Chapter 1, which were stress-shielding effect, low tribocorrosion resistance, and lack of bioactivity. Therefore, the main aim of this project was developing a novel multifunctional material through bio-functionalization of MMC and TiN thin film surfaces by using electrochemical treatment and PVD treatment, respectively, with incorporation of bioactive agents such as calcium, phosphorus and zinc oxide. Also, the investigation of degradation mechanisms of bio-functionalized hybrid surfaces and TiN/ZnO coated surfaces were studied. A systematic and multidisciplinary approach was carried out in order to reach these aims based on new scientific knowledge. The development of this project from initial to final steps comprised with several independent works, which were reported in different scientific papers.

Before surface functionalization, the degradation behavior of novel low Young's modulus β-type Ti alloys, which were selected to reduce stress shielding effect, have been investigated through different corrosion and tribocorrosion conditions. The corrosion and tribocorrosion behavior of α + β-type Ti-Nb and β-type Ti-Nb alloys were reported in three scientific papers from Chapter 3 to Chapter 5. The Ti-12Nb alloy was processed to obtain a α + β alloy, while the Ti-40Nb was studied to obtain fully β alloy. As it well known in literature, in order to fully diffuse the Nb powders in Ti matrix, high temperatures are needed, leading some structural and mechanical problems. Therefore, Ti-25Nb-5Fe alloy was processed with small addition of Fe, which is one of the most effective β stabilizer element, presented fully dispersed alloying elements in Ti matrix and also showed better corrosion and tribocorrosion behavior as compared to Ti-40Nb alloy (Chapter 3). Regarding the cast alloys, the degradation behavior of Ti-15Nb and Ti-40Nb alloys, in comparison with commercial Ti-6Al-4V, was studied by performing corrosion tests during prolonged times of immersion, as well, by performing tribocorrosion tests against a hard and inert counter material. While α + β-type alloy presented a comparable degradation behavior, β-type Ti-Nb alloy showed drastically lower tribocorrosion resistance, mainly due to the low strain hardening behavior of the β phase. Regarding to the processing route, which is reported in Chapter 5, Ti-12Nb alloy processed by P/M presented slightly better degradation resistance resulted from its more uniform and homogenous microstructure.

The low tribocorrosion behavior of β-type Ti-Nb alloys was aimed to be improved by two preliminary studies that reported in scientific research papers as showed in Chapter 6 and Chapter 7. The tribocorrosion resistance of β-type Ti-40Nb alloy was aimed to be improved by the formation of an oxide nanotubular structure, however, it has been reported that the nanotubes grown on Ti have significantly poor adhesion to the substrate. In Chapter 6, in order to overcome the poor adhesion of the TNT layer to the bare metal, an additional anodic treatment was performed in fluoride-free electrolyte after the formation of the nanotubes in the conventional fluoride-containing electrolyte in order to form an additional oxide layer at the interface between the bare metal and the nanotubes. Results showed that the adhesion, corrosion, and tribocorrosion behavior of the nanotubular layer was drastically improved due to the formation of an additional oxide layer in the interface, and a following heat treatment yielded with a crystalline transformation. In Chapter 7, a preliminary understanding to the influence of the deposition conditions on the corrosion and tribocorrosion behavior of TiN thin films produced by RF sputtering on cp-Ti grade 4 was studied in a 9 g/L NaCl solution at body temperature. Increased coating thickness and promotion of the formation of Ti_2N phase gave a resistance against abrasive wear, adhesive wear, and plastic deformation, thus, led to obtain a clear improvement on the tribocorrosion resistance.

In order to overcome on the major limiting factors for non-toxic and low Young's modulus β-type Ti alloys, a work aimed to develop a novel multi-functional material not only to improve the tribocorrosion behavior of β-type Ti alloys, but also to improve their biological behavior. For this reason, a β-type Ti-25Nb-5Fe alloy reinforced with hard TiN particles was bio-functionalized through MAO treatment with incorporation of Ca and P (Chapter 8). Also, the corrosion and tribocorrosion behavior of this novel material was investigated in physiological solution at body temperature. Results revealed that although bio-functionalization drastically improved the corrosion and tribocorosion behavior of the unreinforced and reinforced samples, the bio-functionalized reinforced β-type alloy presented the best tribocorrosion behavior due to the load-carrying role of the hard reinforcement phase. Similarly, the reinforced β-type Ti-40Nb alloy with hard TiN particles was functionalized through TNT layer formation by anodic treatment, and its degradation behavior was investigated by corrosion and tribocorrosion tests (Chapter 9). Results indicated that the corrosion and tribocorrosion behavior of sample was significantly improved through surface functionalization due to the formation of a well-adhered anatase-rutile TiO_2-based nanotubular layer.

In Chapter 10, TiN and ZnO duplex coatings were employed onto cast Ti-12Nb alloy to improve its tribocorrosion resistance and biological properties. While single TiN coating did not give enough support against sliding most probably due to the mismatch between Young's modulus of TiN and Ti-12Nb substrate, ZnO/TiN coating presented excellent wear resistance due to smeared inorganic ZnO layer.

11.2. Final conclusions

This thesis focused on the development of a novel multi-functional material to overcome the major limiting factors for non-toxic and low Young's modulus β-type Ti-Nb alloys to be used in load-bearing biomedical applications. The following conclusions can be drawn:

❖ The α + β-type cast and P/M Ti-Nb alloys presented better corrosion and tribocorrosion resistance than their both β-type Ti-Nb alloys. The better corrosion resistance of α + β-type alloys evidenced by their higher resistance of the native oxide film and higher constant phase element values compared to β-type alloys, the low tribocorrosion behavior of β-type alloys was resulted from poor strain hardening of β phase during sliding.

Bio-functionalization by anodic treatment:

❖ TNT surfaces formed conventionally on Ti-40Nb alloy by anodic treatment presented poor adhesion. The adhesion of nanotubes was improved drastically by a combined route, where a second-step anodic treatment in fluoride-free electrolyte resulted in formation of an additional oxide layer in the interface, and a following heat treatment yielded with a crystalline transformation. The combination of formation of an additional oxide layer in the interface and heat treatment mainly played a role in improving the corrosion behavior by preventing the formation of defects at the interface thus blocking the penetration of electrolyte to the substrate.

❖ The Ti-40Nb/TiN composites functionalized through TNT formation presented excellent corrosion and tribocorrosion resistance due to the well adhered and wear resistant anatase-rutile nanotubular layer. While both TNT-formed alloy and MMC showed relatively similar tribocorrosion behavior mainly due to the protective behavior of the nanotubular layer, TNT formed MMC presented significantly better corrosion resistance due to the contribution of nobler reinforcement phases.

❖ The Ti-25Nb-5Fe/TiN composite bio-functionalized with incorporation Ca and P through MAO treatment showed improved corrosion and tribocorrosion as compared to the bare alloy, mostly due to the formation of a thick rutile-anatase TiO_2 layer. The MAO layer formed on the

composites stayed mostly intact after tribocorrosion due to the pillar effect given by the reinforcements.

Bio-functionalization by PVD coatings:

❖ TiN thin films produced by RF sputtering on Ti grade 4 can have a noticeable influence on the tribocorrosion mechanisms. It was shown that longer deposition time led to lower corrosion rate and led to obtain a clear improvement on the tribocorrosion resistance. Therefore, these results pointed that deposition time should be carefully adjusted according to the contact conditions of the targeted applications.

❖ The TiN layer coating on Ti-12Nb alloy did not show good tribocorrosion resistance. Further functionalization through ZnO coating presented promising corrosion and tribocorrosion resistance due to its nobler nature and physical barrier role of the smeared ZnO film in the contact region, respectively.

Thus, from the results obtained during this PhD work, it can be concluded that developed novel multi-functional material by hard TiN particle reinforcement following by bio-functionalization of its surface can be considered as an implant material for load-bearing biomedical applications.

11.3. Future works

The novel-developed multi-functional materials are promising for load-bearing biomedical applications. However, further improvements upon the current findings and proposed a topic may bring new insights to the proposed system as follow:

❖ Since the mechanical properties of load-bearing implants are crucial for a long-time lifespan of implants, the mechanical behavior of developed novel materials, namely, their mechanical strength, Young's modulus, fatigue properties, and fracture behavior need to be deeply investigated by using compression tests, ultrasound technique, and nano-micro indentations.

❖ The MMCs were processed as a bulk material that most probably may lead an increase in Young's modulus of β-type Ti alloys. In order to avoid that possible increment, MMCs are suggested to be processed as functionally graded metal matrix composites (FGMMCs) through a gradually increased amount of hard reinforcement particles from core to the surface.

❖ The degradation behavior of the developed materials has been investigated by different corrosion and tribocorrosion tests in physiological solutions. However, the real environment of implants is more complex. Therefore, it is suggested to study the corrosion and tribocorrosion tests in electrolytes including proteins and micro-organisms. Also, the fretting tribocorrosion behavior of

these materials should be employed, since some parts of hip implants are under micro and nano motion during human moving.

- A multilayer hard coating can be employed instead of a single TiN coating to overcome the mismatch between Young's modulus of the substrate and hard coatings. Also, the influence of sustained release of Zn ions on degradation and anti-bacterial behavior needs to be employed by using long-term immersion and cell culture tests, respectively.
- *In vitro* and *in vivo* biological studies should be performed to evaluate the biological performance of the novel materials.